

1-1-2002

Controlled foaming of polystyrene using supercritical CO₂.

Christopher M. Stafford
University of Massachusetts Amherst

Follow this and additional works at: https://scholarworks.umass.edu/dissertations_1

Recommended Citation

Stafford, Christopher M., "Controlled foaming of polystyrene using supercritical CO₂." (2002). *Doctoral Dissertations 1896 - February 2014*. 1030.

https://scholarworks.umass.edu/dissertations_1/1030

This Open Access Dissertation is brought to you for free and open access by ScholarWorks@UMass Amherst. It has been accepted for inclusion in Doctoral Dissertations 1896 - February 2014 by an authorized administrator of ScholarWorks@UMass Amherst. For more information, please contact scholarworks@library.umass.edu.



312066 0288 0616 9

- I. CONTROLLED FOAMING OF POLYSTYRENE USING SUPERCRITICAL CO₂.
- II. POLYMER ADSORPTION TO SILANE-MODIFIED SILICA SURFACES.
- III. PROTEIN ADSORPTION TO SILANE-MODIFIED SILICA SURFACES.

A Dissertation Presented

by

CHRISTOPHER M. STAFFORD

Submitted to the Graduate School of the
University of Massachusetts Amherst in partial fulfillment
of the requirements for the degree of

DOCTOR OF PHILOSOPHY

February 2002

Polymer Science and Engineering

© Copyright by Christopher M. Stafford 2002

All Rights Reserved

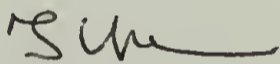
- I. CONTROLLED FOAMING OF POLYSTYRENE USING SUPERCRITICAL CO₂.
- II. POLYMER ADSORPTION TO SILANE-MODIFIED SILICA SURFACES.
- III. PROTEIN ADSORPTION TO SILANE-MODIFIED SILICA SURFACES.

A Dissertation Presented

by

CHRISTOPHER M. STAFFORD

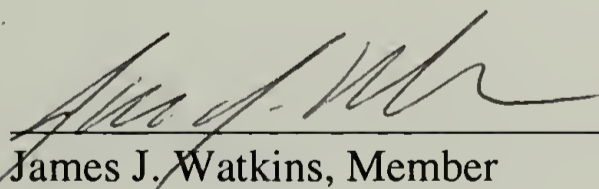
Approved as to style and content by:



Thomas J. McCarthy, Co-Chair



Thomas P. Russell, Co-Chair



James J. Watkins, Member



Thomas J. McCarthy, Department Head
Polymer Science and Engineering

DEDICATION

To my parents, Rod and Marie, who have taught me the importance of learning and, by way of example, the value of limitless patience and unselfish generosity, for these timeless lessons have been my guide and will continue to shape my future.

ACKNOWLEDGEMENTS

I have crossed paths with countless people who have helped mold and shape my development as a scientist and researcher. The two most obvious people are my advisors, Dr. McCarthy and Dr. Russell, whose guidance and direction propelled me to hone and polish my skills and my mind. They also allowed me the freedom to explore my abilities and follow my intuition wherever it may lead, yet provided the focus to keep me from straying too far. Special thanks also to my final committee member, Dr. Watkins, for his careful and critical examination of the research presented in this thesis.

I would like to thank the members, both past and present, of the McCarthy and Russell research groups. I enjoyed countless discussions and participated in numerous disagreements along the way, which not only allowed me to develop my reasoning ability but also my patience. In particular, I am grateful for the unconditional friendship of Meng Hsieh, Vivek Prabhu, and Jeff Youngblood. At times, it has been speculated that Jeff and I are two individuals sharing one mind, which makes us not only a rare combination but also half as smart as the rest of the world. I would also like to thank some of my classmates and labmates who have made my time here enjoyable: Kristi, Scott, Elbert, Lee, Joel, Ed, Didem, and Margarita.

Finally, I cannot begin to express my eternal gratitude to my parents, Rod and Marie, and my brother, Cory. Their patience and encouragement have been a source for solace during my tenure as a graduate student. And I want to thank Kristen, my continued source for inspiration and support as I close out this section of my career. May her love, encouragement, and patience remain unwavering.

ABSTRACT

- I. CONTROLLED FOAMING OF POLYSTYRENE USING SUPERCRITICAL CO₂.
- II. POLYMER ADSORPTION TO SILANE-MODIFIED SILICA SURFACES.
- III. PROTEIN ADSORPTION TO SILANE-MODIFIED SILICA SURFACES.

February 2002

CHRISTOPHER M. STAFFORD, B.S., UNIVERSITY OF SOUTHERN MISSISSIPPI

Ph.D., UNIVERSITY OF MASSACHUSETTS AMHERST

Directed by: Professors Thomas J. McCarthy and Thomas P. Russell

Part I of this dissertation focuses on the use of supercritical CO₂ as a blowing agent to produce microcellular foams. The goal of this research was to determine the origins of observed differences between the foaming behavior of commercial materials and those materials produced in our laboratory. It was shown that polymer molecular weight and polydispersity are not important factors in determining cell size and are not responsible for the disparity in cell sizes observed. This disparity was, however, a result of the presence of a very low molecular weight component (~270 g/mol) found in the commercial samples. Extraction of this component reduced the cell diameter of resulting foams to that of the NMW distribution samples. Addition of a styrene oligomer (285 g/mol) to a NMW distribution sample resulted in foams with larger cell diameters. Varying the concentration of this oligomer allows control of cell size in foams.

Part II concentrates on the adsorption behavior of end-functionalized polymers to monochlorosilane-modified silica surfaces. Chemically grafted tris(trimethylsiloxy)silyl (sub)monolayers (tris(TMS)) were prepared on the native oxide of silicon by the vapor phase reaction of the monochlorosilane at elevated temperatures. By exploiting the

inherently sluggish kinetics of the silanization reaction, the grafting density of the tris(TMS) (sub)monolayer can be tuned. Unreacted silanol groups on the substrate surface were used as adsorption sites for carboxylic acid end-functionalized polystyrenes (PS-COOH). The thickness of the adsorbed layer could be controlled by the tris(TMS) surface coverage, adsorbing solvent, and polymer molecular weight. The topography of the adsorbed layers was investigated by AFM.

Part III probes the adsorption behavior of a specific protein, albumin, to monochlorosilane-modified silica surfaces. Covalently attached monolayers were prepared on the native oxide of silicon by reaction of various chlorosilanes at room temperature. Both one-component (pure) surfaces and two-component (mixed) surfaces were investigated. The adsorption of albumin to these surfaces was carried out under physiological conditions, and ellipsometry was used to determine the total adsorbed amount of protein to these surfaces. The adsorption of albumin closely follows the surface energy of the substrate as seen by plotting adsorbance (Γ) versus the cosine of the water contact angle. The morphology of the adsorbed albumin layer was examined by AFM and was correlated to the mode of adsorption of the albumin molecule as directed by the surface chemistry.

TABLE OF CONTENTS

	Page
ACKNOWLEDGEMENTS	v
ABSTRACT	vi
LIST OF TABLES	xi
LIST OF FIGURES	xiii
CHAPTER	
1. CONTROLLED FOAMING OF POLYSTYRENE USING SUPERCRITICAL CARBON DIOXIDE	1
1.1. Introduction	1
1.2. Experimental.....	10
1.2.1. Materials	10
1.2.2. Polymerizations	10
1.2.3. Sample Preparation	11
1.2.4. Foam Preparation.....	11
1.2.5. Foam Characterization.....	12
1.3. Results and Discussion	13
1.4. Conclusions	43
1.5. References Cited.....	45
2. POLYMER ADSORPTION TO SILANE-MODIFIED SURFACES.....	47
2.1. Introduction	47
2.2. Experimental.....	57
2.2.1. Materials	57
2.2.2. Pretreatment of Silicon Substrates.....	57
2.2.3. Preparation of Substrates via Solution Reaction.....	58
2.2.4. Preparation of Substrates via Vapor Phase Reaction.....	58
2.2.5. Adsorption of PS-COOH to Silane-modified Surfaces	60
2.2.6. Dewetting Studies	60
2.2.7. Characterization	61
2.3. Results and Discussion	62
2.3.1. Preparation of Tris(trimethylsiloxy)silyl (Tris(TMS)) Surfaces	62

2.3.2. Synthesis of Mixed Tris(TMS)/ABDMS Surfaces	70
2.3.3. Adsorption of PS-COOH to Silane-modified Surfaces	76
2.3.4. Dewetting of Polymer Thin Films on Tris(TMS) Surfaces	94
2.4. Conclusions	102
2.5. References Cited	104
3. PROTEIN ADSORPTION TO SILANE-MODIFIED SURFACES	107
3.1. Introduction	107
3.2. Experimental.....	110
3.2.1. Materials	110
3.2.2. Pretreatment of Silicon Substrates.....	110
3.2.3. Preparation of Substrates via Solution Reaction.....	111
3.2.4. Adsorption of Proteins to Silane-modified Surfaces	113
3.2.5. Characterization	114
3.3. Results and Discussion	115
3.3.1. Substrate Characterization	115
3.3.2. Protein Adsorption Protocol	119
3.3.3. Protein Adsorption to Silane-modified Surfaces	121
3.3.4. AFM Studies of Adsorbed Protein Morphology.....	128
3.4. Conclusions	156
3.5. Future Work.....	157
3.5. References Cited.....	159
APPENDICES	
A. LIVING ANIONIC POLYMERIZATION	161
A.1. Introduction.....	161
A.2. Experimental.....	164
A.2.1. Materials	164
A.2.2. Methods.....	165
A.3. Synthesis of Polystyrene Homopolymers.....	168
A.4. Synthesis of Carboxylic Acid End-functionalized Polystyrene.....	170
A.5. Synthesis of P(S-b-MMA) Block Copolymers.....	174
A.6. Synthesis of Fluorescently Labeled Polystyrene	183
A.7. References Cited	195
B. FOAMING OF THIN FILMS / TRSAXS.....	196

B.1. Introduction.....	196
B.2. Experimental	201
B.2.1. Sample Preparation	201
B.2.2. Foaming of Thin Films.....	202
B.2.3. TRSAXS	203
B.3. Results and Discussion	205
B.3.1. Foaming of Thin Films.....	205
B.3.2. Kinetics of Foaming Followed by Time-resolved SAXS	218
B.4. Conclusions.....	227
B.5. References Cited	229
C. SUPPLEMENTAL DATA FOR CHAPTERS 2 AND 3	230
C.1. XPS Data for Polymer Adsorption to Silane-modified Surfaces.....	230
C.2. XPS Data for Protein Adsorption to Silane-modified Surfaces	234
BIBLIOGRAPHY	238

LIST OF TABLES

Table	Page
1.1. Polymer sample characteristics.	14
1.2. Average cell size diameters and cell densities of foams produced by rapid expansion of SC CO ₂	39
2.1. Contact angle data for Tris(TMS) surfaces prepared by vapor phase reaction for increasing amounts of time.....	67
2.2. XPS and contact angle data for Tris(TMS)/ABDMS mixed surfaces prepared by consecutive vapor phase reactions.	73
2.3. Contact angle data for 11K PS-COOH adsorption from toluene onto Tris(TMS) surfaces.	78
2.4. Number of chains per aggregate as calculated by average dimensions from AFM image analysis.....	93
2.5. Contact angles of dewetted PS on various Tris(TMS) surfaces as determined by AFM analysis.	97
2.6. Molecular weight and T _g data for the polymers used in the dewetting studies.....	99
2.7. Dewetting data of selected polymers spun-cast on Tris(TMS) surfaces before and after adsorption of 11K PS-COOH. Surfaces that dewet are labeled with 'D' and those that wet are labeled 'W', as determined by optical microscopy.....	100
3.1. Contact angle and thickness data for one-component (pure) surfaces.	117
3.2. Contact angle and thickness data for two-component (mixed) surfaces.	118
3.3. Contact angle and adsorbance data for one-component (pure) surfaces after BSA adsorption.	122
3.4. Contact angle and adsorbance data for two-component (mixed) surfaces after BSA adsorption.	123
3.5. BSA adsorbance (Γ) data for various surfaces reported in literature for comparison to the values reported in this study.	127
B.1. Foaming of free standing thin films under various conditions.....	206

C.1. XPS data (75° take-off angle) for surfaces modified with Tris(TMS) via vapor phase reaction for increasing amounts of time.....	230
C.2. XPS data (75° take-off angle) for surfaces modified with Tris(TMS)/ABDMS via vapor phase reaction.....	231
C.3. XPS data (75° take-off angle) for 11K PS-COOH adsorbed from toluene to surfaces modified with Tris(TMS) via vapor phase reaction for increasing amounts of time.....	231
C.4. XPS data (75° take-off angle) for 11K PS-COOH adsorbed from cyclohexane (35 °C) to surfaces modified with Tris(TMS) via vapor phase reaction for increasing amounts of time.....	232
C.5. XPS data (75° take-off angle) for 41K PS-COOH adsorbed from toluene to surfaces modified with Tris(TMS) via vapor phase reaction for increasing amounts of time.....	232
C.6. XPS data (75° take-off angle) for 11K PS-COOH adsorbed from toluene to surfaces modified with Tris(TMS)/ABDMS via vapor phase reaction.....	233
C.7. XPS data (75° take-off angle) for 11K PS-COOH adsorbed from THF to surfaces modified with Tris(TMS)/ABDMS via vapor phase reaction.....	233
C.8. XPS data (75° take-off angle) for organosilane-modified surfaces before and after protein (BSA) adsorption.....	234
C.9. XPS data (75° take-off angle) for Tris(TMS) mixed surfaces before and after protein (BSA) adsorption.	236
C.10. XPS data (75° take-off angle) for Tris(TMS) / TMS mixed surfaces before and after protein (BSA) adsorption.....	236
C.11. XPS data (75° take-off angle) for Tris(TMS) / TVS-OH mixed surfaces before and after protein (BSA) adsorption	237
C.12. XPS data (75° take-off angle) for Tris(TMS) / APDMS mixed surfaces before and after protein (BSA) adsorption	237

LIST OF FIGURES

Figure	Page
1.1. P-T phase diagram illustrating the position of the supercritical fluid region. The critical point for carbon dioxide is 31.1 °C and 1070 psi.....	2
1.2. Pressure-temperature-density curves for CO ₂ , illustrating the tunable solvating strength in the supercritical region. Listed in the table are other defining characteristics of SCFs in comparison to conventional liquids and gases.	3
1.3. CO ₂ -induced plasticization of polystyrene as measure by creep compliance. ¹⁸	4
1.4. Schematic drawing of the TIPS process for producing microcellular foams.....	5
1.5. Schematic representation depicting the generation of a microcellular foam using sorption of inert gases.....	6
1.6. Effect of foaming pressure and temperature on the average cell diameter of foams produced by rapid decompression of SC CO ₂ -swollen polystyrene. ¹⁶	8
1.7. GPC chromatograms of three different commercial polystyrene samples: (from top to bottom) ^{COM} PS ¹ (SP ²), ^{COM} PS ² (Aldrich), and ^{COM} PS ³ (Acros).	16
1.8. SEM micrographs of fracture surfaces of foams prepared from three different commercial polystyrene samples: (a) ^{COM} PS ¹ (SP ²), (b) ^{COM} PS ² (Aldrich), and (c) ^{COM} PS ³ (Acros). Foaming conditions were 100 °C and 3400 psi.	17
1.9. GPC chromatograms of one commercial and four narrow molecular weight polystyrene materials: (from top to bottom) ^{COM} PS ¹ , PS ^{25K} , PS ^{147K} , PS ^{514K} , and PS ^{1050K}	18
1.10. SEM micrographs of fracture surfaces of foams prepared from four narrow molecular weight polystyrene materials: (a) PS ^{25K} , (b) PS ^{147K} , (c) PS ^{514K} , and (d) PS ^{1050K} . Foaming conditions were 100 °C and 3400 psi.	19
1.11. GPC chromatogram of six narrow molecular weight polystyrenes used in calculating blend composition.....	22
1.12. Geometric construction for determining the percentage of each molecular weight to be added to the blend.....	23
1.13. GPC chromatogram of a simulated polydisperse polystyrene sample, ^B PS ¹ , which is a 6-component blend of PS ^{6K} , PS ^{25K} , PS ^{62K} , PS ^{147K} , PS ^{514K} and PS ^{1050K}	24

1.14. GPC chromatogram of a polystyrene sample (PS^R) prepared by bulk radical polymerization initiated by AIBN in toluene at 70 °C.....	25
1.15. SEM micrographs of fracture surfaces of foams prepared from (a) PS^R as well as (for comparison) (b) $^{COM}PS^1$ and (c) PS^{147K} . Foaming conditions were 100 °C and 3400 psi.	26
1.16. GPC chromatogram of the simulated polydisperse polystyrene sample $^BPS^2$, which contains the samples in $^BPS^1$ plus 7.4 wt% of a 560 g/mol styrene oligomer.....	27
1.17. GPC chromatogram of the simulated polydisperse polystyrene sample $^BPS^3$, which contains the samples in $^BPS^1$ plus 13.0 wt% of a 560 g/mol styrene oligomer.....	28
1.18. SEM micrographs of fracture surfaces of foams prepared from the simulated polydisperse polystyrene samples (a) $^BPS^1$, (b) $^BPS^2$, (c) $^BPS^3$, and (d) $^{COM}PS^1$ (for comparison). Foaming conditions were 100 °C and 3400 psi.....	29
1.19. GPC chromatograms showing the removal of a low molecular weight (LMW) component from $^{COM}PS^1$ by repeated reprecipitation from THF in methanol: (from top to bottom) $^{COM}PS^1$ (3.8% LMW component), $^{COM}PS^{1EX1}$ (1.3% LMW component), $^{COM}PS^{1EX2}$ (0.9% LMW component), $^{COM}PS^{1EX3}$ (0.1% LMW component).....	32
1.20. SEM micrographs of fracture surfaces of foams prepared from the extracted polydisperse samples: (a) $^{COM}PS^1$, (b) $^{COM}PS^{1EX1}$, (c) $^{COM}PS^{1EX2}$, and (d) $^{COM}PS^{1EX3}$. Foaming conditions were 100 °C and 3400 psi.	33
1.21. GPC chromatograms of the fractionated products recovered after repeated rotary evaporation of the filtrate from extraction of $^{COM}PS^1$ by reprecipitation.	34
1.22. Thermally-induced initiation of styrene, producing radical species that can recombine to form inactive oligomers.....	36
1.23. GPC chromatograms of blends prepared from PS^{147K} and a 285 g/mol styrene oligomer: $^BPS^4$ (3.6 wt% oligomer), $^BPS^5$ (7.3 wt% oligomer), and $^BPS^6$ (9.9 wt% oligomer).....	37
1.24. SEM micrographs of PS^{147K} with added oligomer: (a) PS^{147K} (0.0 wt% oligomer), (b) $^BPS^4$ (3.6 wt% oligomer), (c) $^BPS^5$ (7.3 wt% oligomer), and (d) PS^6 (9.9 wt% oligomer). Foaming conditions were 100 °C and 3400 psi.....	38
2.1. End-grafted polymer adsorption as a function of solvent quality.	48
2.2. Illustration of the two regimes for copolymer adsorption: buoy-dominated and anchor-dominated copolymer adsorption.....	50

2.3. Chemical structure of tris(trimethylsiloxy)chlorosilane, Tris(TMS)-Cl.	52
2.4. Contact angle hysteresis as a function of molar volume of the probe fluid for Tris(TMS) surfaces prepared in the vapor phase for 3 days. The observed transition in hysteresis allows for determination of an average pore size. ²⁷	53
2.5. Schematic of the Schlenk tube used for vapor-phase reaction of monochlorosilanes. Similar reaction flasks were used for solution reactions with the exception that the top included a 4mm Teflon joint capped with a rubber septum to facilitate cannulation and additions via syringe under an inert atmosphere.....	59
2.6. Schematic illustrating the reaction of Tris(TMS)-Cl with surface silanol groups, leaving unreacted silanol groups which can be used for subsequent modification of the surface.	64
2.7. Kinetics of the Tris(TMS)-Cl vapor phase reaction as monitored by advancing (●) and receding (○) water contact angles. It is assumed that an advancing CA of 108° is complete coverage.	65
2.8. Kinetics of the Tris(TMS)-Cl solution phase reaction as monitored by advancing (●) and receding (○) water contact angles. It is assumed that an advancing CA of 108° is complete coverage.	66
2.9. Schematic illustrating the 2-D above-view of Tris(TMS) surfaces of increasing surface coverage.....	69
2.10. Schematic illustrating the reaction of Tris(TMS)-Cl with surface silanol groups, followed by subsequent reaction of remaining silanols with a second silane (e.g. ABDMS).	71
2.11. Schematic illustrating the 2-D above-view of Tris(TMS) surfaces (large circles) that have been further reacted with ABDMS (small circles).....	72
2.12. pH-dependent contact angles for pure Tris(TMS) (●) , mixed Tris(TMS)/ABDMS (□), and pure ABDMS (▲) surfaces.	75
2.13. Schematic illustrating the transition of ABDMS from being protonated by surface silanol groups at neutral pH to being protonated by external acid at low pH.	76
2.14. Schematic of adsorption of solvated PS-COOH onto a Tris(TMS)-modified surface.	77
2.15. Adsorption kinetics of 11K PS-COOH from toluene onto surfaces having increasing Tris(TMS) surface coverage: 0% Tris(TMS) (clean Si) (●); 55%	

Tris(TMS) (○); 81% Tris(TMS) (▲); 89% Tris(TMS) (△); and 96% Tris(TMS) (■).....	80
2.16. Adsorbed thicknesses, as determined by ellipsometry, of PS-COOH adsorption to Tris(TMS) surfaces: 11K adsorbed from cyclohexane (▲) and toluene (●); 41K adsorbed from toluene (○); and 11K adsorbed from toluene to mixed Tris(TMS)/ABDMS surfaces (□).....	82
2.17. AFM images obtained in tapping mode of clean silicon. The images are height (top), surface (middle), and phase (bottom) plots of a 0.25 μm^2 sampling area.	85
2.18. AFM images obtained in tapping mode of Tris(TMS)-modified silicon. The images are height (top), surface (middle), and phase (bottom) plots of a 0.25 μm^2 sampling area.....	86
2.19. AFM images obtained in tapping mode of 11K PS-COOH adsorbed from toluene to clean silicon at 23 °C and 1.0 mg/mL for 24h. The images are height (top), surface (middle), and phase (bottom) plots of a 0.25 μm^2 sampling area.....	87
2.20. AFM images obtained in tapping mode of 11K PS-COOH adsorbed from toluene to Tris(TMS) 1h at 23 °C and 1.0 mg/mL for 24h. The images are height (top), surface (middle), and phase (bottom) plots of a 0.25 μm^2 sampling area.	88
2.21. AFM images obtained in tapping mode of 11K PS-COOH adsorbed from toluene to Tris(TMS) 4h at 23 °C and 1.0 mg/mL for 24h. The images are height (top), surface (middle), and phase (bottom) plots of a 0.25 μm^2 sampling area.	89
2.22. AFM images obtained in tapping mode of 11K PS-COOH adsorbed from toluene to Tris(TMS) 24h at 23 °C and 1.0 mg/mL for 24h. The images are height (top), surface (middle), and phase (bottom) plots of a 0.25 μm^2 sampling area.	90
2.23. AFM images obtained in tapping mode of 11K PS-COOH adsorbed from toluene to Tris(TMS) 51h at 23 °C and 1.0 mg/mL for 24h. The images are height (top), surface (middle), and phase (bottom) plots of a 0.25 μm^2 sampling area.	91
2.24. AFM images obtained in tapping mode of 11K PS-COOH adsorbed from toluene to Tris(TMS) 72h at 23 °C and 1.0 mg/mL for 24h. The images are height (top), surface (middle), and phase (bottom) plots of a 0.25 μm^2 sampling area.	92

2.26. Chemical structures of the polymers used in dewetting studies on Tris(TMS)/PS-COOH surfaces: (from left to right) poly(styrene), poly(2-chlorostyrene), poly(n-butyl methacrylate), poly(cyclohexyl methacrylate), and poly(vinyl methyl ether).....	98
2.27. Schematic illustrating dewetting experiments conducted on Tris(TMS) surfaces having anchored PS-COOH with an overlying, spun-cast film of PVME. Shown are typical optical micrographs of the dewetted structure.	101
3.1. Two proposed ribbon diagrams for albumin: rotational ellipsoid or heart-shaped.....	108
3.2. Schematic of the Schlenk tube used for solution reactions that included a 4mm Teflon joint capped with a rubber septum to facilitate cannulation and additions via syringe under an inert atmosphere.....	112
3.3. Schematic illustrating the two possible modes of adsorption for albumin: end-on (long axis perpendicular to the surface) and side-on (long-axis parallel to the surface) conformations.	124
3.4. Master plot of adsorbance (Γ) as a function of surface energy ($\cos \theta_A$) for all surfaces studied, showing a linear increase of adsorbance with increasing hydrophobicity of the surface.....	126
3.5. AFM images obtained in tapping mode of BSA adsorbed to a C_{18} CAM for 1h at 37 °C and 0.1 mg/mL. The images are height (top), surface (middle), and phase (bottom) plots of a $1 \mu\text{m}^2$ sampling area.....	134
3.6. AFM images obtained in tapping mode of BSA adsorbed to a C_6F_{13} surface for 1h at 37 °C and 0.1 mg/mL. The images are height (top), surface (middle), and phase (bottom) plots of a $1 \mu\text{m}^2$ sampling area.....	135
3.7. AFM images obtained in tapping mode of BSA adsorbed to a DMDC surface for 1h at 37 °C and 0.1 mg/mL. The images are height (top), surface (middle), and phase (bottom) plots of a $1 \mu\text{m}^2$ sampling area.	136
3.8. AFM images obtained in tapping mode of BSA adsorbed to a C_{18} SAM for 1h at 37 °C and 0.1 mg/mL. The images are height (top), surface (middle), and phase (bottom) plots of a $1 \mu\text{m}^2$ sampling area.....	137
3.9. AFM images obtained in tapping mode of BSA adsorbed to a TMS surface for 1h at 37 °C and 0.1 mg/mL. The images are height (top), surface (middle), and phase (bottom) plots of a $1 \mu\text{m}^2$ sampling area.....	138
3.10. AFM images obtained in tapping mode of BSA adsorbed to a CF_3 surface for 1h at 37 °C and 0.1 mg/mL. The images are height (top), surface (middle), and phase (bottom) plots of a $1 \mu\text{m}^2$ sampling area.....	139

3.11. AFM images obtained in tapping mode of BSA adsorbed to a carbomethoxy surface for 1h at 37 °C and 0.1 mg/mL. The images are height (top), surface (middle), and phase (bottom) plots of a 1 μm^2 sampling area.	140
3.12. AFM images obtained in tapping mode of BSA adsorbed to an acetoxo surface for 1h at 37 °C and 0.1 mg/mL. The images are height (top), surface (middle), and phase (bottom) plots of a 1 μm^2 sampling area.	141
3.13. AFM images obtained in tapping mode of BSA adsorbed to a mercaptopropyltriethoxysilane surface for 1h at 37 °C and 0.1 mg/mL. The images are height (top), surface (middle), and phase (bottom) plots of a 1 μm^2 sampling area.....	142
3.14. AFM images obtained in tapping mode of BSA adsorbed to a TPS surface for 1h at 37 °C and 0.1 mg/mL. The images are height (top), surface (middle), and phase (bottom) plots of a 1 μm^2 sampling area.....	143
3.15. AFM images obtained in tapping mode of BSA adsorbed to an APS surface for 1h at 37 °C and 0.1 mg/mL. The images are height (top), surface (middle), and phase (bottom) plots of a 1 μm^2 sampling area.	144
3.16. AFM images obtained in tapping mode of BSA adsorbed to a TVS-OH surface for 1h at 37 °C and 0.1 mg/mL. The images are height (top), surface (middle), and phase (bottom) plots of a 1 μm^2 sampling area.	145
3.17. AFM images obtained in tapping mode of BSA adsorbed to clean silicon for 1h at 37 °C and 0.1 mg/mL. The images are height (top), surface (middle), and phase (bottom) plots of a 1 μm^2 sampling area.....	146
3.18. AFM section analysis of BSA adsorbed to C ₁₈ CAM showing the typical height (8 nm) of the observed features on the surface.	147
3.19. AFM section analysis for BSA adsorbed to TMS showing the typical height (4.6 nm) of the observed features on the surface.	148
3.20. Schematic illustrating two possible modes of adsorption of BSA to hydrophobic surfaces: rigid surfaces that force restructuring of the albumin to increase contact points, and soft surfaces that allow for a large number of contact points without the need to restructure.....	149
3.21. AFM images obtained in tapping mode of BSA adsorbed to a Tris(TMS) 1h surface for 1h at 37 °C and 0.1 mg/mL. The images are height (top), surface (middle), and phase (bottom) plots of a 1 μm^2 sampling area.	150
3.22. AFM images obtained in tapping mode of BSA adsorbed to a Tris(TMS) 24h surface for 1h at 37 °C and 0.1 mg/mL. The images are height (top), surface (middle), and phase (bottom) plots of a 1 μm^2 sampling area.	151

3.23. AFM images obtained in tapping mode of BSA adsorbed to a Tris(TMS) 72h surface for 1h at 37 °C and 0.1 mg/mL. The images are height (top), surface (middle), and phase (bottom) plots of a 1 μm^2 sampling area.	152
3.24. AFM images obtained in tapping mode of BSA adsorbed to a Tris(TMS) 140h surface for 1h at 37 °C and 0.1 mg/mL. The images are height (top), surface (middle), and phase (bottom) plots of a 1 μm^2 sampling area.	153
3.25. AFM images obtained in tapping mode of BSA adsorbed to a Tris(TMS) 1h / TMS surface for 1h at 37 °C and 0.1 mg/mL. The images are height (top), surface (middle), and phase (bottom) plots of a 1 μm^2 sampling area.....	154
3.26. AFM images obtained in tapping mode of BSA adsorbed to a Tris(TMS) 1h / TVS-OH surface for 1h at 37 °C and 0.1 mg/mL. The images are height (top), surface (middle), and phase (bottom) plots of a 1 μm^2 sampling area.....	155
A.1. Schematic mechanism for living anionic polymerization with controlled termination.	162
A.2. Custom-designed glassware for monomer purification (A) and polymerization reactions (B).	167
A.3. Anionic polymerization of styrene initiated with sec-butyllithium and terminated with a simple alcohol.....	169
A.4. Representative GPC chromatogram of a polystyrene homopolymer synthesized by living anionic polymerization.....	171
A.5. Anionic polymerization of styrene followed by several steps to yield the carboxylated polymer.....	172
A.6. Anionic polymerization of styrene followed by capping with diphenylethylene, which is then used to polymerize methyl methacrylate to produce a block copolymer, P(S-b-MMA).	175
A.7. Representative GPC chromatogram of P(S-b-MMA) synthesis: aliquot removed to characterize the molecular weight of the PS block.	178
A.8. Representative GPC chromatogram of P(S-b-MMA) synthesis: block copolymer before extraction to remove residual PS homopolymer and diphenylethylene.	179
A.9. Representative GPC chromatogram of P(S-b-MMA) synthesis: block copolymer after purification.....	180
A.10. Representative ^1H NMR trace of P(S-b-MMA) for determination of block copolymer composition.	181

A.11. Representative quantitative ^{13}C NMR trace of P(dPS-b-MMA) for determination of block copolymer composition where one block is deuterated.	182
A.12. Synthesis of chromophore monomers that contain anthryl (A) and phenanthryl (B) moieties. Monomer A required synthesis of the starting material, 2-acetyl anthracene.....	186
A.13. ^1H NMR of starting material, 2-acetyl anthracene, after purification.....	187
A.14. ^1H NMR of 1-(2-anthryl)-1-phenylethylene after purification.....	188
A.15. ^1H NMR of 1-(2-phenanthryl)-1-phenylethylene after purification.....	189
A.16. Anionic polymerization of styrene initiated with sec-butyllithium and terminated with fluorescent monomer (A).	190
A.17. One-batch reaction for synthesizing both anthryl- and phenanthryl-labeled PS having exactly the same molecular weight and polydispersity.	192
A.18. GPC chromatogram of PS-Anth showing the removal of residual anthryl monomer by reprecipitation.	193
A.19. GPC chromatogram of PS-Phen showing the removal of residual phenanthryl monomer by reprecipitation.	194
B.1. Effect saturation pressure on the skin thickness of bulk PMMA foaming using SC CO_2 . The solid line is a model prediction. ¹	197
B.2. Critical radius for homogeneous nucleation as a function of saturation pressure in a PMMA/ CO_2 system undergoing a rapid pressure quench. ²	199
B.3. Schematic drawings of (a) the high-pressure view cell used in the foaming of thin films and (b) the high-pressure x-ray scattering cell with diamond windows.	204
B.4. SEM micrographs of fracture surfaces of unconfined thin film foams: (a) 172 μm , (b) 78 μm , and (c) 41 μm . Foaming conditions were 40 $^\circ\text{C}$ and 3000 psi.....	209
B.5. SEM micrographs of fracture surfaces of unconfined thin film foams: (a) 80 μm , (b) 40 μm , and (c) 11 μm . Foaming conditions were 60 $^\circ\text{C}$ and 3000 psi.....	210
B.6. SEM micrographs of fracture surfaces of confined thin film foams: (a) 100 μm M/F, (b) 100 μm M/M, and (c) 50 μm M/M. Foaming conditions were 40 $^\circ\text{C}$ and 3000 psi. M denotes metallized surface and F denotes free surface on each side of the film, respectively.	211
B.7. Schematic illustrating film preparation having a metallized layer on one complete side of the film, but only on half of the opposite side.	212

B.8. SEM micrographs of fracture surfaces of a 100 μm confined thin film foam that has been metallized on one side only (top image) and metallized on both sides (bottom image), along with the transition region. Foaming conditions were 80 $^{\circ}\text{C}$ and 8000 psi.	214
B.9. SEM micrographs of fracture surfaces of a 50 μm confined thin film foam that has been metallized on one side only (top image) and metallized on both sides (bottom image), along with the transition region. Foaming conditions were 80 $^{\circ}\text{C}$ and 8000 psi.	215
B.10. SEM micrographs of fracture surfaces of a 10 μm confined thin film foam that has been metallized on one side only (top image) and metallized on both sides (bottom image). Foaming conditions were 80 $^{\circ}\text{C}$ and 8000 psi.	216
B.11. SEM micrograph of the fracture surface of a bulk PS sample foamed at 80 $^{\circ}\text{C}$ and 8000 psi.	217
B.12. Scattered intensity as a function of q for pressure quenches (ΔP) of 2000 psi and 3000 psi at 40 $^{\circ}\text{C}$	219
B.13. Scattered intensity as a function of q for pressure quenches (ΔP) of 4000 psi and 5000 psi at 40 $^{\circ}\text{C}$	220
B.14. Scattered intensity as a function of q for pressure quenches (ΔP) of 2000 psi and 3000 psi at 50 $^{\circ}\text{C}$	221
B.15. Scattered intensity as a function of q for pressure quenches (ΔP) of 4000 psi and 5000 psi at 50 $^{\circ}\text{C}$	222
B.16. Guinier plot for a pressure quench (ΔP) of 2000 psi at 40 $^{\circ}\text{C}$. Included is a model Guinier plot for a growth rate of 15 $\text{\AA} / \text{sec}$	225
B.17. Schematic illustrating two possible mechanisms for pore formation defined in terms of electron densities.	226

CHAPTER 1

CONTROLLED FOAMING OF POLYSTYRENE USING SUPERCRITICAL CARBON DIOXIDE

1.1. Introduction

Supercritical (SC) fluids have received increased attention as alternatives to conventional liquid solvents in areas such as polymerization,¹⁻⁶ polymer modification,⁷⁻⁹ polymer fractionation,¹⁰⁻¹² and the preparation of microcellular foams.¹³⁻¹⁷ A supercritical fluid is defined as any substance above its critical temperature and pressure (see Figure 1.1). SC carbon dioxide (CO₂), in particular, has proven to be quite advantageous since it possesses an experimentally accessible critical point ($T_c \sim 31$ °C, $P_c \sim 1070$ psi) and is environmentally benign. In this condensed state, SC CO₂ exhibits properties that are unique and different from traditional solvents, such as adjustable solvating strength, gas-like diffusivity coupled with liquid-like density, low viscosity, and zero surface tension (see Figure 1.2). SC CO₂ has also been shown to swell but not dissolve most common polymers, the exceptions being a few fluoropolymers and polysiloxanes. The SC CO₂-induced swelling acts to plasticize the polymer matrix, thus lowering its glass transition temperature. The effect of CO₂ on the glass transition temperature of polystyrene is shown in Figure 1.3. This plasticization effect can be utilized in the production of microcellular foams at temperatures much lower than the bulk glass transition temperature.

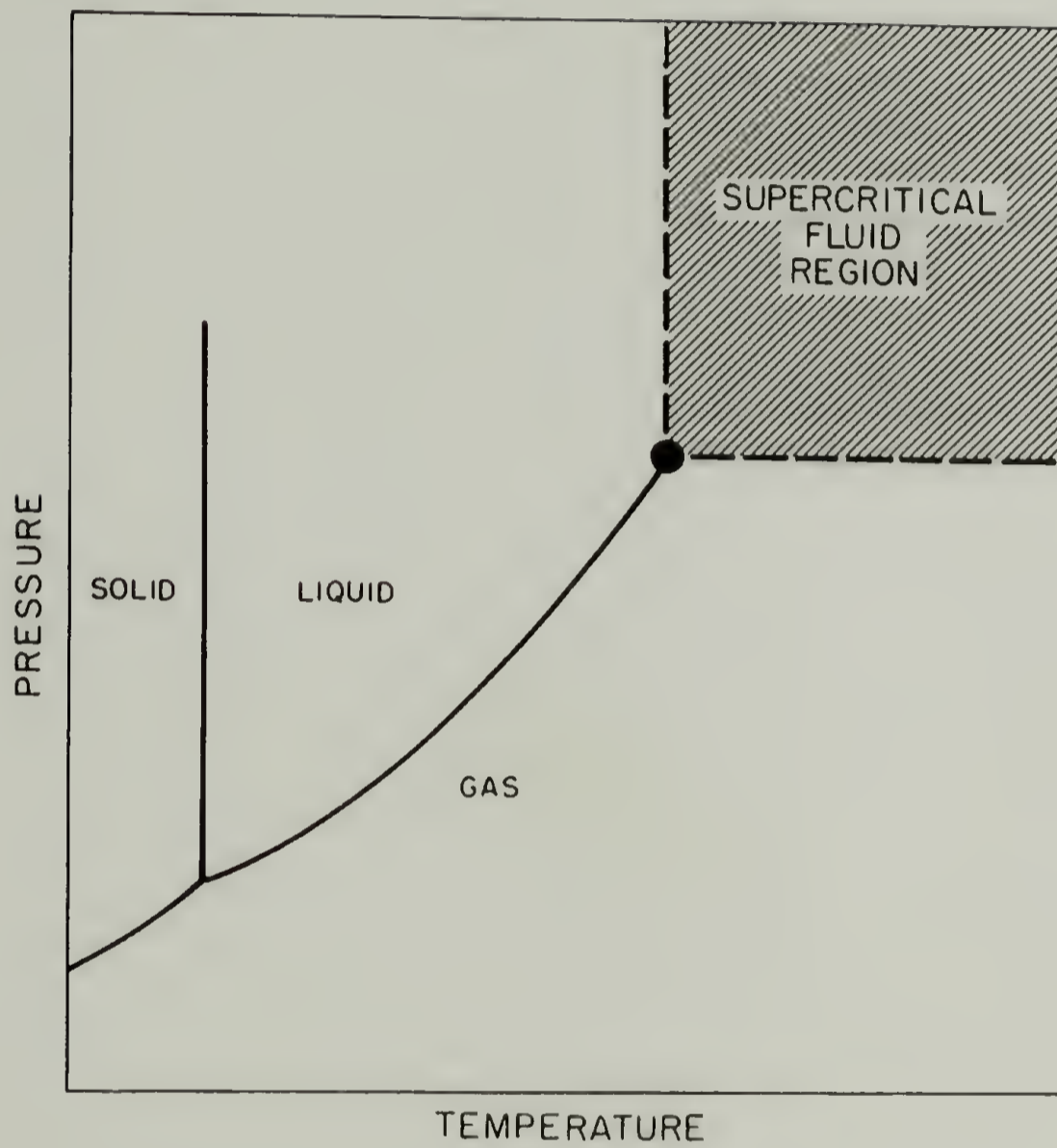
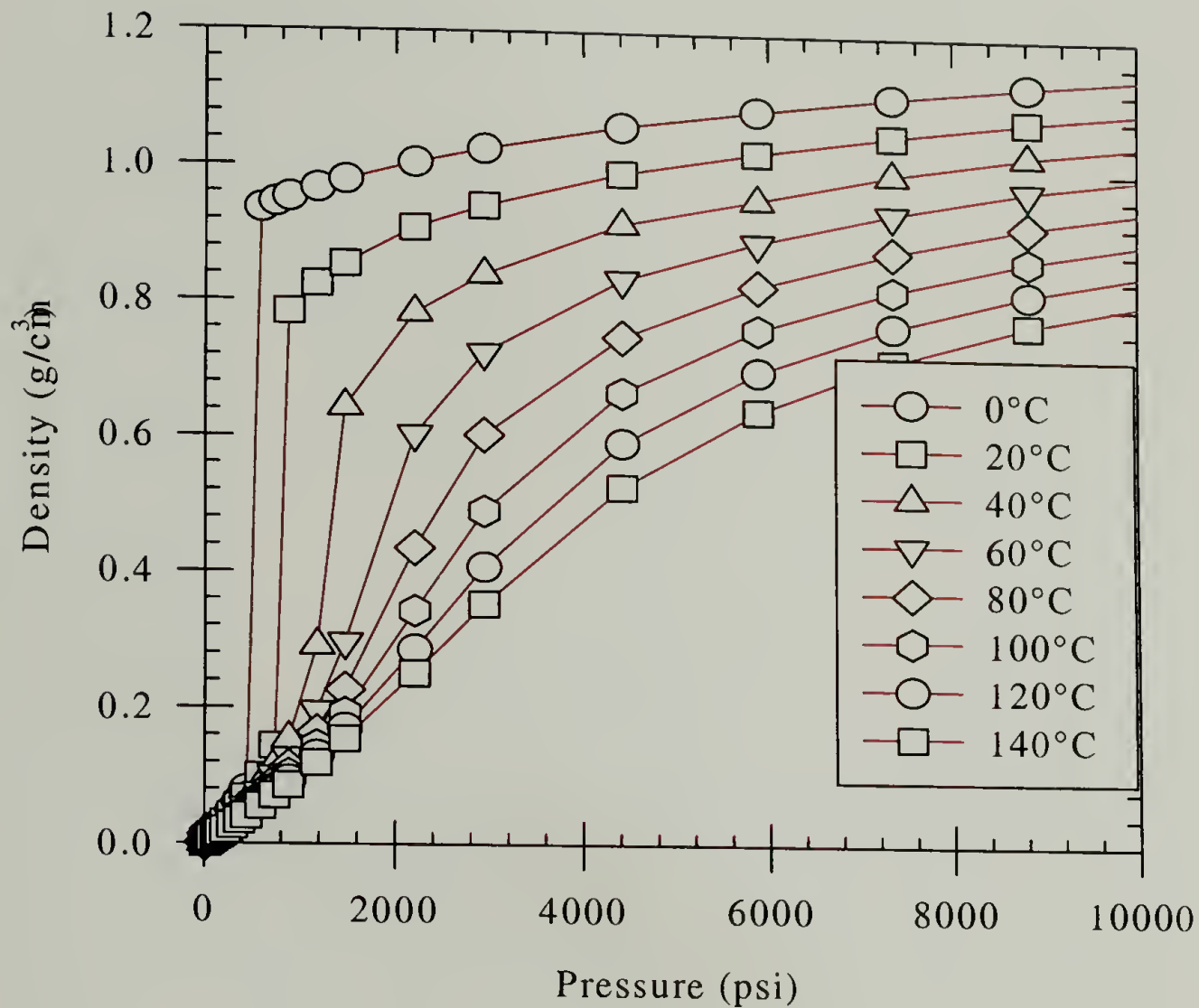


Figure 1.1. P-T phase diagram illustrating the position of the supercritical fluid region. The critical point for carbon dioxide is 31.1 °C and 1070 psi.



	<u>diffusivity</u>	<u>viscosity</u>	<u>density</u>	<u>surface tension</u>
Liquid	10^{-5} cm ² /sec	1 cps	1.0 g/mL	20-50 dyn/cm
Supercritical Fluid	10^{-3}	0.03	0.2-1.2	0
Gas	10^{-1}	10^{-5}	10^{-3}	-

Figure 1.2. Pressure-temperature-density curves for CO₂, illustrating the tunable solvating strength in the supercritical region. Listed in the table are other defining characteristics of SCFs in comparison to conventional liquids and gases.

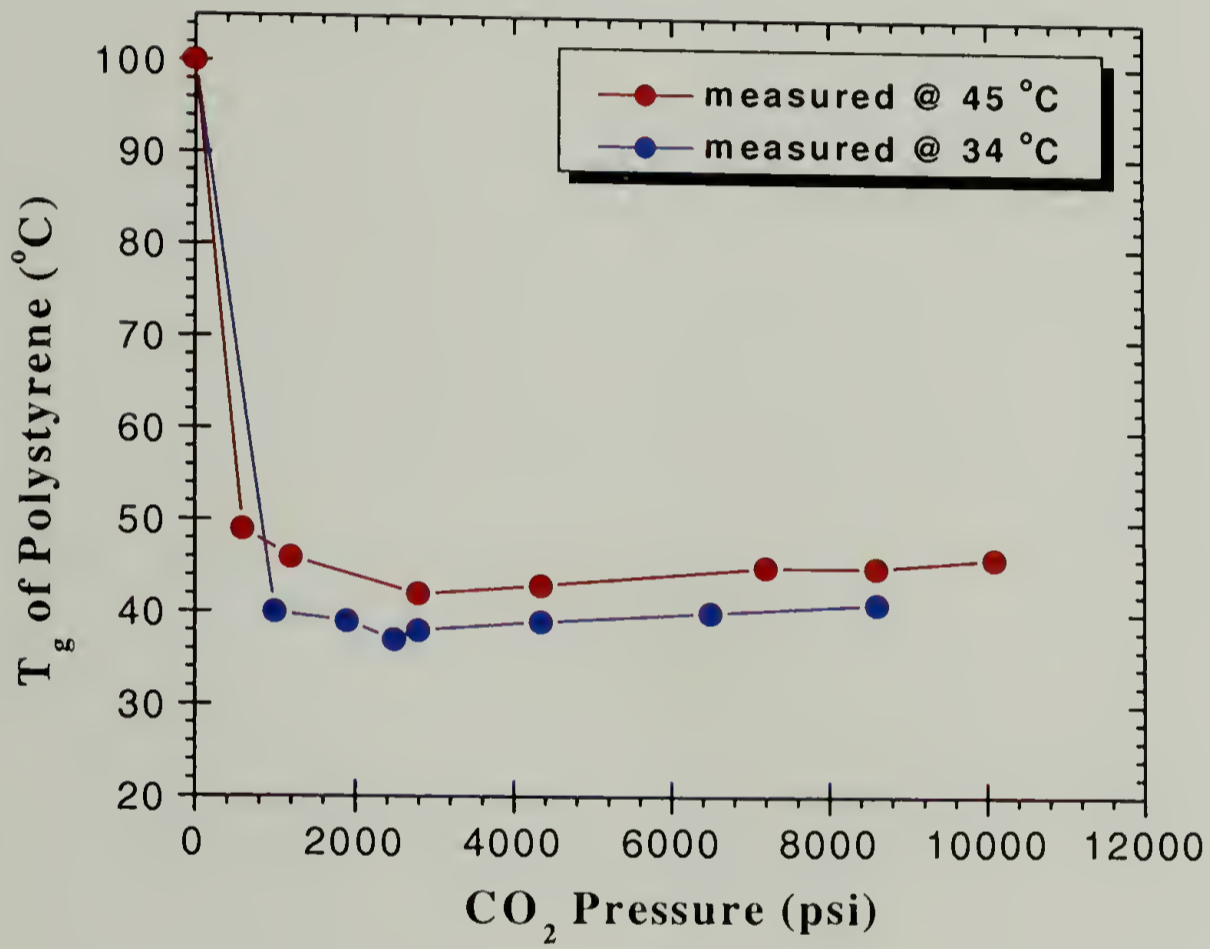


Figure 1.3. CO_2 -induced plasticization of polystyrene as measure by creep compliance.¹⁸

Microcellular foams are defined as materials having cell sizes less than $10\ \mu\text{m}$. Potential uses for these materials are in the areas of separation membranes, thermal and electrical insulation, and the generation of materials with enhanced mechanical properties. There are several methods by which microcellular foams can be generated. The first and most common method is termed thermally induced phase separation (TIPS).^{19,20} A schematic diagram of this process is shown in Figure 1.4. TIPS employs the dissolution of a nonsolvent in a polymer melt (e.g. polystyrene in cyclohexane) at a temperature and composition where only one phase exists (homogeneous solution). This mixture is then quenched into a two-phase region where the mixture undergoes liquid-liquid phase separation until either the polymer reaches its glass transition temperature or the nonsolvent reaches its freezing point (T_f). The phase separation leaves behind pores of nonsolvent trapped by a glassy polymer, and a microcellular foam is generated by removal of the nonsolvent by freeze-drying or supercritical extraction. Complete solvent removal can be difficult, and surface forces encountered during solvent removal can damage or destroy the microcellular structure.

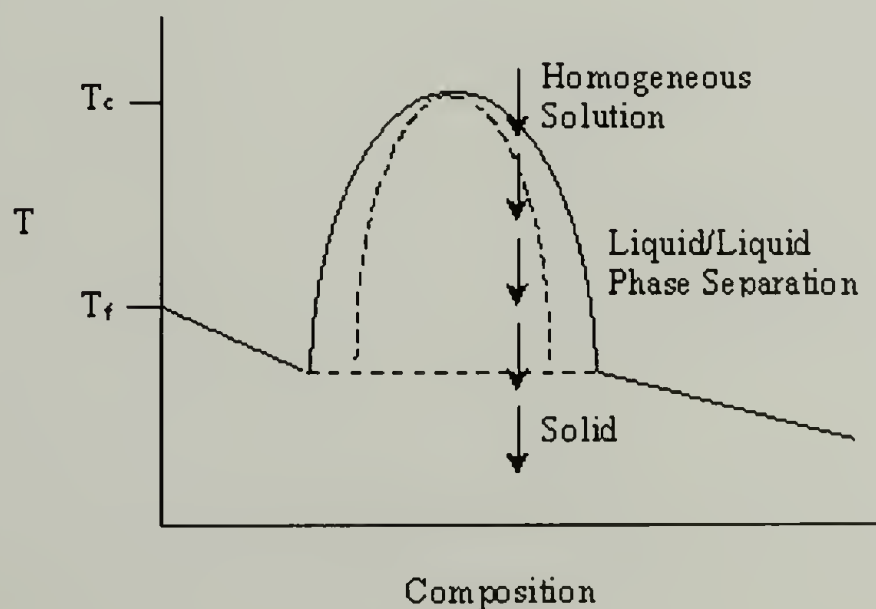


Figure 1.4. Schematic drawing of the TIPS process for producing microcellular foams.

Another method for the generation of microcellular foams was pioneered by Suh et. al.^{21,22} This method involves the saturation of a polymer specimen with an inert gas such as CO₂ or N₂ at moderate pressures and near-room temperatures. The sample is then removed from that environment and quickly immersed in a temperature bath. The temperature of the bath needs to be above the normal glass transition temperature of the polymer sample, at which point the polymer softens and the sorbed gas expands. Thermal quenching of the sample brings it back below its T_g, vitrifying the polymer, and locking in the resulting foamed structure. A schematic of this method is shown in Figure 1.5.

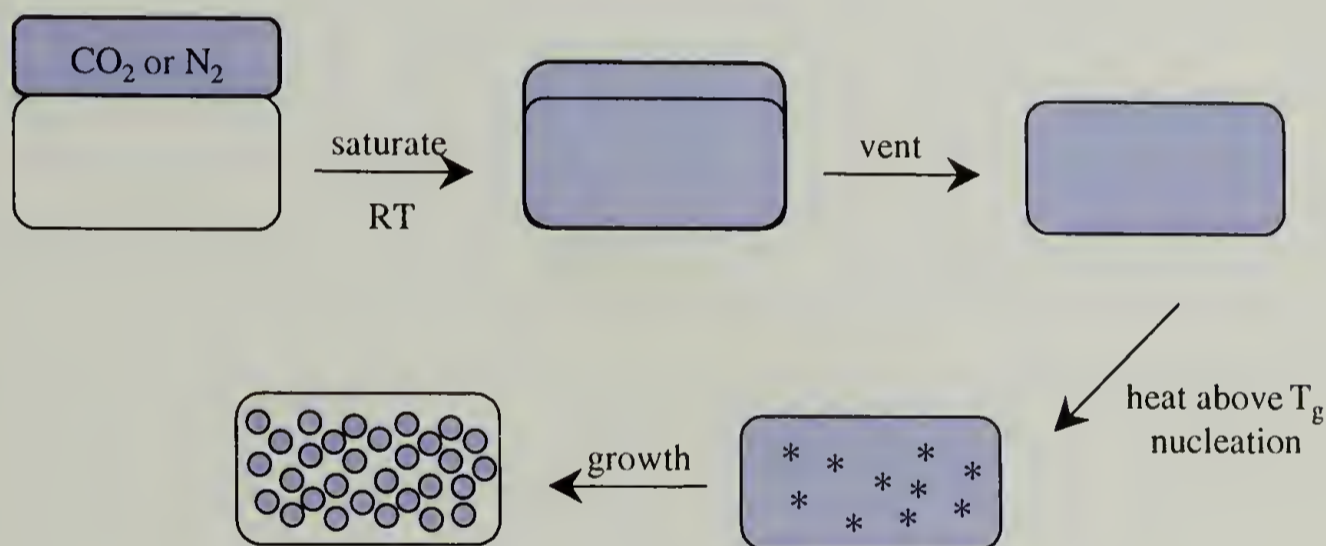


Figure 1.5. Schematic representation depicting the generation of a microcellular foam using sorption of inert gases.

A drawback to such a process is the need to heat the sample above its normal glass transition temperature, which for some polymers can be very high (e.g. polyimide, T_g > 300 °C). Also, foams generated by this process were found to possess a non-porous skin. This can be attributed to a rapid diffusion of gas molecules from the free surface of the

sample, which leads to a depletion layer where no nucleation occurs. This depletion layer has been shown to be dependent on foaming conditions.

Recently Beckman et. al^{13,14,23} reported a novel way of creating microcellular foams by use of SC CO₂. Using this method, a polymer sample is exposed to SC CO₂, which plasticizes the matrix and lowers the apparent T_g to near ambient temperatures. Upon rapid depressurization, the polymer matrix becomes supersaturated with CO₂ gas. Nucleation of cells occurs as a result of this supersaturation and cell growth continues until the polymer vitrifies. The T_g rises as CO₂ leaves the matrix, and the polymer vitrifies when the apparent T_g of the polymer equals that of the operating temperature. The degree of supersaturation is dictated by the equilibrium uptake of CO₂ by the polymer, which in turn is related to the density of the fluid. The major advantage to this method is that it allows foaming of a material well below its ambient glass transition temperature. Another advantage is that SC CO₂ has no surface tension, which eliminates any damage to the cellular structure as the CO₂ diffuses out of the substrate.

We recently reported^{16,24} studies on polystyrene foams prepared using Beckman's technique. We found that temperature, initial pressure, depth of the pressure quench, decompression rate, decompression profile, and geometric constraints of the foaming vessel can be used to control cell size, cell size distribution, and cell shape as well as the compressive properties of the foams. Shown in Figure 1.6 are the effects of temperature and initial pressure on the average cell diameter of the microcellular foam. Here, we report the investigation of several other parameters that may affect the foaming process using SC CO₂ as the blowing agent. We address the effects of polymer molecular weight and polydispersity on the final structure of the foam using polystyrene and blends of

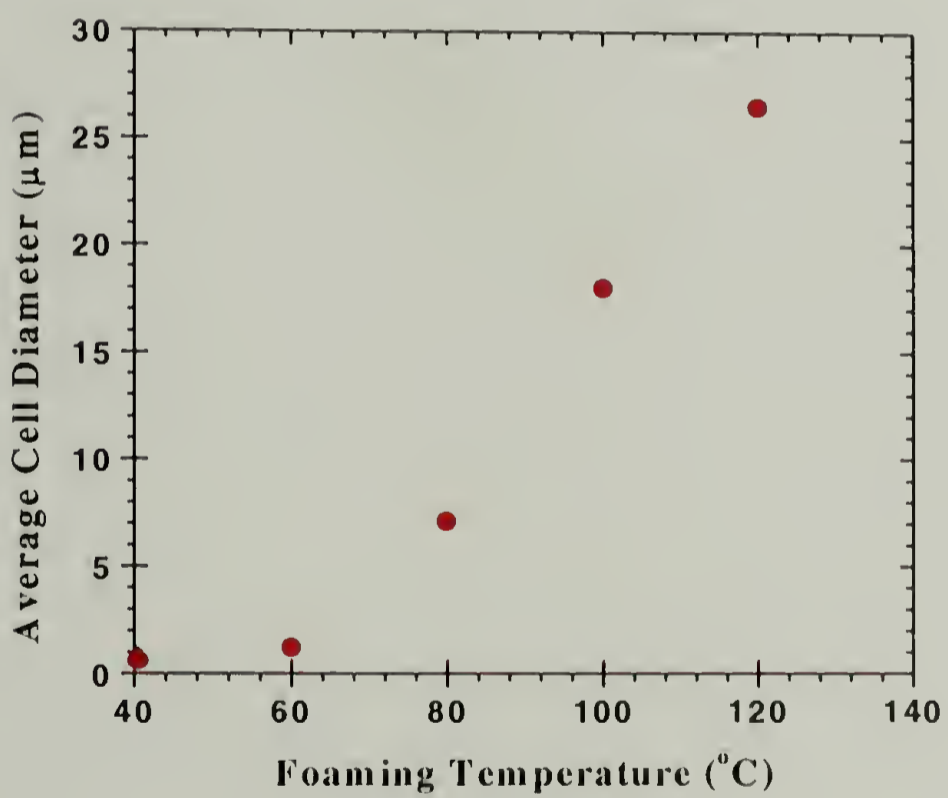
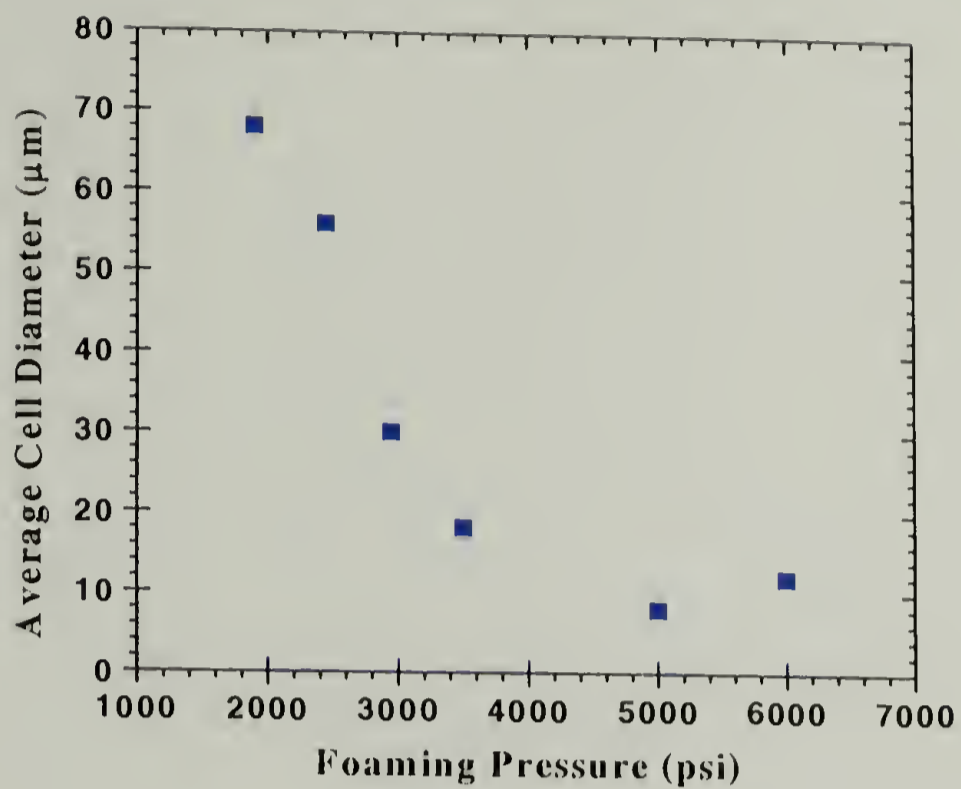


Figure 1.6. Effect of foaming pressure and temperature on the average cell diameter of foams produced by rapid decompression of SC CO₂-swollen polystyrene.¹⁶

polystyrene prepared by mixing samples with narrow molecular weight distributions. We also report the effect of a low molecular weight component found in commercial polystyrene samples and show that its presence dramatically changes the resulting foam structure. By varying the concentration of this oligomer, control of the cell size in foams can be achieved.

1.2. Experimental

1.2.1. Materials

All materials were purchased from Aldrich and used as received, unless otherwise indicated. Carbon dioxide (Coleman grade) was purchased from Merriam Graves and was dried by passing it through activated alumina to remove polar impurities and a copper catalyst (Q-5 - Engelhardt) to remove traces of oxygen. For radical polymerizations, styrene was distilled from CaH_2 and azobisisobutyronitrile (AIBN) was recrystallized from methanol. Polymer molecular weights and distributions were determined by gel permeation chromatography (GPC) relative to calibration with polystyrene using a system equipped with Polymer Laboratories PL gel columns (10^4 , 10^3 , 10^2 Å), a Polymer Laboratories LC 1120 HPLC pump with THF as the mobile phase, and an IBM LC9563 Variable UV detector set at 254 nm. Differential scanning calorimetry (DSC) was performed using a DuPont Instruments DSC2910 and a heating rate of 10 °C/min. The polystyrene samples, $\text{PS}^{514\text{K}}$ and $\text{PS}^{1050\text{K}}$ and the 580 g/mol styrene oligomer were purchased from Polymer Laboratories; the 285 g/mole sample was obtained from Polysciences. Commercial polystyrene samples, COMPS^1 , COMPS^2 , and COMPS^3 were purchased from SP², Acros and Aldrich, respectively.

1.2.2. Polymerizations

Homopolymers of polystyrene were synthesized using anionic polymerization techniques as described in Appendix A. Bulk radical polymerization of styrene was carried out in a 100 mL round bottom flask to which AIBN (0.020 g) and styrene (50 mL)

were introduced. This mixture was heated at 90 °C for 4 h, cooled, diluted with toluene, precipitated in methanol, recovered and dried under vacuum at 70 °C for several days.

1.2.3. Sample Preparation

Homopolymer blends were prepared by solvent casting from THF onto glass slides. The films were allowed to dry at room temperature for 1 day, dried under vacuum for 1 day, and finally dried at 120 °C for 6 h to remove last traces of solvent. The blends were then compression molded into 1/32-in. plaques at 175 °C. Homopolymer samples were compression molded under the same conditions.

1.2.4. Foam Preparation

Foams were prepared in 316 stainless steel high-pressure vessels using an ISCO syringe pump to fill the vessels with SC CO₂. A range of foaming conditions (P,T) were explored throughout this research and are too numerous to expound upon here, so an example is shown as follows. Samples were placed in high-pressure vessels, heated to 60 °C in a circulating bath, and filled to a pressure of 2050 psi (14.1 MPa) in convenient incremental stages. The vessels were then transferred to a circulating oil bath (100 °C) and maintained at this temperature for 3 h. At the end of this period, vessels were depressurized in ~4 sec at constant temperature. It should be noted that a slight cooling occurs inside the vessels due to the rapid expansion of the CO₂, thus the actual depressurization temperature is less than 100 °C. The vessels were then removed from the temperature bath, allowed to cool to room temperature, and the samples were recovered.

1.2.5. Foam Characterization

The foams were characterized primarily by scanning electron microscopy (SEM). Samples were cryo-fractured after immersion in liquid N₂, sputter-coated with ~200 Å of gold, and viewed using a JEOL 35CF SEM. The resulting micrographs were analyzed by Zeiss Image Analysis software to determine average cell diameters. Cell densities were calculated according to method proposed by Kumar and Suh.²² First, the number of cells nucleated per cm³ of foamed material (N_f) was calculated using the following equation:

$$N_f = \left(\frac{nM^2}{A} \right)^{3/2} \quad (1)$$

where n is the number of cells in the micrograph, M is the magnification factor, and A is the physical area of the micrograph in cm². The volume fraction of voids (V_f) in the sample can be then be calculated as follows:

$$V_f = \left(\frac{\pi}{6} \right) D^3 N_f \quad (2)$$

where D is the average cell diameter as determined by image analysis, and N_f is calculated as described above. But, N_f cells were actually nucleated in $(1-V_f)$ cm³ of original material. Therefore, the number of cells nucleated per cm³ of unfoamed material (N_o) can be calculated as follows:

$$N_o = \frac{N_f}{1 - V_f} \quad (3)$$

This is the number (N_o) that will be presented as cell density in this work.

1.3. Results and Discussion

Sorption experiments¹⁶ indicate that polystyrene can be swollen with supercritical carbon dioxide (SC CO₂) to a maximum level of ~12 wt%. This swelling lowers the glass transition temperature to slightly above room temperature.¹⁸ Upon decompression of the SC solution, the polystyrene foams as the sample becomes supersaturated with CO₂ gas. As the concentration of CO₂ in the polystyrene decreases (by partitioning into the pores), the glass transition temperature increases and when it exceeds the temperature of the experiment, the sample vitrifies, freezing in the foam structure. The number and size of the pores in the foam depend on the concentration of CO₂ in the polystyrene, the number of nucleation sites and the growth rate of the pores. The rate at which the CO₂ diffuses from the matrix to the growing pores depends on the temperature of the experiment, the pressure of the experiment and the viscosity of the swollen polymer. As a result of the viscosity dependence, the molecular weight and polydispersity of the polymer should influence the structure of the foam developed during decompression.

Foaming experiments were performed on a series of narrow molecular weight distribution polystyrenes and commercial polystyrene samples of molecular weight and polydispersity summarized in Table 1.1. The polymer of choice for these experiments was polystyrene due to its commercial availability as well as the ease of synthesis by living anionic techniques. Figure 1.7 shows the GPC chromatograms of three different commercial polystyrene samples purchased from SP², Aldrich, and Acros. These materials are designated ^{COM}PS¹, ^{COM}PS², and ^{COM}PS³, respectively. As seen in the chromatograms, these materials have broad molecular weight distributions and possess

Table 1.1. Polymer sample characteristics.

sample	M_n (kg/mol)	M_w (kg/mol)	M_w/M_n	T_g
PS ^{6K}	6.6	6.8	1.03	95
PS ^{25K}	24.4	25.4	1.04	104
PS ^{62K}	62.1	64.0	1.03	107
PS ^{147K}	147	153	1.03	108
PS ^{514K}	514	540	1.05	107
PS ^{1050K}	1030	1080	1.05	109
COMPS ¹	66.5	204	3.07	105
COMPS ²	65.7	246	3.74	103
COMPS ³	120	288	2.38	105
PS ^R	96	214	2.22	106
^B PS ¹	61	188	3.07	
^B PS ²	12.8	179	13.95	
^B PS ³	8.4	175	20.76	

very similar number and weight average molecular weights. Scanning electron micrographs of foams produced by decompression at 100 °C and 3400 psi (23.4 MPa) are shown in Figure 1.8 for the three commercial samples. The results of image analysis of these micrographs are shown in Table 1.2. The commercial samples exhibit average cell diameters of 20-25 μm and cell densities of 10^7 cells / cm^3 . This is in good agreement with the results of Arora et. al¹⁶ for these conditions.

Next, polystyrene samples possessing well-defined molecular weights and narrow molecular weight distributions were prepared by living anionic techniques. Figure 1.9 shows the GPC chromatograms of four polymers with increasing molecular weight, with the chromatogram of ^{COM}PS¹ included for comparison. The narrow molecular weight distribution materials are designated with the following notation: PS^{25K}, PS^{147K}, PS^{514K}, and PS^{1050K}, where the superscript indicates the weight average molecular weight of the polymer. Scanning electron micrographs of foams produced by decompression at 100 °C and 3400 psi (23.4 MPa) are shown in Figure 1.10. cursory examination of these micrographs shows a striking difference between the commercial and narrow molecular weight distribution polystyrene samples. The cell size (diameter) in each of the narrow molecular weight distribution polymer foams is $\sim 5 \mu\text{m}$. The results of image analysis of these micrographs are shown in Table 1.2. The cell size is independent of molecular weight over a very large molecular weight range. The only exception to this is the PS^{25K} sample that shows a smaller cell diameter (2.2 μm), which may be a result of the molecular weight being fairly close to the entanglement molecular weight of polystyrene. The PS^{25K} sample was brittle after compression molding, and the foamed sample easily crumbled during handling, making characterization precarious. In marked contrast to

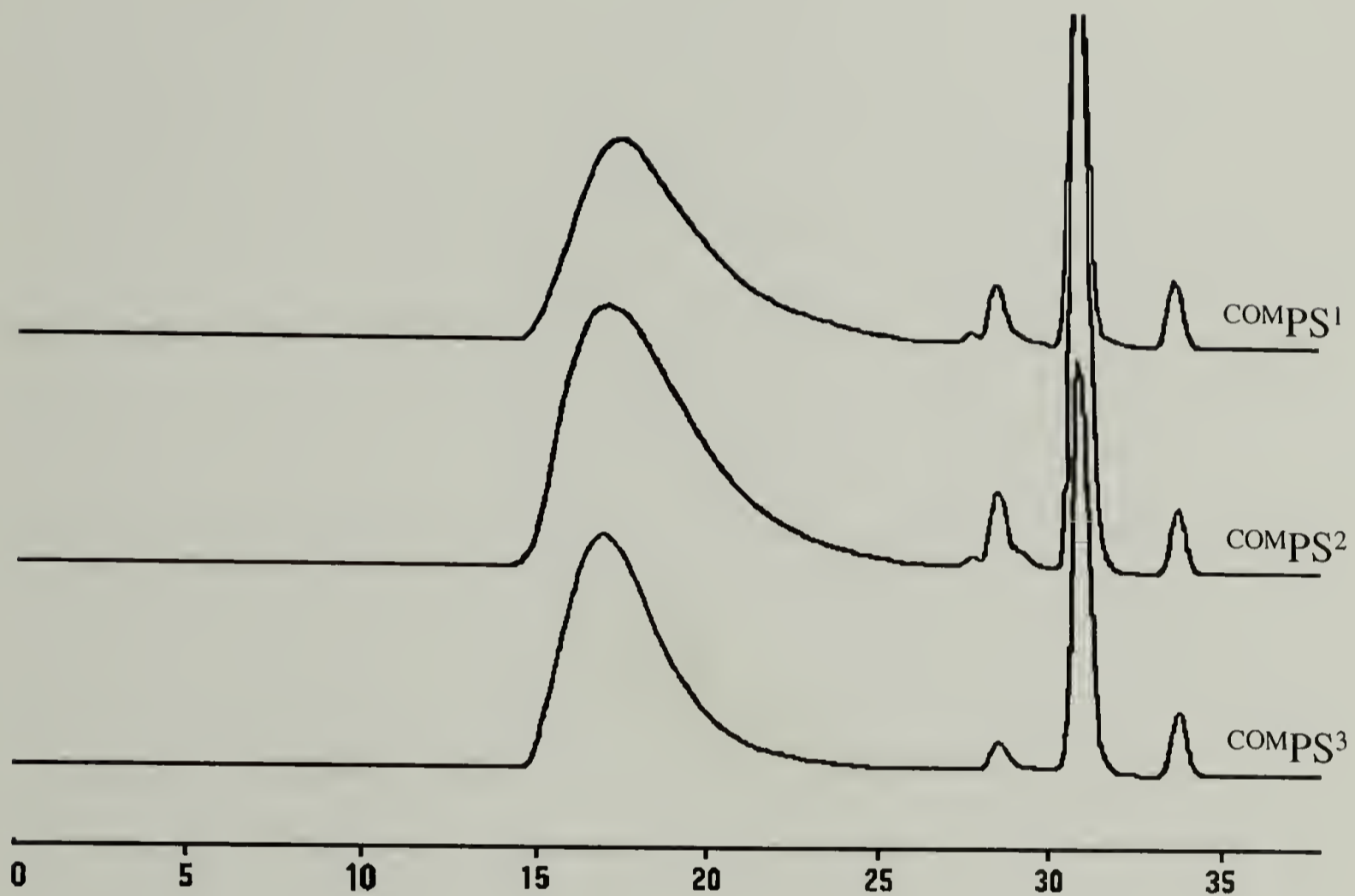
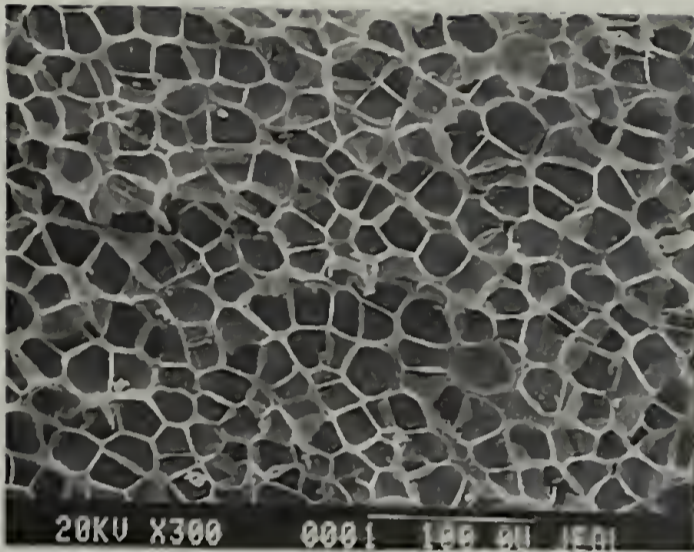
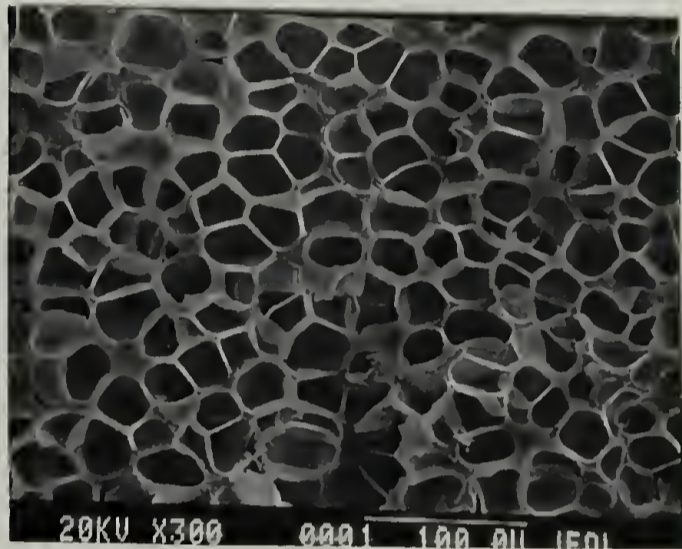


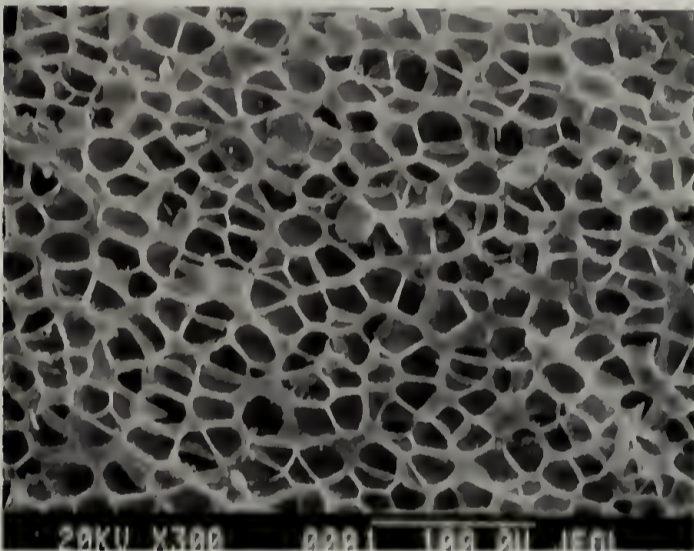
Figure 1.7. GPC chromatograms of three different commercial polystyrene samples: (from top to bottom) $^{COM}PS^1$ (SP²), $^{COM}PS^2$ (Aldrich), and $^{COM}PS^3$ (Acros).



(a)



(b)



(c)

Figure 1.8. SEM micrographs of fracture surfaces of foams prepared from three different commercial polystyrene samples: (a) $^{COM}PS^1$ (SP²), (b) $^{COM}PS^2$ (Aldrich), and (c) $^{COM}PS^3$ (Acros). Foaming conditions were 100 °C and 3400 psi.

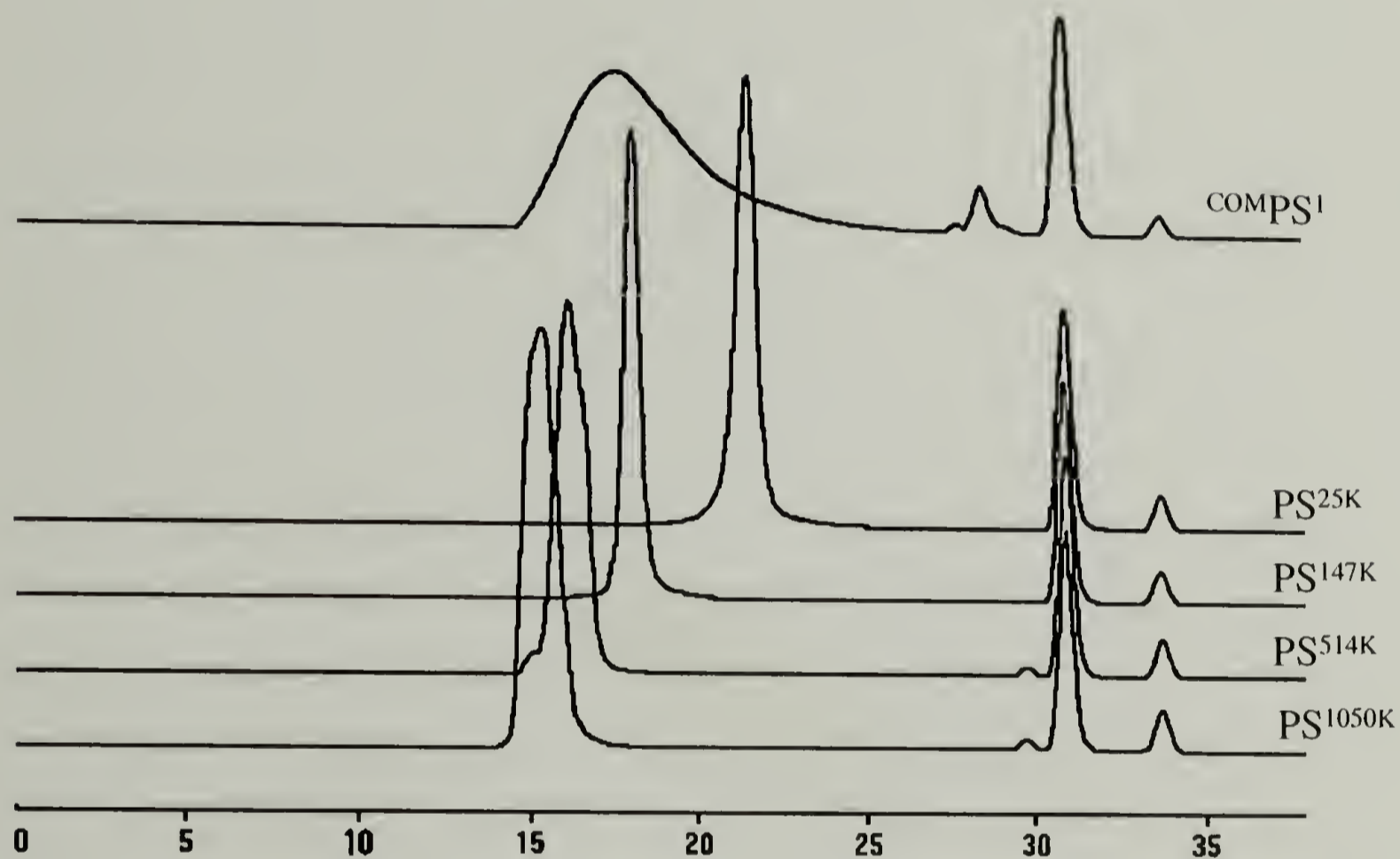
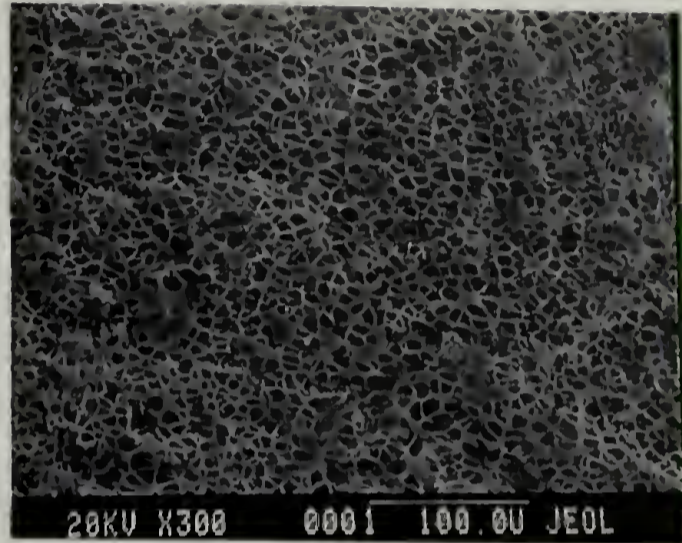


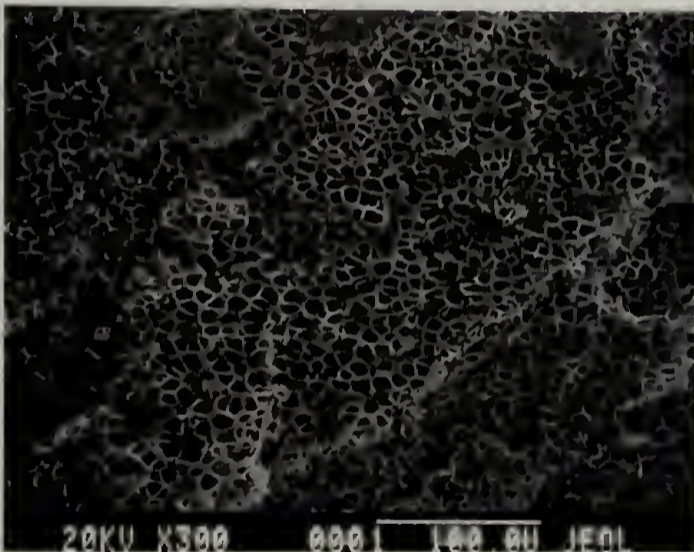
Figure 1.9. GPC chromatograms of one commercial and four narrow molecular weight polystyrene materials: (from top to bottom) $^{COM}PS^1$, PS^{25K} , PS^{147K} , PS^{514K} , and PS^{1050K} .



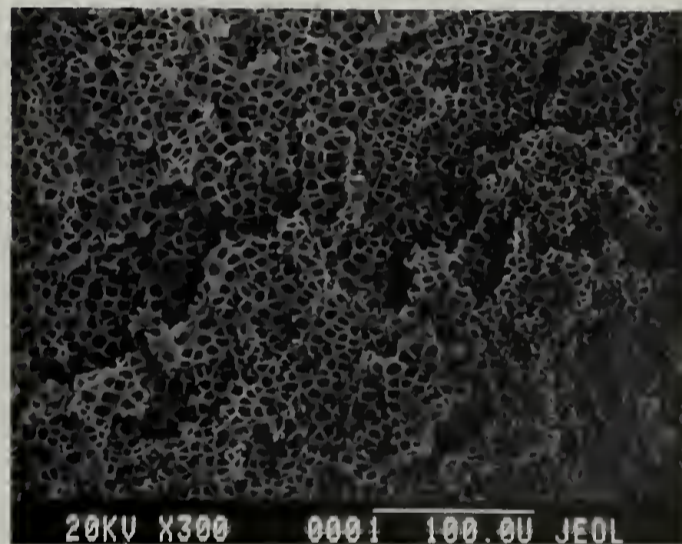
(a)



(b)



(c)



(d)

Figure 1.10. SEM micrographs of fracture surfaces of foams prepared from four narrow molecular weight polystyrene materials: (a) PS^{25K}, (b) PS^{147K}, (c) PS^{514K}, and (d) PS^{1050K}. Foaming conditions were 100 °C and 3400 psi.

this, the commercial foamed polymer exhibits a cell diameter of $\sim 24 \mu\text{m}$; the cell diameter is nearly five times larger and the cell volume is more than 100 times that of the narrow molecular weight distribution polystyrenes.

The most obvious difference between the narrow molecular weight distribution polymers and the commercial materials is the molecular weight distribution. The large disparity between cell sizes indicates that either the nucleation density of the pores is much greater in the narrow molecular weight distribution polymers or that the growth rate of the pores is much faster for the broad molecular weight distribution polymers. This may arise from a change in the free energy associated with the formation of a nucleus of critical size or, in the case of homogeneous nucleation, a change in the growth rate of the pores. The increase in pore size for the broad molecular weight distribution polymers can also suggest that both high and low molecular weight components are necessary to support the large cell structure. The high molecular weight component would serve to enhance the number of intermolecular entanglements, whereas the lower molecular weight component would promote rapid cell growth.

To address the latter possibility, a polydisperse sample was prepared by blending several narrow molecular weight distribution polymers to yield a sample that had approximately the same M_n and M_w as $^{\text{COM}}\text{PS}^1$. This blend was comprised of six different molecular weight polystyrene samples, $\text{PS}^{6\text{K}}$, $\text{PS}^{25\text{K}}$, $\text{PS}^{62\text{K}}$, $\text{PS}^{147\text{K}}$, $\text{PS}^{514\text{K}}$ and $\text{PS}^{1050\text{K}}$. To determine the blend ratio, a GPC chromatogram of all six narrow molecular weight samples was obtained and is shown in Figure 1.11. The peaks were then overlaid onto the GPC chromatogram of a commercial sample ($^{\text{COM}}\text{PS}^1$) and rectangles were constructed of equal width. The position of the rectangles corresponded to the peak

elution time for each of the narrow molecular weight materials. By measuring the height of the rectangles at the point of intersection with the chromatogram, an area could be calculated for each molecular weight. The individual peak areas were then divided by the sum of all the areas and these ratios were used for determining blend composition. This process is illustrated in Figure 1.12. The simulated polydisperse sample had molecular weights of $M_n = 61\text{K}$, $M_w = 188\text{K}$ ($M_w/M_n = 3.07$); the GPC chromatogram of this blend ($^B\text{PS}^1$) is shown in Figure 1.13. Foams from this sample, however, showed cell sizes in the range of 5-6 μm (see Figure 1.18.). The similarity in the cell size of the foams produced from the simulated polydisperse material and from the narrow molecular weight distribution polymers indicates that polydispersity is not critical in defining cell size. This was further demonstrated by foaming a polystyrene sample prepared by bulk free radical polymerization of styrene. GPC indicates that this sample (PS^R) has $M_n = 96\text{K}$ and $M_w = 214\text{K}$ ($M_w/M_n = 2.22$). The chromatogram is shown in Figure 1.14. The sample was foamed under identical conditions and the cell sizes were $\sim 5\ \mu\text{m}$, identical to that of narrow molecular weight distribution polymers and the simulated polydisperse sample (see Figure 1.15).

This result prompted a closer examination of any differences between the commercial materials and those prepared in our laboratories. The commercial samples show a peak in the size exclusion chromatogram at a retention time of ~ 28 minutes which corresponds to a molecular weight of ~ 270 g/mole. This indicates the presence of a low molecular weight material, lower than any component of the simulated polydisperse sample. Consequently, a seventh component was added to the 6-component simulated polydisperse system ($^B\text{PS}^1$): a styrene oligomer of molecular weight of 580 g/mole. Two

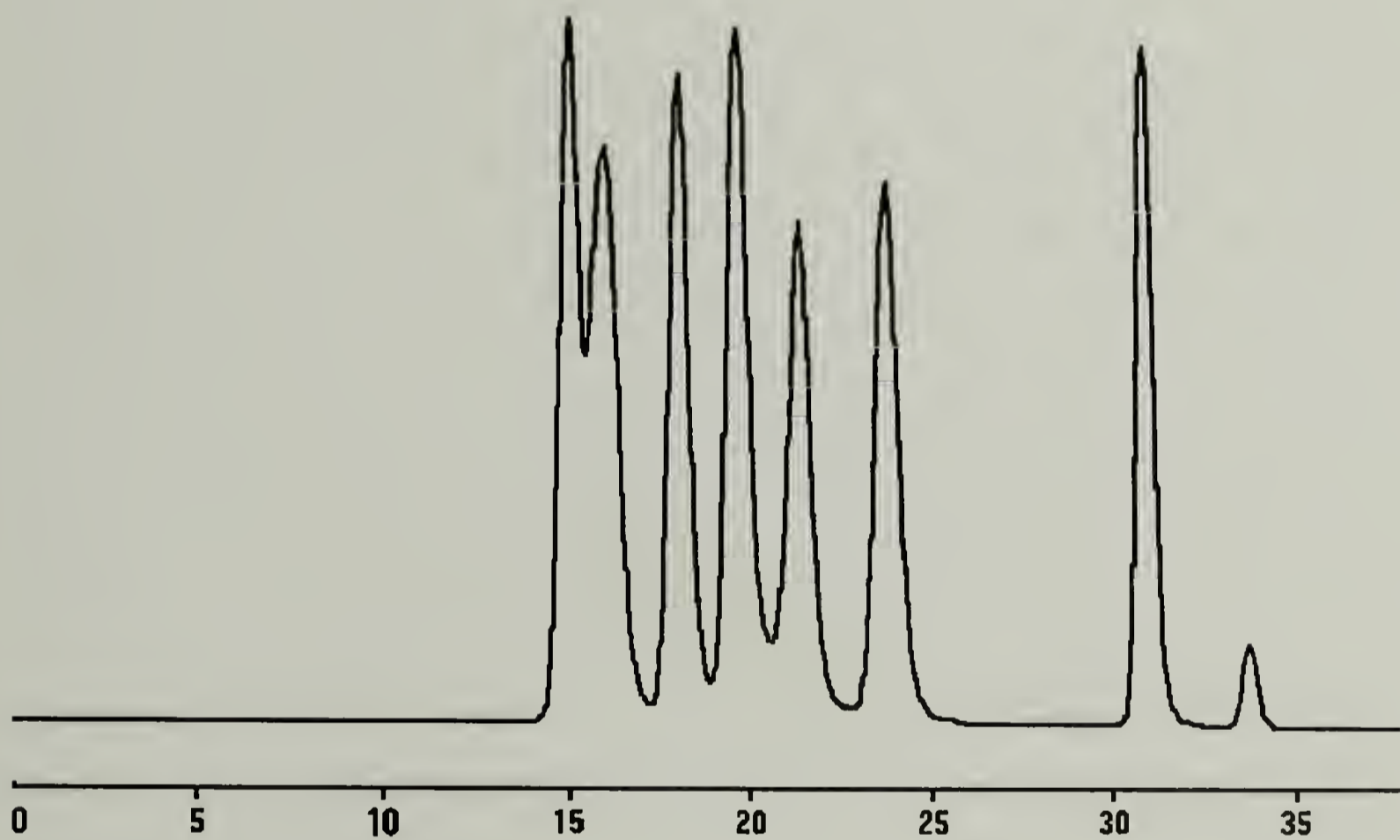


Figure 1.11. GPC chromatogram of six narrow molecular weight polystyrenes used in calculating blend composition.

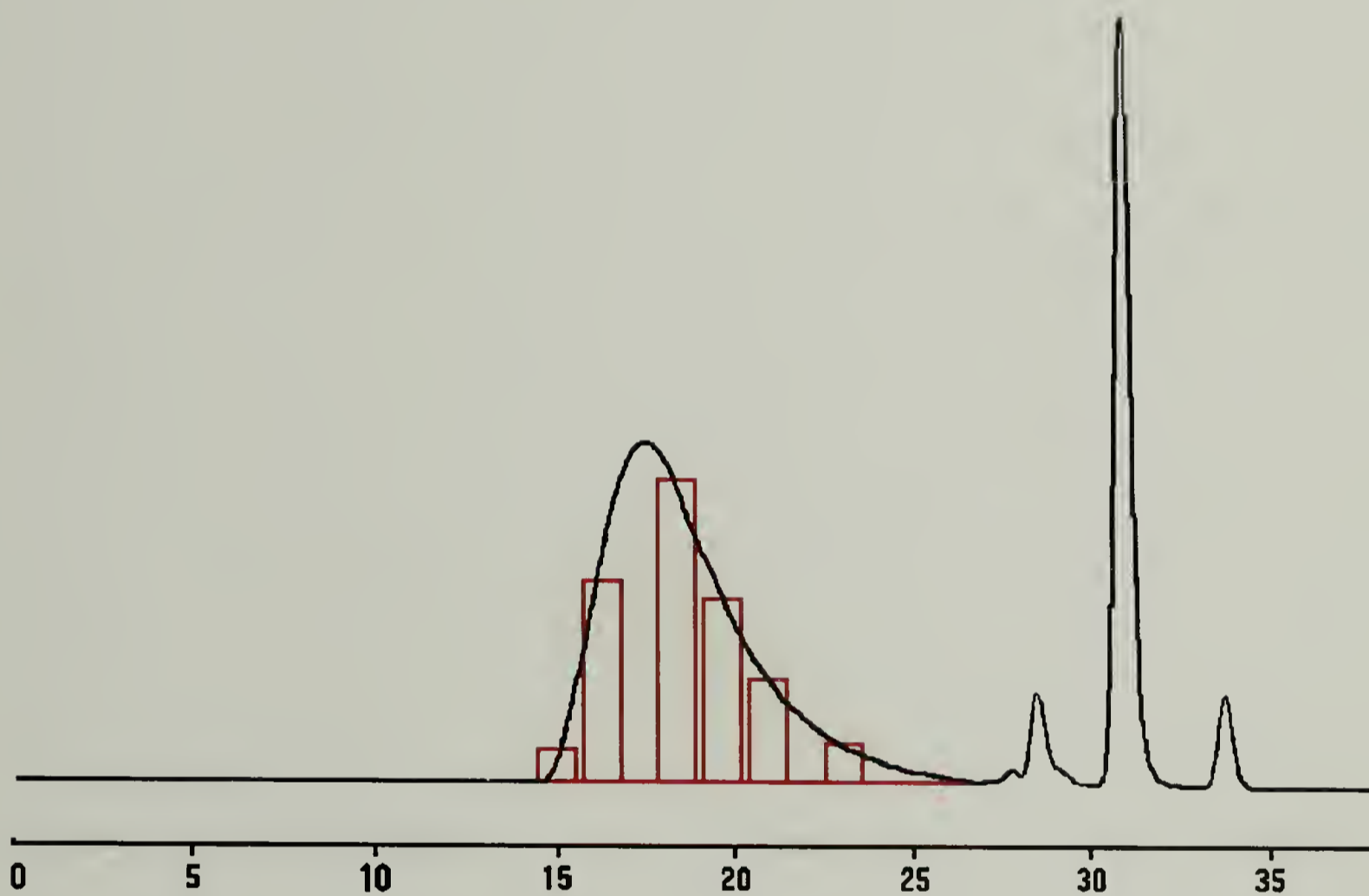


Figure 1.12. Geometric construction for determining the percentage of each molecular weight to be added to the blend.

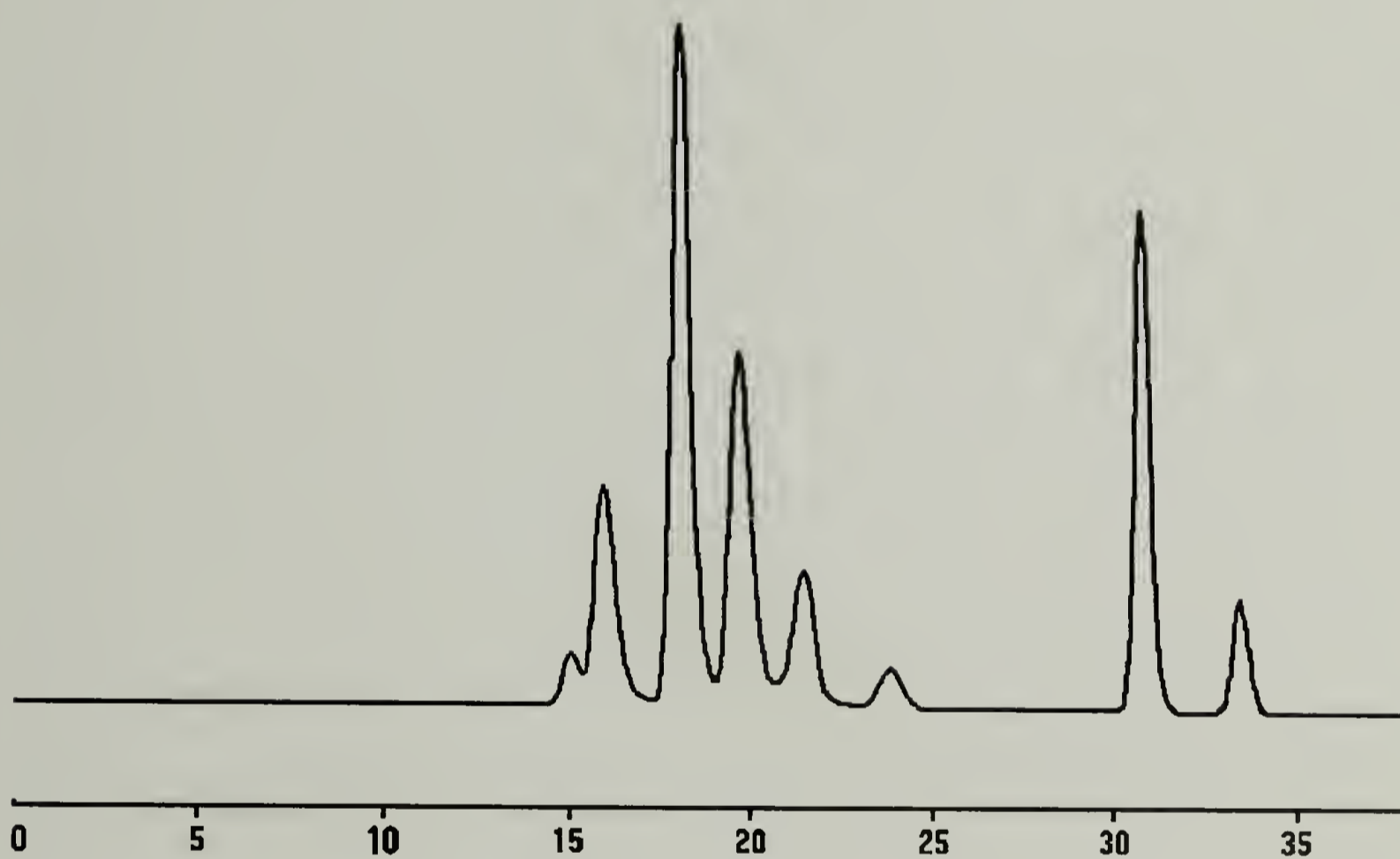


Figure 1.13. GPC chromatogram of a simulated polydisperse polystyrene sample, $^B\text{PS}^1$, which is a 6-component blend of $\text{PS}^{6\text{K}}$, $\text{PS}^{25\text{K}}$, $\text{PS}^{62\text{K}}$, $\text{PS}^{147\text{K}}$, $\text{PS}^{514\text{K}}$ and $\text{PS}^{1050\text{K}}$.

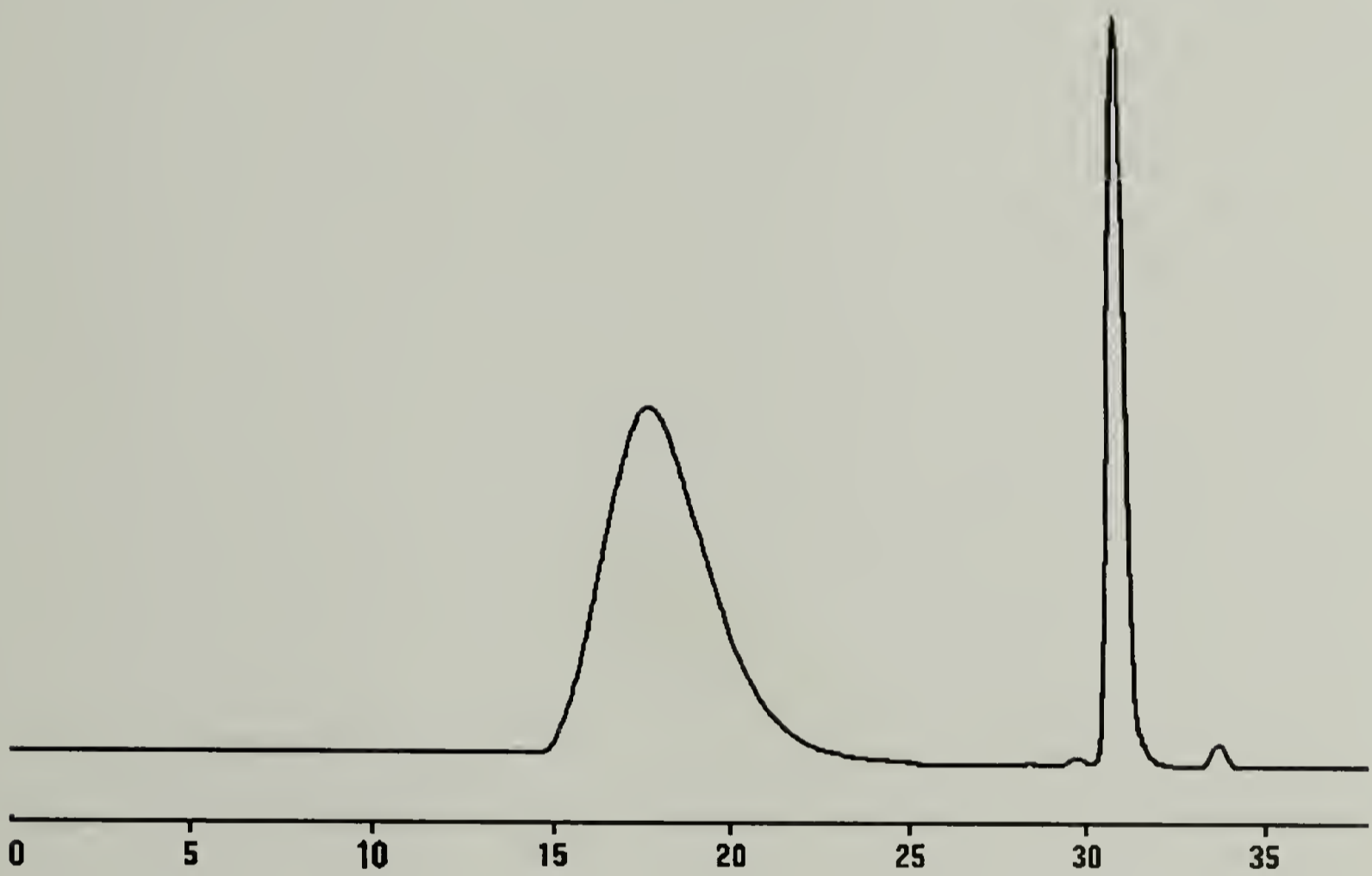
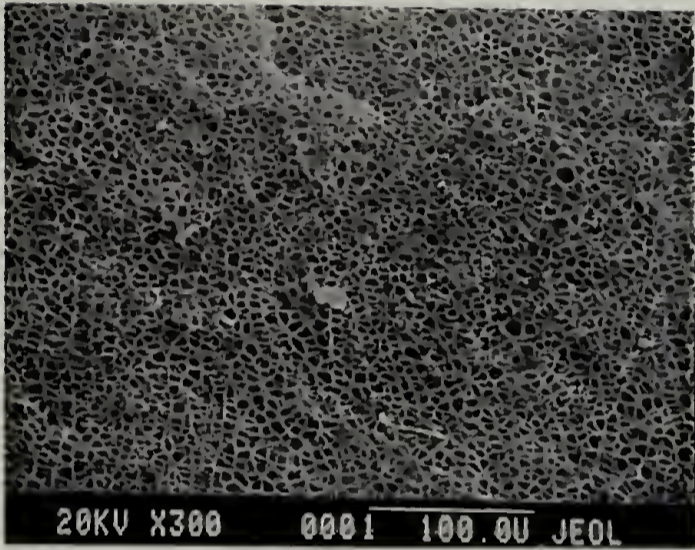
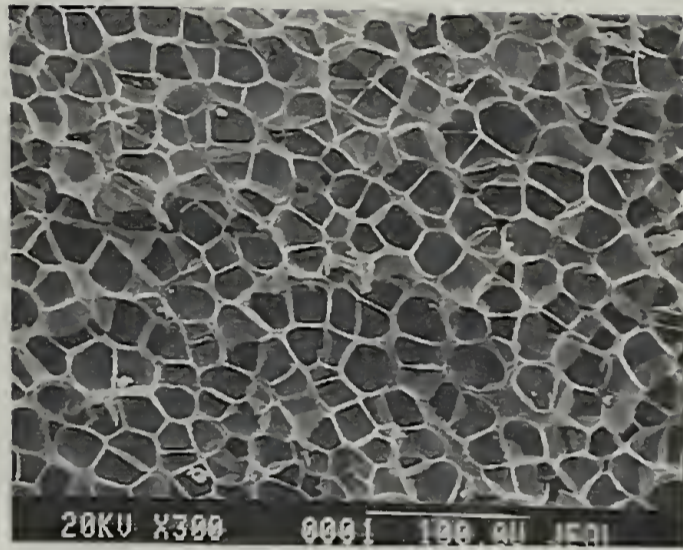


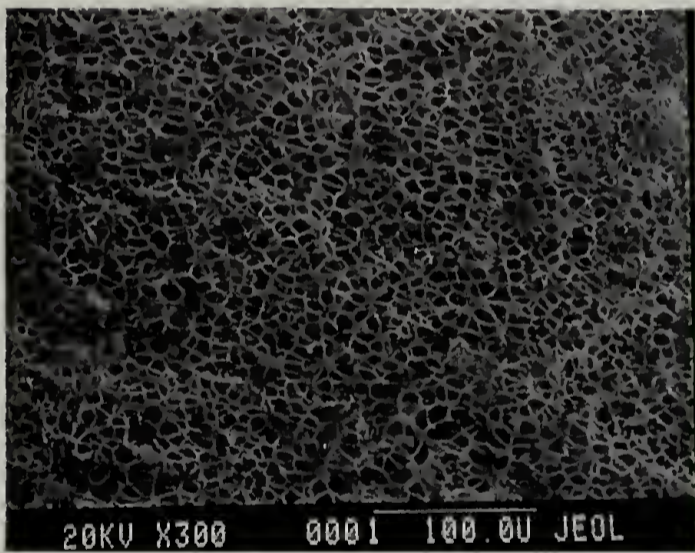
Figure 1.14. GPC chromatogram of a polystyrene sample (PS^R) prepared by bulk radical polymerization initiated by AIBN in toluene at $70\text{ }^\circ\text{C}$.



(a)



(b)



(c)

Figure 1.15. SEM micrographs of fracture surfaces of foams prepared from (a) PS^R as well as (for comparison) (b) $^{COM}PS^I$ and (c) PS^{147K} . Foaming conditions were $100^\circ C$ and 3400 psi.

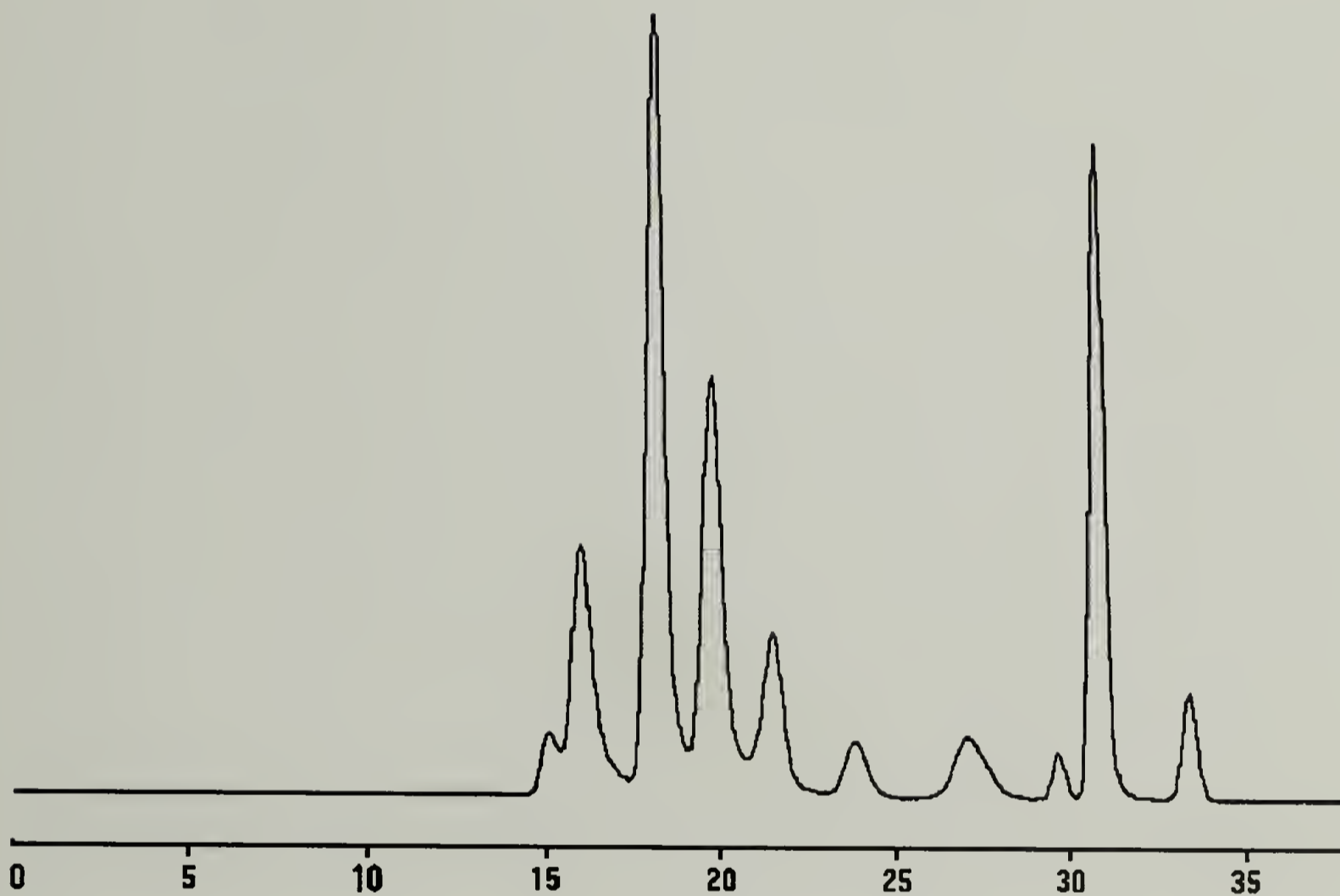


Figure 1.16. GPC chromatogram of the simulated polydisperse polystyrene sample $^B\text{PS}^2$, which contains the samples in $^B\text{PS}^1$ plus 7.4 wt% of a 560 g/mol styrene oligomer.

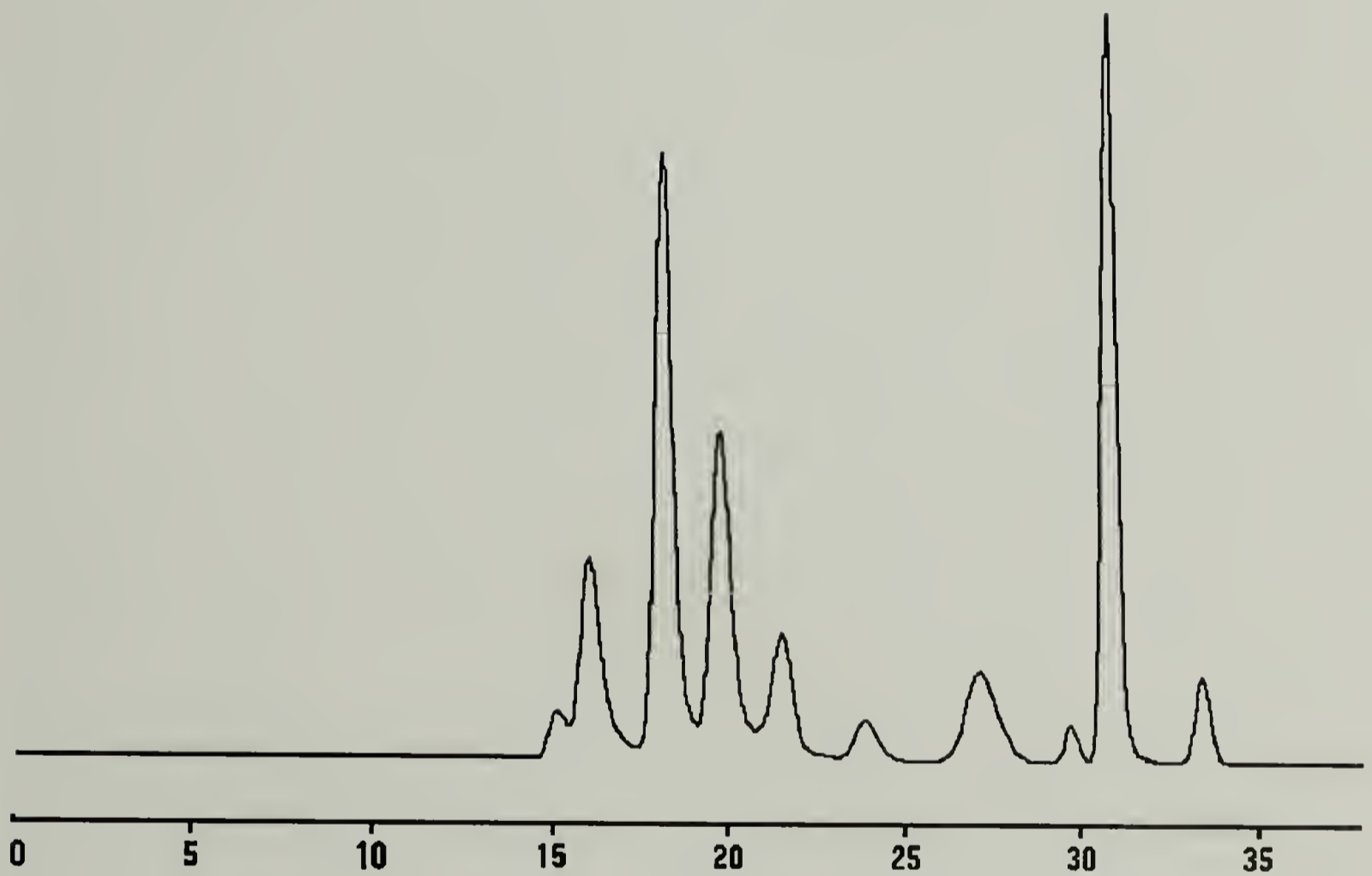
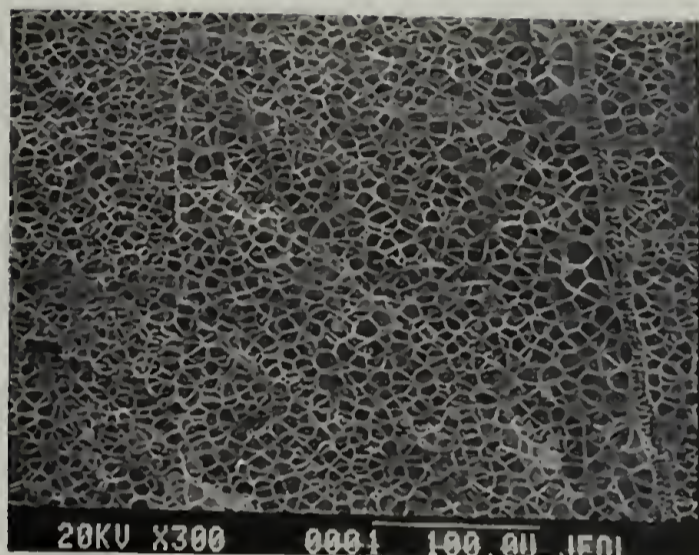
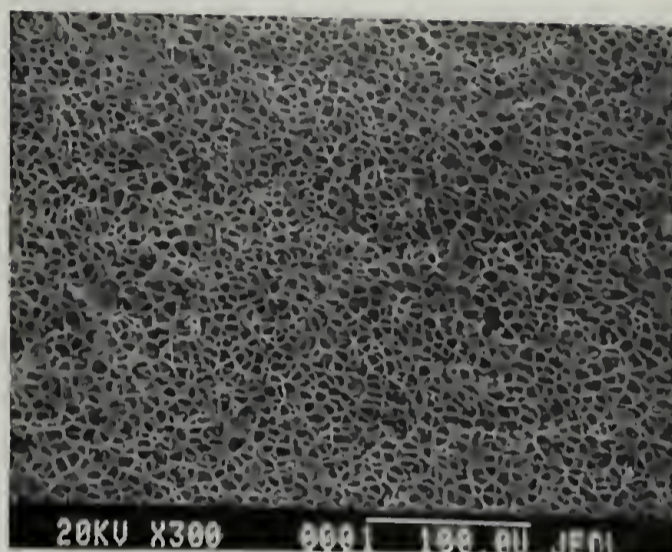


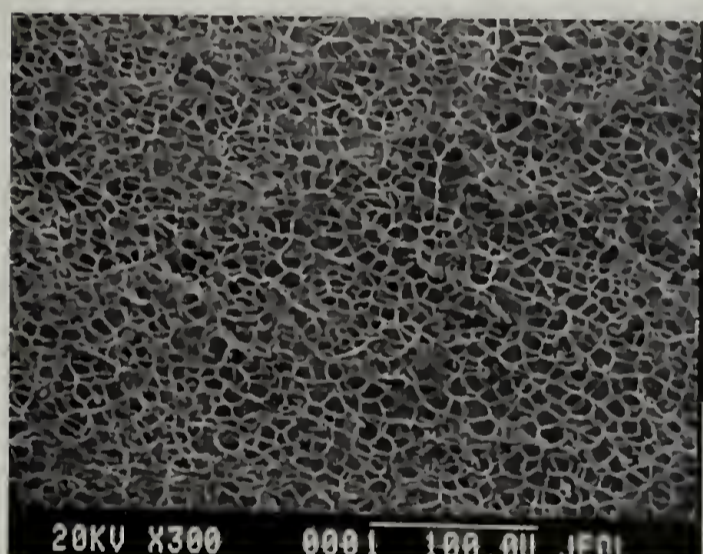
Figure 1.17. GPC chromatogram of the simulated polydisperse polystyrene sample ${}^B\text{PS}^3$, which contains the samples in ${}^B\text{PS}^1$ plus 13.0 wt% of a 560 g/mol styrene oligomer.



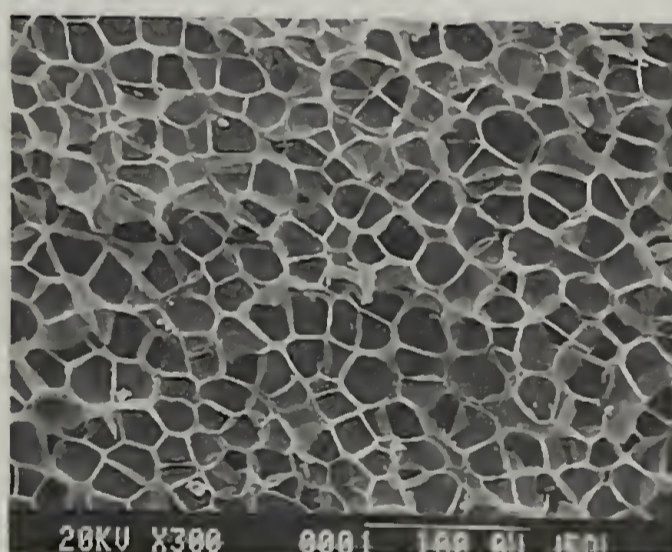
(a)



(b)



(c)



(d)

Figure 1.18. SEM micrographs of fracture surfaces of foams prepared from the simulated polydisperse polystyrene samples (a) BPS^1 , (b) BPS^2 , (c) BPS^3 , and (d) $COMPS^1$ (for comparison). Foaming conditions were 100 °C and 3400 psi.

blends were prepared with this oligomer, one with 7.4 wt% oligomer (^BPS²) and one with 13 wt% oligomer (^BPS³). The size exclusion chromatograms for these blends are shown in Figures 1.16 - 1.17 and the foam structures prepared with these samples are displayed in Figure 1.18. The average cell diameters were in the range of 6-8 μm, which is slightly greater than those of the narrow molecular weight distribution samples but still much smaller than those of the commercial samples.

Using a different strategy to determine whether the low molecular weight component is responsible for the increase in cell size, this component was extracted from ^{COM}PS¹ prior to foaming. ^{COM}PS¹ was reprecipitated from a THF solution into methanol, filtered and vacuum dried as described earlier. The first reprecipitation lowered the concentration of the oligomer from 3.8% to 1.3% as is shown in Figure 1.19. The percentages reported here are area percentages obtained by dividing the area under the peak at 270 g/mole by the total area of the entire distribution, excluding the area due to the toluene flow marker (~31 min) and beyond. The resulting foam (^{COM}PS^{1EX1}) shows pore sizes of 8.9 μm, as indicated in Figure 1.20. Second and third reprecipitations lowered the concentration of low molecular weight material to 0.9% and 0.1% respectively. The cell diameters in foams of these samples (^{COM}PS^{1EX2} and ^{COM}PS^{1EX3}), as shown in Figure 1.20, are 7.2 μm and 5.9 μm, respectively, essentially identical, in the case of ^{COM}PS^{1EX3}, to those prepared with narrow molecular weight distribution samples. These results indicate that manipulating the concentration of this low molecular weight component can control cell size of the resulting foam.

The filtrate could then be isolated by evaporation of the solvent and characterized. This was accomplished by rotary evaporating the filtrate and recovering the product. An

interesting observation was made during this process. As solvent was removed, a solid product precipitated and was separated by filtration. Further removal of solvent from the filtrate resulted in the same sequence of events, and another solid product was recovered. This process was repeated several times with the same results, with the exception that the precipitate became more of a viscous substance than a solid, but could still be isolated. The transition from recovering a solid product to recovering a viscous liquid suggests that molecular weight of each aliquot is decreasing. Therefore, the samples were then characterized by GPC to identify the molecular weight of each material. The chromatogram from this experiment is shown in Figure 1.21. Interestingly, it appears that the rotary evaporation process results in a fractionation of the filtrate that was extracted out during the reprecipitations. Even more interesting is that the first aliquot recovered from the rotary evaporation fractionation is fairly high in molecular weight (~2000 g/mol), indicating that the extraction process removes part of the low molecular weight tail in the polydisperse sample. The final aliquot overlaps perfectly with the low molecular weight oligomer seen in the ^{13}C NMR trace, and the trace clearly reveals the presence of three fragments of discrete molecular weights. This final fraction was also characterized by both IR and NMR to probe for the presence of specific functional groups that might enhance interactions between the SC CO₂ and the sample containing this oligomer. No detectable functionality, such as carboxyl or hydroxyl groups, was found in the oligomer. All characterization methods indicated that the material was styrenic in chemical nature.

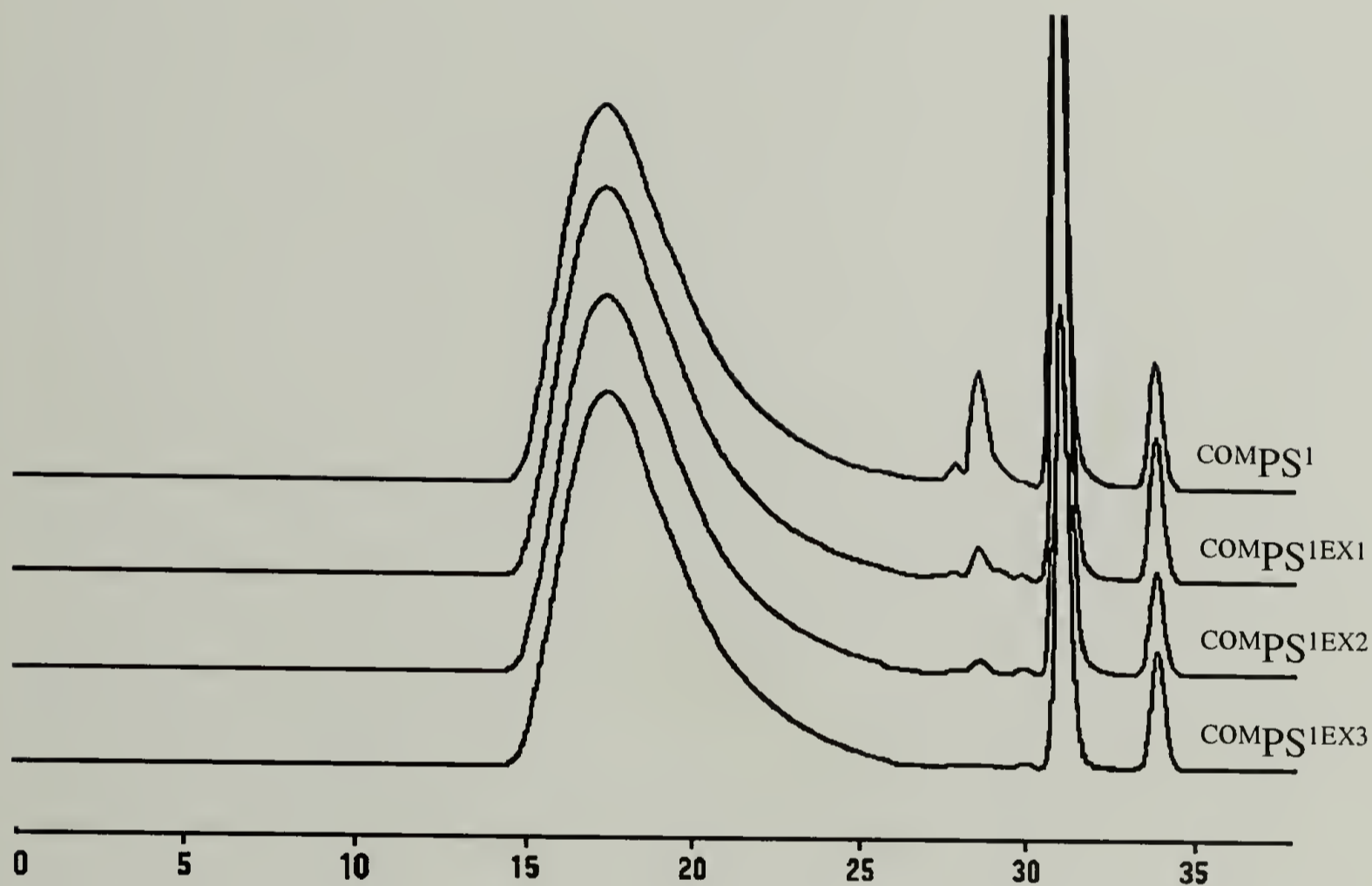
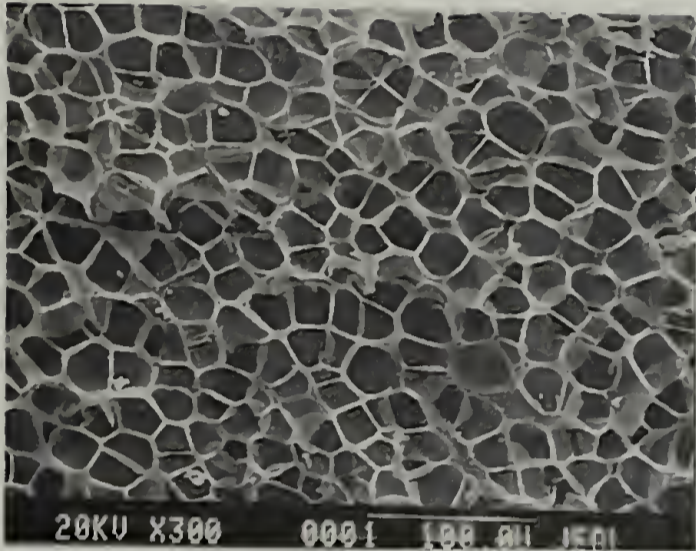
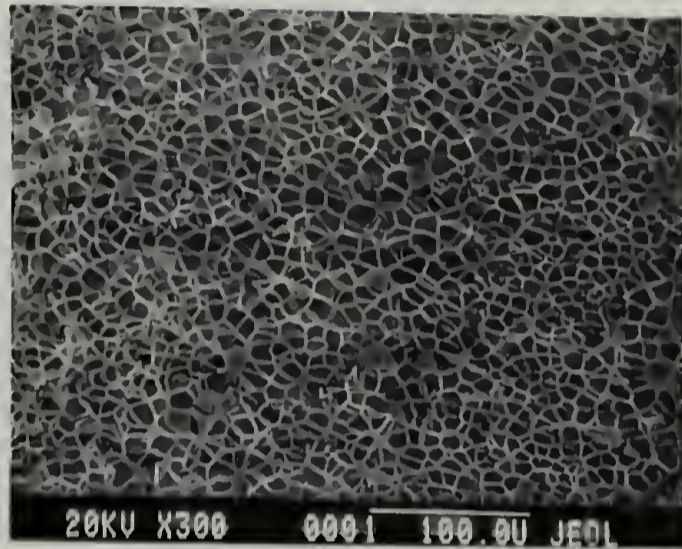


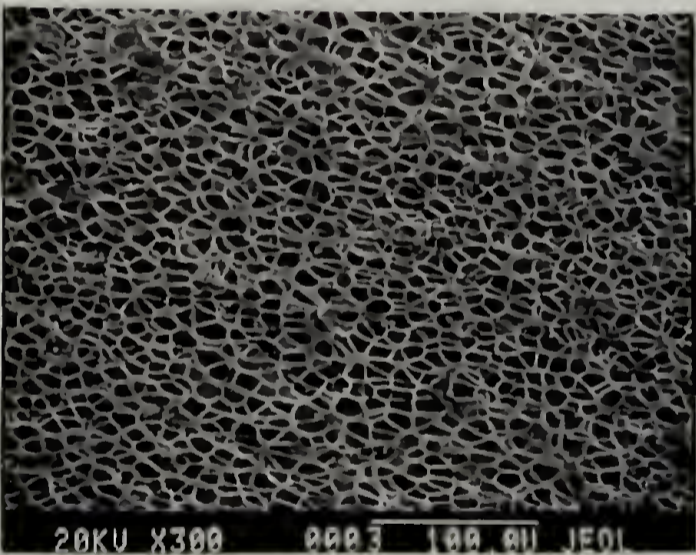
Figure 1.19. GPC chromatograms showing the removal of a low molecular weight (LMW) component from $^{\text{COM}}\text{PS}^1$ by repeated reprecipitation from THF in methanol: (from top to bottom) $^{\text{COM}}\text{PS}^1$ (3.8% LMW component), $^{\text{COM}}\text{PS}^{1\text{EX}1}$ (1.3% LMW component), $^{\text{COM}}\text{PS}^{1\text{EX}2}$ (0.9% LMW component), $^{\text{COM}}\text{PS}^{1\text{EX}3}$ (0.1% LMW component).



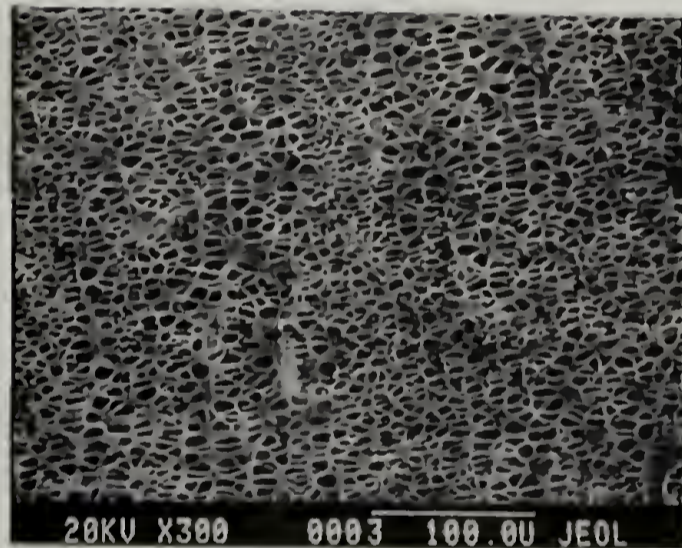
(a)



(b)



(c)



(d)

Figure 1.20. SEM micrographs of fracture surfaces of foams prepared from the extracted polydisperse samples: (a) COMPS1 , (b) COMPS1EX1 , (c) COMPS1EX2 , and (d) COMPS1EX3 . Foaming conditions were 100 °C and 3400 psi.

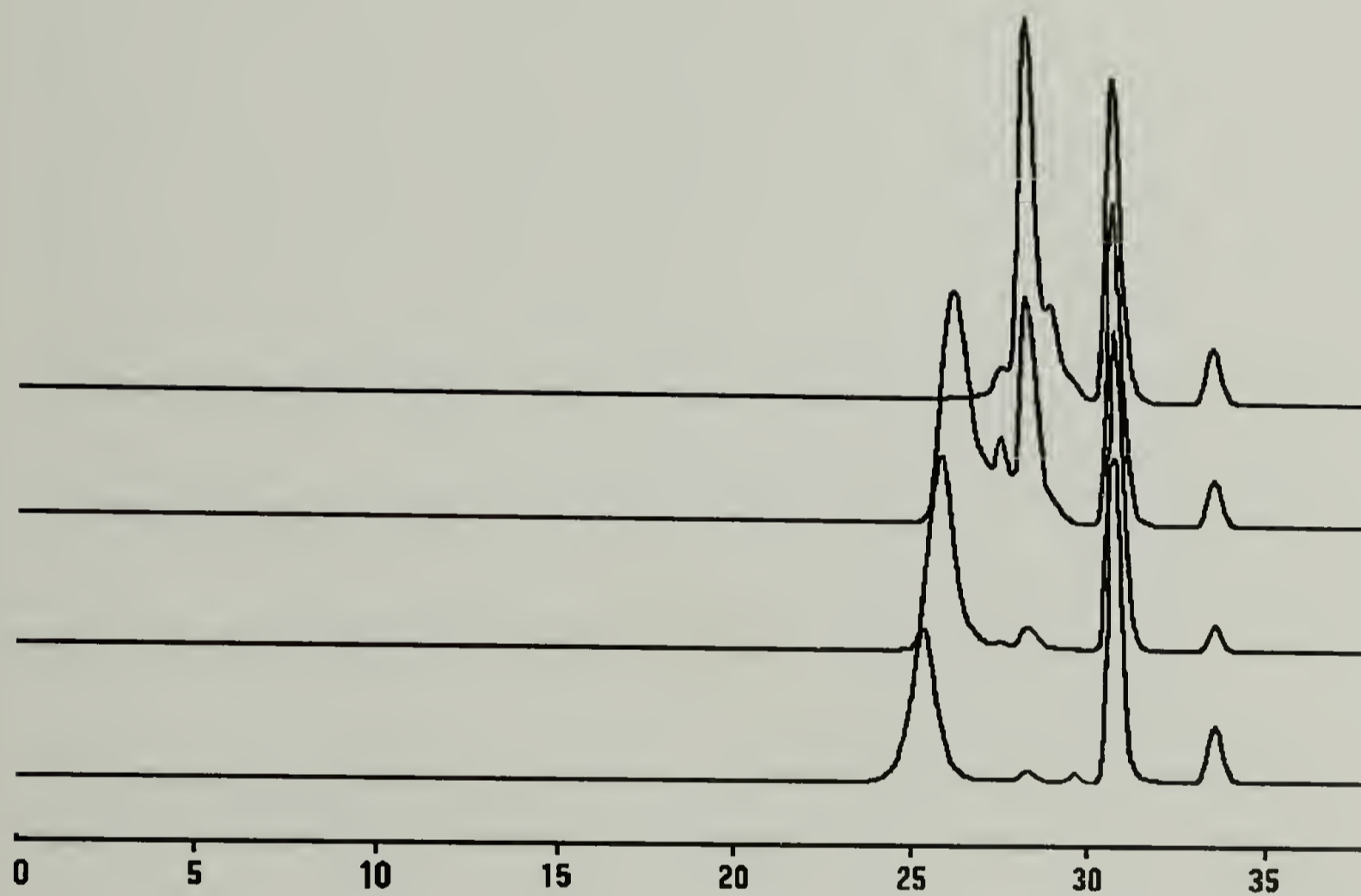


Figure 1.21. GPC chromatograms of the fractionated products recovered after repeated rotary evaporation of the filtrate from extraction of ^{COM}PS^I by reprecipitation.

To determine whether this low molecular weight component acted in a unique manner to affect the observed foam structure, a polystyrene standard (styrene oligomer) having a molecular weight of 285 g/mole and a PDI of 1.20 was purchased. This low molecular weight sample was blended with PS^{147K}. Three different samples were made containing 3.6 wt% (^BPS⁴), 7.3 wt% (^BPS⁵), and 9.9 wt% (^BPS⁶) of the 285 g/mole oligomer. The GPC chromatograms are shown in Figure 1.23. Foamed samples of pure PS^{147K} exhibit cell diameters ~5 μm (Table 1.2) before addition of any low molecular weight component. Upon addition of the 285 g/mole component, the resulting foams show an increase in cell size up to 19 μm for the 9.9 wt% sample, as shown in Figure 1.24. This indicates that there is nothing unique about the low molecular weight impurity found in the commercial samples, and that the effect of this low molecular weight component can be reproduced by the addition of a low molecular weight polystyrene standard. While the overall efficiency of the low molecular weight impurity in the commercial samples may be greater than that seen for the low molecular weight polystyrene (3.8 area% compared to 9.9 wt%), the end result in terms of pore density and increased pore size is the same. The presence of a low molecular weight component having a molecular weight of 270-285 g/mole, but less than the 580 g/mole (that was added in the simulated polydisperse blends), leads to the formation of large cells with dimensions in the range of 19-24 μm.

The first question to be asked is where does this low molecular weight material come from? And why is it present in commercial materials but not in materials synthesized in-house, even by free-radical polymerization? The answer may lie in the initiation step of the polymerization of styrene prepared by commercial processes.

Radical polymerization of styrene can be initiated either by adding an external initiator (e.g. AIBN) that decomposes either thermally or by exposure to light, or it can be self-initiated (thermal polymerization). Thermal polymerization involves heating neat styrene to induce a Diels-Alder reaction between two styrene monomers, which rearranges to form radical species A and B. This reaction is illustrated in Figure 1.22.

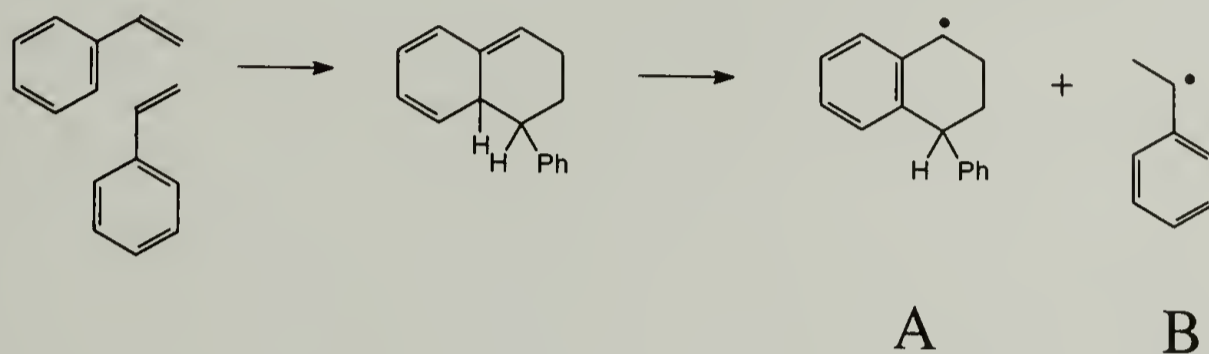


Figure 1.22. Thermally-induced initiation of styrene, producing radical species that can recombine to form inactive oligomers.

The radical species can either initiate polymerization or they can recombine through a radical cage-effect. The potential reactions that could lead to the formation of inactive oligomers are as follows: (a) B-proton – 106: g/mol, (b) A-proton – 208 g/mol, (c) B-B – 208 g/mol, (d) A-B – 311 g/mol, and (e) A-A – 414 g/mol. Reaction (a) would be masked by the toluene flow marker in the GPC chromatograms, but reactions (b) through (e) could be the discrete steps in molecular weight seen in Figure 1.21. Therefore, it is speculated here that the source of the oligomer present in the commercial polystyrene samples is simply the decomposition products of the thermally initiated polymerization of styrene, and no steps are taken to remove this material before processing the polymer into pellet form. Hence, polymerization initiated using AIBN (as performed in-house) would not contain this oligomer, and therefore behaves very differently during the foaming process.

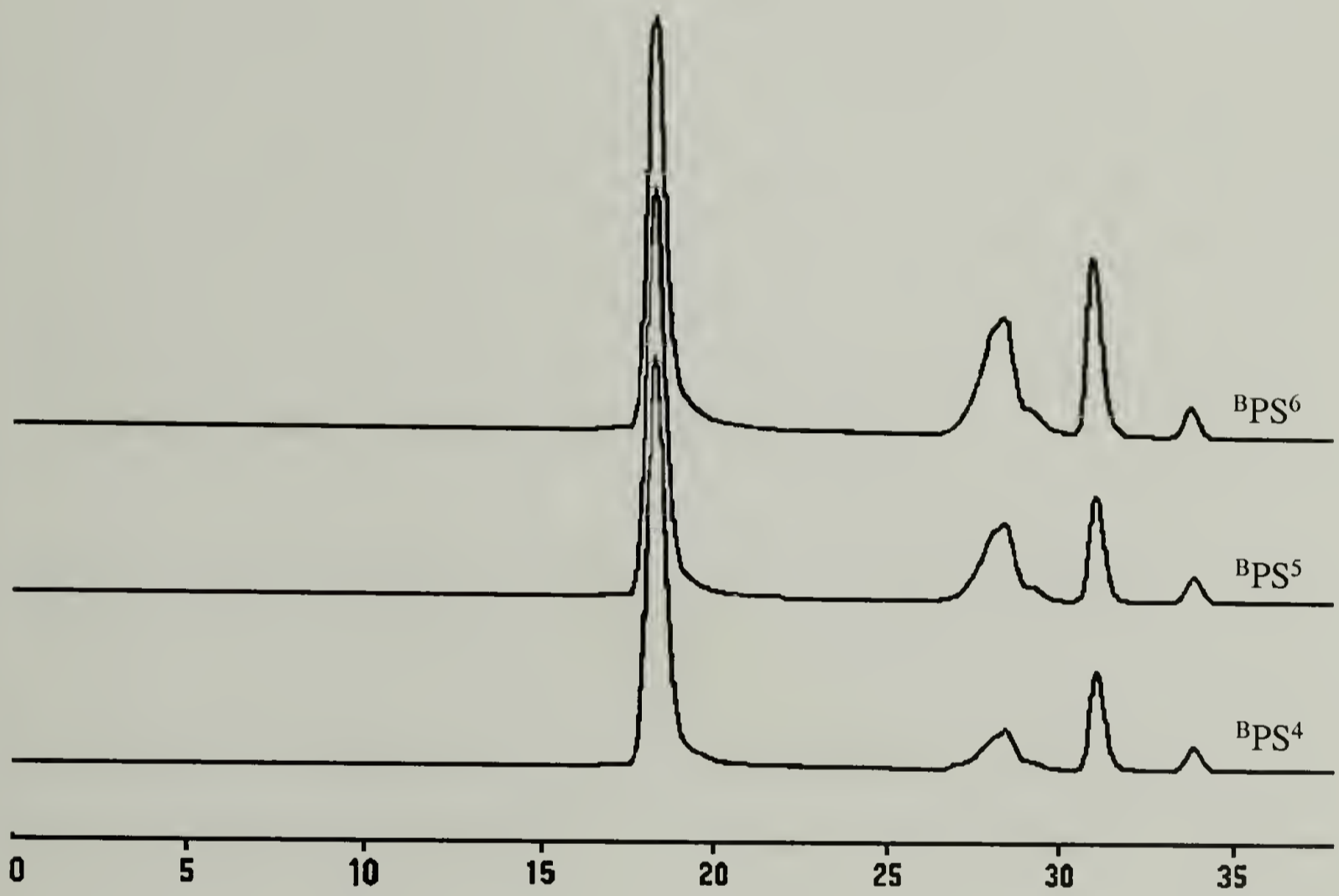
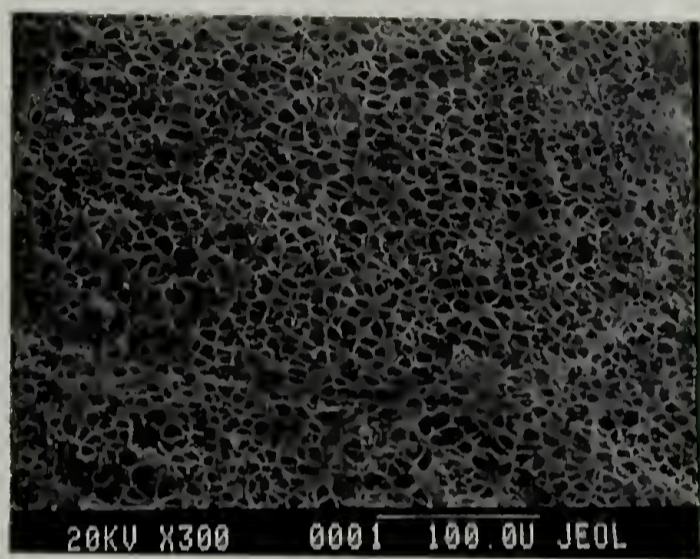
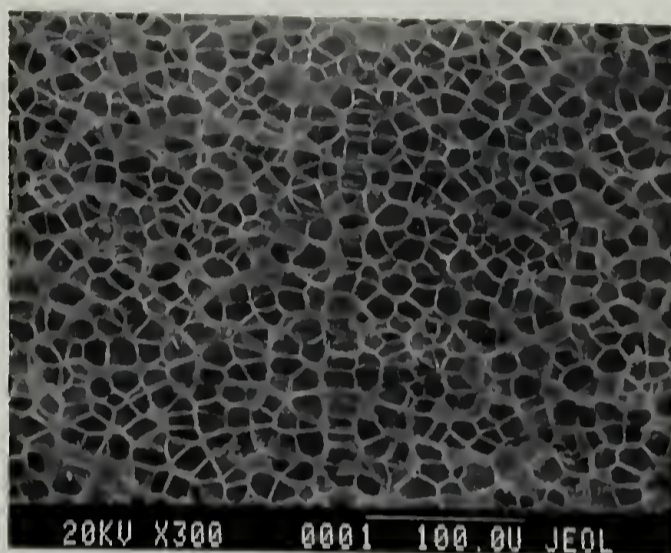


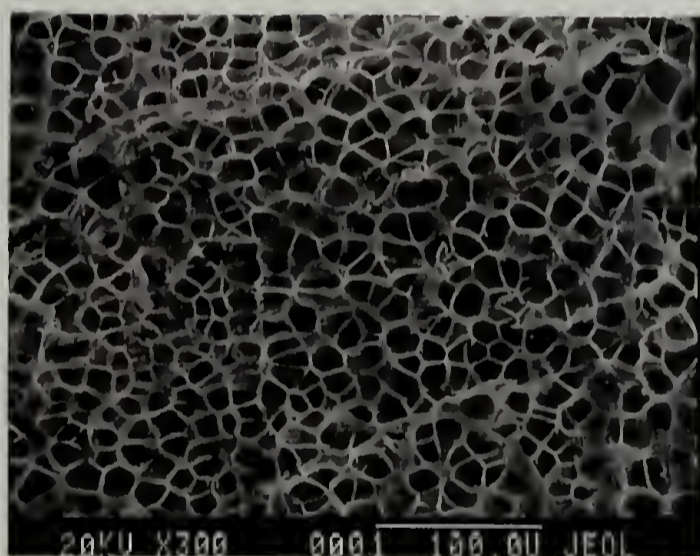
Figure 1.23. GPC chromatograms of blends prepared from PS^{147K} and a 285 g/mol styrene oligomer: BPS⁴ (3.6 wt% oligomer), BPS⁵ (7.3 wt% oligomer), and BPS⁶ (9.9 wt% oligomer).



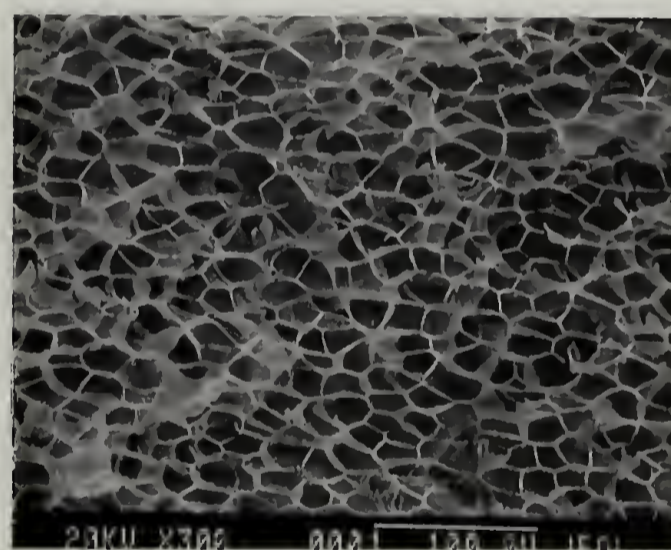
(a)



(b)



(c)



(d)

Figure 1.24. SEM micrographs of PS^{147K} with added oligomer: (a) PS^{147K} (0.0 wt% oligomer), (b) ^BPS⁴ (3.6 wt% oligomer), (c) ^BPS⁵ (7.3 wt% oligomer), and (d) PS⁶ (9.9 wt% oligomer). Foaming conditions were 100 °C and 3400 psi.

Table 1.2. Average cell size diameters and cell densities of foams produced by rapid expansion of SC CO₂.

sample ^a	avg. cell diameter (μm)	cell density (# cells/cm ³)
PS ^{25K}	2.2	4.11x10 ¹⁰
PS ^{147K}	5.3	4.28x10 ⁹
PS ^{514K}	5.9	2.16x10 ⁹
PS ^{1050K}	5.7	3.74x10 ⁹
PS ^R	4.7	2.36x10 ⁹
COM ^{PS} ¹	24	6.54x10 ⁷
COM ^{PS} ²	24	1.21x10 ⁷
COM ^{PS} ³	19	1.83x10 ⁸
^B PS ¹	5.2	
^B PS ²	5.8	
^B PS ³	7.9	
^B PS ⁴	11.9	9.79x10 ⁸
^B PS ⁵	13.9	5.18x10 ⁸
^B PS ⁶	18.4	3.27x10 ⁸
COM ^{PS} ^{1EX1}	8.9	1.12x10 ⁹
COM ^{PS} ^{1EX2}	7.2	1.97x10 ⁹
COM ^{PS} ^{1EX3}	5.9	3.24x10 ⁹

^asuperscripts with K indicate narrow molecular weight distribution samples, with COM indicate commercial broad molecular weight distribution samples, with a B indicate a blend and with EX indicate extracted samples.

The second question to be asked is what role does this oligomer play in the supercritical foaming of polystyrene? A few observations can be made which allow for certain arguments to be dismissed. From the image analysis data, we can calculate the number of pores nucleated per cm^3 of the foam by applying a method proposed by Kumar and Suh.²² The cell densities obtained for most of the samples discussed earlier are shown in Table 1.2. What is immediately obvious from these data is that the presence of this low molecular weight component (270 g/mol) has a dramatic influence on cell density. Nearly a two-order of magnitude decrease in the cell density is evident. Since the glass transition temperature of the polymers and the extent of swelling of the polymers with SC CO_2 is the same, i.e. the depressed glass transition temperatures of the swollen polymers are essentially the same, we cannot attribute this difference to the rate of cell growth. No evidence was found for cell coalescence. Consequently, the differences caused by the presence of the low molecular weight component must be attributed solely to a reduction in the number of nucleation sites.

Colton and Suh,^{21,25,26} using classical nucleation arguments, derived an expression for the rate of nucleation of pores in microcellular foams. Whether the nucleation occurs by a homogeneous or heterogeneous process, the nucleation rate N is given by

$$N_i = f_i C_o \exp(-\Delta G_i^* / kT) \quad (4)$$

where the subscript i denotes whether the nucleation is homogeneous or heterogeneous, f_i is a frequency factor of gas molecules merging with the nucleus, C_o is the concentration of gas molecules and ΔG_i^* is the Gibbs free energy associated with the formation of a nucleus. If the nucleation is homogeneous,

$$\Delta G^* = \frac{16\pi\gamma^3}{3(\Delta P)^2} \quad (5)$$

where γ is the surface energy at the cell-polymer interface and ΔP is the pressure exerted by the SC CO₂ on the cell walls. In the case of heterogeneous nucleation,

$$\Delta G^* = \frac{16\pi\gamma^3}{3(\Delta P)^2} f(\theta) \quad (6)$$

where the factor $f(\theta) = (1/4)(2 + \cos\theta)(1 - \cos\theta)^2$ and θ is the contact angle of the polymer/nucleation site/gas interface.

The dramatic changes in N observed in our studies cannot be explained by changes in either f_i or C_o . C_o is dictated by the swelling of the polymer by the SC CO₂, which is the same in all cases. While there may be changes in f_i due to the presence of the 270 g/mol component, a two-order of magnitude change in f_i would not be expected based on the concentration of the impurity. Therefore, the change in nucleation density must originate with changes in ΔG^* , provided the mode of nucleation, i.e. homogeneous versus heterogeneous, remains unchanged. If N_i and N_i' are the cell nucleation rates in the absence of and presence of the low molecular weight component and the decrease in the nucleation rate is two orders of magnitude, then (assuming f_i and C_o are constant),

$$\ln\left(\frac{N_i'}{N_i}\right) = \ln(0.01) = -\frac{\Delta G^{*'} - \Delta G^*}{kT} \quad (7)$$

With a pressure drop of 3400 psi ($\sim 2.34 \times 10^8$ erg/cm³), and using equations (2) or (3), the change in the surface tension of the cells by the addition of the 270 g/mol would be

$\gamma' - \gamma = 9.2$ erg/cm². This result, however, shows that the presence of the low molecular

weight component must increase the surface tension to bring about a reduction in the nucleation rate, a result that would contradict most results found in the literature.

Can the change in the nucleation rate be associated with a change in the mode of nucleation? Examination of all the cell structures produced in this study shows that the cell sizes are uniform, i.e. the distribution of cell sizes is narrow. A narrow cell size distribution requires that the nucleation sites be uniformly distributed in the system and that the nucleation of all the pores occurs within a narrow time regime. This is characteristic of a heterogeneous nucleation process with a uniform distribution of nucleation sites. Similar behavior is seen, for example, in the nucleation of polymer spherulites where, after crystallization, the spherulites have a characteristic size. Homogeneous nucleation, on the other hand, requires that nucleation occurs over a broad time period and would necessarily give rise to a broad distribution of cell sizes. No evidence was found in our studies to indicate that homogeneous nucleation occurred. Indeed, for most polymer systems, attaining conditions suitable for homogeneous nucleation is extremely difficult. Thus, contrary to the findings of Colton and Suh, where a dramatic reduction in the nucleation density was attributed to a change from homogeneous to heterogeneous nucleation, our data suggest that no such change has occurred.

Consequently, arguments based on nucleation and growth of cells fail to explain the observations described here. An alternative mechanism that needs to be considered is that of spinodal phase separation followed by a coarsening process. The system of SC CO₂-swollen polymer is quenched into a metastable regime by a rapid pressure drop. Upon quenching, concentration fluctuations with many different length scales are present.

With time, as a result of the balance between thermodynamics, which favors cell formation, and dynamics, which requires transport of the CO₂ molecules to the less dense regions, a characteristic wavelength begins to emerge. The amplitudes of the concentration fluctuations continue to grow until the saturation point, at which time, a cell forms and begins to coarsen. The presence of the low molecular weight component could, in fact, serve to suppress the shorter wavelength fluctuations and lead to a reduction in the number of effective nucleation sites. Such a mechanism would lead to a uniform distribution of cells and, consequently, to a narrow distribution of cell sizes. A key element in this alternative mechanism of cell formation is the growth of concentration fluctuations with a characteristic wavelength. Studies are currently in progress using time-resolved x-ray scattering from quenched systems to investigate this. If the spinodal mechanism is active, a maximum in the scattering profile will be evident prior to cell formation, whereas with nucleation and growth, only a monotonic decrease in the scattering will be observed.

1.4. Conclusions

The effects of both molecular weight and sample polydispersity on SC CO₂ expansion of polystyrene has been examined in some detail. The data suggest that molecular weight and polydispersity do not significantly affect the foaming process. The presence of a low molecular weight component (~270 g/mole), however, was found to greatly influence the final structure of the foam. The chemical nature of the oligomer has been determined to be styrenic, possessing no detectable functionality that would enhance

interactions with the supercritical fluid. The origin of this oligomer has been speculated to be the remnants of the thermal initiation of styrene polymerization used in commercial processes. This component does not have to present in large amounts ($< 4\%$) to cause a substantial increase in cell size, and by adjusting its concentration, control of cell size can be achieved. Addition of a low molecular weight oligomer to polymer samples offers a way to control cell structure in SC CO₂ foaming systems. Small amounts of a low molecular weight polystyrene component produce nearly a two-order of magnitude decrease in the nucleation density following the quenching of SC CO₂-swollen PS. This reduced nucleation density gives rise to a 3-10-fold increase in the average cell diameter. Classical nucleation theory fails to explain the observations, suggesting that an alternative mechanism of cell formation, perhaps a spinodal mechanism, is active. Another hypothesis that remains unproven is that the presence of the oligomer lowers the depressed T_g of polystyrene further, allowing for foaming to occur for a slightly longer period of time before vitrification of the polymer occurs.

1.5. References Cited

1. Clark, M.; Kendall, J., and DeSimone, J. *Macromolecules*, **1997**, *30*, 6011.
2. DeSimone, J.; Guan, Z., and Elsbernd, C. *Science*, **1992**, *257*, 945.
3. DeSimone, J.; Maury, E.; Menciloglu, Y.; McClain, J.; Romack, T., and Combes, J. *Science*, **1994**, *265*, 356.
4. Kung, E.; Lesser, A., and McCarthy, T. *Macromolecules*, **2000**, *33*, 8192.
5. Stassin, F.; Halleux, O., and Jérôme, R. *Macromolecules*, **2001**, *34*, 775.
6. Xia, J.; Johnson, T.; Gaynor, S.; Matyjaszewski, K., and DeSimone, J. *Macromolecules*, **1999**, *32*, 4802.
7. Kung, E.; Lesser, A., and McCarthy, T. *Macromolecules*, **1998**, *31*, 4160.
8. Hayes, H. and McCarthy, T. *Macromolecules*, **1998**, *31*, 4813.
9. Watkins, J. and McCarthy, T. *Macromolecules*, **1994**, *27*, 4845.
10. Bungert, B.; Sadowski, G., and Arlt, W. *Fluid Phase Equilib.*, **1997**, *139*, 349.
11. Kumar, S.; Suter, U., and Reid, R. *Fluid Phase Equilib.*, **1986**, *29*, 373.
12. Pradhan, D.; Chen, C., and Radosz, M. *Ind. Eng. Chem. Res.*, **1994**, *33*, 1984.
13. Goel, S. and Beckman, E. *Polym. Eng. Sci.*, **1994**, *34*, 1137.
14. Goel, S. and Beckman, E. *Polym. Eng. Sci.*, **1994**, *34*, 1148.
15. Arora, K.; Lesser, A., and McCarthy, T. *Macromolecules*, **1999**, *32*, 2562.
16. Arora, K.; Lesser, A., and McCarthy, T. *Macromolecules*, **1998**, *31*, 4614.
17. Shi, C.; Huang, A.; Kilic, S.; Xu, J.; Enick, R.; Beckman, E.; Carr, A.; Melendez, R., and Hamilton, A. *Science*, **1999**, *286*, 1540.
18. Wang, W.; Kramer, E., and Sachse, W. *J. Polym. Sci. Polym. Phys. Ed.*, **1982**, *20*, 1371.
19. Aubert, J. and Clough, R. *Polymer*, **1985**, *26*, 2047.

20. Young, A. J. *Cell. Plast.*, **1987**, 23, 55.
21. Colton, J. and Suh, N. *Polym. Eng. Sci.*, **1987**, 27, 500.
22. Kumar, V. and Suh, N. *Polym. Eng. Sci.*, **1990**, 30, 1323.
23. Goel, S. and Beckman, E. *AIChE J.*, **1995**, 41, 357.
24. Arora, K.; Lesser, A., and McCarthy, T. *Polym. Eng. Sci.*, **1998**, 38, 2055.
25. Colton, J. and Suh, N. *Polym. Eng. Sci.*, **1987**, 27, 485.
26. Colton, J. and Suh, N. *Polym. Eng. Sci.*, **1987**, 27, 493.

CHAPTER 2

POLYMER ADSORPTION TO SILANE-MODIFIED SURFACES

2.1. Introduction

There has been considerable theoretical¹⁻⁵ and experimental⁶⁻¹³ interest in the adsorption of functionalized polymers to solid/liquid interfaces, which makes use of one or multiple functional groups on the polymer to pin the polymer to an “attractive” wall. This concept has been utilized in such areas as colloid stabilization,^{14,15} enhanced wetting and adhesion,^{16,17} fabrication of chemical microsensors,¹⁸ and biocompatibility.^{19,20} Recently, significant attention has been given to the adsorption of A-B type block copolymers where one block interacts preferentially with the surface, which serves to anchor the polymer to the solid/liquid interface. End-functionalized polymers such as PS-COOH represent the simplest A-B type block copolymer, having a single anchoring point (i.e. carboxylic acid) that exhibits a preferential interaction with a silica surface. The trends in the adsorption of such end-functionalized polymers should provide basic insight into how more complex macromolecules may adsorb under similar experimental conditions.

Polymer adsorption is a thermodynamic process that requires the global free energy of the system to be negative. Unlike small molecule adsorption, polymer adsorption results in the loss of conformational entropy due to pinning the polymer to a solid surface. This loss in entropy must be compensated by gains in enthalpic interactions of the polymer with the surface. Those interactions can be defined as

follows: polymer segment-solvent (Flory-Huggins χ parameter), solvent-surface, and polymer segment-surface, the difference in the latter two being the exchange free energy associated with replacing a solvent molecule with a polymer segment. Thus, by changing the chemistry of the polymer (monomer repeat, block copolymers, etc.) or by changing the adsorbing solvent (χ), one can dramatically modify the adsorption behavior of a polymer to a given surface. As an example, the effect of solvent quality is shown schematically in Figure 2.1. In a good solvent, the polymer chains adopt a highly expanded conformation, which excludes neighboring chains from packing closely to one another. In a theta solvent, the polymer chains are in a condensed globular conformation, having a smaller excluded volume that allows for a higher packing density.

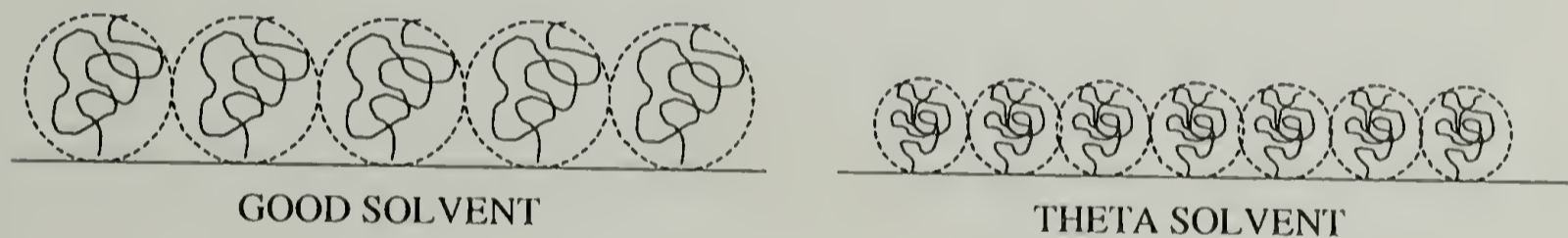


Figure 2.1. End-grafted polymer adsorption as a function of solvent quality.

Simple homopolymer adsorption results in the formation of loops and trains, the numbers of which are dictated by the total number and distribution of adsorbing sites along the polymer backbone. In end-grafted polymer adsorption, the situation becomes less complicated as there is only one monomer unit at the end of the polymer that can interact with the surface (increased surface affinity). The remaining monomer units are assumed to have a non-favorable or repulsive interaction with the surface. Theoretical arguments predict that the adsorbed thickness (L) is dependent on the number of repeats

(N) in the polymer, the grafting density (σ) and monomer length (a), and can be summarized by the following scaling relationship:

$$L \sim N \sigma a^{1/3} \quad (1)$$

The non-adsorbing block extends away from the surface and into the solution. Steric requirements dictate that the polymer chains stretch perpendicular to the surface, forming what is referred to as a polymer brush. In this highly stretched state, the polymer chain adopts a conformation that deviates greatly from the equilibrium chain dimensions in solution.

When studying the adsorption of copolymers, there exists two possible adsorption regimes termed buoy-dominated and anchor-dominated adsorption (see Figure 2.2).²¹ Buoy-dominated adsorption occurs when the adsorbing block (footprint) is small in comparison to the non-adsorbing block (solvated), and the osmotic forces among the buoy blocks dictate the grafting density. Anchor-dominated adsorption occurs when the adsorbing block (footprint) is large with respect to the buoy block, and grafting density is limited by the packing efficiency of anchor block on the surface. In end-grafted polymer adsorption, the grafting density is directly proportional to the number of end-groups adsorbed to the substrate, with the remaining portion of the chains extended away from the surface. This can be viewed as a variation of buoy-dominated adsorption behavior. When the grafting density exceeds a critical value, repulsive interactions between chains cause the adsorbed layers to stretch away from the substrate forming a polymer brush.

Considerable attention has been given to the adsorption of polymers to a variety of surfaces, including mica, silica, metal oxides, and liquid-air interfaces. A large volume of literature focuses on the adsorption of end-functionalized polymers due to the

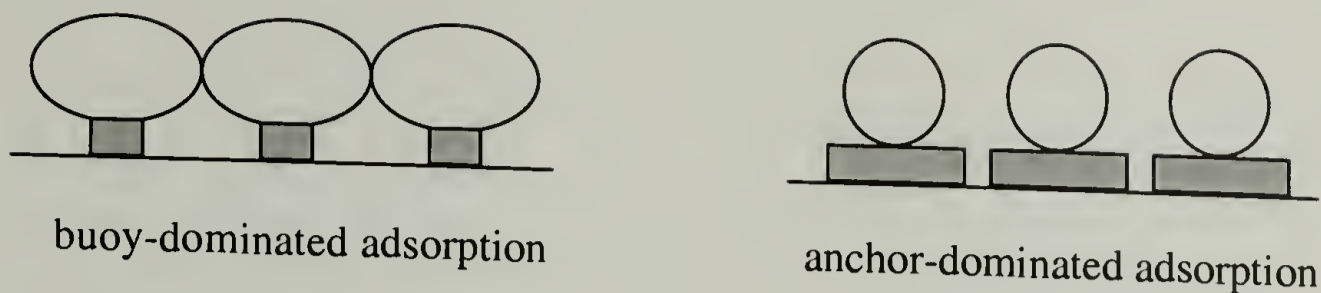


Figure 2.2. Illustration of the two regimes for copolymer adsorption: buoy-dominated and anchor-dominated copolymer adsorption.

simplicity of the system. Experimental and theoretical work has even been carried out to elucidate the effect of surface roughness on the adsorption of end-functionalized polymers.²² There lacks, however, a literature base concerned with the adsorption of end-functionalized polymers to chemically heterogeneous surfaces. Chemically modifying silica surfaces provides a rich and robust route to study the trends in the adsorption of these types of polymers to chemically heterogeneous surfaces.

Reaction of silicon surfaces with alkyltrichlorosilanes provides a simple and effective way to vary the surface properties from hydrophobic to hydrophilic.^{23,24} These surfaces are termed self-assembled monolayers and consist of close-packed alkyl chains where the primary interaction between neighboring chains is van der Waals interactions. One drawback to this process is that it is very dependent on the surface preparation and reaction conditions. Depending on the extent of hydration of the surface silanol groups, the reaction of trichlorosilanes can lead to the formation of oligomeric species that are sparsely attached to the surface via covalent bonds. In contrast, monochlorosilanes can also be used to modify the surface properties and wettability of a substrate, but the nature of the chemistry requires that every silane group be covalently attached to the surface. Dimeric species can be formed in solution but those species are no longer reactive and thus cannot participate in surface reactions. Typical monochlorosilanes include alkyl,

fluoroalkyl, aryl, and haloalkyl. Mixed monolayers can be prepared by using a combination of two organosilanes, but since this process relies on competitive adsorption the extent of mixing is rarely known and hardly reproducible. Depending on the kinetics of each individual silane reacting with the surface, the reaction may lead to a uniformly mixed monolayer ($k_1=k_2$) or a surface enrichment of one silane ($k_1 \gg k_2$).

An alternative approach has been proposed which utilizes a two-step technique involving the formation of a submonolayer of a single chlorosilane, then subsequent reaction of that surface with a second chlorosilane. This approach has proven to be very successful, albeit more time consuming, in the creation of a wide range of binary mixed monolayers.^{25,26} The major drawback to this technique is that the distribution, or level of mixing, of the two components is dictated solely by the distribution of the first component during reaction. If component 1 reacts in a patchy fashion (i.e. island formation), the mixed monolayer will be patchy; if it reacts randomly, the mixed monolayer will be randomly mixed. Recently, Fadeev et al.²⁷ described the preparation and properties of tris(trimethylsiloxy)silyl monolayers (Tris(TMS)) and their use as patterns for the synthesis of uniformly mixed binary monolayers of organosilanes on oxidized silicon wafers. The chemical structure of Tris(TMS) is shown in Figure 2.3. Due to the bulky nature of this molecule, the packing efficiency of Tris(TMS) on a surface is very poor. Contact angle studies using probe fluids of increasing molecular size showed that even closely packed monolayers of Tris(TMS) have interstitial holes (nanopores) that can be used to modify the surface further. The results of this experiment are shown in Figure 2.4. If the molecular size of the probe fluid is smaller than the average separation distance between Tris(TMS) molecules, the probe fluid can penetrate

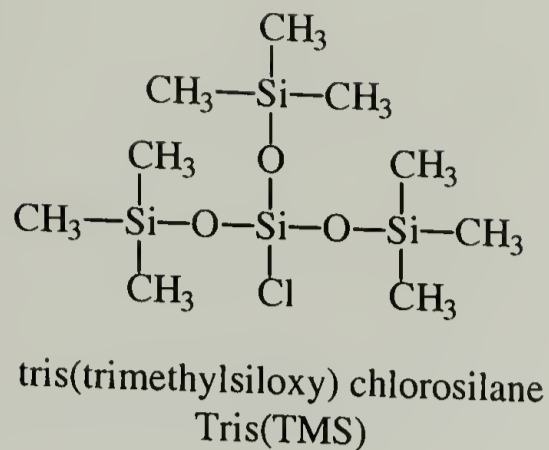


Figure 2.3. Chemical structure of tris(trimethylsiloxy)chlorosilane, Tris(TMS)-Cl.

through the Tris(TMS) layer and interact with the underlying surface (Si-OH). Thus, the probe fluid senses a heterogeneous surface, which causes the measured hysteresis to be large ($\sim 10^\circ$). If the molecular size of the probe fluid is larger than the average separation distance between Tris(TMS) molecules, the probe fluid is excluded from penetrating the monolayer and only 'senses' a homogeneous layer comprised of Tris(TMS) molecules. In this case, the observed hysteresis will be low ($\sim 2^\circ$). The transition from penetrating to non-penetrating probe fluids is an indication of the average pore size of the Tris(TMS) monolayer. In the case of a fully covered Tris(TMS) surface, the size of the pores was shown to be between 0.49 and 0.54 nm².

Adsorption of polymers to such surfaces should be rich and enlightening. The surface is no longer a continuum of surface silanols (attractive) but now contains varying amounts of Tris(TMS) groups (repulsive). Also, the polymer chain must adopt a conformation that allows for the carboxylic acid group to interact and adsorb to the surface. Increasing the molecular weight of the polymer chain incurs two disadvantages: the concentration of end-groups decreases, while the probability that the chain end is buried deep within the polymer coil increases. The polymer chain must also adsorb

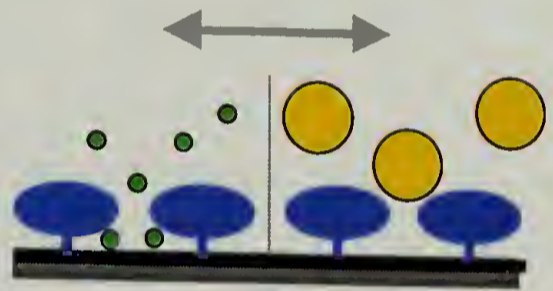
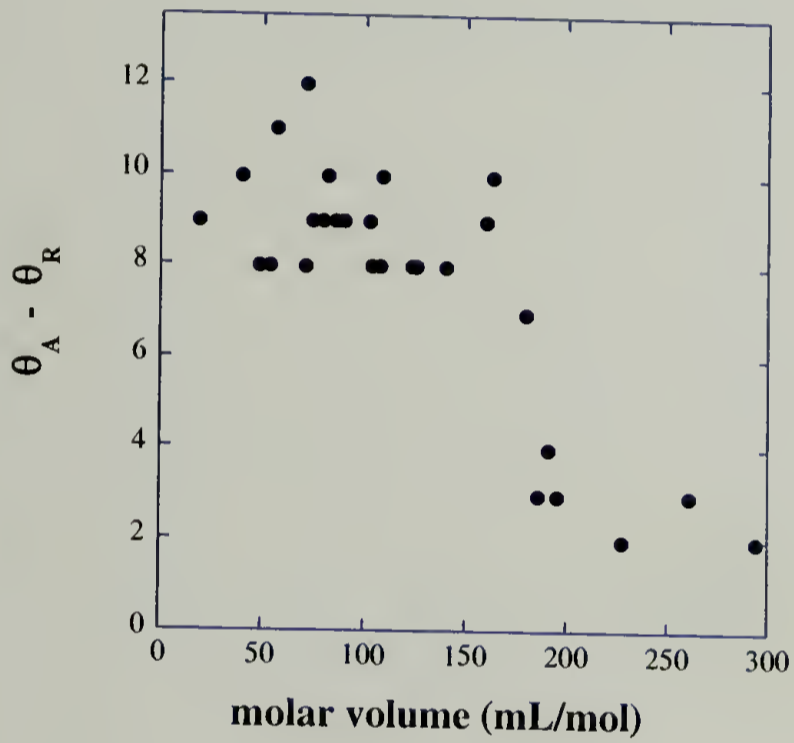


Figure 2.4. Contact angle hysteresis as a function of molar volume of the probe fluid for Tris(TMS) surfaces prepared in the vapor phase for 3 days. The observed transition in hysteresis allows for determination of an average pore size.²⁷

between Tris(TMS) groups, which for a completely reacted Tris(TMS) surface is $\sim 0.5 \text{ nm}^2$. Thus, there are several factors that will dictate the extent of adsorption to these modified surfaces: polymer molecular weight, solvent quality, Tris(TMS) coverage, and the strength of interaction between the surface and the polymer end group. These parameters will be explored in some detail in this chapter.

Several studies have utilized end-grafted polymer brushes to aid in preventing the dewetting of polymer thin films. These approaches typically involve spin casting a mixture of the functionalized and non-functionalized polymers onto a substrate, followed by annealing the film to allow for diffusion of the functionalized polymer to the polymer/substrate interface.²⁸⁻³¹ The resulting monolayer modifies interfacial interactions and promotes entanglements, thereby suppressing dewetting. For example, Kajiyama et. al.³² prepared films containing proton-terminated, monocarboxyl-terminated, and dicarboxy-terminated polystyrenes and observed their dewetting behavior on clean silicon as well as on amino-functionalized silicon. These experiments utilized adsorption of PS-COOH and HOOC-PS-COOH from a bulk film upon heating the samples above the bulk glass transition temperature. The authors observed retarded dewetting of both carboxy-terminated samples, with respect to the proton-terminated PS, when the films were prepared on clean silicon. They also observed no dewetting of either carboxy-terminated film when prepared on the amino-silanized surfaces. If, on the other hand, the polymer brush is formed prior to spin coating the non-functionalized film^{33,34} (in contrast to forming the brush *in situ* as described above), a phenomenon termed autophobic dewetting occurs where a densely packed polymer brush monolayer is formed. It then becomes entropically unfavorable for the non-grafted film to diffuse into

the brush layer. These films were shown to be highly unstable and dewetting occurred rapidly. The studies here will utilize the templating ability of Tris(TMS) monolayers to direct and control the grafting (brush) density of PS-COOH chains to the surface, such that a densely packed brush layer is not formed. Also, the underlying surface will be comprised of a non-interacting layer of Tris(TMS) molecules, in contrast to the typical silicon oxide layer found in other experiments. The adsorbed chains of PS-COOH will help anchor the overlying film to this non-interacting Tris(TMS) layer, and could suppress the dewetting process of an overlying film.

Another targeted application for these templated surfaces is in the formation of single, isolated chains on the surface, which can then be used to measure the mechanical properties of a single polymer chain. The widespread emergence of atomic force microscopy (AFM) in the research environment has allowed for pioneering work to be done on single-chain elasticity studies. Maaloum et al.³⁵ used chemisorption of telechelic PEO to a hydrophobized AFM tip to 'pick up' a polymer chain and measure the elastic restoring force exerted by the adsorbed chain. Yamamoto et al.³⁶ prepared surface-grafted PMMA by surface-initiated ATRP and end-capped the PMMA with a short block of PVP, where the PVP segment could adhere to the hydrophilic AFM tip. Ortiz et al.³⁷ prepared isolated poly(methacrylic acid) (PMAA) chains by mixed monolayer adsorption of alkanethiols and thiol-functionalized PMAA on gold, and again relied on physisorption of the polymer to the hydrophilic AFM tip. The surfaces to be prepared in this work have significant advantages over the aforementioned studies. Although the reaction of Tris(TMS) is a random, ballistic process, the surfaces have been shown to have a very well defined pore size. Surfaces having high Tris(TMS) coverage should dictate the

lateral distance between adsorbed chains more controllably than relying on random processes such as competitive adsorption of alkanethiols or physisorption on hydrophobized surfaces. The research discussed in this chapter will not address this area of study, but there is no reason the chemistry could not be modified to tackle these questions.

2.2. Experimental

2.2.1. Materials

All chemicals were used as received unless noted otherwise. Toluene (HPLC), cyclohexane (HPLC), toluene (anhydrous), ethanol (anhydrous), sulfuric acid, sodium dichromate, and hydrogen peroxide (30%) were purchased from Fisher. All silane reagents were purchased from Gelest with the exception of 4-(aminobutyl)dimethylmethoxysilane, which was purchased from United Chemical. Ethyldiisopropylamine and hexadecane (anhydrous) were purchased from Aldrich. Carboxylic acid end-functionalized polystyrenes were synthesized as described in Appendix A. House-purified water (reverse osmosis) was used in substrate preparation and cleaning.

2.2.2. Pretreatment of Silicon Substrates

Silicon wafers (4") were obtained from International Wafer Service (100 orientation, P/B doped, resistivity of 20-40 Ω /cm) and were cut into 1.5 x 1.5 cm pieces to facilitate handling and XPS measurements. The samples were placed in a custom-designed holder and placed into a modified Schlenk tube (Figure 2.5). The samples were then submerged in a freshly prepared solution of $\text{H}_2\text{SO}_4/\text{Na}_2\text{Cr}_2\text{O}_7/\text{H}_2\text{O}_2$. The sodium dichromate (~5 wt %) was first dissolved in stirring concentrated sulfuric acid (30 mL). Hydrogen peroxide (15 mL) was then poured directly into the Schenk tube containing the wafers to be cleaned, and the $\text{H}_2\text{SO}_4/\text{Na}_2\text{Cr}_2\text{O}_7$ solution was poured directly on top of the peroxide/wafers. The solution turns from red-brown to green upon mixing, warms up considerably, and bubbles profusely due to the formation of ozone and oxygen. The

samples were left submerged overnight for convenience. The wafers were rinsed with copious amounts of water to remove all traces of the cleaning solution, and were dried in a clean oven at 130 °C for 1½ hours.

2.2.3. Preparation of Substrates via Solution Reaction

Silicon wafers were cleaned and dried as described above. The wafers were immediately placed into the reaction flasks and purged with N₂ for 30 minutes. Dry toluene (~20 mL) was then cannulated into the reaction tube and ethyldiisopropylamine (0.3 mL) was added via syringe as a promoter, followed by the organosilane (0.5 mL) of choice. The reaction tube was placed in an oil bath and heated to 68 ± 1 °C for 3 days, unless otherwise noted. After silanization, the wafers were rinsed in the following order: 2 x 10 mL toluene, 3 x 10 mL ethanol, 2 x 10 mL ethanol/water mixture (1:1), 2 x 10 mL water, 2 x 10 mL ethanol, 2 x 10 mL water and then dried in a clean oven at 130 °C for 10-15 min. The samples were then placed into scintillation vials for storage until characterization or further use. Reactions involving aminosilanes were carried out as described above with the exception that no amine promoter was added to the reaction (self-promoted).

2.2.4. Preparation of Substrates via Vapor Phase Reaction

Silicon wafers were cleaned and dried as described above. The wafers were immediately placed in a reaction tube containing the organosilane of choice. Samples were placed in a custom-made wafer holder and suspended in a reaction tube containing 0.5 mL of silane (see Figure 2.5). There was no direct contact between the silane and the

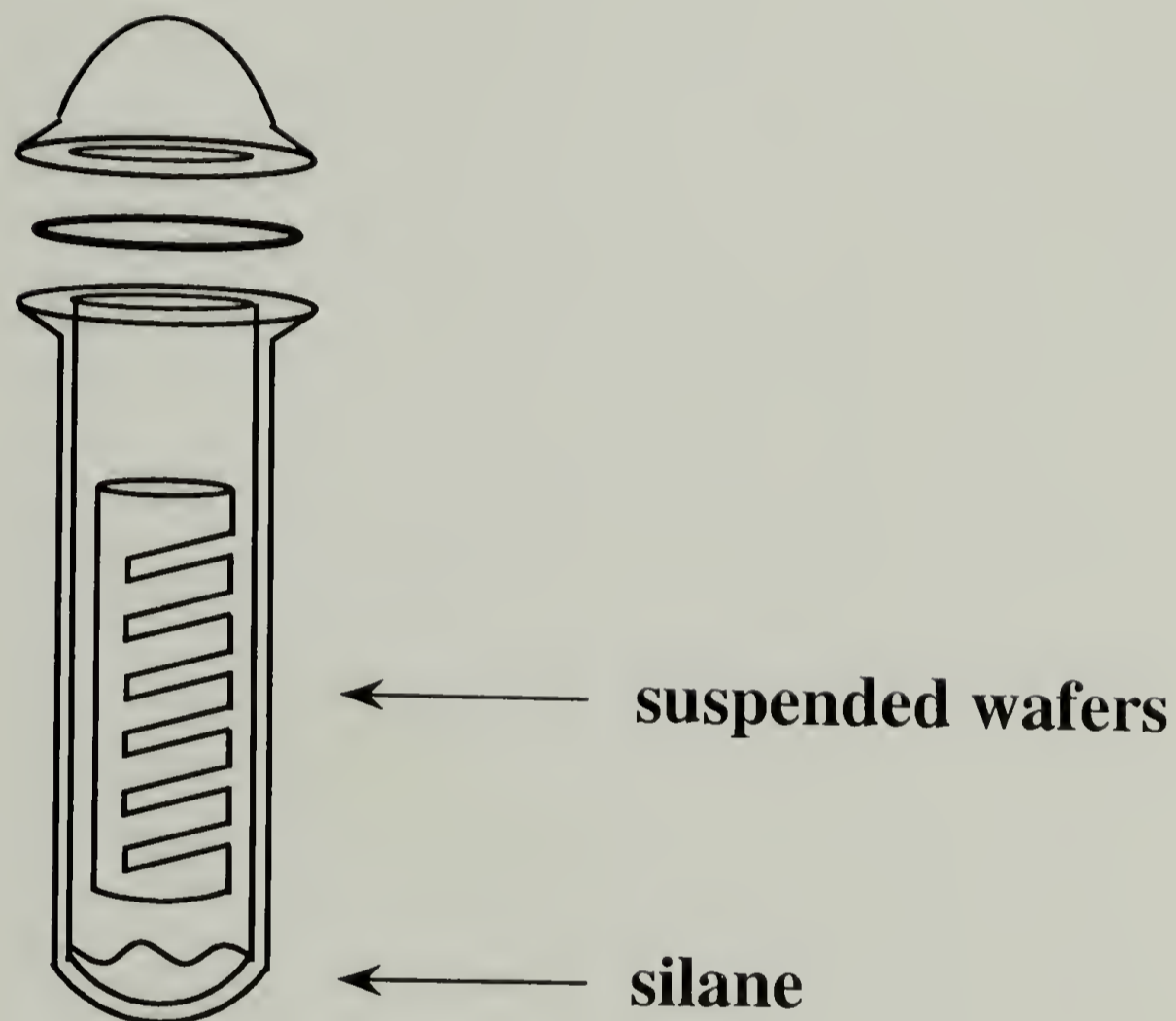


Figure 2.5. Schematic of the Schlenk tube used for vapor-phase reaction of monochlorosilanes. Similar reaction flasks were used for solution reactions with the exception that the top included a 4mm Teflon joint capped with a rubber septum to facilitate cannulation and additions via syringe under an inert atmosphere.

silicon substrates. The reaction tube was placed in an oil bath and heated to 68 ± 1 °C for 3 days, unless otherwise noted. After silanization, the wafers were rinsed in the following order: 2 x 10 mL toluene, 3 x 10 mL ethanol, 2 x 10 mL ethanol/water mixture (1:1), 2 x 10 mL water, 2 x 10 mL ethanol, 2 x 10 mL water and then dried in a clean oven at 130 °C for 10-15 min.

2.2.5. Adsorption of PS-COOH to Silane-modified Surfaces

Solutions for adsorption were prepared by dissolving PS-COOH in toluene at a concentration of 1 mg/mL. The solutions were filtered using a 0.45 μm Acrodisc filter just prior to adsorption. The surfaces prepared by vapor phase reaction of Tris(TMS) and/or ABDMS were placed in scintillation vials containing 5 mL of the PS-COOH solution. Adsorptions were carried out at 23 ± 1 °C for 24 h. The solutions were then decanted from the vials and the wafers were rinsed with 2 x 5 mL of toluene for 2 min. This removes any PS that is not chemisorbed to the surface. The samples were dried under vacuum for 1 day and characterized by ellipsometry, contact angle, AFM, and XPS. Adsorptions from cyclohexane (theta-solvent) were carried out as described above with the exception that the temperature was kept at 35 ± 0.1 °C. This ensures that the polymer is indeed adsorbing and not precipitating onto the surface.

2.2.6. Dewetting Studies

Several samples from each adsorption study were kept for studying the dewetting of thin polymer films from these surfaces. Dewetting studies were performed on Tris(TMS) surfaces before and after adsorption of 11K PS-COOH from toluene and from

cyclohexane. Initially, the overlying polymer film was comprised of polystyrene, but the study was expanded to include several other polymers. A 0.75% solution of each polymer was prepared in toluene and spin-coated onto the samples at 4000 rpm. This resulted in a $230 \pm 10 \text{ \AA}$ film as determined by ellipsometry. The films were then annealed at $160 \text{ }^\circ\text{C}$ for 24 h, and then quenched rapidly to room temperature to freeze in the dewetted structure. Quenching was accomplished by placing the samples onto an aluminum block at room temperature immediately upon removal from the oven. The dewetted structures were examined by both optical microscopy and AFM.

2.2.7. Characterization

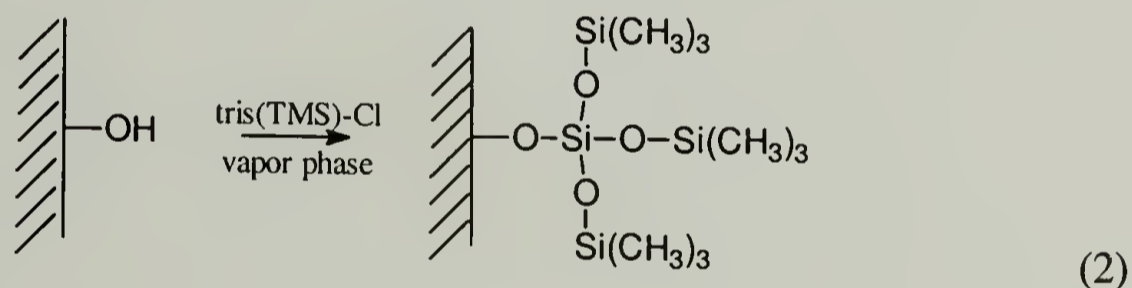
Contact angle measurements were made with a Ramé-Hart telescopic goniometer equipped with a Gilmont syringe and a 24-gauge flat-tipped needle. Probe fluids used were water and *n*-hexadecane. Advancing (θ_A) and receding (θ_R) contact angles were recorded while the probe fluid was added to and withdrawn from the drop, respectively. pH dependent contact angles were measured using buffer solutions prepared as described elsewhere. X-ray photoelectron spectra (XPS) were obtained on a Perkin-Elmer Physical Electrons 5100 with Mg K_α excitation (400W). Spectra were taken at two take-off angles, 15° and 75° (between the plane of the surface and the entrance lens of the detector optics). The attenuation of the Si^0 peak was used to determine layer thickness. Film thickness was also measured using a Rudolph Research ellipsometer equipped with a helium-neon laser ($\lambda = 6328 \text{ \AA}$) at an incidence angle of 70° . AFM images were obtained using a Digital Instruments DimensionTM 3100 Scanning Probe Microscope operated in

tapping mode. Optical micrographs were obtained on an Olympus BX-60 microscope operated in reflectance mode.

2.3. Results and Discussion

2.3.1. Preparation of Tris(trimethylsiloxy)silyl (Tris(TMS)) Surfaces

Chemically grafted (sub)monolayers of Tris(TMS) were prepared by reaction of the corresponding chlorosilane in both the vapor phase and the solution phase. Reaction occurs between silanol groups on the surface and the chlorosilane, liberating HCl gas as the by-product (see equation 2).



Molecular modeling of the Tris(TMS) molecule shows that it has a height of 0.7 nm and a diameter of 1.5 nm. The height of the Tris(TMS) molecule was experimentally verified to be 7 Å by conducting ellipsometry on a fully covered Tris(TMS) surface (CA – 108/96). The refractive index used was that of the corresponding hydridosilane ($n = 1.385$) since the refractive index of Tris(TMS)-Cl was not available. The cross-sectional area, or molecular footprint, of the Tris(TMS) molecule would be $\sim 177 \text{ \AA}^2$, which is considerably larger than simple alkyldimethylsilyl groups ($\sim 32\text{-}38 \text{ \AA}^2$) as well as alkyltrichlorosilane SAMs ($\sim 20 \text{ \AA}^2$). It has also been shown that the surface density of

silanols on the native oxide of silicon is approximately 5 silanols/nm².^{38,39} Therefore it can be estimated that for every Tris(TMS) molecule that reacts with the surface, there remains at least four unreacted silanols that are now blocked from reaction with subsequent Tris(TMS) molecules due to steric constraints. Since the attachment of monochlorosilanes to the surface occurs by a random process, the actual number of unreacted silanol groups on the surface after reaction with Tris(TMS) will be greater than estimated above due to the poor packing efficiency of Tris(TMS) molecules. This concept is illustrated in Figure 2.6.

Due to the high degree of steric hindrance of the reactive site, the kinetics of the Tris(TMS) reaction was expected to be very sluggish. To follow this in more detail, the kinetics of both the vapor phase and solution phase reactions were explored in some detail. The extent of reaction can easily be monitored by measuring the water contact angle of the surface as a function of reaction time. The upper limit for contact angle is assumed to be the angle for a completely covered TMS surface (108°), since it presents a high density of methyl groups to the probe fluid yet lacks the perfection of a C₁₈ SAM (114°). The results of the kinetic experiments conducted in both the vapor phase and in the solution phase are shown in Figures 2.7 and 2.8, respectively. It is clear that the solution reaction occurs much more slowly than the corresponding vapor phase reaction, but it is unclear whether the vapor phase reaction results in a more densely packed monolayer than the solution reaction. The kinetics of the solution phase reaction may simply lag behind the vapor phase reaction.

With this in mind, the vapor phase reaction allows for a variety of surface coverages to be prepared in the shortest amount of time (0-5 days), and so will be the

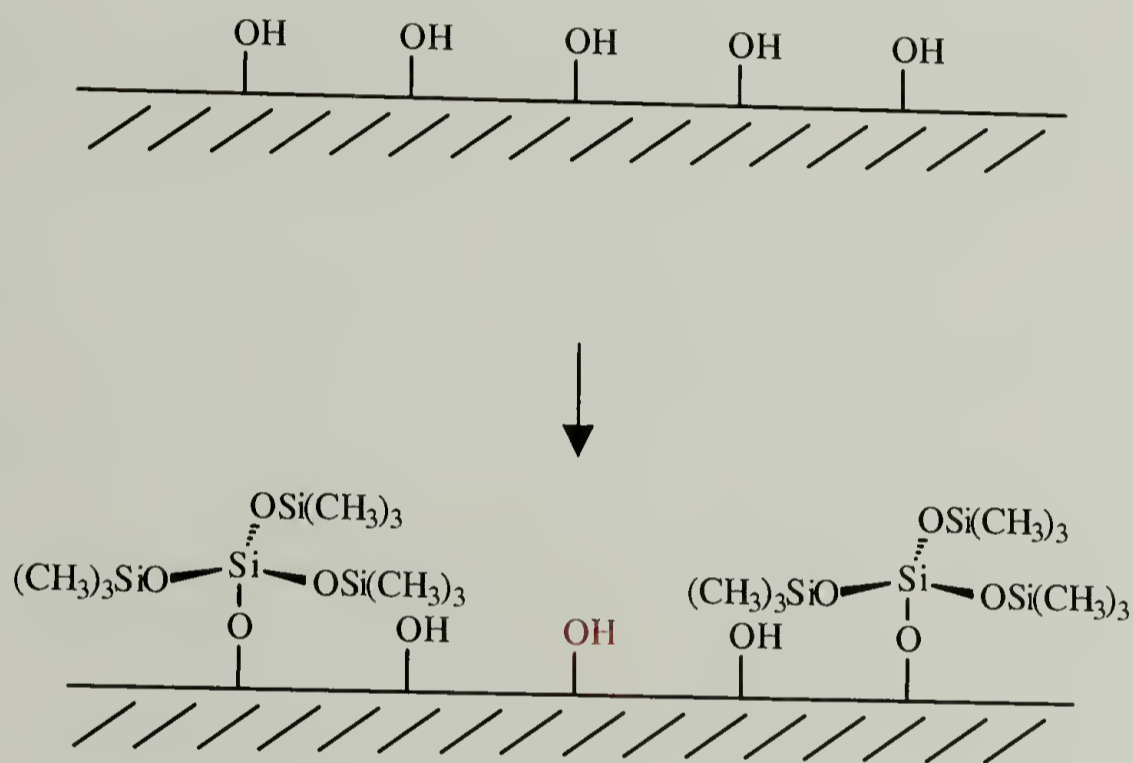


Figure 2.6. Schematic illustrating the reaction of Tris(TMS)-Cl with surface silanol groups, leaving unreacted silanol groups which can be used for subsequent modification of the surface.

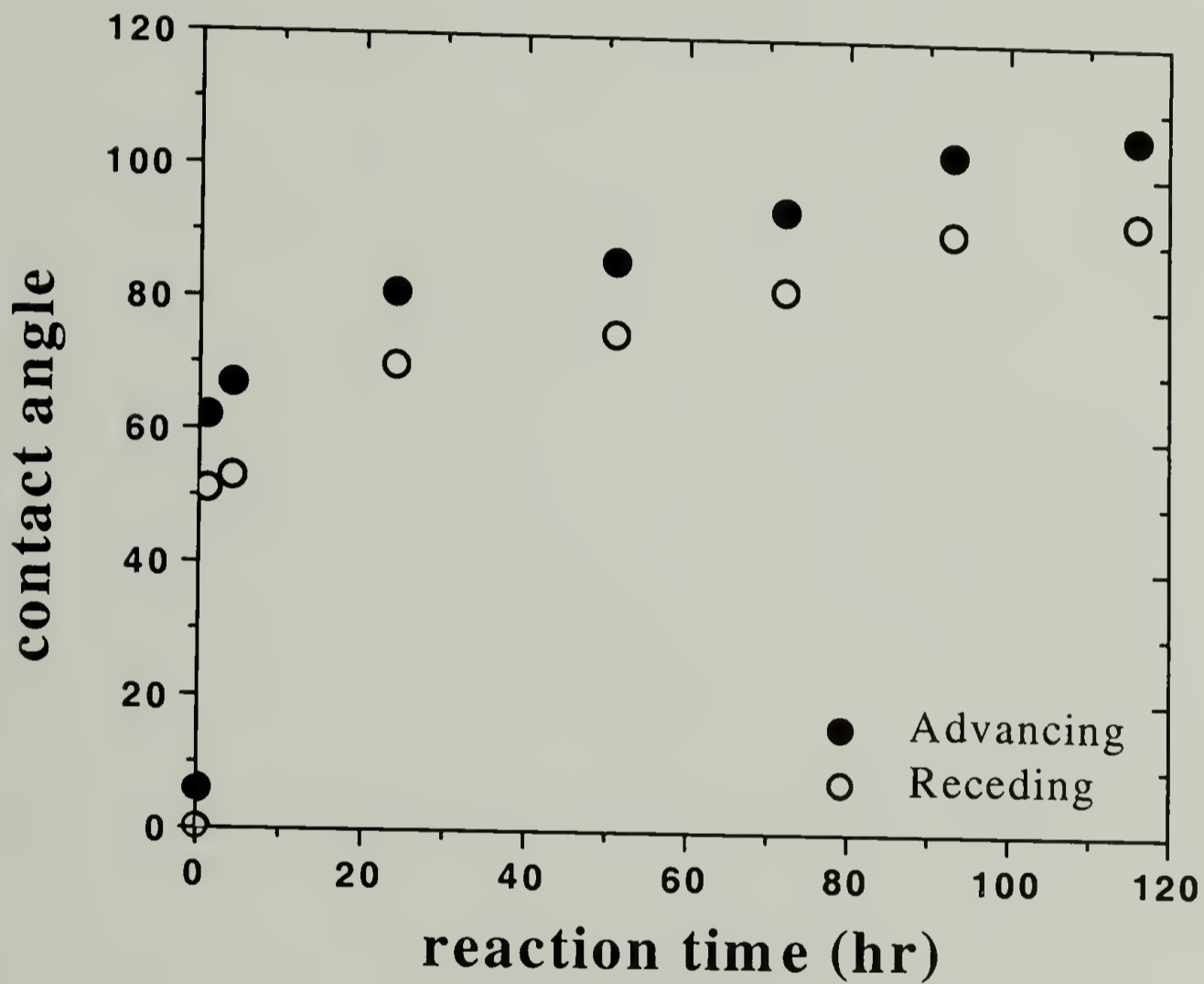


Figure 2.7. Kinetics of the Tris(TMS)-Cl vapor phase reaction as monitored by advancing (●) and receding (○) water contact angles. It is assumed that an advancing CA of 108° is complete coverage.

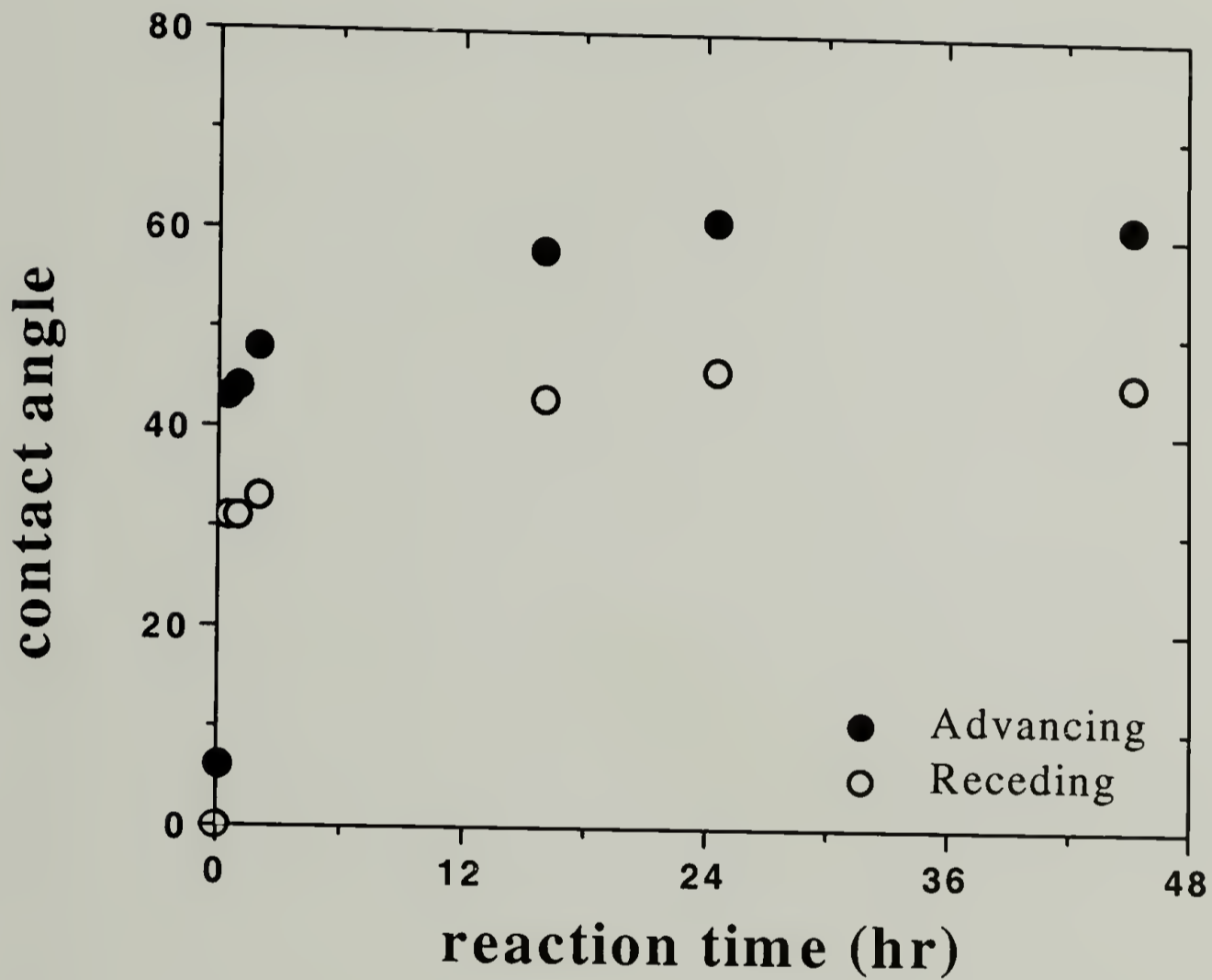


Figure 2.8. Kinetics of the Tris(TMS)-Cl solution phase reaction as monitored by advancing (●) and receding (○) water contact angles. It is assumed that an advancing CA of 108° is complete coverage.

Table 2.1. Contact angle data for Tris(TMS) surfaces prepared by vapor phase reaction for increasing amounts of time.

sample	θ_A/θ_R (°)		coverage ^a
	water	hexadecane	
clean Si	spreads	spreads	0%
Tris(TMS) 1h	62/51	24/9	52%
Tris(TMS) 4h	67/53	24/11	58%
Tris(TMS) 24h	81/70	31/20	76%
Tris(TMS) 51h	86/75	30/20	81%
Tris(TMS) 72h	94/82	34/22	89%
Tris(TMS) 93h	103/90	36/33	96%

^a as calculated from the Israelachvili-Gee equation (3).

reaction of choice for all subsequent experiments. As seen in Figure 2.7, the vapor phase reaction results in a rapid increase in contact angle to $\sim 60^\circ$, followed by a slow but steady increase up to angle of $\sim 106^\circ$. This is due to the bulkiness of the Tris(TMS) molecule and its inability to pack efficiently on the surface. Initially the surface is barren and contains an abundance of available reactive sites, allowing for a high number of reaction events to take place on the surface. As the surface becomes partially covered with Tris(TMS) molecules, it becomes increasingly more difficult for subsequent molecules to find reactive sites as well as have the right orientation for successful reaction with the surface. Thus the reaction kinetics slow down dramatically as the density of Tris(TMS) groups on the surface increases. The contact angle reaches a final plateau of $\sim 106^\circ$ which is in good agreement with the upper limit of 108° established earlier. This slow but steady increase in water contact angle allows for the preparation of a series of surfaces having a range of surface coverages of Tris(TMS) simply by controlling the time of the vapor phase reaction of Tris(TMS)-Cl. Figure 2.9 shows a 2-D representation of the range of surfaces that can be prepared by vapor phase reaction of Tris(TMS)-Cl for varying amounts of time. The discs on the surface represent single Tris(TMS) molecules.

The contact angle data can be analyzed in a manner proposed by Israelachvili and Gee⁴⁰ for molecularly mixed heterogeneous surfaces. The observed contact angle, θ_{obs} , can be described in terms of the mole fractions of each component, f_1 and f_2 , as well as the contact angles for the pure surface of each component, θ_1 and θ_2 , by the following equations:

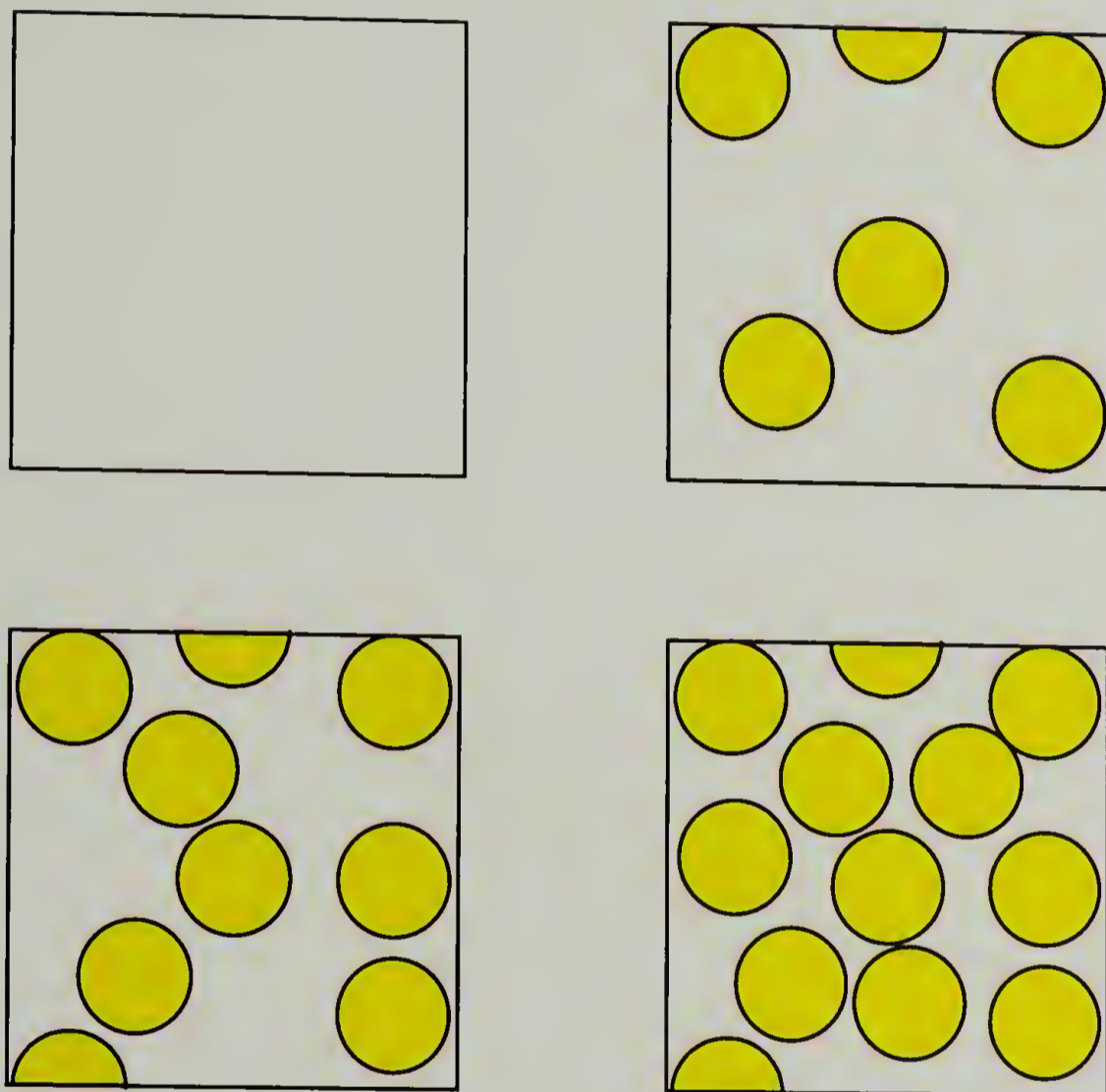


Figure 2.9. Schematic illustrating the 2-D above-view of Tris(TMS) surfaces of increasing surface coverage.

$$(1 + \cos(\theta_{obs}))^2 = f_1(1 + \cos(\theta_1))^2 + f_2(1 + \cos(\theta_2))^2 \quad (3)$$

$$f_1 + f_2 = 1$$

In this study the surface was treated as a mixture of trimethylsilyl groups (TMS) ($\theta_1 = 108^\circ$)⁴¹ and silanols ($\theta_2 = 0^\circ$). It should be noted that the advancing contact angle was used for θ_{obs} in all of these studies (see Table 1). Using this method, the percentage of Tris(TMS) covering the surface was calculated by measuring the contact angle. The residual silanols, not blocked by Tris(TMS), are sites available for adsorption or chemical reaction.

2.3.2. Synthesis of Mixed Tris(TMS)/ABDMS Surfaces

Mixed surfaces containing Tris(TMS) and amino groups were prepared by subsequent reaction of the Tris(TMS) surfaces with 4-(aminobutyl)dimethylmethoxysilane (ABDMS) in the vapor phase (see Figures 2.10 – 2.11). Mixed monolayers with different compositions were prepared by controlling the initial reaction time of Tris(TMS). The chemical composition of the mixed monolayers was determined by XPS. The XPS data along with the contact angle results are shown in Table 2.2. The carbon-to-nitrogen ratio increases as the amount of Tris(TMS) increases, showing that there are fewer sites available for subsequent reaction with ABDMS, as expected. From the carbon-to-nitrogen ratio of the pure ABDMS and Tris(TMS) surfaces, the relative ratio of Tris(TMS) to ABDMS for each of the surfaces was determined. The contact angle measured for a pure ABDMS surface was 73/39, and the contact angles for the mixed surfaces increase as the amount of Tris(TMS) originally on the surface increases and the contribution from the ABDMS decreases. The contact angle data, combined with

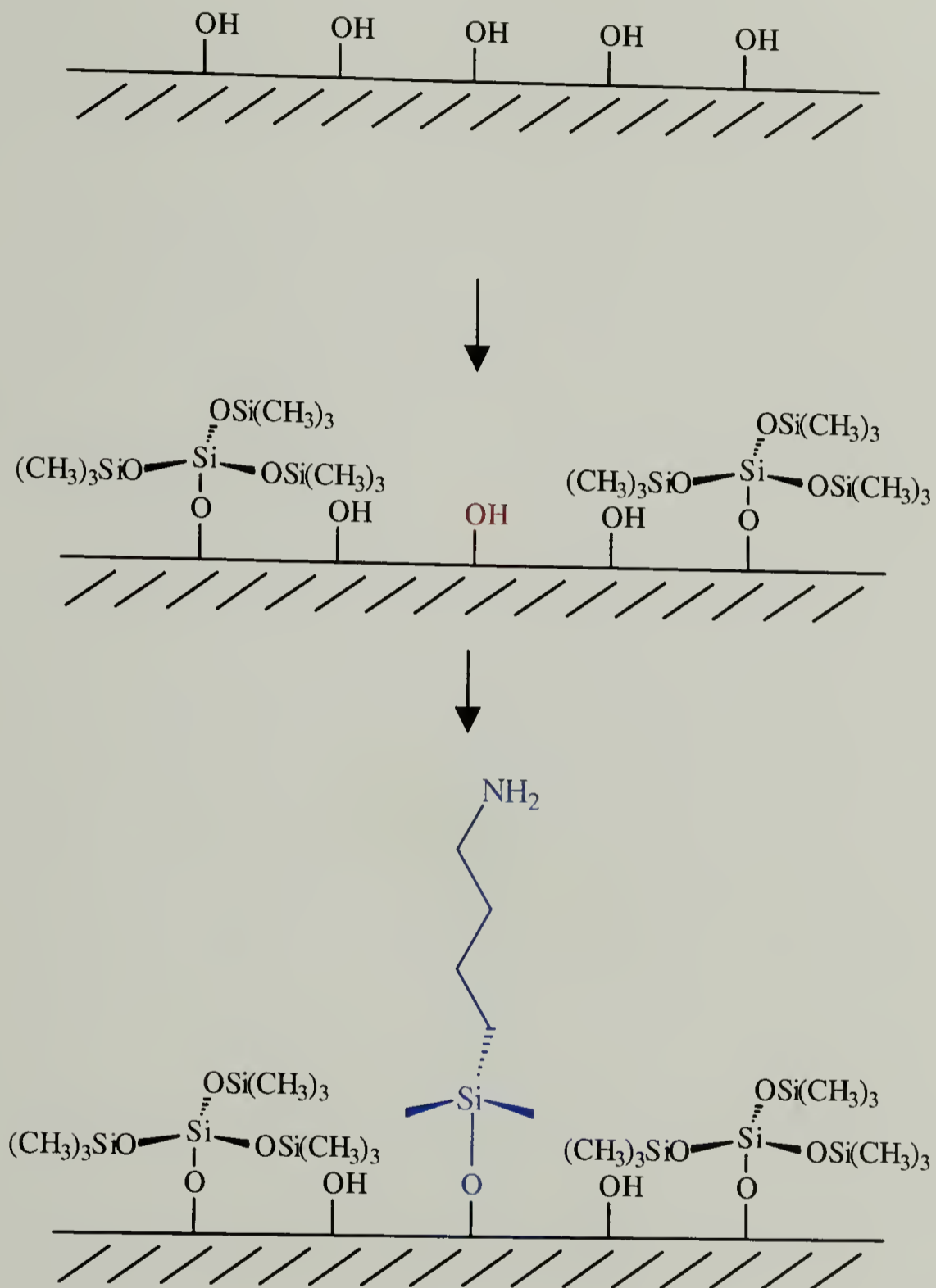


Figure 2.10. Schematic illustrating the reaction of Tris(TMS)-Cl with surface silanol groups, followed by subsequent reaction of remaining silanols with a second silane (e.g. ABDMS).

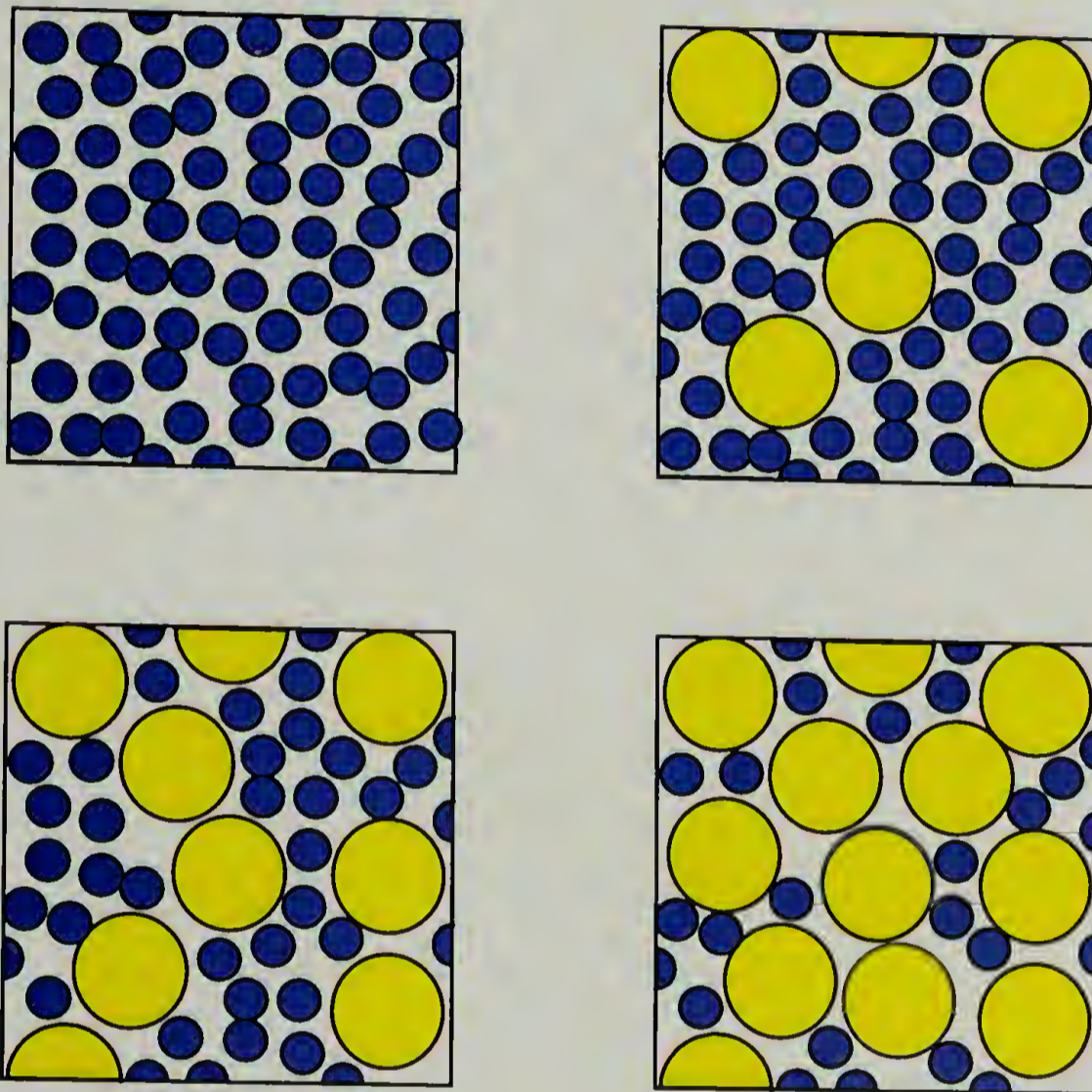


Figure 2.11. Schematic illustrating the 2-D above-view of Tris(TMS) surfaces (large circles) that have been further reacted with ABDMS (small circles).

Table 2.2. XPS and contact angle data for Tris(TMS)/ABDMS mixed surfaces prepared by consecutive vapor phase reactions.

sample	C/N ratio -XPS-	ratio Tris:ABDMS	θ_A/θ_R ($^\circ$) before	θ_A/θ_R ($^\circ$) after
Clean Si / ABDMS	12/1	0 : 1	spreads	73/39
Tris(TMS) 1h / ABDMS	14/1	1 : 3.9	62/51	73/54
Tris(TMS) 4h / ABDMS	15/1	1 : 2.4	67/53	77/57
Tris(TMS) 24h / ABDMS	17/1	1 : 1.6	81/70	85/69
Tris(TMS) 72h / ABDMS	23/1	1 : 0.8	94/82	94/73
Tris(TMS) 93h / ABDMS	-	1 : 0	103/89	103/89

the XPS results, is direct evidence that the original Tris(TMS) surface is effective in templating the surface to subsequent reactions and modifications.

Tris(TMS)/ABDMS mixed surfaces were also characterized by measurement of the contact angle using water solutions having different pHs. This approach, referred as contact angle titration, is widely used for the characterization of acid-base surface properties of polymers,^{42,43} oxides,⁴⁴ and supported monolayers.⁴⁵⁻⁴⁷ Figure 2.12 shows advancing contact angles for different Tris(TMS)/amino mixed surfaces plotted as a function of the probe fluid pH. With decreasing pH, a transition in the contact angle from a more hydrophobic to less hydrophobic surface is observed at a pH ~ 3.5. This transition is most evident for the pure amine surface, and gradually decreases in magnitude for mixed surfaces containing less amine functionality. It is worth noting that this transition can still be detected for the pure Tris(TMS) surface, which obviously does not contain any amine groups. This behavior can be explained with the schematic shown in Figure 2.13. For pH > 4, the amine groups are protonated by the residual surface silanols, exposing methylene groups from the butyl segment, and producing a more hydrophobic surface. Such protonation has been observed directly by a variety of spectroscopic techniques.⁴⁸⁻⁵⁰ Near pH ~ 3.5 the acidic buffer solution competes with the surface silanols (pKa ~ 4)³⁹ to protonate the amine. This frees the amino group to interact with the probe fluid and produces a less hydrophobic surface. Since this transition can be seen even without the presence of amine, the data show that the silanol surface is being titrated.

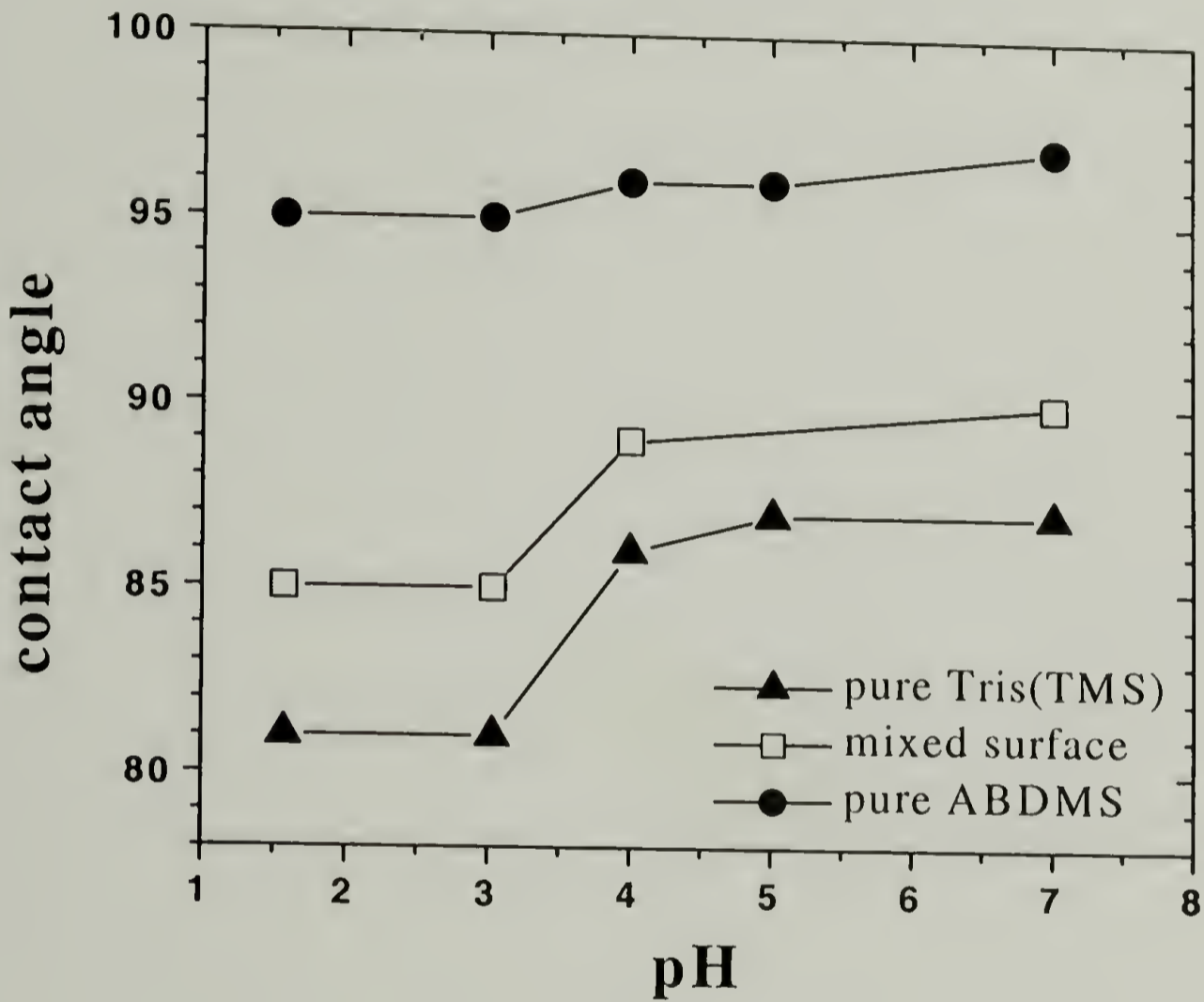


Figure 2.12. pH-dependent contact angles for pure Tris(TMS) (●), mixed Tris(TMS)/ABDMS (□), and pure ABDMS (▲) surfaces.

Neutral pH

Low pH

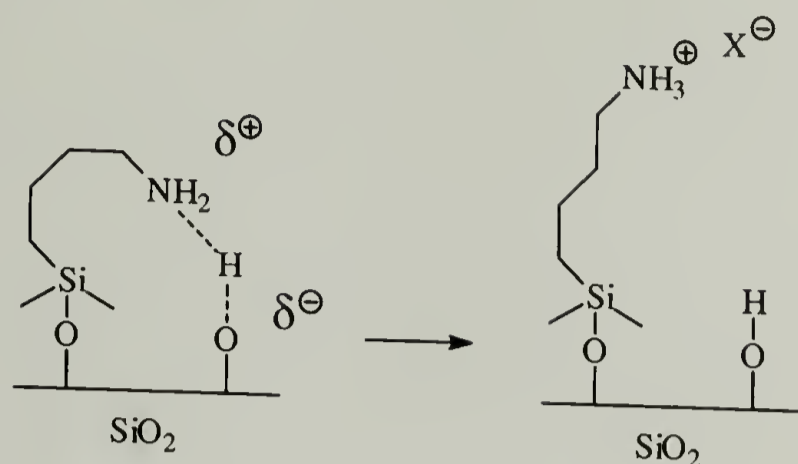


Figure 2.13. Schematic illustrating the transition of ABDMS from being protonated by surface silanol groups at neutral pH to being protonated by external acid at low pH.

2.3.3. Adsorption of PS-COOH to Silane-modified Surfaces

The adsorption of carboxylic acid end-functionalized polystyrene on Tris(TMS)-modified surfaces is shown schematically in Figure 2.14. The adsorption of PS-COOH onto these surfaces is rapid and irreversible. Contact angle data for the Tris(TMS) surfaces before and after adsorption are given in Table 2.3. The water contact angle for a smooth film of PS was measured to be 95°/79°, whereas the contact angle for 11K PS-COOH adsorbed onto clean silicon was 89°/49°. The difference observed could arise from either chemical heterogeneity of the surface (i.e. penetration and interaction of the water to the underlying oxide), surface roughness of the adsorbed layer, or surface restructuring. It should be noted that, although the advancing water contact angle remains constant for the first four samples, the receding contact angle steadily increases. This again indicates that the probe fluid is penetrating the adsorbed layer and sensing the underlying layer, which is no longer the hydrophilic oxide but rather the hydrophobic Tris(TMS) surface. For the Tris(TMS) 72 h sample, the underlying Tris(TMS) layer begins to influence the advancing contact angle, hinting at the possibility that the

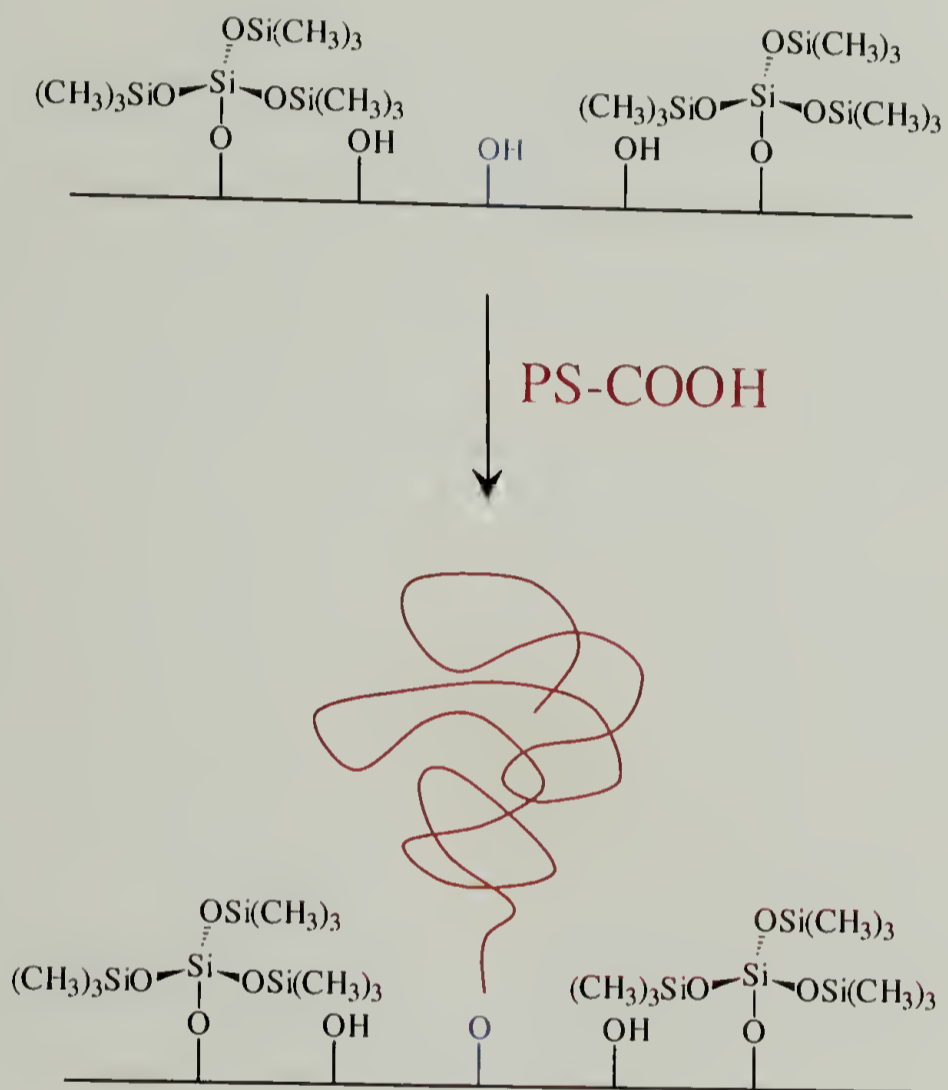


Figure 2.14. Schematic of adsorption of solvated PS-COOH onto a Tris(TMS)-modified surface.

Table 2.3. Contact angle data for 11K PS-COOH adsorption from toluene onto Tris(TMS) surfaces.

sample	before adsorption		after adsorption	
	θ_A/θ_R ($^\circ$)		θ_A/θ_R ($^\circ$)	
	H ₂ O	C ₁₆ H ₃₄	H ₂ O	C ₁₆ H ₃₄
clean Si	spreads	spreads	89/49	8/0
Tris(TMS) 1h	62/51	24/9	90/50	8/0
Tris(TMS) 4h	67/53	24/11	89/54	10/0
Tris(TMS) 24h	81/70	31/20	90/67	20/7
Tris(TMS) 51h	86/75	30/20	90/68	19/10
Tris(TMS) 72h	94/82	34/22	94/75	22/10
Tris(TMS) 93h	103/90	36/33	103/89	36/32

adsorbed PS layer has become partially discontinuous which exposes Tris(TMS). At the highest coverage of Tris(TMS), the water contact angle remains unchanged before and after adsorption, indicating that either no PS-COOH adsorbs to this surface or the contact line of the probe fluid can easily contort around the adsorbed chains on the surface. The hexadecane contact angle behaves very similarly, with the exception that hexadecane begins to probe the underlying surface earlier than seen in the water contact angle. Again, methylene groups (PS backbone) will yield a hexadecane contact around approaching 0° while methyl groups (Tris(TMS)) will exhibit hexadecane contact angles up to 36° . Thus, hexadecane is an effective probe to differentiate between the adsorbed polymer chains and the underlying Tris(TMS)-modified surface.

The kinetics of adsorption of 11K PS-COOH was determined on a series of surfaces having different Tris(TMS) coverages. The thickness of the PS-COOH layer as a function of adsorption time is shown in Figure 2.15. Ellipsometry was conducted before and after adsorption to determine the adsorbed layer thickness, using the refractive index of bulk polystyrene ($n = 1.591$). As seen, the adsorption of PS-COOH occurs quickly, even for surfaces that contain high amounts of Tris(TMS). One might expect that as the number of adsorption sites diminishes, the conformational restrictions placed on the polymer increases, requiring the polymer to explore a vast number of conformations before adopting the correct one that allows for adsorption. The surface is also very hydrophobic and lyophobic at high coverages of Tris(TMS), which could also complicate the adsorption kinetics. But these kinetics data indicate that in all cases the adsorption of PS-COOH saturates within 24 h. Therefore, all remaining experiments were conducted for this amount of time.

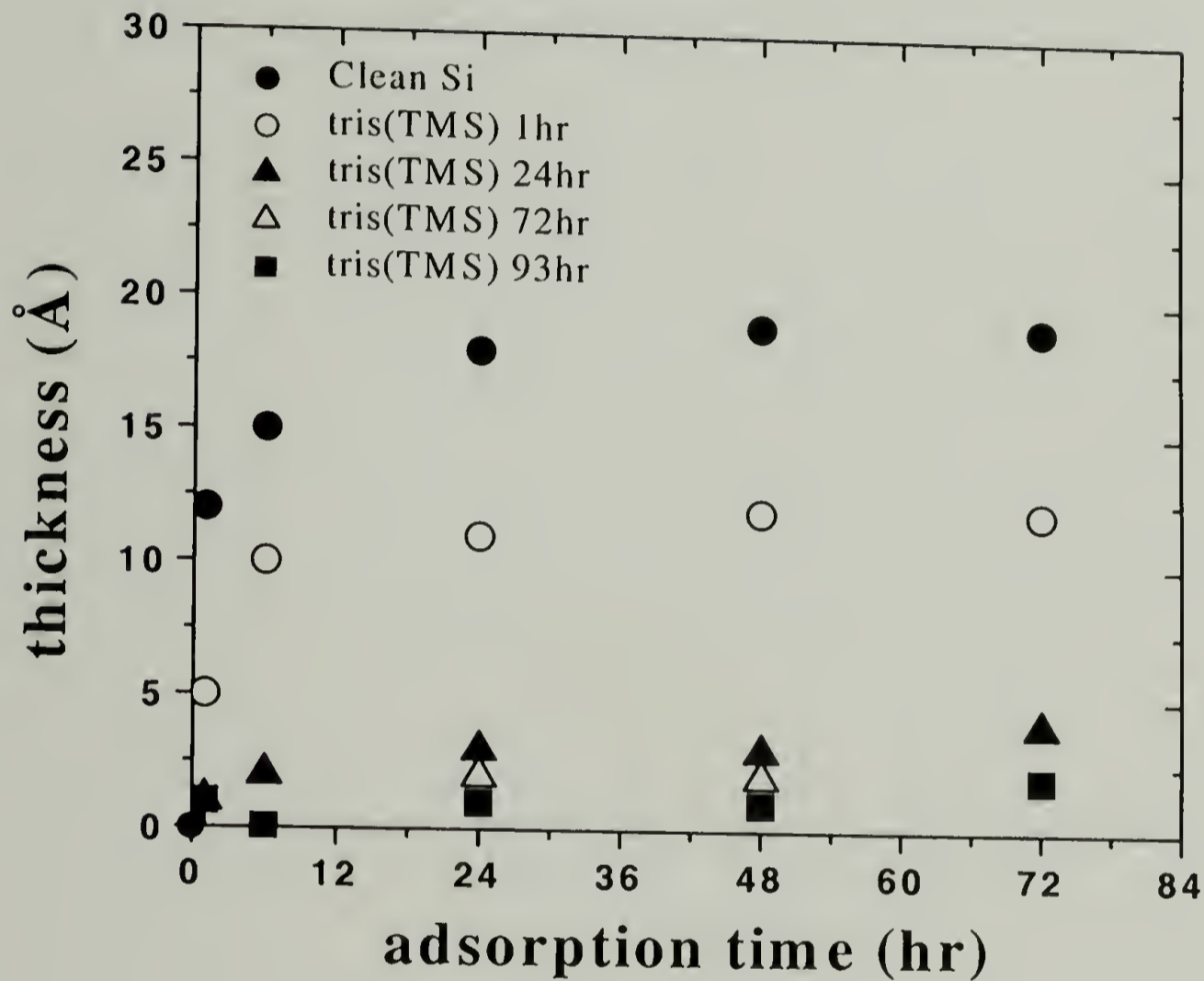


Figure 2.15. Adsorption kinetics of 11K PS-COOH from toluene onto surfaces having increasing Tris(TMS) surface coverage: 0% Tris(TMS) (clean Si) (●); 55% Tris(TMS) (○); 81% Tris(TMS) (▲); 89% Tris(TMS) (△); and 96% Tris(TMS) (■).

The adsorption data of 11K and 41K PS-COOH to Tris(TMS) surfaces from toluene, as well as 11K PS-COOH from cyclohexane (35 °C) are shown in Figure 2.16 . As expected, the amount of adsorbed polymer decreases with increasing Tris(TMS) coverage, demonstrating that the Tris(TMS) surfaces are effective in molecularly templating the oxide surface and dictating the adsorption behavior of PS-COOH. This will be further verified by AFM in a later section. Also, the 41K PS-COOH shows a decrease in the amount of adsorption. For a given number of chains anchored to the surface, an increase in the total adsorbed thickness would be expected as the molecular weight of the polymer increases. The observed decrease can be understood by a fine balance between the energetic gain of pulling the chain into solution (buoyancy effect) and the energy associated with anchoring the chain to the surface. The entropic loss of pinning a polymer of that size to a solid surface is greater than the enthalpic gain of a single hydrogen bond with the surface.¹² Adsorbing from cyclohexane (theta-solvent) offers versatility in the process by allowing thicker layers to be obtained. This is due to the polymer adopting a more globular conformation, which results in a higher packing density on the surface in comparison to adsorption from a good solvent (toluene). The adsorption results for 11K PS-COOH to mixed Tris(TMS)/ABDMS surfaces are also shown in Figure 2.16. To ensure that the ABDMS was not protonated by external acidic groups, the adsorption protocol was altered to include a rinse with EDIPA just prior to adsorption. Adsorption to these mixed monolayers resulted in thinner adsorbed layers, which can be attributed to the lower surface energy of the amine surface compared to the silanol surface as well as the decreased availability of the amine group due to surface protonation.

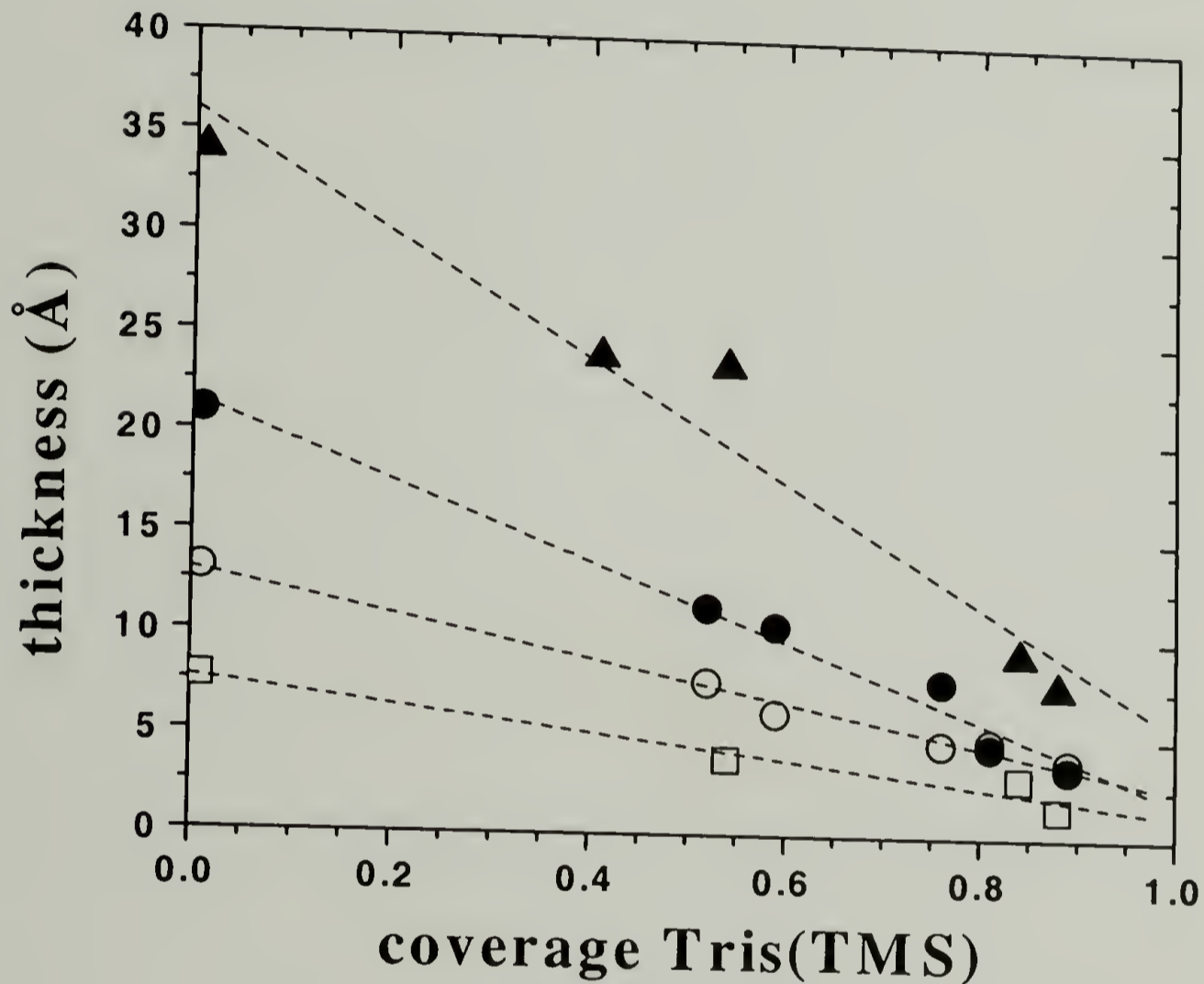


Figure 2.16. Adsorbed thicknesses, as determined by ellipsometry, of PS-COOH adsorption to Tris(TMS) surfaces: 11K adsorbed from cyclohexane (▲) and toluene (●); 41K adsorbed from toluene (○); and 11K adsorbed from toluene to mixed Tris(TMS)/ABDMS surfaces (□).

Finally, AFM was used to study in detail the surface topography for the 11K PS-COOH adsorbed to Tris(TMS)-modified surfaces. Figures 2.17 and 2.18 show AFM images for a silica surface and one modified with Tris(TMS) prior to adsorption, respectively. In comparison to a clean substrate, the modified surface exhibits texture arising from the incomplete coverage of the surface with Tris(TMS). It could be further argued that the texture seen on the Tris(TMS) surface is due the presence of the nanopores on the surface as a result of the poor packing efficiency of Tris(TMS) molecules. This is a reasonable argument since we know the Tris(TMS) molecule has a height of 7 Å and the height image from AFM is on a 1 nm scale. Figures 2.19 through 2.24 show images obtained for 11K PS-COOH adsorbed to surfaces having Tris(TMS) coverages ranging from 0% (clean silicon) to 86%. One would expect that PS-COOH adsorbed to clean silicon would appear fairly smooth since the polymer layer should be in a brush-like conformation. The AFM image clearly shows that this is not the case, and aggregates are evident on the surface. These aggregates are most likely due to a solvent-induced dewetting of the adsorbed polystyrene chains as the sample was dried. It is well known that polystyrene will dewet clean silicon oxide, but the lateral length scale of the dewetting in the case presented here is limited due to the fact that the polymer chains are physically anchored to the surface.

Aggregation is also evident for the adsorbed layers on Tris(TMS) surfaces, again possibly due to a dewetting process with the minor difference that the oxide is slowly being replaced with an equally non-attractive Tris(TMS) surface. As the coverage of Tris(TMS) increases, the lateral correlation of these aggregates decrease as the polymer chains become more separated from one another by a sea of Tris(TMS) molecules. At

high coverages of Tris(TMS) (Figures 2.23 and 2.24), it appears that the Tris(TMS) surface has separated individual polymer chains from each other since the size scale of the features does not change between these two samples. The separation distance between features increases as the coverage of Tris(TMS) increases further, clearly indicating that the surface is effective in diluting the grafting density of adsorbed polymer chains.

Analysis of the AFM images for adsorption of 11K PS-COOH onto clean silicon (Figure 2.19) shows aggregates of polystyrene having an average height of 1.2 nm and diameter of 22 nm. Contact angle data, however, show that the entire surface is covered with polystyrene. If there is no lateral broadening due to the AFM tip shape, then the average number of chains within one of these aggregates can be calculated. Using the bulk density (1.05 g/cm^3) of PS, the volume occupied by one PS chain (V_{mol}) can be written as:

$$V_{mol} = \left(\frac{M}{\rho}\right)\left(\frac{1}{N_A}\right) \quad (4)$$

where M is the molecular weight, ρ is the bulk density, and N_A is Avogadro's number. For an 11K PS chain, $V_{mol} = 1.7 \times 10^4 \text{ \AA}^3$. The volume of a cylindrical disk is given by

$$V = \frac{\pi d^2}{4} h \quad (5)$$

Using the height and diameter data from the AFM image, the average volume of the observed clusters is $4.6 \times 10^5 \text{ \AA}^3$. This corresponds to ~ 26 polystyrene chains in each cluster. This represents an upper limit since we are assuming the tip to be infinitely sharp. Similar calculations were performed for the remaining samples and the results are shown in Table 2.4. If we assume that the diameter of the tip is 5 nm, a first order

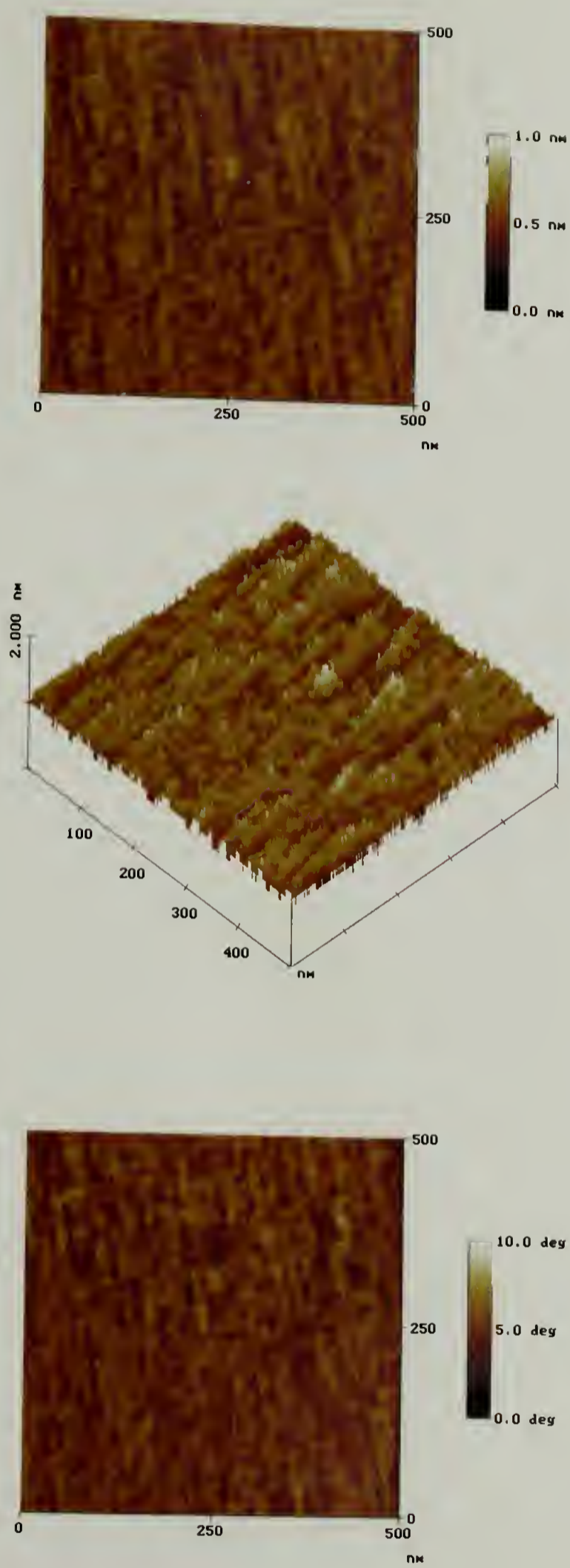


Figure 2.17. AFM images obtained in tapping mode of clean silicon. The images are height (top), surface (middle), and phase (bottom) plots of a $0.25 \mu\text{m}^2$ sampling area.

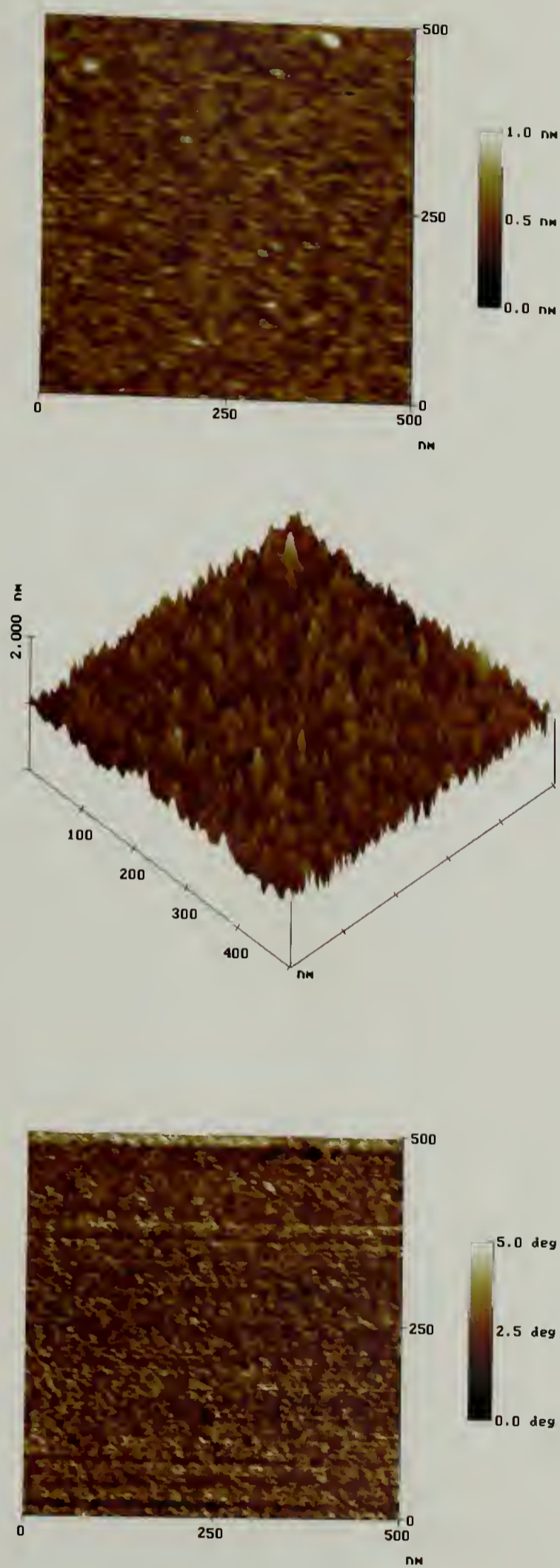


Figure 2.18. AFM images obtained in tapping mode of Tris(TMS)-modified silicon. The images are height (top), surface (middle), and phase (bottom) plots of a $0.25 \mu\text{m}^2$ sampling area.

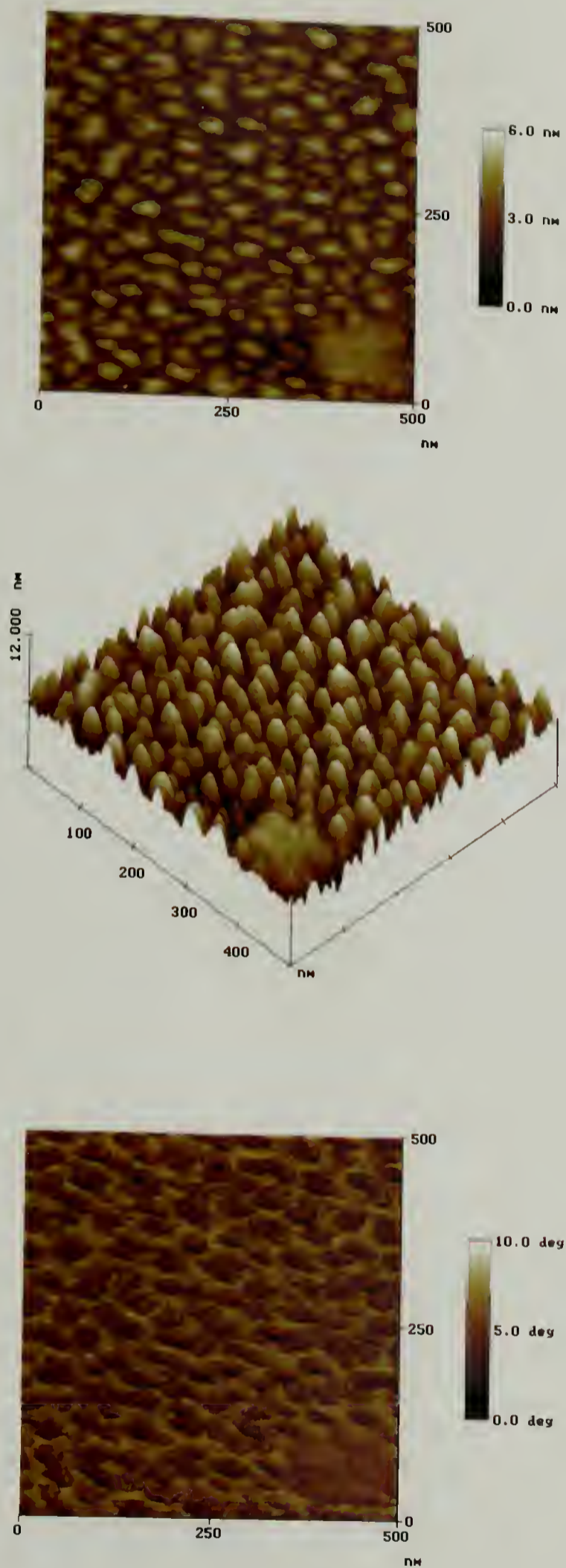


Figure 2.19. AFM images obtained in tapping mode of 11K PS-COOH adsorbed from toluene to clean silicon at 23 °C and 1.0 mg/mL for 24h. The images are height (top), surface (middle), and phase (bottom) plots of a 0.25 μm² sampling area.

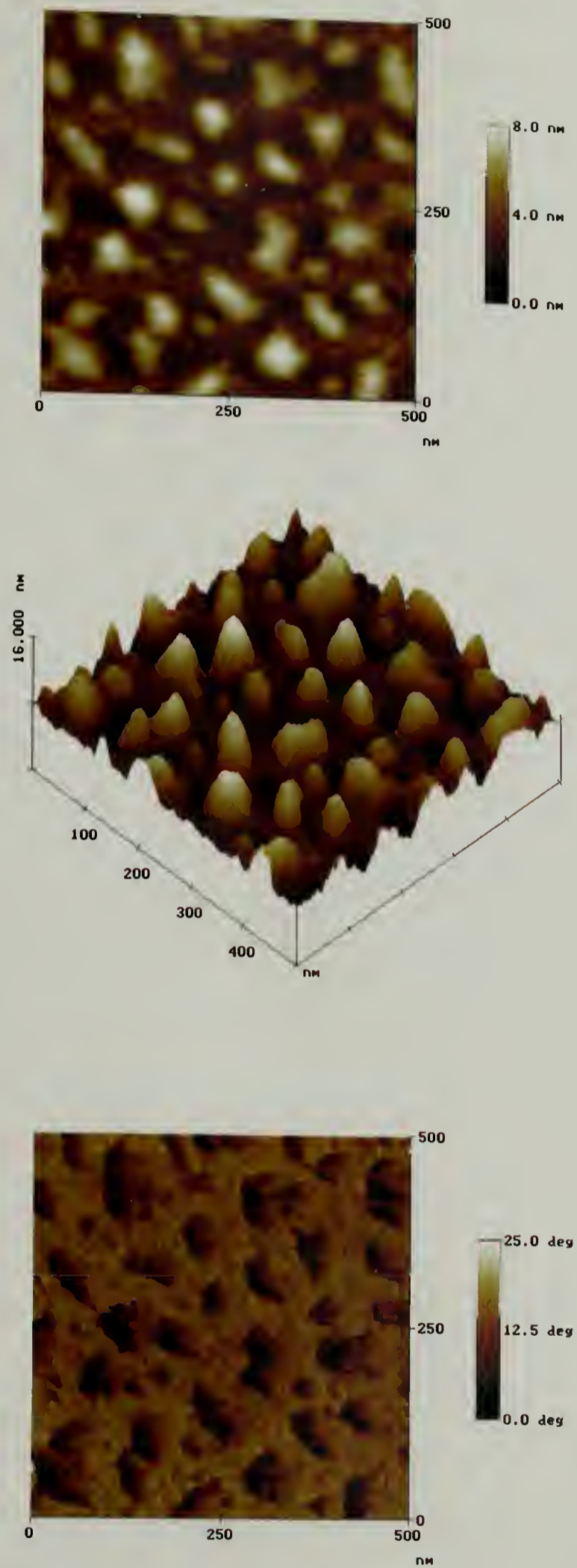


Figure 2.20. AFM images obtained in tapping mode of 11K PS-COOH adsorbed from toluene to Tris(TMS) 1h at 23 °C and 1.0 mg/mL for 24h. The images are height (top), surface (middle), and phase (bottom) plots of a 0.25 μm² sampling area.

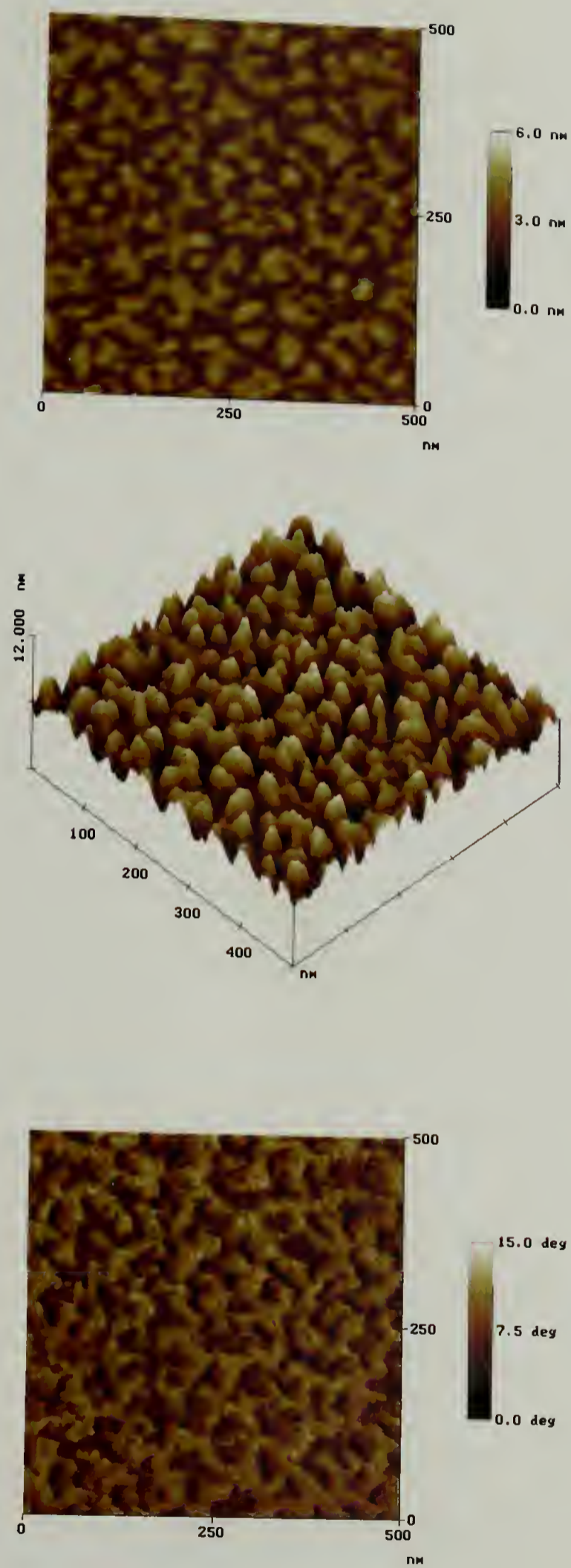


Figure 2.21. AFM images obtained in tapping mode of 11K PS-COOH adsorbed from toluene to Tris(TMS) 4h at 23 °C and 1.0 mg/mL for 24h. The images are height (top), surface (middle), and phase (bottom) plots of a 0.25 μm² sampling area.

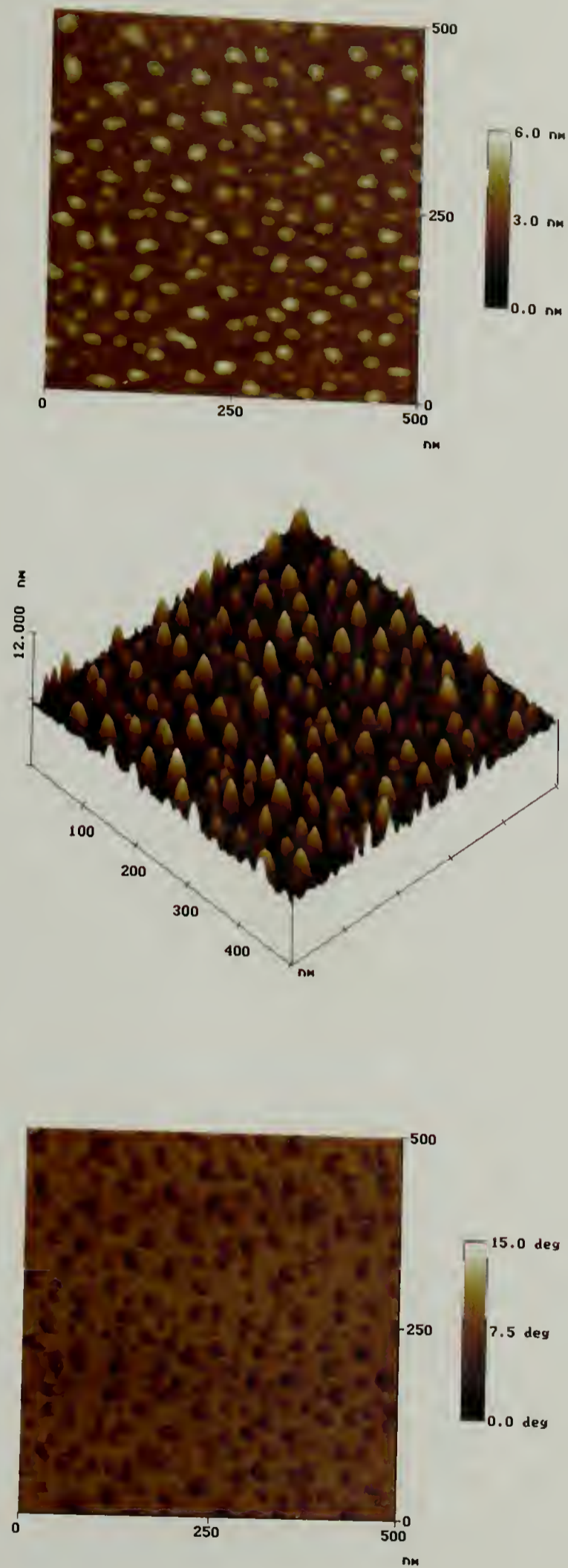


Figure 2.22. AFM images obtained in tapping mode of 11K PS-COOH adsorbed from toluene to Tris(TMS) 24h at 23 °C and 1.0 mg/mL for 24h. The images are height (top), surface (middle), and phase (bottom) plots of a 0.25 μm² sampling area.

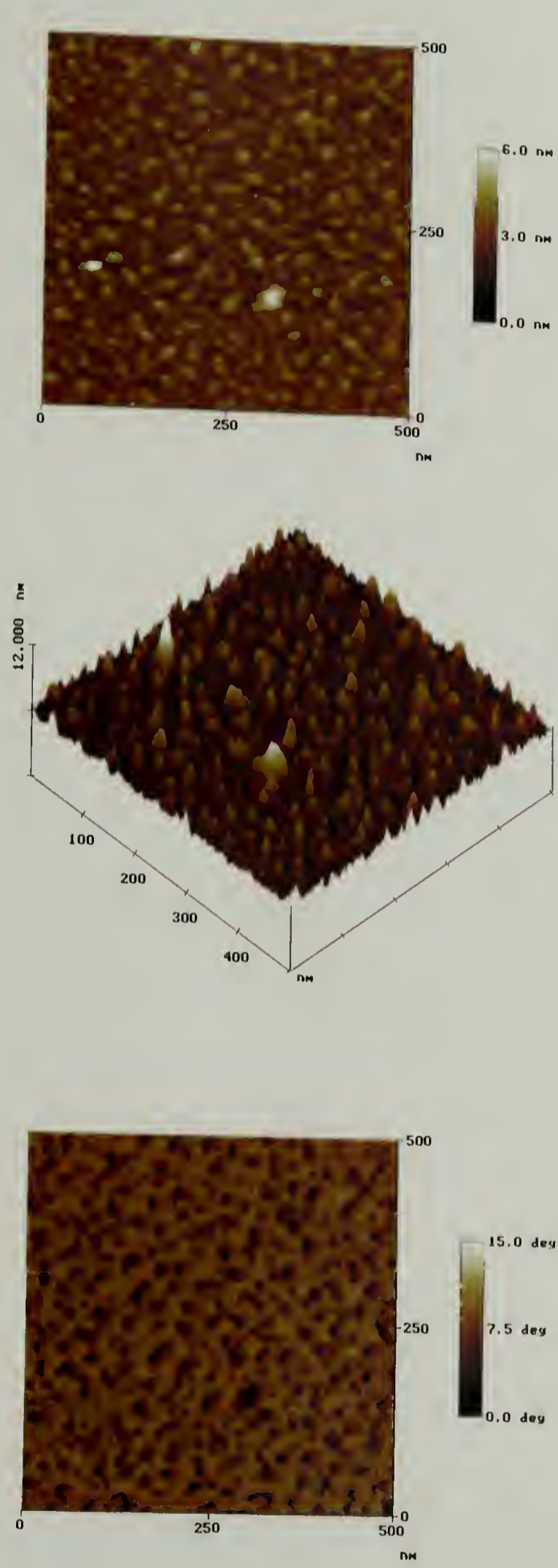


Figure 2.23. AFM images obtained in tapping mode of 11K PS-COOH adsorbed from toluene to Tris(TMS) 51h at 23 °C and 1.0 mg/mL for 24h. The images are height (top), surface (middle), and phase (bottom) plots of a 0.25 μm² sampling area.

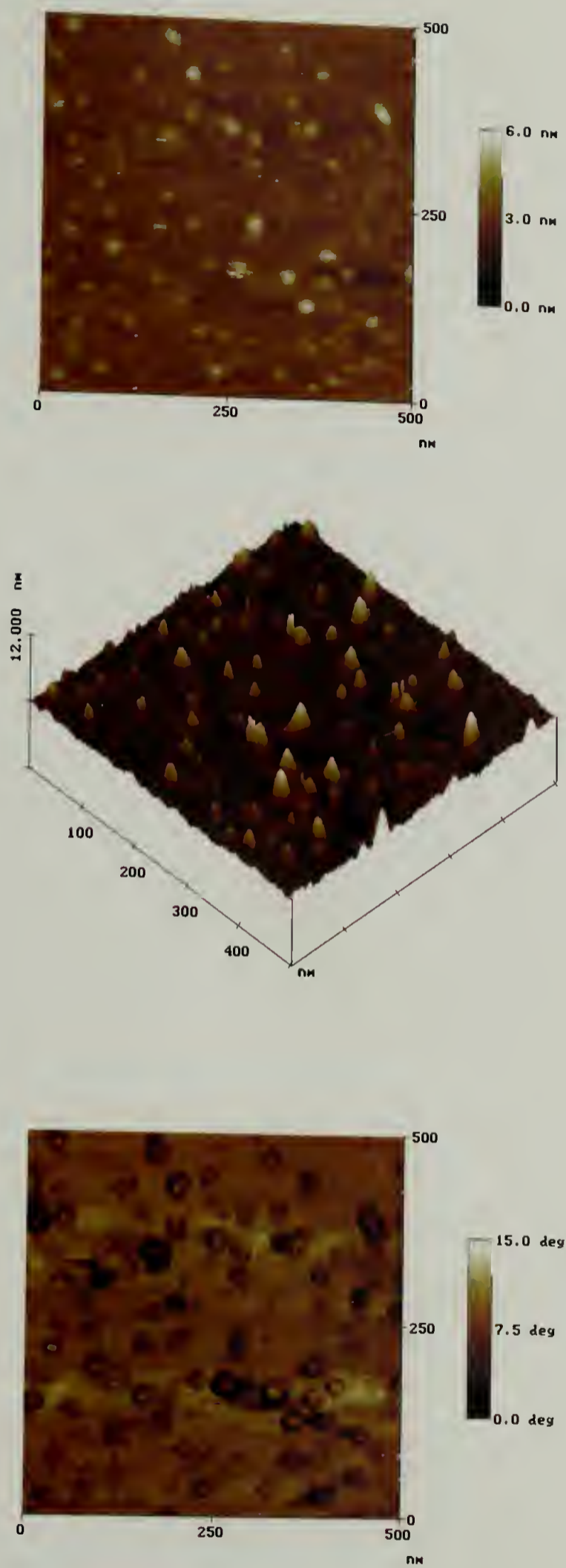


Figure 2.24. AFM images obtained in tapping mode of 11K PS-COOH adsorbed from toluene to Tris(TMS) 72h at 23 °C and 1.0 mg/mL for 24h. The images are height (top), surface (middle), and phase (bottom) plots of a 0.25 μm² sampling area.

Table 2.4. Number of chains per aggregate as calculated by average dimensions from AFM image analysis.

sample	dimensions of aggregates in AFM image		corrected for a tip diameter of 5 nm	
	D/H (nm)	# chains	D*/H (nm)	# chains
clean Si	22/1.2	26	17/1.2	15
Tris(TMS) 1h	36/1.8	105	31/1.8	78
Tris(TMS) 4h	32/1.2	55	27/1.2	39
Tris(TMS) 24h	19/1.0	16	14/1.0	9
Tris(TMS) 51h	12/0.8	5	7/0.8	1
Tris(TMS) 93h	12/0.9	6	7/0.9	1

correction for the smearing of the data by the tip shape can be made since the observed image is a convolution of the real image and the tip shape. The data in Table 2.4 strongly suggest that single PS molecules are being observed for high Tris(TMS) coverages.

2.3.4. Dewetting of Polymer Thin Films on Tris(TMS) Surfaces

PS films, 230 Å in thickness, were spin coated onto surfaces modified with Tris(TMS) and onto surfaces to which 11K PS-COOH was adsorbed onto Tris(TMS) surfaces from either toluene or cyclohexane. The surfaces were then annealed at 160 °C for 24 h, giving the polymer film mobility, and allowing for dewetting. The procedure is illustrated in Figure 2.25. Also shown in this figure is an optical micrograph of the dewetted structure typically seen in these films after annealing. The film dewets into droplets that form a typical Voronoi pattern of polygons. Several droplets on the surface can then be imaged using AFM to yield the quasi-equilibrium contact angle.⁵¹ It should be noted that the contact angle of a dewetted droplet actually should resemble a receding contact angle since the material is being withdrawn across the surface. The results of the dewetting studies are shown in Table 2.5. For the surfaces treated only with Tris(TMS) dewetting was found in all cases with little change in the contact angle of the dewetted droplets as a function of coverage. NOTE: The contact angle described here is of the static, dewetted droplet of PS on the surface as measured by AFM, and should not be confused with the dynamic contact angle of a liquid probe fluid described earlier. For the surfaces to which PS-COOH was anchored, the dewetted contact angles were highly dependent on the grafting density. For Tris(TMS) coverages greater than 60%, no substantial improvement in the wetting characteristics was found. However, as the

thickness of the adsorbed PS-COOH layer increases, a considerable reduction in the contact angle and consequently, the interfacial energy is observed. It should be noted that PS does not wet the surface covered with PS-COOH due to an autophobic dewetting process described by Leibler³⁰ and subsequently Shull.³⁴

Obviously, what is lacking in this system (PS-COOH/PS) is an enthalpic gain that could offset the entropic loss of stretching the surface-grafted chains, allowing for a net gain in total energy in the system and wetting to occur. Therefore, other polymers were studied that exhibit strong, favorable interactions with polystyrene and which are miscible with polystyrene in the bulk. These polymers included poly(2-chlorostyrene), poly(*n*-butyl methacrylate), poly(cyclohexyl methacrylate), and poly(vinyl methyl ether). These polymers will be abbreviated PoClS, PnBMA, PCMA, and PVME, respectively. The chemical structures of these polymers are shown in Figure 2.26 and the physical properties are listed in Table 2.6. The dewetting of polystyrene was performed again in this section as a control experiment, and can be compared with the previous results described earlier. The results of the dewetting experiments for these selected polymers are shown in Table 2.7. A few noteworthy points can be made in light of this data. Polystyrene, as seen in the previous experiments, dewets not only the Tris(TMS) surfaces but also those surfaces with anchored PS-COOH chains. Interestingly, PoClS does not dewet the same surfaces with or without an anchored PS-COOH layer. It is not clear at this time why this behavior is observed. Either the surface energy of the PoClS is quite different than polystyrene, which drives the system to wet the surface, or the molecular weight of the PoClS is so high that the mobility of the chains is too low to allow for large-scale dewetting on the surface. Both acrylate polymers wet all the surfaces studied.

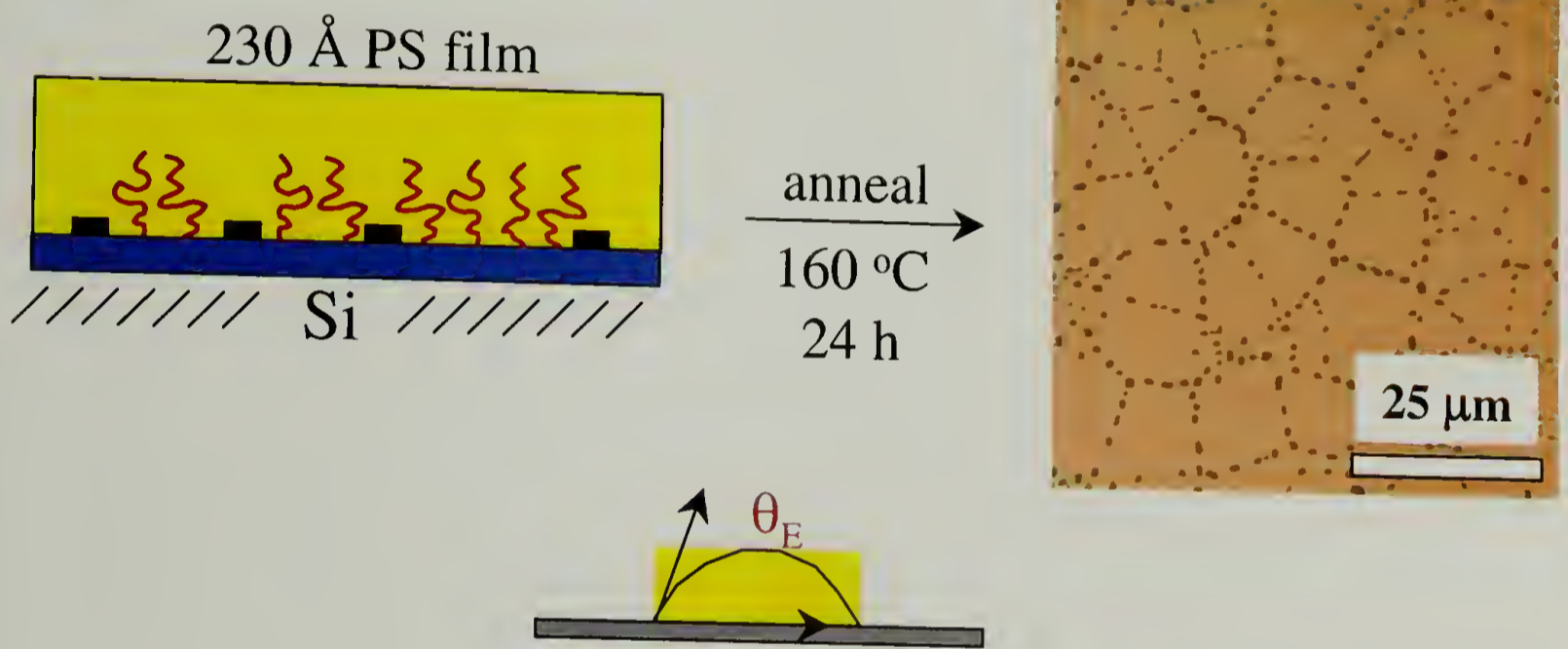


Figure 2.25. Schematic illustrating dewetting experiments conducted on Tris(TMS) surfaces having anchored PS-COOH chains with an overlying, spun-cast film of PS. Shown on the right is a typical optical micrograph of the dewetted structure.

Table 2.5. Contact angles of dewetted PS on various Tris(TMS) surfaces as determined by AFM analysis.

	coverage (%)	adsorbed thickness (Å)	R/H (μm)	θ_E (°)
Tris(TMS)	0	0	1.17/0.48	42
	52	0	1.45/0.66	46
	59	0	1.43/0.63	45
	76	0	1.09/0.57	52
	81	0	0.94/0.44	47
Tris(TMS) 11K PS-COOH toluene	0	19	1.88/0.24	14
	52	13	2.09/0.57	28
	59	12	1.88/0.68	37
	76	8	0.98/0.47	48
	81	5	1.21/0.56	46
Tris(TMS) 11K PS-COOH cyclohexane	0	36	2.87/0.20	7
	30	24	14.5/0.90	7
	42	23	4.65/0.42	10
	75	10	1.15/0.48	42
	80	8	0.82/0.36	45

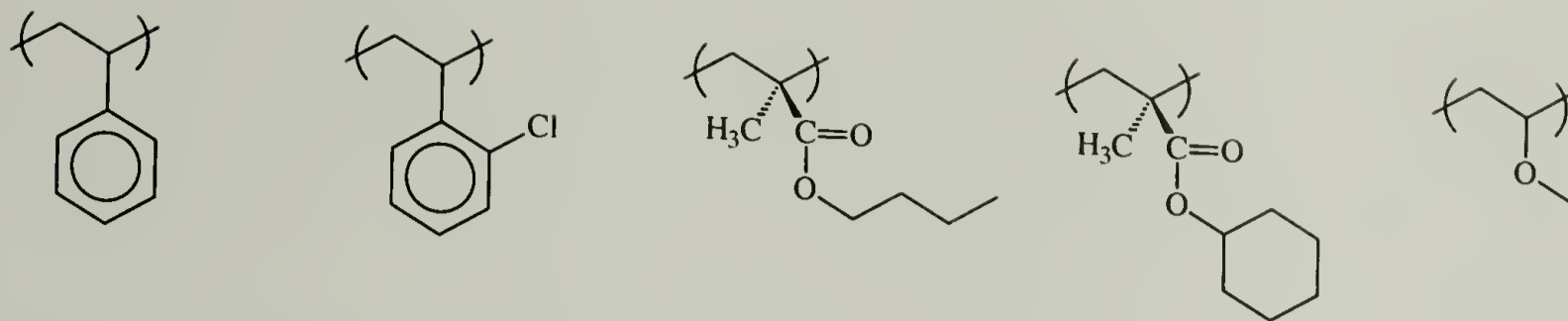


Figure 2.26. Chemical structures of the polymers used in dewetting studies on Tris(TMS)/PS-COOH surfaces: (from left to right) poly(styrene), poly(2-chlorostyrene), poly(n-butyl methacrylate), poly(cyclohexyl methacrylate), and poly(vinyl methyl ether).

This is most likely due to not only the miscibility of the polymers with polystyrene but also their strong attraction and interaction with the underlying substrate (silicon oxide). Unfortunately, the purpose of this work, in part, was to negate the strong interactions of an overlying polymer film with the underlying substrate while maintaining a wetting film. This is obviously not the case when dealing with acrylate polymers as was observed in these dewetting studies.

Even more interesting is the wetting behavior of PVME on these adsorbed layers. PS/PVME exhibits weakly attractive interactions that result in phase mixing at moderate temperatures, but undergoes phase separation (LCST) upon heating due to the inability of this weakly attractive force to offset the increasing entropic loss of keeping the chains in close proximity to one another. When PVME was cast onto the Tris(TMS)/PS-COOH layers, the films were stable at room temperature for several days. The T_g of PVME is well below room temperature (see Table 2.6), so the film has more than enough mobility at room temperature to dewet if it needed to. Annealing the films above 160 °C negates the weakly attractive interaction between PS/PVME and so the film undergoes phase separation-induced dewetting. This behavior is shown in Figure 2.27. Unlike the

Table 2.6. Molecular weight and T_g data for the polymers used in the dewetting studies.

polymer	Mw (g/mole)	pdi	T_g (°C)
poly(styrene)	51k	1.03	105
poly(2-chlorostyrene)	420k	2.30	119
poly(n-butyl methacrylate)	188k	2.49	27 - 34
poly(cyclohexyl methacrylate)	75k	2.98	83 - 104
poly(vinyl methyl ether)	90k	3.00	-31 - -22

Table 2.7. Dewetting data of selected polymers spun-cast on Tris(TMS) surfaces before and after adsorption of 11K PS-COOH. Surfaces that dewet are labeled with 'D' and those that wet are labeled 'W', as determined by optical microscopy.

sample	adsorbed thickness (Å)	<u>overlying polymer film</u>				
		PS	PoClS	PnBMA	PCMA	PVME
clean Si	0	D	W	W	W	W
Tris(TMS) 1h	0	D	W	W	W	D
Tris(TMS) 24h	0	D	W	W	W	D
Tris(TMS) 72h	0	D	W	W	W	D
clean Si	20	D	W	W	W	W ^a
Tris(TMS) 1h	13	D	W	W	W	W ^a
Tris(TMS) 24h	8	D	W	W	W	W ^a
Tris(TMS) 72h	5	D	W	W	W	W ^a

^a dewets upon heating above LCST

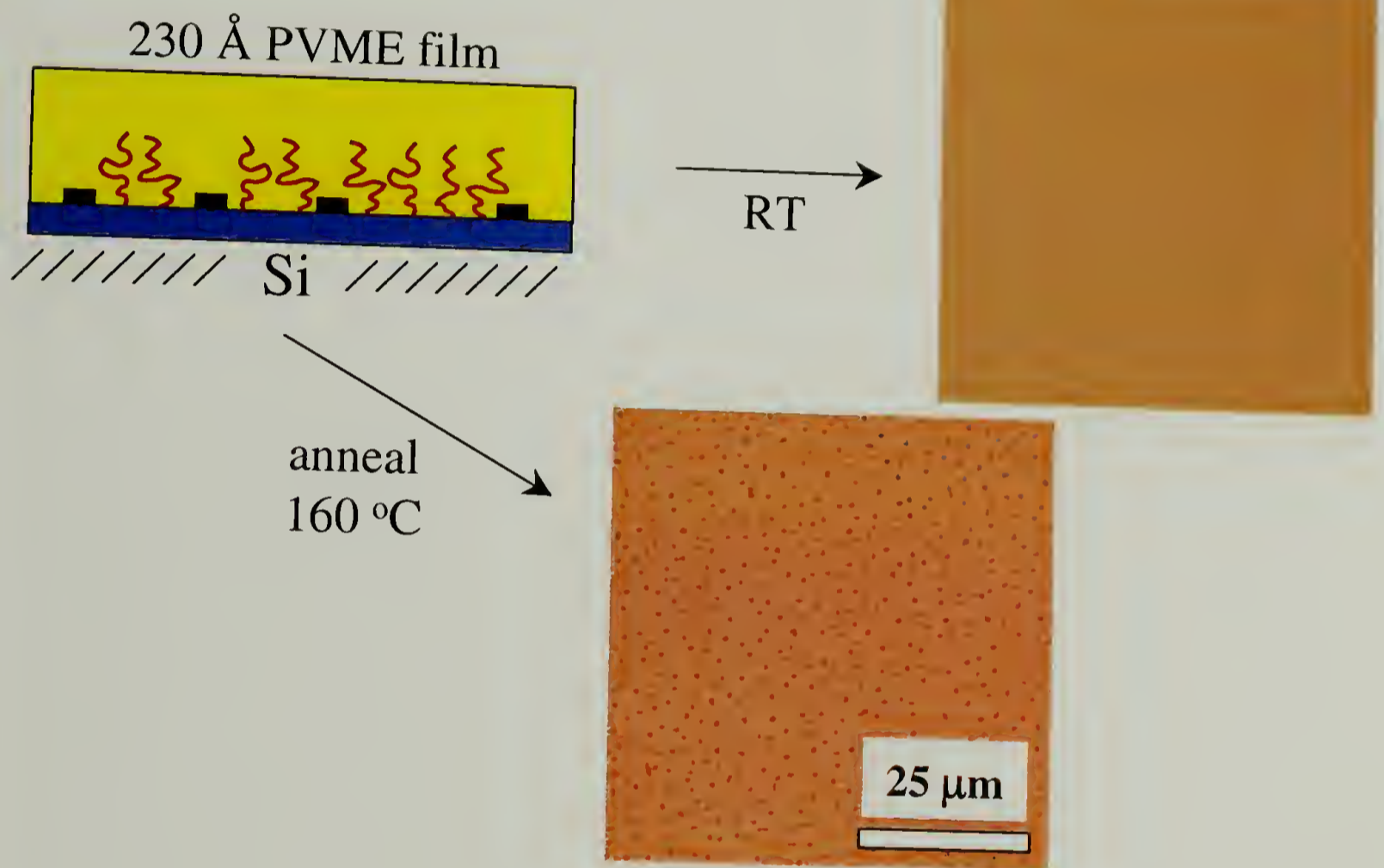


Figure 2.27. Schematic illustrating dewetting experiments conducted on Tris(TMS) surfaces having anchored PS-COOH with an overlying, spun-cast film of PVME. Shown are typical optical micrographs of the dewetted structure.

PS-COOH/PS case, the contact angles of the dewetted drops could not be measured by AFM since the PVME droplets are above their T_g and thus are in a liquid state. One would expect that the dewetted droplets of PVME should, given enough time, revert back to a continuous film since the system is now back below the LCST. The kinetics of this process is unknown, and the experiments conducted here did not address that possibility.

2.4. Conclusions

Chemically grafted (sub)monolayers of Tris(TMS) were prepared by vapor phase reaction of the corresponding monochlorosilane. By controlling reaction kinetics, a series of surfaces were prepared having increasing coverages of Tris(TMS). The inherently poor packing efficiency of such a bulky silane allowed for the preparation of a unique class of surfaces that can be used as templates for polymer adsorption. The adsorption behavior of a model polymer system, carboxylic acid end-functionalized polystyrene, was studied extensively as a function of Tris(TMS) surface coverage. The adsorbed thickness of PS-COOH can be controlled by a number of variables such as polymer molecular weight, adsorption solvent, and surface chemistry. The topography of the adsorbed layers indicated the presence of aggregate structures on the surface, and the size scale of these aggregates diminished as Tris(TMS) surface coverage increased. The wetting properties of an overlying polymer thin film of polystyrene were investigated on these surfaces. As the Tris(TMS) coverage increases, and consequently the amount of adsorbed polymer chains decreases, the wettability of these surfaces diminishes as probed by contact angles measured by AFM. Replacing the overlying film with polymers having

strong enthalpic interactions with the adsorbed polymer layer results in drastically different wetting behaviors. Poly(2-chlorostyrene) wets the Tris(TMS)/PS-COOH layer regardless of Tris(TMS) coverage. The acrylate polymers wet these layers as well, but this observation could be a result of a tunneling effect of the acrylate chains to the underlying oxide surface. Poly(vinyl methyl ether) films wet all the surfaces at room temperature (well above the T_g of PVME) but dewet when annealed above the LCST of PS/PVME. The dewetting of PVME from adsorbed PS-COOH layers can be more accurately described as a 2-D phase separation on a surface.

2.5. References Cited

1. Scheutjens, J. and Fler, G. *J. Phys. Chem.*, **1979**, *83*, 1619.
2. Scheutjens, J. and Fler, G. *J. Phys. Chem.*, **1980**, *84*, 178.
3. de Gennes, P. *Macromolecules*, **1980**, *15*, 492.
4. Fler, G.; van Male, J., and Johner, A. *Macromolecules*, **1999**, *32*, 825.
5. Fler, G.; van Male, J., and Johner, A. *Macromolecules*, **1999**, *32*, 845.
6. Singh, N.; Karim, A.; Bates, F., and Tirrell, M. *Macromolecules*, **1994**, *27*, 2586.
7. Siqueira, D.; Reiter, J.; Breiner, U.; Stadler, R., and Stamm, M. *Langmuir*, **1996**, *12*, 972.
8. Stouffer, J. and McCarthy, T. *Macromolecules*, **1988**, *21*, 1204.
9. Su, Z.; Wu, D.; Hsu, S., and McCarthy, T. *Macromolecules*, **1997**, *30*, 840.
10. Taunton, H.; Toprakcioglu, C.; Fetters, L., and Klein, J. *Macromolecules*, **1990**, *23*, 571.
11. Kim, M.; Fetters, L.; Chen, W., and Shen, Y. *Macromolecules*, **1991**, *24*, 4216.
12. Iyengar, D. and McCarthy, T. *Macromolecules*, **1990**, *23*, 4344.
13. Carvalho, B.; Tong, P.; Huang, J.; Witten, T., and Fetters, L. *Macromolecules*, **1993**, *26*, 4632.
14. Napper, D., *Polymeric Stabilization of Colloidal Dispersions*. 1983, London: Academic Press. 428.
15. Vincent, B. *Adv. Colloid Interface Sci.*, **1974**, *4*, 193.
16. Yoo, D.; Shiratori, S., and Rubner, M. *Macromolecules*, **1998**, *31*, 4309.
17. Mittal, K., ed. *Adhesion Aspects of Polymeric Coatings*. 1983, Plenum Press: New York. 657.
18. Yang, X.; Shi, J.; Johnson, S., and Swanson, B. *Langmuir*, **1998**, *14*, 1505.

19. Kumakura, M.; Yoshida, M., and Asano, M. *J. Appl. Polym. Sci.*, **1990**, *41*, 177.
20. Freij-Larsson, C.; Jannasch, P., and Wesslen, B. *Biomaterials*, **2000**, *21*, 307.
21. Munch, M. and Gast, A. *Polym. Commun.*, **1989**, *30*, 324.
22. Singh, N.; Karim, A.; Bates, F.; Tirrell, M., and Furusawa, K. *Macromolecules*, **1994**, *27*, 2586.
23. Maoz, R. and Sagiv, J. *J. Colloid Int. Sci.*, **1984**, *100*, 465.
24. Wasserman, S.; Tao, Y., and Whitesides, G. *Langmuir*, **1989**, *5*, 1074.
25. Heid, S.; Effenberger, F.; Bierbaum, K., and Grunze, M. *Langmuir*, **1996**, *12*, 2118.
26. Mathauer, K. and Frank, C. *Langmuir*, **1993**, *9*, 3446.
27. Fadeev, A. and McCarthy, T. *Langmuir*, **1999**, *15*, 7238.
28. Henn, G.; Bucknall, D.; Stamm, M.; Vanhoorne, P., and Jérôme, R. *Macromolecules*, **1996**, *29*, 4305.
29. Ferreira, P.; Ajdari, A., and Leibler, L. *Macromolecules*, **1998**, *32*, 3994.
30. Leibler, L.; Ajdari, A.; Mourran, A.; Coulon, G., and Chatenay, D., in *Ordering in Macromolecular Systems*, A. Teramoto, M. Kobayashi, and T. Norisuje, Editors. 1994, Springer-Verlag: Berlin, Heidelberg. p. 353.
31. Shull, K. *Macromolecules*, **1996**, *29*, 2659.
32. Mounir, E.; Takahara, A., and Kajiyama, T. *Polymer Journal*, **1999**, *31*, 89.
33. Reiter, G.; Auroy, P., and Auvray, L. *Macromolecules*, **1996**, *29*, 2150.
34. Shull, K. *Faraday Discuss.*, **1994**, *98*, 203.
35. Maaloum, M. and Courvoisier, A. *Macromolecules*, **1999**, *32*, 4989.
36. Yamamoto, S.; Tsujii, Y., and Fukuda, T. *Macromolecules*, **2000**, *33*, 5995.
37. Ortiz, C. and Hadziioannou, G. *Macromolecules*, **1999**, *32*, 780.
38. Zhuravlev, L. *Langmuir*, **1986**, *3*, 316.
39. Iler, R., *The Chemistry of Silica*. 1979, New York: John Wiley & Sons.

40. Israelachvili, J. and Gee, M. *Langmuir*, **1989**, *5*, 288.
41. Fadeev, A. and McCarthy, T. *Langmuir*, **1999**, *15*, 3759.
42. Holmes-Farley, S.; Reamey, R.; McCarthy, T.; Deutch, J., and Whitesides, G. *Langmuir*, **1985**, *1*, 725.
43. Holmes-Farley, S.; Bain, C., and Whitesides, G. *Langmuir*, **1988**, *4*, 921.
44. McCafferty, E. and Wightman, J. *J. Colloid Int. Sci.*, **1997**, *194*, 344.
45. Bain, C. and Whitesides, G. *Langmuir*, **1988**, *5*, 1370.
46. Creager, S. and Clarke, J. *Langmuir*, **1994**, *10*, 3675.
47. Zhang, H.L.; Zhang, H.; Zhang, J.; Liu, Z., and Li, H. *J. Colloid Int. Sci.*, **1999**, *214*, 46.
48. Leyden, D.; Kendall, D., and Waddell, T. *Anal. Chim. Acta*, **1981**, *126*, 207.
49. Culler, S.; Ishida, H., and Koenig, J. *J. Colloid Int. Sci.*, **1985**, *106*, 334.
50. Mingalyov, P.; Fadeev, A.; Staroverov, S.; Lisichkin, G., and Lunina, E. *J. Chromatogr.*, **1993**, *646*, 267.
51. Vitt, E. and Shull, K. *Macromolecules*, **1995**, *28*, 6349.

CHAPTER 3

PROTEIN ADSORPTION TO SILANE-MODIFIED SURFACES

3.1. Introduction

There has been a concerted effort to understand the complex interactions between proteins and surfaces.^{1,2} When a biomedical device is implanted in the body, the first and probably most significant reaction that occurs at the interface of the device is protein adsorption. This newly adsorbed protein layer, not the surface of the original biomaterial, will then dictate the ensuing cascade of biological reactions, such as platelet adhesion, blood coagulation and thrombus formation. Interestingly, surfaces with a pre-adsorbed layer of albumin have been shown to inhibit thrombus formation,^{3,4} thus decreasing the chance that the body will reject the surface when implanted. Therefore, many studies on protein adsorption have focused on understanding the adsorption behavior of albumin (either human or bovine serum albumin). Serum albumin is a single polypeptide chain with a molecular weight of approximately 66,000 D, and is highly soluble in water. It has a diffusion coefficient of 6×10^{-7} cm²/sec and has an isoelectric point of 4.9, so at physiological conditions (pH – 7.4) it carries a net negative charge. The exact structure of albumin is still debatable. Original evidence showed that it could be modeled as a rotational ellipsoid having dimensions of 14 x 4 x 4 nm³.² More recent studies have proposed that the structure of albumin is more heart-shaped, having a maximum width of 8 nm and a depth of 3 nm.^{5,6} Ribbon diagrams of the two most accepted structures for

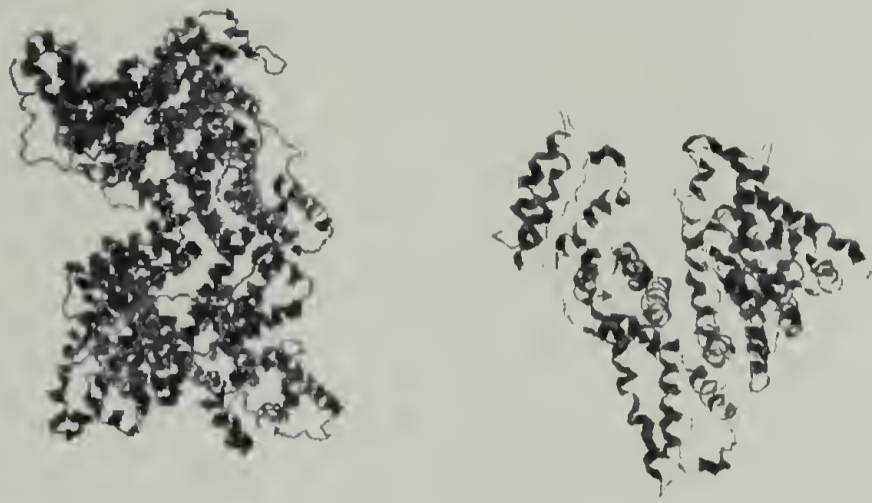


Figure 3.1. Two proposed ribbon diagrams for albumin: rotational ellipsoid or heart-shaped.

albumin are shown in Figure 3.1. Serum albumin plays a large role in the maintenance of osmotic pressure in the blood and also serves to transport free fatty acids.

Because of albumin's high binding affinity for fatty acids, surfaces possessing long alkyl chains have been the focus of a flurry of recent studies.⁷⁻¹⁶ Most of these studies have focused on using trichlorosilane self-assembled monolayers (SAMs) as model surfaces to systematically investigate certain effects such as surface hydrophobicity/hydrophilicity on the adsorption behavior of albumin. In general, it has been shown that albumin adsorbs in greater amounts to hydrophobic surfaces such as long-chain alkyl or fluoroalkyl SAMs. The adsorption of protein to hydrophobic surfaces serves to attenuate the unfavorable interactions between the aqueous liquid phase and the hydrophobic surface. However, there are several limitations in using SAMs to probe the effects of surface chemistry on protein adsorption. In order to form these highly ordered SAMs, one must exercise judicious choice of reaction conditions,¹⁷⁻¹⁹ and even minor deviations from these protocols can have dramatic effects on the quality of SAMs. This in turn can have a tremendous impact on the adsorption behavior of proteins to these

surfaces, as was shown recently by Foster et al.⁹ Also, the range of functional groups that can be incorporated into SAMs is limited due to the requirement that the chains pack into a dense, close-packed layer.

In contrast, recent work by Fadeev et al.^{20,21} has shown that monochlorosilane (Cl-SiR₃) monolayers are equally as robust and versatile as SAMs. The reaction of monochlorosilanes with silicon oxide results in well-defined monolayers where every organosilane must be covalently attached to the surface. This class of surfaces has been termed covalently attached monolayers (CAMs). It has been shown that the packing density of CAMs on a surface is slightly lower than SAMs due to the larger cross-sectional area of simple alkyldimethylsilane CAMs (~32-38 Å²) in comparison to alkyltrichlorosilane SAMs (~20 Å²). Yet, a multitude of functional groups can be incorporated into these monolayers, and molecularly mixed monolayers can be prepared using this method,^{21,22} making them an attractive alternative to SAMs for studying the effects of surface chemistry on protein adsorption. We report here a detailed study of the adsorption behavior of a single protein, albumin, to covalently attached monolayers (CAMs) to better elucidate the response of the protein to the surface chemistry presented at the solid/liquid interface. Further, the morphology of the adsorbed protein layer will be examined by AFM and correlated to the chemical and physical properties of the surface.

3.2. Experimental

3.2.1. Materials

All chemicals were used as received unless noted otherwise. Toluene (HPLC), toluene (anhydrous), ethanol (anhydrous), sulfuric acid, sodium dichromate, and hydrogen peroxide (30%) were purchased from Fisher. Ethyldiisopropylamine, bovine serum albumin (fatty acid free), phosphate buffer saline tablets, hexadecane (anhydrous), borane (1M in THF), polyethylene glycol ($M_w \sim 400$ g/mol), and potassium hydroxide were purchased from Aldrich. PEG was dried by distillation of benzene from a PEG/benzene solution just prior to use. All silane reagents were purchased from Gelest and used without further purification. House-purified water (reverse osmosis) was used in substrate preparation and cleaning. For adsorption studies, the RO water was further purified using a Millipore Milli-Q system and had a final resistivity of 10^{18} Ω/cm .

3.2.2. Pretreatment of Silicon Substrates

Silicon wafers (4") were obtained from International Wafer Service (100 orientation, P/B doped, resistivity of 20-40 Ω/cm) and were cut into 1.5 x 1.5 cm pieces to facilitate handling and XPS measurements. The samples were placed in a custom-designed holder and placed into a modified Schlenk tube. The samples were then submerged in a freshly prepared solution of $\text{H}_2\text{SO}_4/\text{Na}_2\text{Cr}_2\text{O}_7/\text{H}_2\text{O}_2$. The sodium dichromate (~5 wt %) was first dissolved in stirring concentrated sulfuric acid (30 mL). Hydrogen peroxide (15 mL) was then poured directly into the Schenk tube containing the wafers to be cleaned, and the $\text{H}_2\text{SO}_4/\text{Na}_2\text{Cr}_2\text{O}_7$ solution was poured directly on top of the

peroxide/wafers. The solution turns from red-brown to green upon mixing, warms up considerably, and bubbles profusely due to the formation of ozone and oxygen. The samples were left submerged overnight for convenience. The wafers were rinsed with copious amounts of water to remove all traces of the cleaning solution, and were dried in a clean oven at 130 °C for 90 min.

3.2.3. Preparation of Substrates via Solution Reaction

Silicon wafers were cleaned and dried as described above. The wafers were immediately placed into the reaction flasks and purged with N₂ for 30 minutes. Dry toluene (~20 mL) was then cannulated into the reaction tube and ethyldiisopropylamine (0.3 mL) was added via syringe as a promoter, followed by the organosilane (0.5 mL) of choice. The experimental setup is illustrated in Figure 3.2. The reaction was carried out at 23 ± 1 °C for 3 days. After silanization, the wafers were rinsed in the following order: 2 x 10 mL toluene, 3 x 10 mL ethanol, 2 x 10 mL ethanol/water mixture (1:1), 2 x 10 mL water, 2 x 10 mL ethanol, 2 x 10 mL water and then dried under vacuum overnight. The samples were then placed into scintillation vials for storage until characterization or further use. Reactions involving aminosilanes were carried out as described above with the exception that no amine promoter was added to the reaction (self-promoted). As a control, C₁₈ self-assembled monolayers were prepared as described elsewhere.²³ C₁₈ CAMs were Soxhlet extracted with hexanes for 24 h to remove any silanes unbound to the surface. Trivinylsilyl surfaces were oxidized to the triol using BH₃/H₂O₂/KOH as described elsewhere.²⁴ Mercaptopropyltriethoxysilane was oxidized to the sulfonate

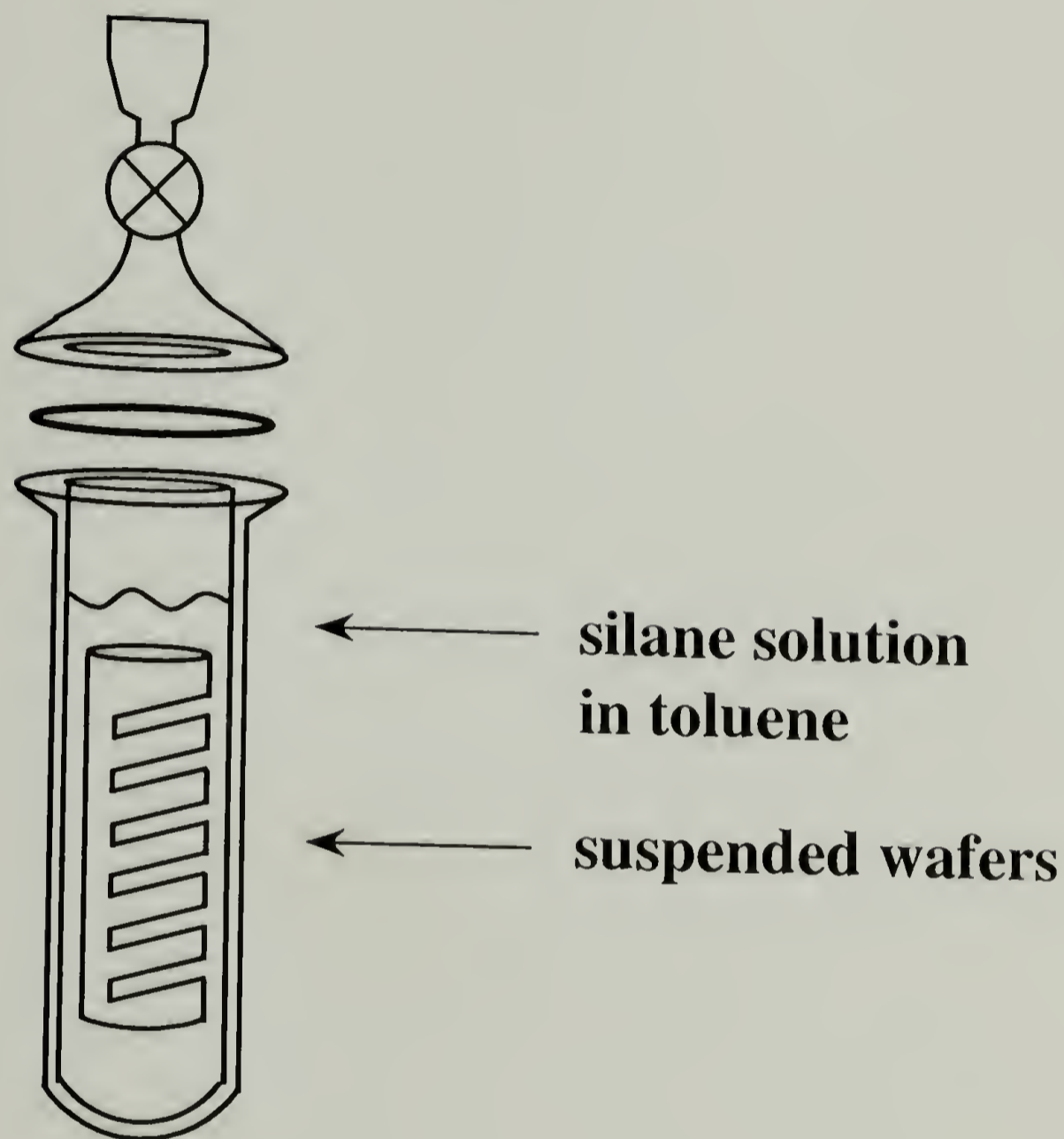


Figure 3.2. Schematic of the Schlenk tube used for solution reactions that included a 4mm Teflon joint capped with a rubber septum to facilitate cannulation and additions via syringe under an inert atmosphere.

in H₂O₂/HOAc at room temperature for 30 min. PEG surfaces were prepared by subsequent reaction of isocyanatopropyldimethylsilyl surfaces with neat PEG (dry) at 70 °C for 4 days. XPS data indicate that the ~ 50% of the isocyanate groups on the surface had reacted with PEG. Mixed monolayers were prepared using the reaction of tris(trimethylsiloxy)chlorosilane (Tris(TMS)) in the vapor phase for varying amounts of time, then subsequent reaction of the (sub)monolayers of Tris(TMS) with a second silane.^{21,22}

3.2.4. Adsorption of Proteins to Silane-modified Surfaces

Phosphate buffered saline (PBS) solutions were prepared by dissolving one PBS tablet in 200 mL of deionized water. This results in a stock solution containing 0.01M phosphate buffer, 0.0027M potassium chloride, and 0.137M sodium chloride and having a pH of 7.4 at 25 °C. Silane-modified wafers were placed in a custom-made wafer holder and suspended in a reaction tube. The wafers were submerged in PBS solution overnight to equilibrate the surfaces. Just prior to the adsorption experiment, a fresh BSA solution was prepared by dissolving 10 mg of BSA in 10 mL of PBS solution, resulting in a concentration of 1 mg/mL. The old PBS solution was then cannulated out of the reaction tube and 18 mL of fresh PBS solution was added via syringe followed by 2 mL of BSA solution (1 mg/mL). The final concentration of BSA was 0.1 mg/mL. This procedure was developed to prevent exposure of the wafers to the protein-air-water interface, which could lead to protein adsorption via a Langmuir-Blodgett deposition. The reaction tube was placed in a circulator bath maintained at 37 ± 0.1 °C for 1 h. After adsorption, the protein solution was removed by dilution with fresh PBS solution five times. Again, this

was chosen to prevent exposure of the wafers to the protein-air-water interface. After sufficient dilution, the samples were removed from the reaction tube and gently rinsed with deionized water to remove any physisorbed salts on the surface. The samples were placed in a dessicator for at least 1 day to dry the samples, and were then characterized by ellipsometry, contact angle, AFM, and XPS.

3.2.5. Characterization

Contact angle measurements were made with a Ramé-Hart telescopic goniometer equipped with a Gilmont syringe and a 24-gauge flat-tipped needle. Probe fluids used were water and *n*-hexadecane. Advancing (θ_A) and receding (θ_R) contact angles were recorded while the probe fluid was added to and withdrawn from the drop, respectively. X-ray photoelectron spectra (XPS) were obtained on a Perkin-Elmer Physical Electronics 5100 with Mg K_α excitation (400W). Spectra were taken at two take-off angles, 15° and 75° (between the plane of the surface and the entrance lens of the detector optics). Film thickness was measured using a Rudolph Research ellipsometer equipped with a helium-neon laser ($\lambda = 6328 \text{ \AA}$) at an incidence angle of 70° . AFM images were obtained using a Digital Instruments DimensionTM 3100 Scanning Probe Microscope operated in tapping mode.

3.3. Results and Discussion

3.3.1. Substrate Characterization

Covalently attached monolayers (CAMs) were prepared by the solution reaction of monochlorosilanes at room temperature. The reaction of monochlorosilanes in the vapor phase has been shown to yield the highest bonding densities,²⁰ but the low vapor pressure of the higher molecular weight silanes prevented the use of vapor phase reaction here. An amine promoter (EDIPA) was added to the reaction mixture in order to increase the reaction yield and obtain higher bonding densities. The amine promoter also serves to scavenge the by-product of the reaction of chlorosilanes with silica (HCl). Reactions were carried out for 3 days to achieve maximum bonding density, unless otherwise noted. Two types of surfaces were prepared for this study: one-component (pure) and two-component (mixed) surfaces.

One-component (pure) surfaces were comprised of a single organosilane reacted under conditions that lead to maximum bonding density with the substrate. A few of the surfaces were prepared by subsequent reactions of monolayers (i.e. TVS-OH, PEG), while others were prepared from dichloro- and trichlorosilanes to further complete the study. The surfaces were characterized by contact angle, ellipsometry, and XPS. Contact angle and thickness data for these one-component surfaces are listed in Table 3.1, along with the structure and abbreviation of each silane. For convenience, the surfaces are listed in order of decreasing advancing contact angle. The thickness data for both the DMDC and MPTES reactions indicate that these surfaces are not monolayers but rather oligomeric. DMDC surfaces were prepared by vapor phase reaction; monolayers of

DMDC have been prepared by solution phase reaction,²⁵ and the reported thickness of these surfaces was 3.5 Å. MPTES was used since a monofunctional silane having a thiol end group was not commercially available, and we wanted to probe the specific interaction of albumin with -SH groups.

Two-component (mixed) surfaces were achieved by the step-wise reaction of Tris(TMS) in the vapor phase for increasing amounts of time, followed by subsequent reaction of the surface with a second silane. The vapor phase reaction of Tris(TMS) is a random process and the surface has been shown to contain 'nanopores' due to the inefficient packing ability of the bulky Tris(TMS) molecules.^{21,22} This allows for subsequent reaction of a second silane to form mixed monolayers. The second silanes were chosen such that mixed hydrophobic/hydrophilic surfaces were created. Four different Tris(TMS) surfaces were prepared by judicious choice of reaction times in order to prepare surfaces with sufficient differences in surface coverage. The reaction of the second silane was carried out in the solution phase for 3 days to ensure complete reaction of all remaining silanols on the surface. The surfaces were characterized by contact angle, ellipsometry, and XPS. Contact angle and thickness data for these two-component surfaces are listed in Table 3.2, along with the identity of the second silane used for the subsequent reaction of the Tris(TMS) (sub)monolayers.

XPS spectra were obtained to further characterize all of the monolayers prepared for this study, and were used as a qualitative method to ensure the surface composition was correct. The XPS atomic concentration data (75° take-off) is tabulated in Appendix C for reference.

Table 3.1. Contact angle and thickness data for one-component (pure) surfaces.

surface (abbreviation)	silane	θ_A/θ_R ($^\circ$)		thickness \AA
		H ₂ O	C ₁₆ H ₃₄	
C ₆ F ₁₃	C ₆ F ₁₃ (CH ₂) ₂ Si(CH ₃) ₂ -Cl	117/100	62/47	8
OTS SAM	C ₁₈ H ₃₇ Si-Cl ₃	113/103	37/36	32
OTS CAM	C ₁₈ H ₃₇ Si(CH ₃) ₂ -Cl	108/95	33/30	15
DMDC	(CH ₃) ₂ Si-Cl ₂	99/92	36/32	11 ^a
Tris(TMS)	(CH ₃ SiO) ₃ Si-Cl	99/88	35/32	7
TMS	(CH ₃) ₃ Si-Cl	98/89	33/32	5
CF ₃	CF ₃ (CH ₂) ₂ Si(CH ₃) ₂ -Cl	97/91	42/38	6
Carbomethoxy	CH ₃ O(O)C(CH ₂) ₁₀ Si(CH ₃) ₂ -Cl	87/78	15/0	8
MPTES	SH(CH ₂) ₃ Si-Cl ₃	84/52	14/0	32 ^a
MPTES-SO ₃ H	SH(CH ₂) ₃ Si-Cl ₃ / oxidation	62/21	15/0	32 ^a
TPS	(Ph) ₃ Si-Cl	80/56	10/0	11
Acetoxy	CH ₃ C(O)O(CH ₂) ₂ Si(CH ₃) ₂ -Cl	77/67	14/0	5
APS	NH ₂ (CH ₂) ₃ Si(CH ₃) ₂ -Cl	72/45	10/0	10
PEG	OCN(CH ₂) ₃ -Si(CH ₃) ₂ -Cl / PEG	49/40	13/0	13
TVS-OH	(CH ₂ =CH ₂) ₃ Si-Cl / hydroboration	48/30	9/0	8
Si-OH	clean silicon oxide	5/0	0/0	0

^a thickness data indicate that these surfaces are oligomeric layers, not monolayers.

Table 3.2. Contact angle and thickness data for two-component (mixed) surfaces.

surface (abbreviation)	second silane	θ_A/θ_R (°)		thickness Å
		H ₂ O	C ₁₆ H ₃₄	
Tris(TMS) 1h	-	65/55	26/16	5
Tris(TMS) 24h	-	78/67	30/20	6
Tris(TMS) 72h	-	92/80	35/29	6
Tris(TMS) 140h	-	99/88	35/32	7
Tris(TMS) 1h	TMS	101/95	34/30	6
Tris(TMS) 24h	TMS	100/95	34/28	7
Tris(TMS) 72h	TMS	102/95	32/28	7
Tris(TMS) 140h	TMS	106/98	30/27	8
Tris(TMS) 1h	APS	70/52	15/0	9
Tris(TMS) 24h	APS	74/57	14/6	11
Tris(TMS) 72h	APS	80/61	20/15	10
Tris(TMS) 140h	APS	91/74	29/22	10
Tris(TMS) 1h	TVS-OH	67/56	18/13	9
Tris(TMS) 24h	TVS-OH	72/59	20/14	11
Tris(TMS) 72h	TVS-OH	79/64	21/14	9
Tris(TMS) 140h	TVS-OH	93/78	22/15	10

3.3.2. Protein Adsorption Protocol

To elucidate the effects of surface chemistry on protein adsorption, the protocol for protein adsorption was kept constant in this study. Others have studied a single surface (i.e. C₁₆ SAMs) while varying other experimental conditions such as concentration, shear rate, adsorption time, temperature, pH and ionic strength of the aqueous solution. Here, a single concentration of protein solution was used (0.1 mg/mL) while the temperature (37 °C) was chosen to mimic physiological conditions. At a concentration of 0.1 mg/mL, the adsorption behavior of albumin should be diffusion-limited, resulting in slow arrival of protein to the interface. Previous studies^{7,26,27} have shown that adsorption of albumin saturates after 30 min as followed by total internal reflectance fluorescence (TIRF). Therefore, the time of adsorption was kept constant at 1 h, ensuring that the adsorption was complete. After adsorption, the samples were rinsed with fresh PBS solution and dried. Since the samples were rinsed with PBS solution after adsorption, only the irreversibly adsorbed proteins could be observed in any of the measurements.

All measurements of the adsorbed protein layers were conducted after drying. It is understood that exposure of the protein layers to air can influence almost all measurements, but it is presumed that any process that could occur (i.e. denaturing) is limited and subtle on the length scales being measured. The primary tool for determining the amount of adsorbed protein on each surface was ellipsometry. The biggest disadvantage of using ellipsometry for protein adsorption is that it is highly dependent on the model used in the analysis. It is understood that ellipsometry yields an average layer thickness over the sampling area (beam size), and error is introduced into the

measurement when the layer is not uniform. As will be seen in the following section, AFM analysis of the surfaces indicates that some of the protein layers are, in fact, not continuous. Therefore the adsorbance (Γ) calculated from ellipsometry can only be a relative measure of actual amount of protein on the surface. Using a method proposed by Stenberg and Nygren,²⁸ the adsorbance (Γ) of a partially dried protein layer could be calculated using the following equation:

$$\Gamma \text{ (ng mm}^{-2}\text{)} \approx K \text{ (g ml}^{-1}\text{)} \cdot d \text{ (nm)} \quad (1)$$

where $K \approx 1.2 \text{ g ml}^{-1}$ is the density of the protein in air, and d is the thickness of the adsorbed layer in nanometers. The refractive index for BSA has been reported to be $n_{\text{BSA}} = 1.542$.²⁹ This method is reviewed by Tengvall et al.³⁰ and is the method of choice for this study.

XPS spectra of the surfaces after protein adsorption were obtained as verification of atomic composition of the adsorbed layers. The appearance of nitrogen in the XPS spectra corroborates the presence of the protein on the surface. Unfortunately, the attenuation of the Si^0 peak cannot be used as a secondary technique for determination of the adsorbed thickness due to the aforementioned non-uniformity of some of the adsorbed protein layers. Therefore, XPS was used only as a qualitative validation of trends seen in the adsorption behavior of albumin. The XPS atomic concentration data (75° take-off) is tabulated in Appendix C for reference.

3.3.3. Protein Adsorption to Silane-modified Surfaces

Protein adsorption was carried out on each of the surfaces prepared as described in the previous section. The thickness of the adsorbed protein layer was determined by ellipsometry, and the total adsorbed amount of protein for each surface was calculated using equation (1). The results of the adsorption experiments on one-component (pure) surfaces and two-component (mixed) surfaces are listed in Tables 3.3 and 3.4, respectively. The observed results of a few surfaces are worth noting. First, a measurable amount of albumin adsorbed to clean silicon oxide ($\Gamma = 0.48 \text{ ng mm}^{-2}$). At first glance, it is unclear whether or not the layer being measured is actually albumin, since silicon oxide is a high-energy surface and will adsorb contaminants quickly in air. However, the presence of nitrogen in the XPS strongly suggests the adsorbed layer is comprised of albumin. One would expect that a hydrophilic surface such as silicon oxide would inhibit the adsorption of albumin due to a large fraction of bound water on the surface, coupled with the fact that silicon oxide has a net negative charge at neutral pH. Recall that albumin carries a net negative charge at neutral pH and thus should be repelled by a negatively charged surface. This ionic repulsion is seen more clearly in the MPTES-SO₃H surface ($\Gamma = 0.24 \text{ ng mm}^{-2}$), which at neutral pH also carries a net negative charge. The PEG₄₀₀ surface showed strong resistance to albumin adsorption as well. It is well known that PEG surfaces inhibit protein adsorption^{31,32} due to its fluidity and high degree of hydration. Interestingly, the thickness of the PEG layer is quite low, yet still inhibits the adsorption of albumin.

Whitesides et al.³³ has also calculated the theoretical adsorbance (Γ) for BSA for a complete monolayer of protein. This calculation assumes that albumin has average

Table 3.3. Contact angle and adsorbance data for one-component (pure) surfaces after BSA adsorption.

surface (abbreviation)	before adsorption		after adsorption	
	θ_A/θ_R ($^\circ$)	θ_A/θ_R ($^\circ$)	thickness	adsorbance
	H ₂ O	H ₂ O	Å	(ng mm ⁻²)
C ₆ F ₁₃	117/100	96/31	22	2.64
OTS SAM	113/103	80/18	20	2.40
OTS CAM	108/95	94/18	23	2.76
DMDC	99/92	89/24	29	3.48
Tris(TMS)	99/88	80/18	25	3.00
TMS	98/89	70/11	23	2.76
CF ₃	97/91	85/22	30	3.60
Carbomethoxy	87/78	77/20	27	3.24
MPTES	84/52	65/17	21	2.52
MPTES-SO ₃ H	62/21	52/17	2	0.24
TPS	80/56	70/11	11	1.32
Acetoxy	77/67	78/12	17	2.04
APS	72/45	68/16	17	2.04
PEG	49/40	49/38	0	0.00
TVS-OH	48/30	76/15	7	0.84
Si-OH	5/0	31/10	4	0.48

Table 3.4. Contact angle and adsorbance data for two-component (mixed) surfaces after BSA adsorption.

surface (abbreviation)	before adsorption		after adsorption	
	θ_A/θ_R ($^\circ$)	θ_A/θ_R ($^\circ$)	thickness	adsorbance
	H ₂ O	H ₂ O	Å	(ng mm ⁻²)
Tris(TMS) 1h	65/55	75/19	11	1.32
Tris(TMS) 24h	78/67	77/27	12	1.44
Tris(TMS) 72h	92/80	73/17	16	1.92
Tris(TMS) 140h	99/88	80/18	25	3.00
Tris(TMS) 1h / TMS	101/95	87/21	22	2.64
Tris(TMS) 24h / TMS	100/95	80/18	20	2.40
Tris(TMS) 72h / TMS	102/95	91/28	24	2.88
Tris(TMS) 140h / TMS	106/98	92/29	26	3.12
Tris(TMS) 1h / APS	70/52	73/20	10	1.20
Tris(TMS) 24h / APS	74/57	74/24	13	1.56
Tris(TMS) 72h / APS	80/61	71/19	14	1.68
Tris(TMS) 140h / APS	91/74	70/18	16	1.92
Tris(TMS) 1h / TVS-OH	67/56	71/20	11	1.32
Tris(TMS) 24h / TVS-OH	72/59	74/21	15	1.80
Tris(TMS) 72h / TVS-OH	79/64	76/15	18	2.16
Tris(TMS) 140h / TVS-OH	93/78	80/19	21	2.52

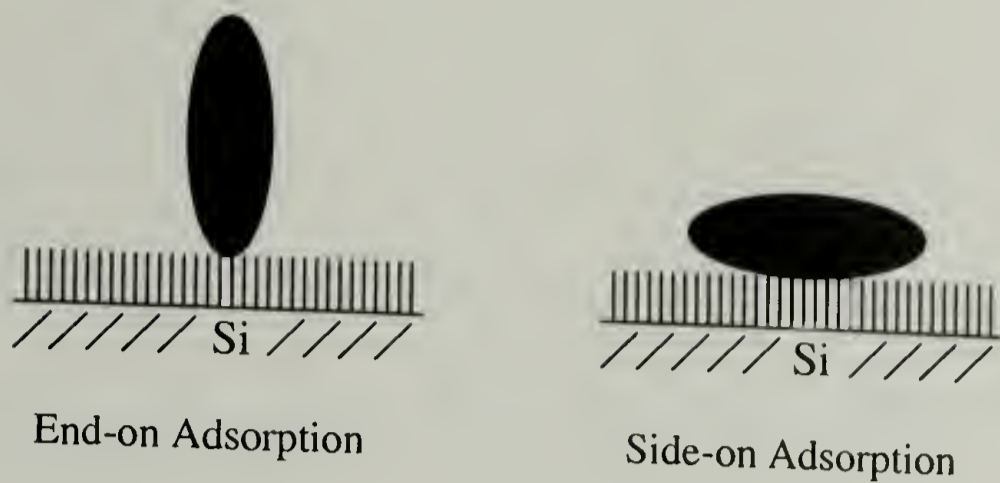


Figure 3.3. Schematic illustrating the two possible modes of adsorption for albumin: end-on (long axis perpendicular to the surface) and side-on (long-axis parallel to the surface) conformations.

dimensions of $14 \times 4 \times 4 \text{ nm}^3$. If the protein adsorbs to the surface in an end-on orientation (long axis being perpendicular to the surface), the maximum adsorbance should be $\Gamma = 6.00 \text{ ng mm}^{-2}$. The maximum adsorbance for side-on adsorption (long axis being parallel to the surface) should be $\Gamma = 2.50 \text{ ng mm}^{-2}$. Therefore if a surface shows an adsorbance greater than 2.50 ng mm^{-2} , it can be concluded that a fraction of the protein (if not all) has adsorbed in an end-on conformation. Conversely, one cannot assume that if the adsorbed amount is less than 2.50 ng mm^{-2} the protein has adsorbed exclusively in the side-on conformation. Instead, the adsorbed state could be a combination of end-on and side-on adsorption, and the adsorbed amount measured could then be a simple average of the two states. Inspection of the values listed in Table 3.3 shows that for many surfaces the adsorbance (Γ) is greater than the limiting value of 2.50 ng mm^{-2} for side-on adsorption, indicating that those layers could be comprised of either entirely end-on adsorbed proteins or a combination of end-on and side-on adsorption. Those surfaces having an adsorbance below 2.50 ng mm^{-2} could be adsorbed in the side-

on conformation, but other techniques such as AFM must be employed to differentiate between the two modes of adsorption.

The adsorption data can be analyzed by correlating the amount of protein adsorbed to the surface energy of each sample prepared. The cosine of the contact angle is related to the surface energy of a substrate by Young's equation:³⁴

$$\cos\theta_E = (\gamma_{SV} - \gamma_{LS}) / \gamma_{LV} \quad (2)$$

where θ_E is the equilibrium contact angle, and γ_{SV} , γ_{LS} , and γ_{LV} are the surface tensions between the solid/vapor, liquid/solid, and liquid/vapor phases, respectively. Shown in Figure 3.4 is a master plot of adsorbance (Γ) versus the cosine of the advancing water contact angle ($\cos\theta_A$) for both the one-component (pure) surfaces and the two-component (mixed) surfaces prepared in this study. The PEG and MPTES-SO₃H surfaces, which were noted above to inhibit protein adsorption by mechanisms different from simple hydrophobic/hydrophilic interactions, are not included in this plot. The data in Figure 3.4 clearly show that there is a strong dependence of adsorption of albumin on hydrophobicity/hydrophilicity (as measured by contact angle) for CAMs, and the dependence is nearly linear with increasing hydrophobicity of the substrate. Again, the amount of adsorbed protein is measured *postmortem*, so only the irreversibly adsorbed protein can be observed, while the loosely adsorbed proteins are rinsed away. Other methods (i.e. TIRF, surface plasmon resonance), that can detect protein adsorption *in situ*, measure the total surface excess of protein at the interface and thus will be able to detect those proteins that are loosely bound to the surface. In general, though, the

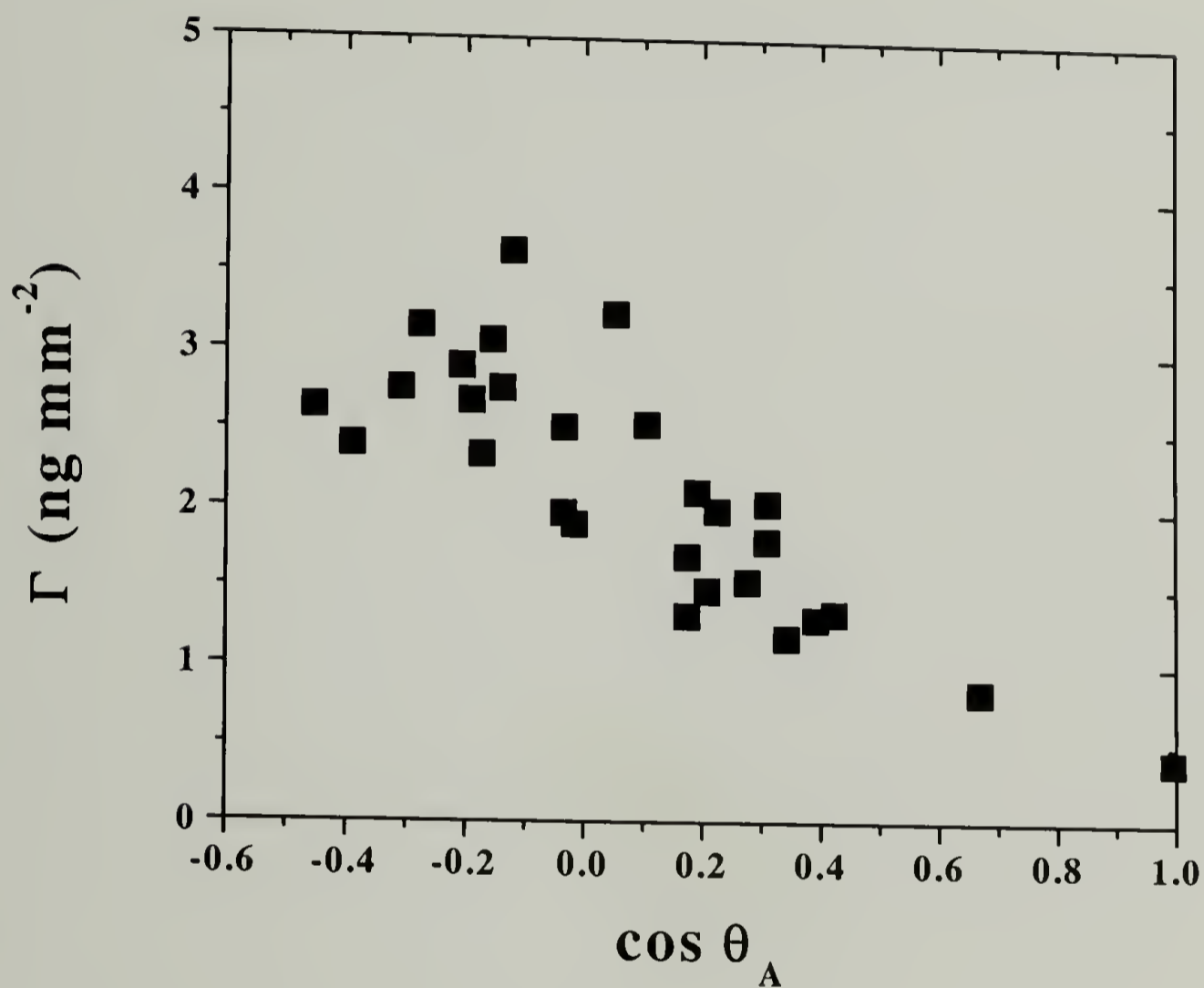


Figure 3.4. Master plot of adsorbance (Γ) as a function of surface energy ($\cos \theta_A$) for all surfaces studied, showing a linear increase of adsorbance with increasing hydrophobicity of the surface.

Table 3.5. BSA adsorbance (Γ) data for various surfaces reported in literature for comparison to the values reported in this study.

surface	Γ (ng mm ⁻²)
C ₁₁ SAM ³³	2.10
C ₁₆ SAM ¹⁰	2.10
C ₁₆ SAM ²⁷	2.40
C ₁₈ CAM ⁷	2.49
Polyethylene ³⁵	2.60
C ₁₈ SAM	2.40
C ₁₈ CAM	2.76

adsorbance measured via ellipsometry agrees closely to literature data for alkyl SAMs and CAMs (see Table 3.5), confirming that ellipsometry is an acceptable to measure adsorbed protein layer thickness.

3.3.4. AFM Studies of Adsorbed Protein Morphology

Atomic force microscopy (AFM) was undertaken to gain a detailed physical understanding of the morphology of the adsorbed protein layers. In the previous section, the surface chemistry of the substrate was shown to play a vital role in controlling the amount of protein adsorbed to each surface, so it is anticipated that the morphology of the adsorbed layers may also show a strong dependence on the chemistry of the surface. Shown in Figures 3.5 – 3.17 are the AFM images for the one-component (pure) surfaces after protein adsorption. Recall that these measurements are made after the samples were removed from the adsorption medium and dried. The images in Figures 3.11 – 3.17 show uniform surface coverage of albumin, and therefore leave little to be discussed about them at the moment. The most interesting images are of the highly hydrophobic surfaces (Figures 3.5 – 3.10). Recall from Table 3.3 that these surfaces exhibit the highest adsorbance (Γ) of all the surfaces studied. Strikingly, the surfaces exhibit vastly different morphologies as seen in the AFM images. Previous studies^{8,10,15} have observed similar structures as those seen in Figure 3.8 for albumin adsorption on SAMs, but the authors neglect to comment on the origins of the observed morphology.

To better understand the origins of the observed patterns, let us focus first on the morphologies of the C₁₈ CAM and TMS surfaces (see Figures 3.5 and 3.9). The amount of protein adsorbed to each of these surfaces are identical ($\Gamma = 2.76 \text{ ng mm}^{-2}$), yet the

morphology of the adsorbed protein layer is quite different. The C₁₈ CAM surface exhibits non-uniform coverage and a highly branched, finger-like pattern, while the protein adsorbed to the TMS surface is fairly uniform with a few holes. AFM section analyses for the C₁₈ CAM and TMS surfaces are shown in Figures 3.18 and 3.19, respectively. Interestingly, the AFM section analysis on the C₁₈ surface indicates that the observed morphology has an average height of 8.1 nm, suggesting that the protein has adsorbed predominantly in the end-on orientation. For the TMS surface, the average height was found to be 4.6 nm, which corresponds to a majority of protein being adsorbed in the side-on orientation with some in the end-on state. One explanation for the observed behavior can be detailed as follows. It has been speculated that albumin initially adsorbs in the end-on conformation due to the high density of hydrophobic groups located on the 'tip' of the molecule. If necessary, the molecule can then 'roll over' to the side-on adsorbed state to increase the number on contact points with the surface and help anchor the protein to the surface. This can be accompanied by slight denaturing of the albumin's secondary structure to expose more hydrophobic groups to the underlying surface. This interfacial reorientation has been targeted as one means by which albumin can increase its molecular footprint on a surface,¹¹ thus increasing the tenacity of adsorption.

It is argued here that reorientation of albumin occurs predominantly on rigid hydrophobic surfaces (i.e. TMS, CF₃) that present only a limited number of contact points to the protein in the end-on orientation (see Figure 3.20). This forces the protein to roll over in order to maintain adequate interaction with the surface, such that the protein becomes irreversibly adsorbed. For surfaces that are not rigid (i.e. C₁₈ CAM, C₆F₁₃), the

protein can penetrate the monolayer in the end-on orientation and increase the total number of hydrophobic/hydrophobic contact points. This should stabilize the adsorbed protein such that it does not need to roll over to the side-on orientation in order to resist desorption. Due to the high affinity of albumin for binding and transporting fatty acids, it has been speculated that some portions of the monolayer could even become intercalated within the protein structure.¹⁰ The transition from flexible, soft surfaces to rigid surfaces can be observed by following the changes in morphology from Figure 3.5 through Figure 3.10. The morphology shifts from a very open, fractal structure to a more closed, uniform structure as the rigidity of the underlying surface increases. This argues that the rigidity of the underlying surface is playing a critical role in directing the adsorption of albumin to hydrophobic surfaces. The most noticeable significance is that the rigidity of the surface dictates the need for the protein to reassemble from the end-on adsorbed state to the side-on adsorbed state in order to increase protein-surface interactions.

Let us now focus on the observed structures for the C_{18} CAM and C_6F_{13} surfaces (Figures 3.5 and 3.6), and contemplate the origins of this very open, fractal structure. Recall that the adsorption protocol was chosen such that the adsorption is conducted under static conditions (not under shear) and at low concentrations, both of which result in slow arrival of protein to the interface (diffusion-limited adsorption). Therefore, the albumin molecules are relying on simple diffusion to approach and adsorb to the surface. From the AFM section analysis shown in Figure 3.18, it is clear that the protein has adsorbed in an end-on conformation. Moreover, the adsorbed proteins are ordered into a fractal-like structure on the surface, which closely resembles patterns observed in diffusion-limited aggregation (DLA) of particles. DLA is one of the simplest models for

fractal growth, and results in a very open structure containing a high degree of branching (dendritic). In this model, the surface originally contains a single 'seed' particle, which is immobilized on the surface. A second particle is introduced and is allowed to randomly diffuse (random walk) on the surface until it comes into contact with the seed particle, at which time the second particle becomes irreversibly immobilized and becomes part of the aggregate. If this cycle is repeated numerous times, the aggregate structure will be highly branched and fractal in nature. A fractal structure develops because the faster growing branches 'shield' the penetration of particles from diffusing into the internal parts of the aggregate. The fractal dimension for DLA has been shown to be $D_f \sim 1.75$, which relates the number of particles n within a cluster of size r by the following equation: $n = r^{D_f}$. To assess whether this could explain what was observed in these experiments, a Fourier transform was performed on the AFM image of BSA adsorbed to the C₁₈ CAM. Curve fitting these data on a log-log plot yields a slope (D_f) ~ 1.64 , indicating that the protein is adsorbing in a fashion similar to that seen for DLA of particles.

The data suggest the following scenario. The protein approaches the surface in an end-on orientation, followed by weak adsorption to the surface through van der Waals interactions. These interactions are apparently insufficient to irreversibly adsorb the albumin molecule to that surface. If the surface is rigid, the albumin molecule must roll over to the side-on orientation and possibly denature to a limited extent in order to increase its footprint area and number of contact points with the surface. As other protein molecules adsorb, the previously adsorbed protein gains protein-protein interactions in addition to the already formed protein-surface interaction. Collectively, these adsorbed protein molecules form a continuous layer on the surface, as shown by AFM. If, on the

other hand, the surface is soft, the albumin molecule has sufficient interaction with the surface to keep it temporarily bound in the end-on state, but the protein retains lateral mobility/diffusion such that it can add to the growing aggregate structure observed by AFM. The phrase 'temporarily bound' is used here because there is no indication that single albumin molecules exist on the surface outside the aggregate structure, suggesting that those molecules not attached to the aggregate structure are reversibly adsorbed to the surface and can be rinsed away. This scenario argues that protein-surface interaction itself is not sufficient to irreversibly adsorb albumin to a hydrophobic surface, but rather a complex combination of protein-protein and protein-surface interactions are necessary to render the protein resistant to desorption. More experiments need to be conducted to further strengthen this scenario.

AFM images for a few of the two-component (mixed) surfaces are shown in Figures 3.21 – 3.26. Let us focus first on the surfaces where albumin was adsorbed to the original Tris(TMS) surfaces prior to being reacted with a second silane (Tris(TMS)/silanol). At the lowest coverage of Tris(TMS) (Figure 3.21), the morphology of the adsorbed layer is very uniform with minimal amount of texture in the image. It could be argued that the texture seen in the height image is a result of albumin's inability to adsorb in the areas containing a high concentration of silanol groups (hydrophilic), thus limiting adsorption to the most hydrophobic areas. As the coverage of Tris(TMS) increases, the adsorbed layer becomes more non-uniform with areas (holes) on surface remaining uncovered, with the size of the patches increasing with increasing Tris(TMS) coverage. This transition can be rationalized to occur in a similar fashion as was postulated for the one-component surfaces. At low Tris(TMS) coverage, the number and

lateral density of hydrophobic groups on the surface are low, forcing the adsorbed protein to roll over from the end-on to side-on conformation to increase protein-surface interactions. As the Tris(TMS) coverage increases, the density of hydrophobic groups on the surface increases, thus increasing the number of contact points the protein can make with the surface. Recall that the Tris(TMS) molecule is very flexible due to the ability to rotate along the Si-O-Si bonds, making the Tris(TMS) layer a fairly 'soft' surface as described earlier. This allows the protein to adsorb in the end-on orientation to a larger extent, but not to the degree as seen for the highly flexible C₁₈ CAM. Subsequent reaction of Tris(TMS) with TMS leads to a slightly different morphology as seen in Figure 3.25. In this case, the Tris(TMS) layer has been mixed with a rigid, hydrophobic surface (TMS) and so the morphology again appears to argue for reorientation to the side-on conformation. The adsorbed layer appears more uniform since the hydrophilic silanols have been replaced by hydrophobic TMS moieties. Similar results are seen for Tris(TMS) / TVS-OH mixed surfaces as seen in Figure 3.26.

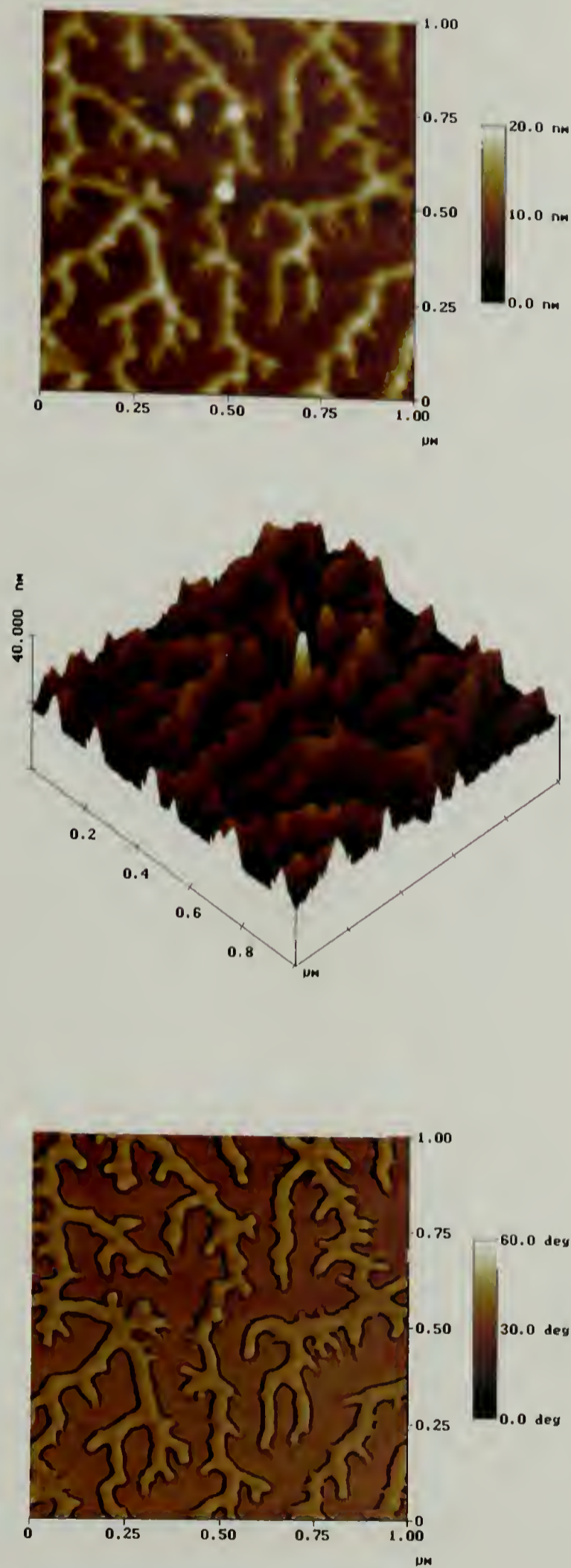


Figure 3.5. AFM images obtained in tapping mode of BSA adsorbed to a C₁₈ CAM for 1h at 37 °C and 0.1 mg/mL. The images are height (top), surface (middle), and phase (bottom) plots of a 1 μm² sampling area.

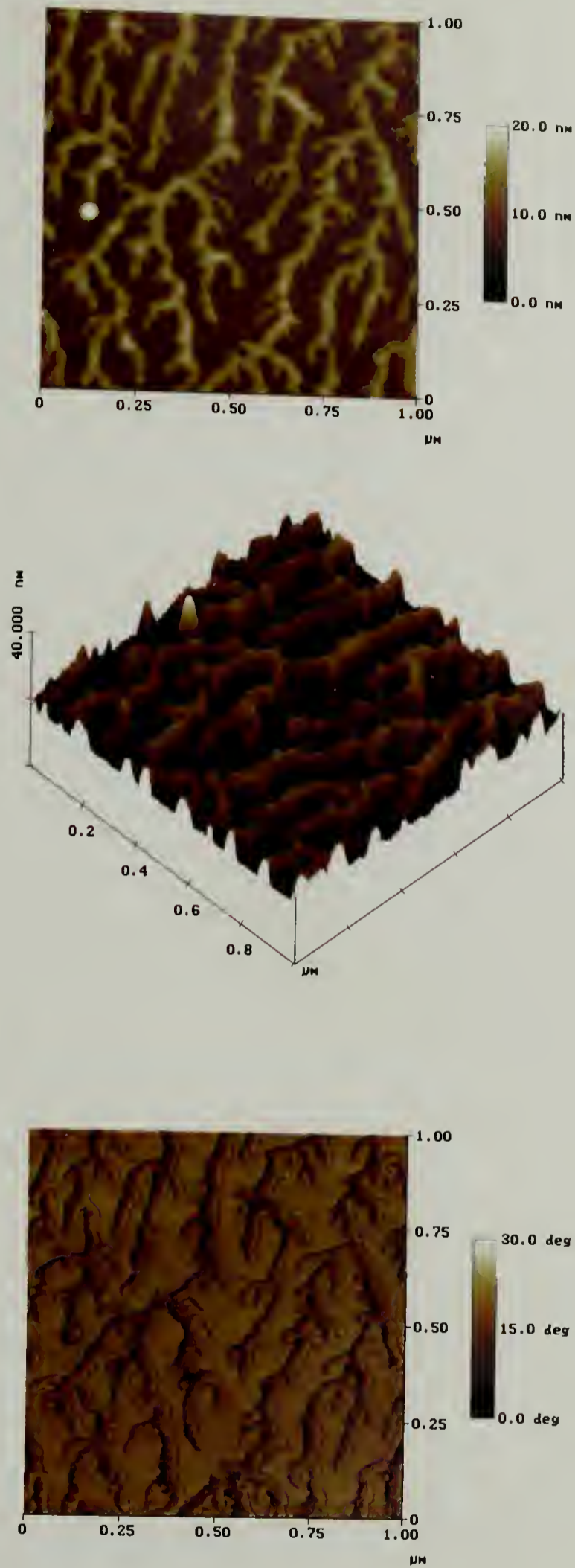


Figure 3.6. AFM images obtained in tapping mode of BSA adsorbed to a C_6F_{13} surface for 1h at 37°C and 0.1 mg/mL . The images are height (top), surface (middle), and phase (bottom) plots of a $1 \mu\text{m}^2$ sampling area.

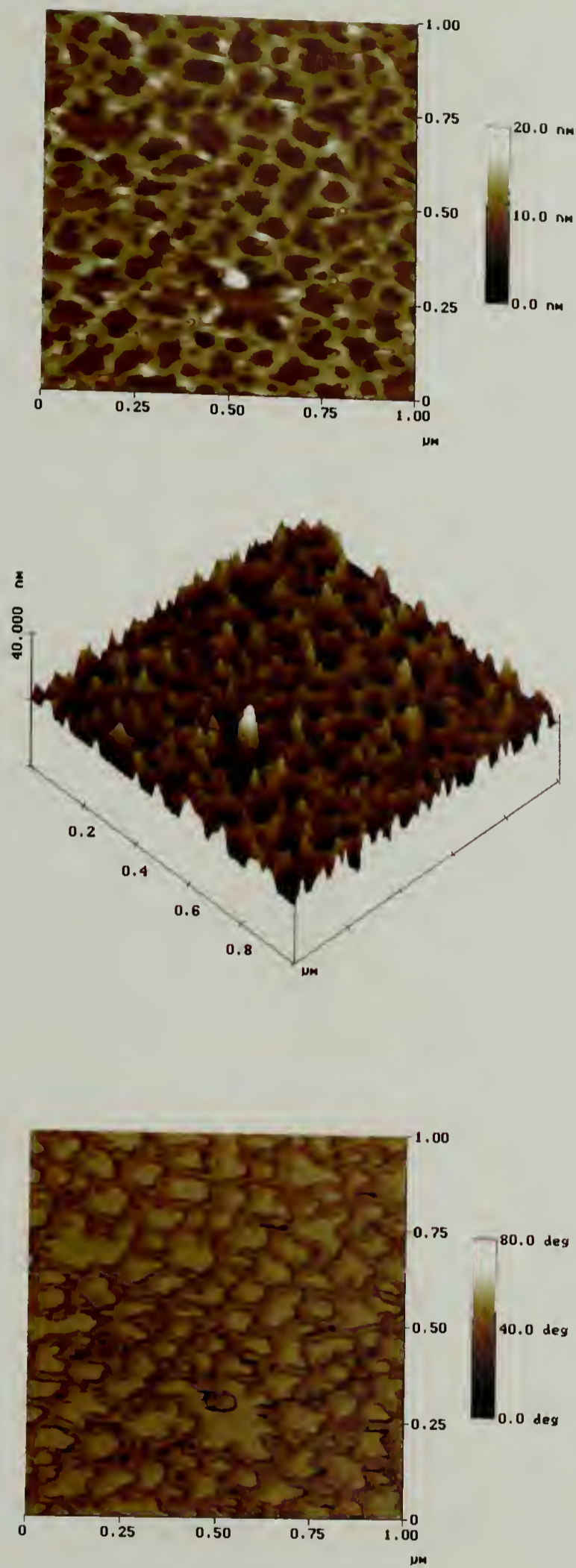


Figure 3.7. AFM images obtained in tapping mode of BSA adsorbed to a DMDC surface for 1h at 37 °C and 0.1 mg/mL. The images are height (top), surface (middle), and phase (bottom) plots of a 1 μm² sampling area.

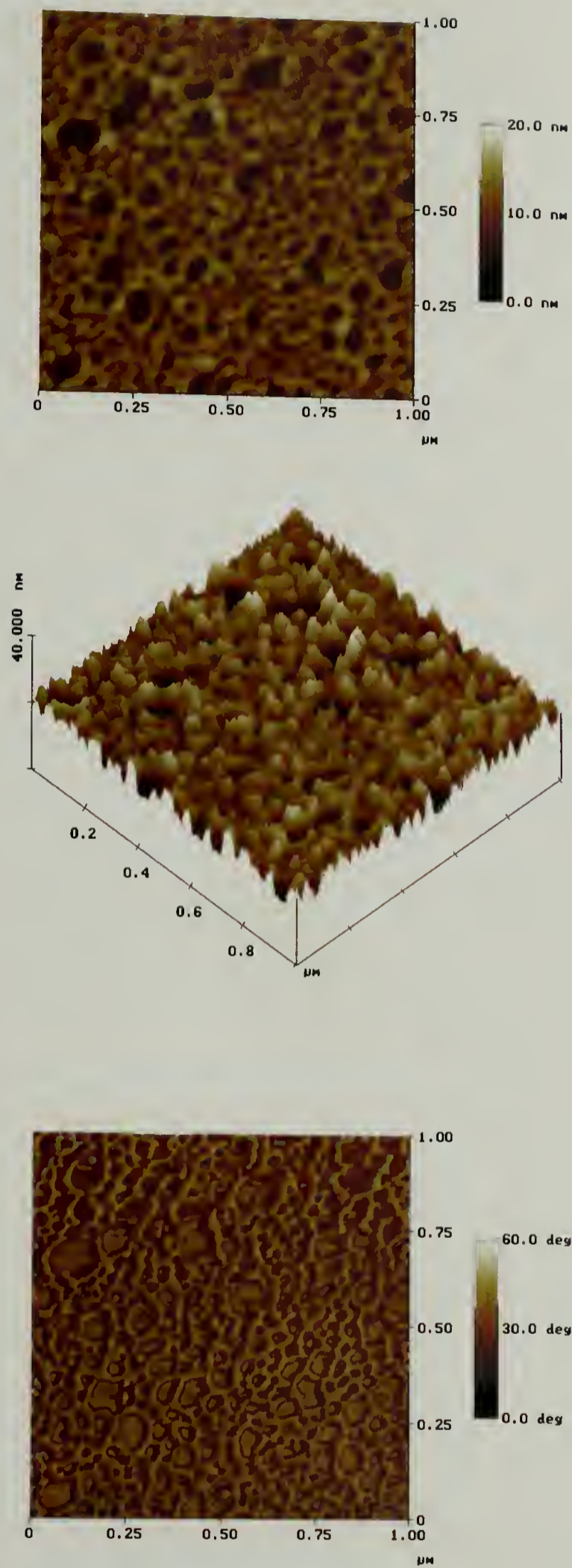


Figure 3.8. AFM images obtained in tapping mode of BSA adsorbed to a C₁₈ SAM for 1h at 37 °C and 0.1 mg/mL. The images are height (top), surface (middle), and phase (bottom) plots of a 1 μm² sampling area.

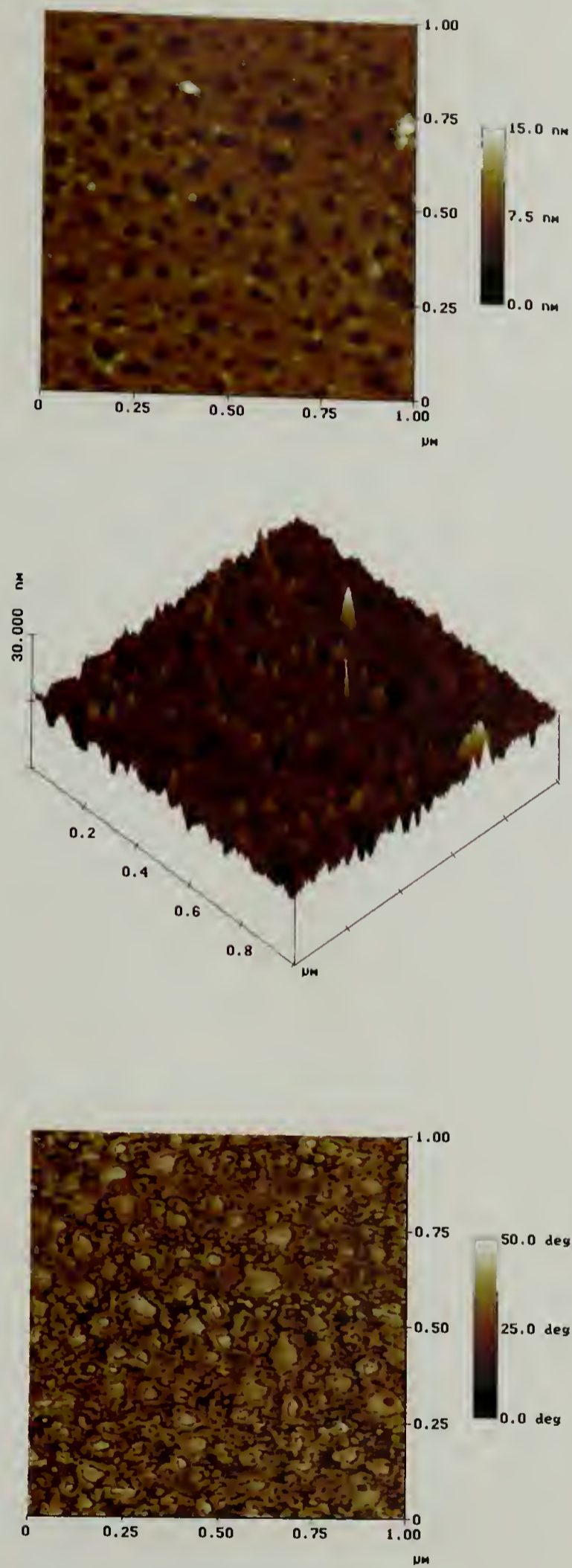


Figure 3.9. AFM images obtained in tapping mode of BSA adsorbed to a TMS surface for 1h at 37 °C and 0.1 mg/mL. The images are height (top), surface (middle), and phase (bottom) plots of a 1 μm² sampling area.

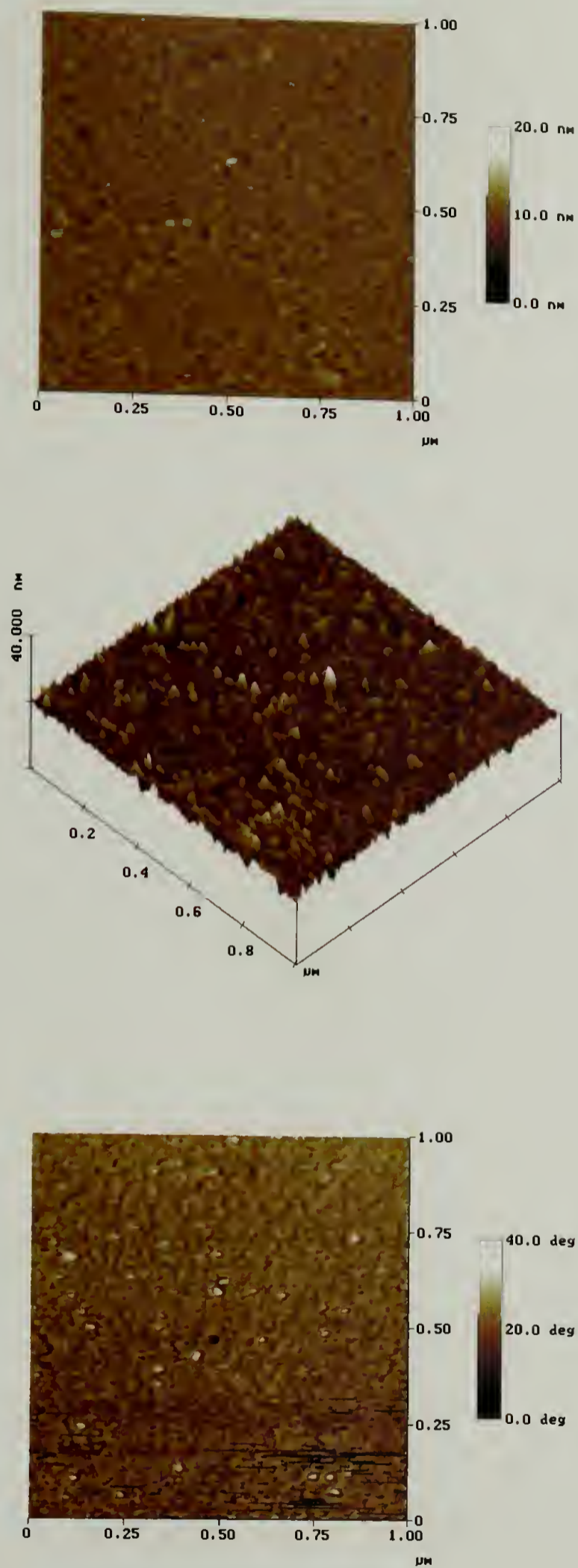


Figure 3.10. AFM images obtained in tapping mode of BSA adsorbed to a CF₃ surface for 1h at 37 °C and 0.1 mg/mL. The images are height (top), surface (middle), and phase (bottom) plots of a 1 μm² sampling area.

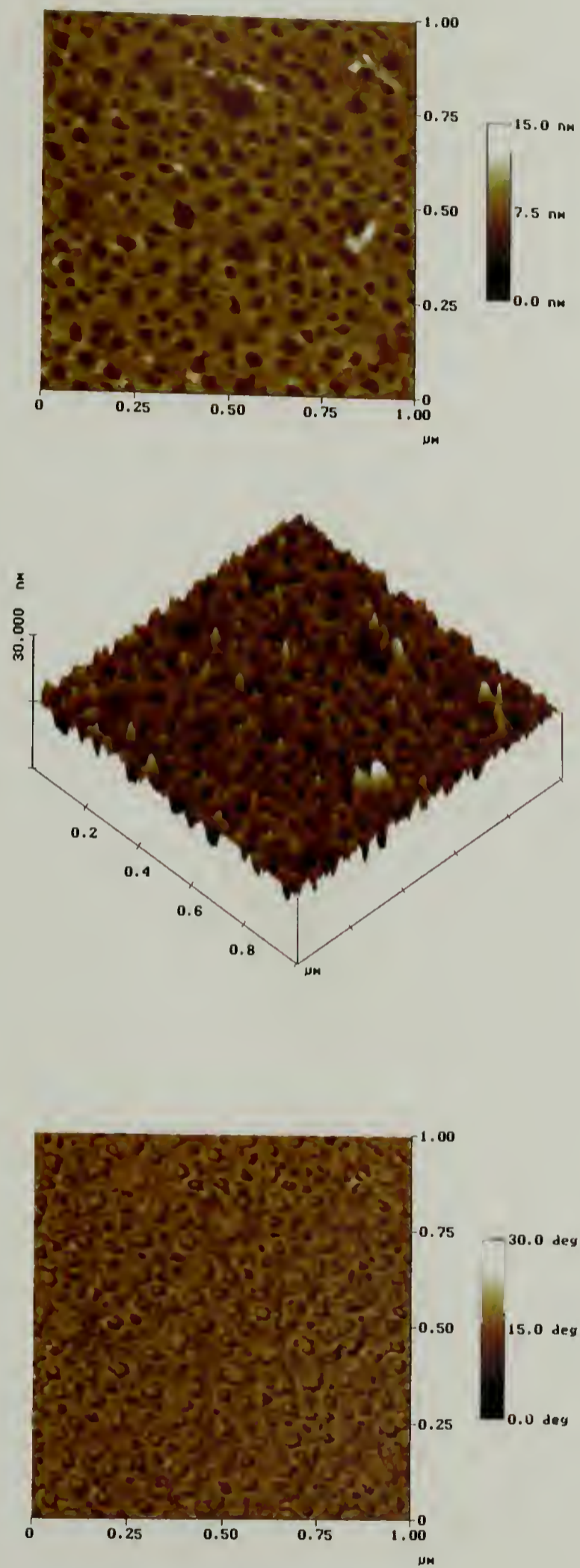


Figure 3.11. AFM images obtained in tapping mode of BSA adsorbed to a carbomethoxy surface for 1h at 37 °C and 0.1 mg/mL. The images are height (top), surface (middle), and phase (bottom) plots of a 1 μm² sampling area.

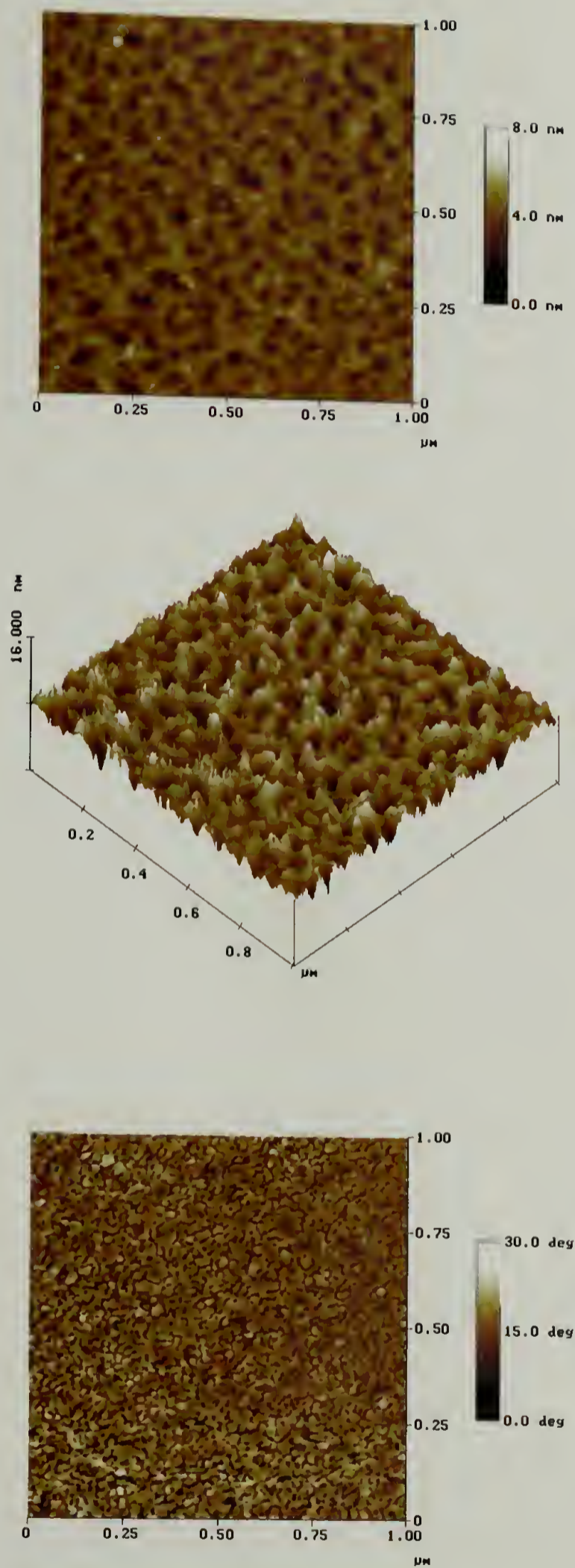


Figure 3.12. AFM images obtained in tapping mode of BSA adsorbed to an acetoxys surface for 1h at 37 °C and 0.1 mg/mL. The images are height (top), surface (middle), and phase (bottom) plots of a 1 μm² sampling area.

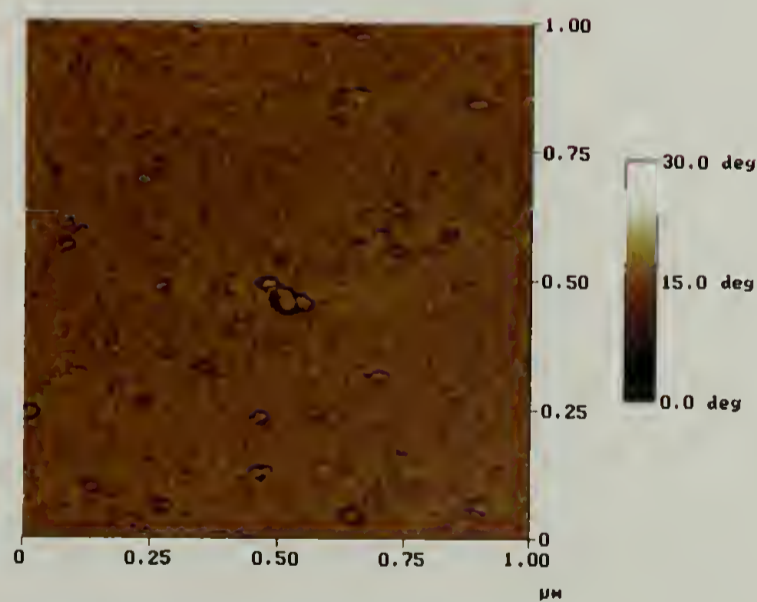
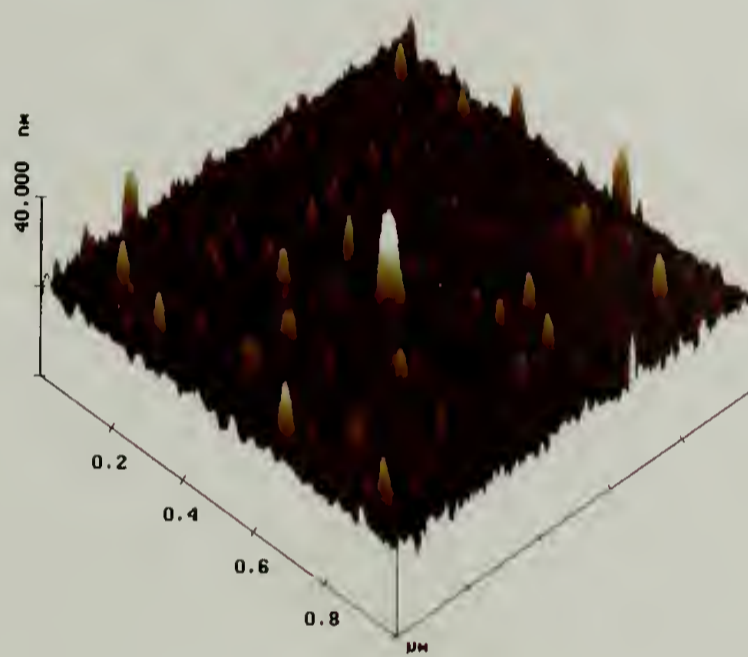
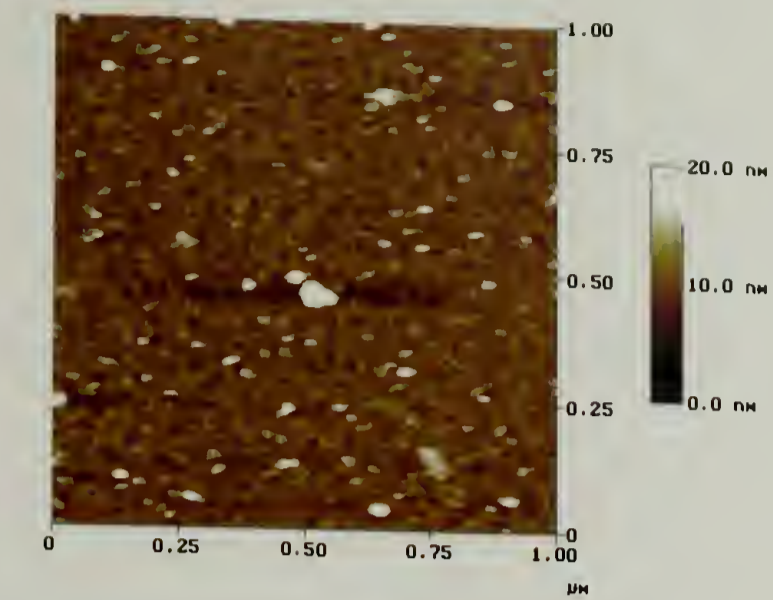


Figure 3.13. AFM images obtained in tapping mode of BSA adsorbed to a mercaptopropyltriethoxysilane surface for 1h at 37 °C and 0.1 mg/mL. The images are height (top), surface (middle), and phase (bottom) plots of a 1 μm² sampling area.

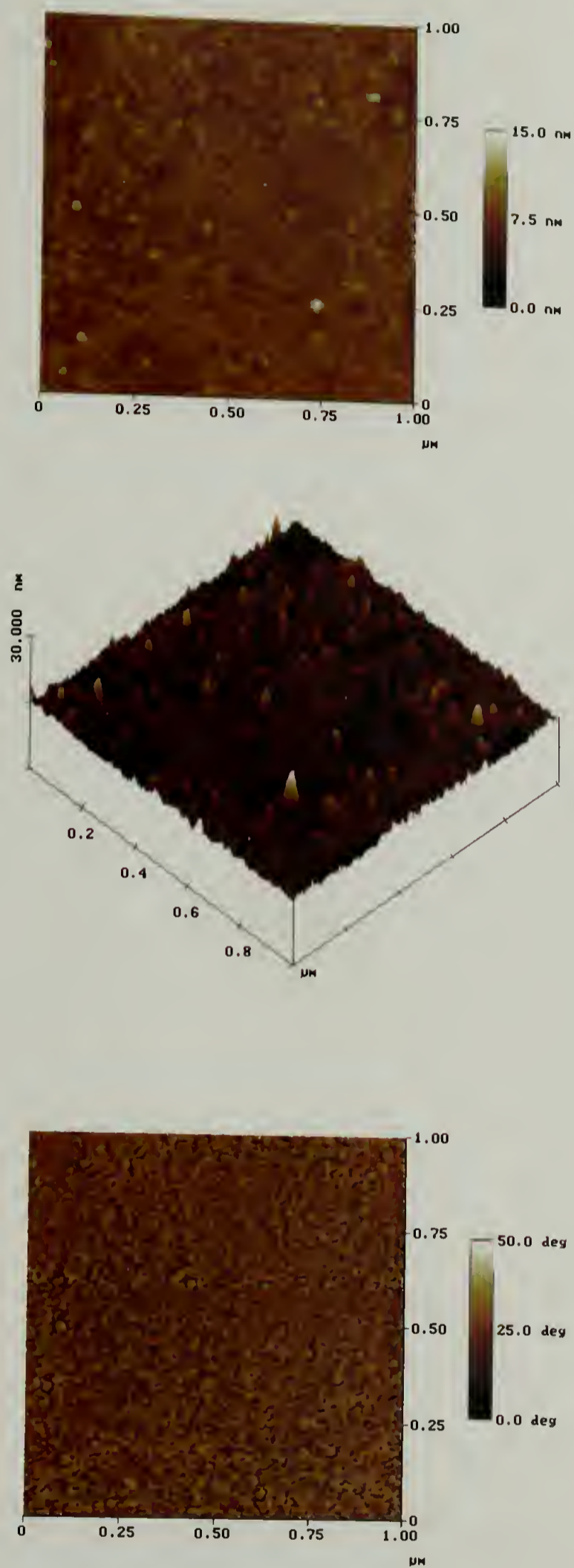


Figure 3.14. AFM images obtained in tapping mode of BSA adsorbed to a TPS surface for 1h at 37 °C and 0.1 mg/mL. The images are height (top), surface (middle), and phase (bottom) plots of a 1 μm² sampling area.

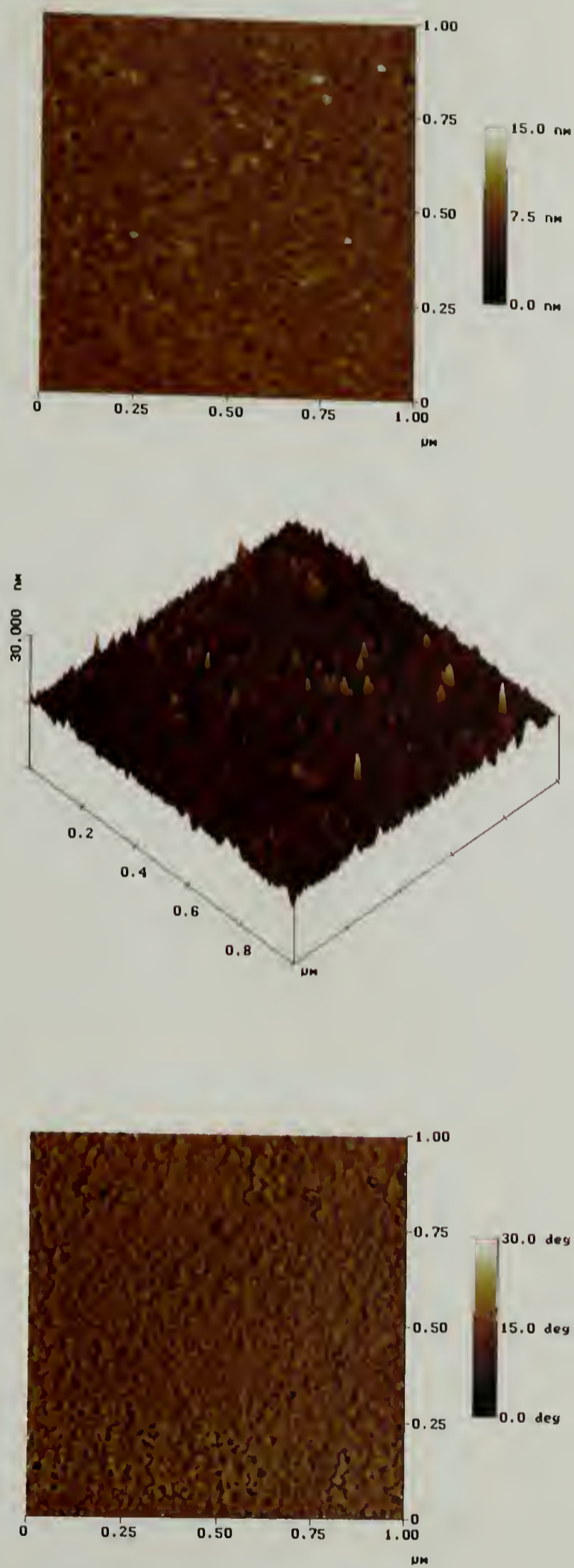


Figure 3.15. AFM images obtained in tapping mode of BSA adsorbed to an APS surface for 1h at 37 °C and 0.1 mg/mL. The images are height (top), surface (middle), and phase (bottom) plots of a 1 μm² sampling area.

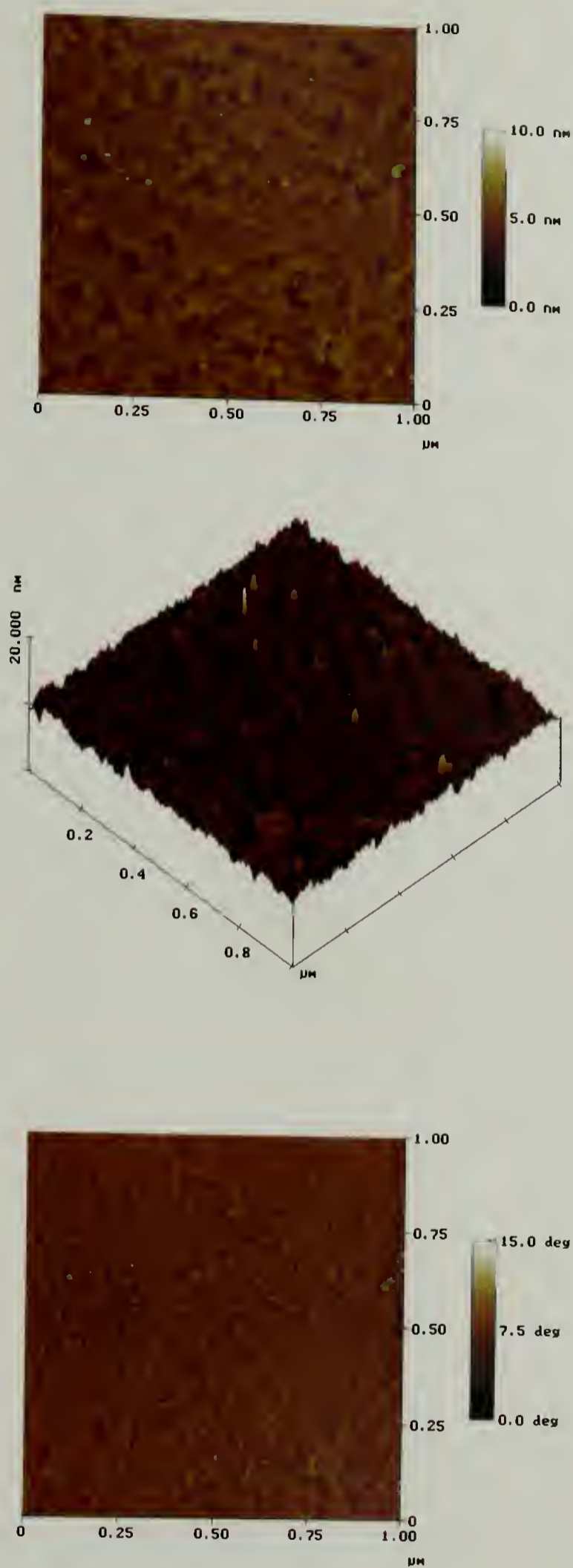


Figure 3.16. AFM images obtained in tapping mode of BSA adsorbed to a TVS-OH surface for 1h at 37 °C and 0.1 mg/mL. The images are height (top), surface (middle), and phase (bottom) plots of a $1 \mu\text{m}^2$ sampling area.

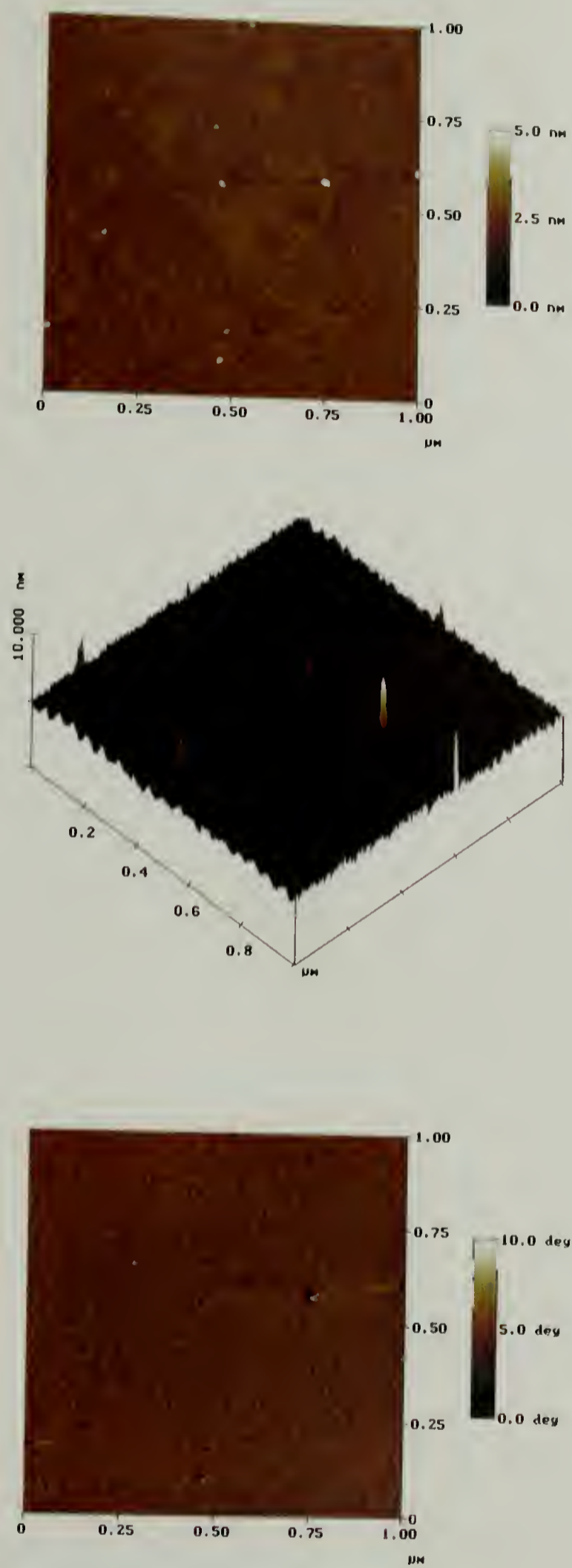


Figure 3.17. AFM images obtained in tapping mode of BSA adsorbed to clean silicon for 1h at 37 °C and 0.1 mg/mL. The images are height (top), surface (middle), and phase (bottom) plots of a $1 \mu\text{m}^2$ sampling area.

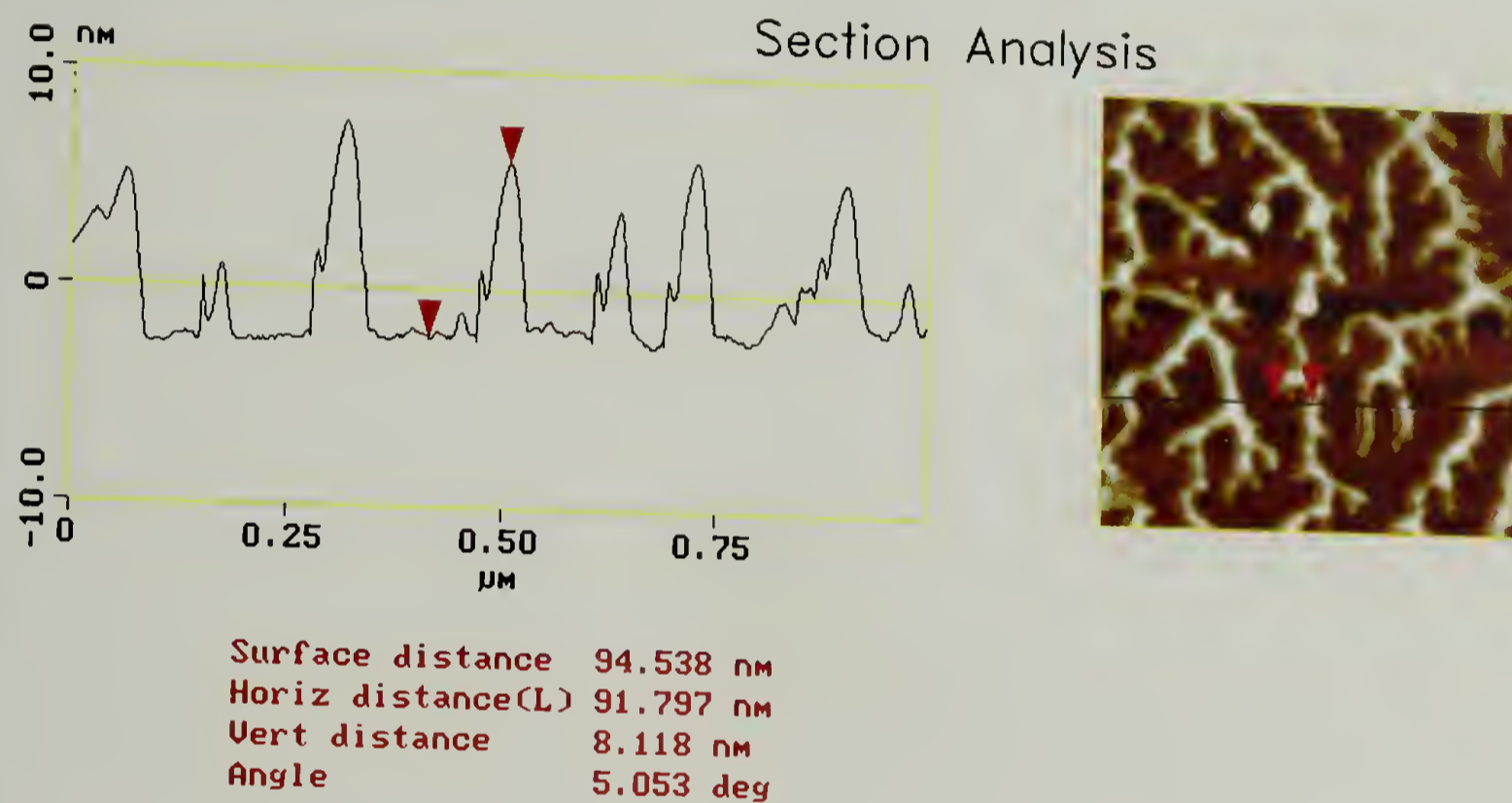
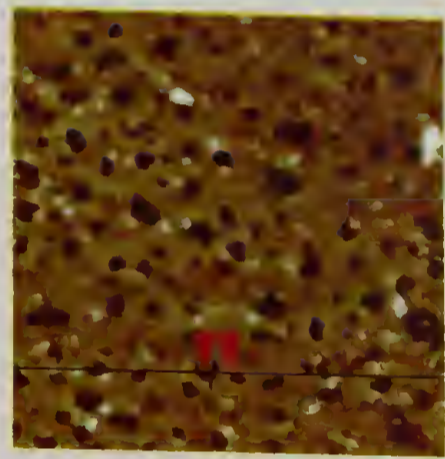
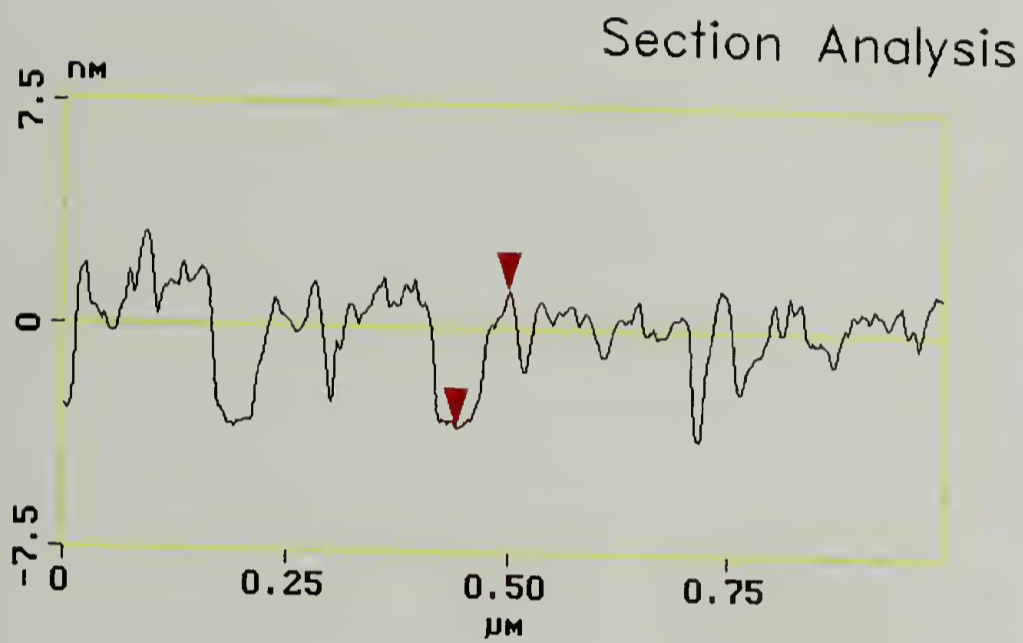


Figure 3.18. AFM section analysis of BSA adsorbed to C_{18} CAM showing the typical height (8 nm) of the observed features on the surface.



Surface distance	58.990 nm
Horiz distance(L)	58.594 nm
Vert distance	4.630 nm
Angle	4.518 deg

Figure 3.19. AFM section analysis for BSA adsorbed to TMS showing the typical height (4.6 nm) of the observed features on the surface.

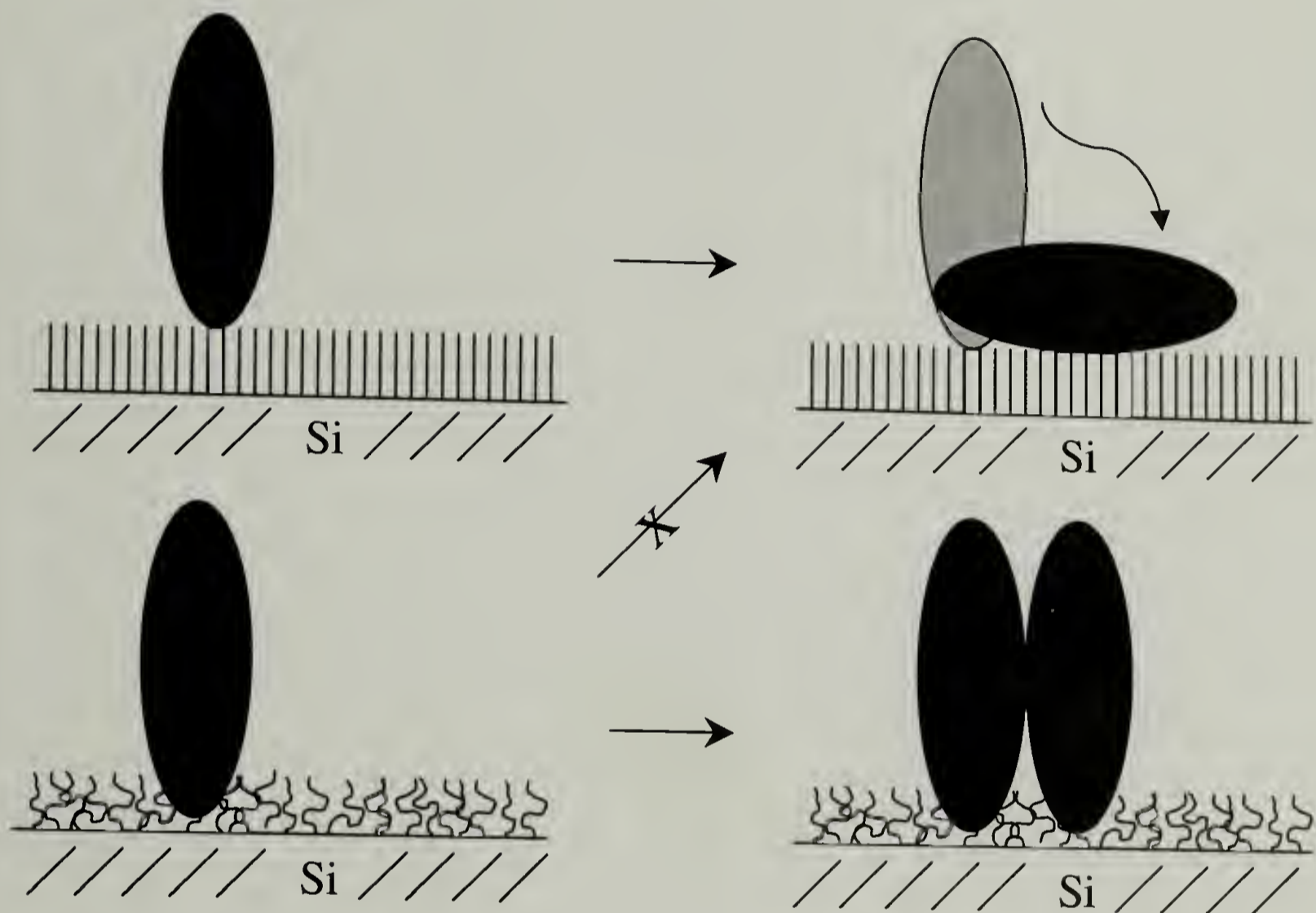


Figure 3.20. Schematic illustrating two possible modes of adsorption of BSA to hydrophobic surfaces: rigid surfaces that force restructuring of the albumin to increase contact points, and soft surfaces that allow for a large number of contact points without the need to restructure.

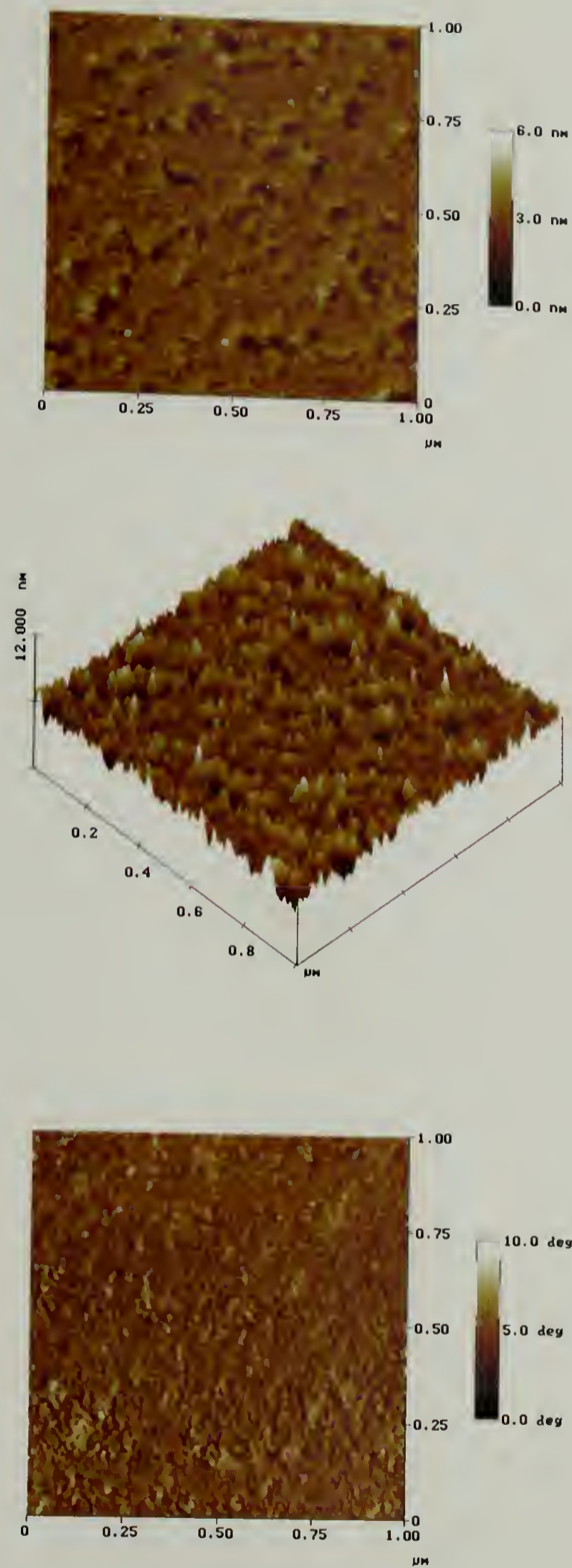


Figure 3.21. AFM images obtained in tapping mode of BSA adsorbed to a Tris(TMS) 1h surface for 1h at 37 °C and 0.1 mg/mL. The images are height (top), surface (middle), and phase (bottom) plots of a $1 \mu\text{m}^2$ sampling area.

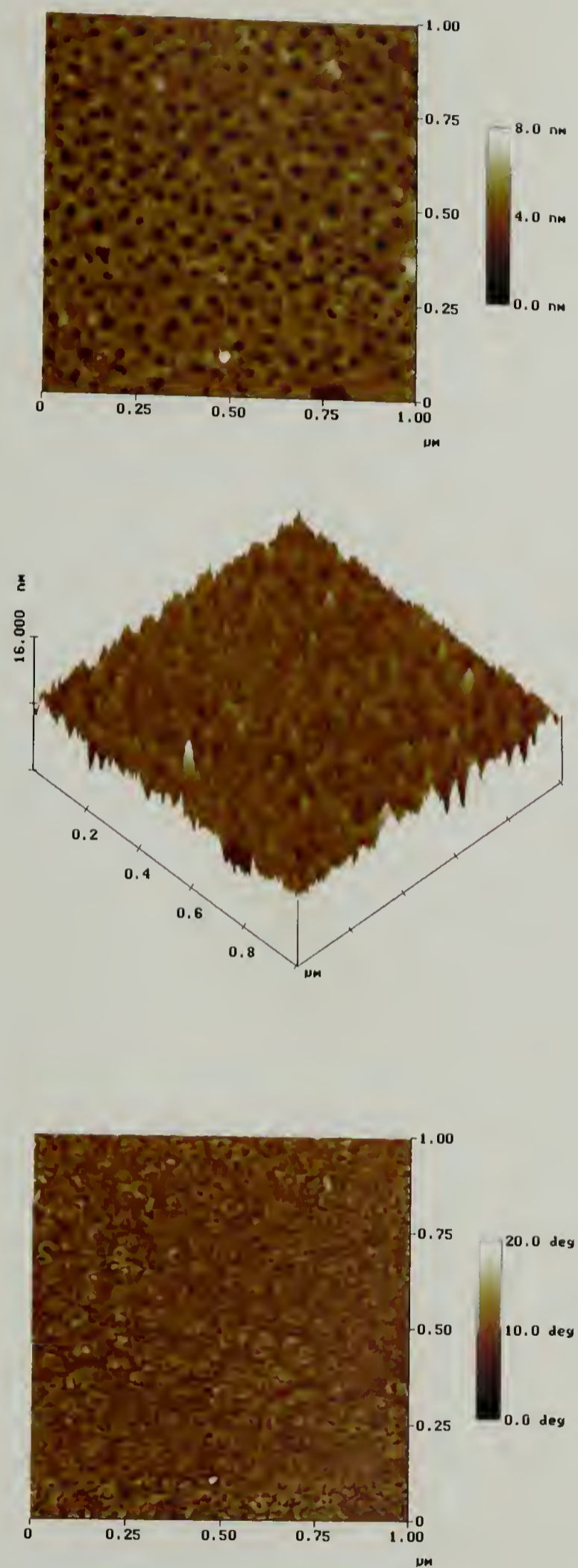


Figure 3.22. AFM images obtained in tapping mode of BSA adsorbed to a Tris(TMS) 24h surface for 1h at 37 °C and 0.1 mg/mL. The images are height (top), surface (middle), and phase (bottom) plots of a 1 μm² sampling area.

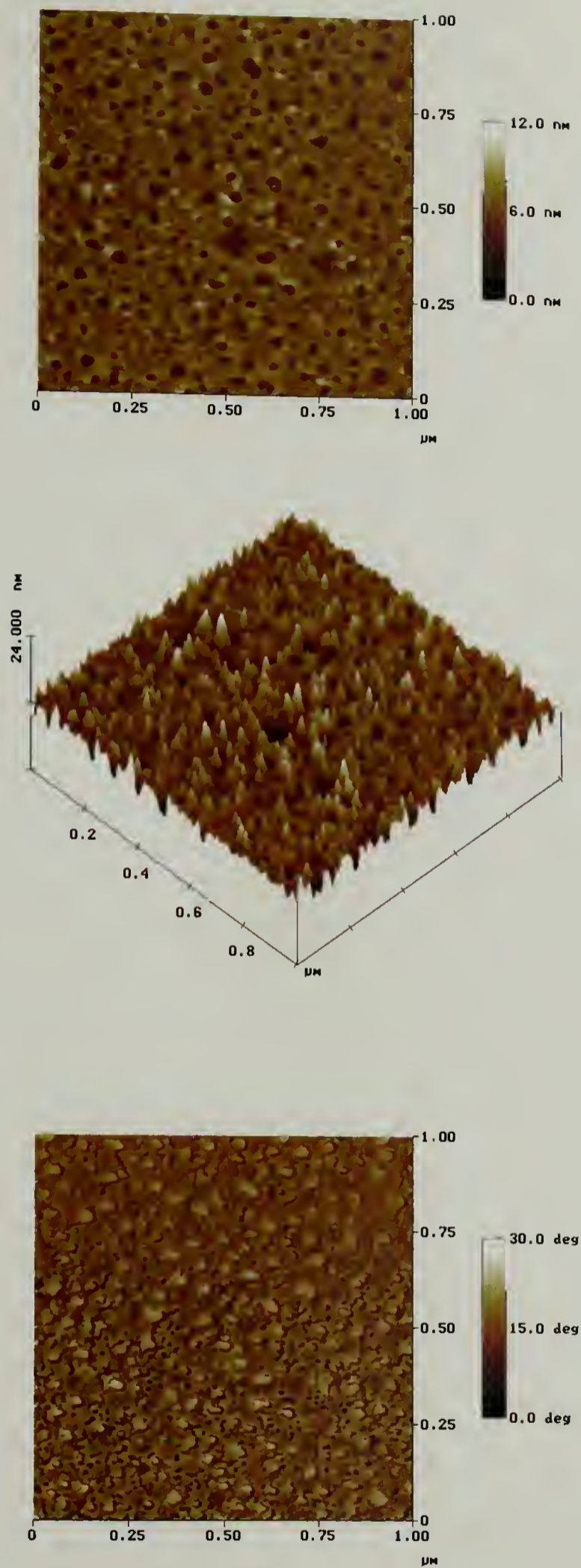


Figure 3.23. AFM images obtained in tapping mode of BSA adsorbed to a Tris(TMS) 72h surface for 1h at 37 °C and 0.1 mg/mL. The images are height (top), surface (middle), and phase (bottom) plots of a 1 μm² sampling area.

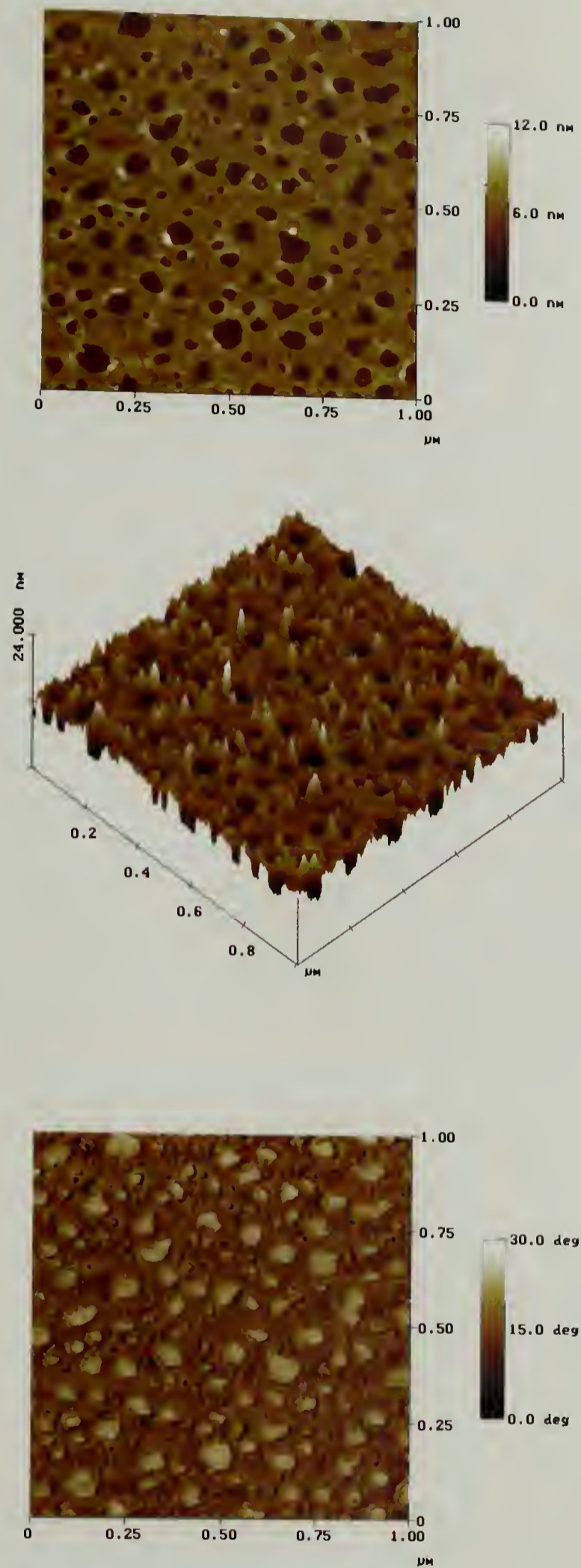


Figure 3.24. AFM images obtained in tapping mode of BSA adsorbed to a Tris(TMS) 140h surface for 1h at 37 °C and 0.1 mg/mL. The images are height (top), surface (middle), and phase (bottom) plots of a 1 μm² sampling area.

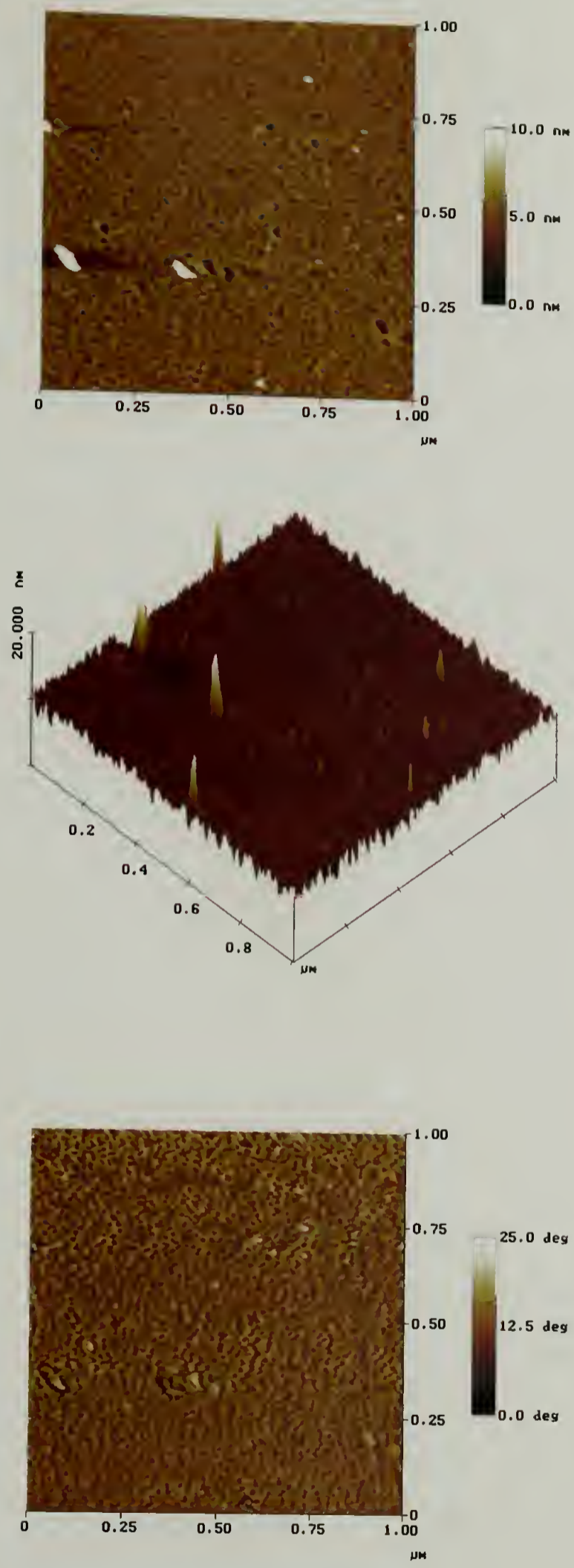


Figure 3.25. AFM images obtained in tapping mode of BSA adsorbed to a Tris(TMS) 1h / TMS surface for 1h at 37 °C and 0.1 mg/mL. The images are height (top), surface (middle), and phase (bottom) plots of a 1 μm² sampling area.

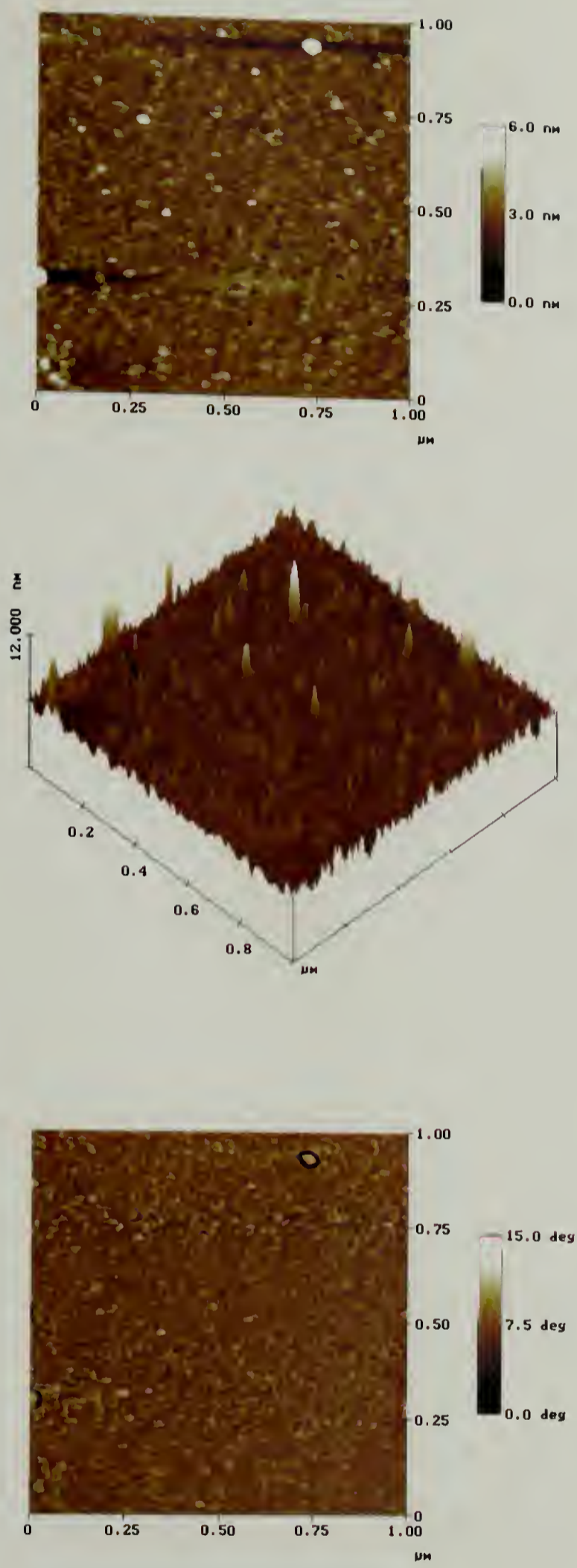


Figure 3.26. AFM images obtained in tapping mode of BSA adsorbed to a Tris(TMS) 1h / TVS-OH surface for 1h at 37 °C and 0.1 mg/mL. The images are height (top), surface (middle), and phase (bottom) plots of a 1 μm² sampling area.

3.4. Conclusions

Covalently attached monolayers (CAMs) were prepared by solution reaction of various monochlorosilanes. CAMs present a versatile technique to survey a range of surface chemistry typically inaccessible by traditional self-assembly methods. The monolayers were utilized to probe the effects of surface chemistry on the adsorption of a specific protein, albumin. It was determined that the adsorbance (Γ) was linearly dependent on the surface energy of the monolayers, as shown by plotting the adsorbance as a function of the cosine of the advancing contact angle. Two surfaces showed exceptional protein repellency: surface-grafted PEGs and sulfonate monolayers. The morphology of the adsorbed protein layers were examined by AFM, and correlated to the chemical and physical properties of the surface. For hydrophobic surfaces, it was found that the rigidity of the monolayers played a critical role in directing the orientation of the adsorbed protein molecules. Highly rigid surfaces (i.e. SAMs) offer very few contact points between the surface and the adsorbed protein, requiring the protein to roll over from the end-on to the side-on adsorbed state to increase the strength of interaction. This resulted in a fairly uniform surface coverage of protein molecules. Soft surfaces (i.e. long alkyl or fluoroalkyl CAMs) could stabilize the end-on orientation due to the larger number of contact points as well as the presence of specific binding sites for long alkyl fatty acids. The protein, though, appears to maintain sufficient mobility in-plane to order in a fractal-like pattern that closely resembles diffusion-limited aggregation of particles. It was argued that both protein-surface interactions and protein-protein interactions are necessary to render the adsorbed proteins irreversibly adsorbed such that they are not

rinsed away with fresh buffer solution. More experiments need to be conducted to strengthen the arguments presented here, which should yield more insight on the adsorption mechanism of albumin to hydrophobic surfaces.

3.5. Future Work

There are numerous questions that have been left unanswered concerning albumin adsorption to silane-modified surfaces. There will always be skepticism that the observed structures presented earlier are simply due to the drying process. Although I highly doubt that this is the case, the data would be more credible if AFM was conducted *in situ* so that the morphology of the protein layer remains unperturbed. Also, it would of interest to study the formation of this fractal-like structure shown in Figure 3.6 or 3.7 by conducting a kinetics experiment of adsorption. Desorption experiments could also be conducted as a function of surface rigidity to further establish the tenacity of adsorption more quantitatively than experiments conducted by Foster et al.⁹ Another interesting series of experiments would be to prepare a homologous series of *n*-alkyl CAMs (methyl, ethyl, butyl,....., octadecyl) to strengthen the argument regarding the role of surface rigidity on albumin adsorption, as well as to observe whether or not there is a critical alkyl chain length that stabilizes albumin adsorbed in the end-on state. Albumin has also been shown to interact even more strongly with oleic acid (mono-unsaturated) than stearic acid or even linoleic acid (di-unsaturated). Therefore, it might be interesting to study the effects of unsaturation of long alkyl chains on the adsorption of albumin to silane-modified surfaces. Outside the realm of albumin, it should also be enlightening to

conduct experiments on other proteins (i.e. lysozyme, fibrinogen) and ascertain the role of surface chemistry on adsorption of those proteins to CAMs. Collaborations are also in place to study the adsorption and spreading rate of several proteins on CAMs, and the initial results are very promising and should lead to a more complete understanding of protein adsorption to this class of surfaces.

3.5. References Cited

1. Brash, J. and Horbett, T., eds. *Proteins at Interfaces: Physiochemical and Biochemical Studies*. 1987, American Chemical Society: Washington, DC. 706.
2. Horbett, T. and Brash, J., eds. *Proteins at Interfaces II: Fundamentals and Applications*. 1995, American Chemical Society: Washington, DC. 561.
3. Eberhart, R.; Munro, M.; Frautschi, J., and Tingey, K. *IEEE/Engineering in Medicine and Biology Society Annual Conference*, **1986**, 1680.
4. Grasel, T.; Pierce, J., and Cooper, S. *J. Biomed. Mater. Res.*, **1987**, *21*, 815.
5. Bos, O.; Labro, J.; Fischer, M.; Witling, J., and Janssen, L. *J. Biol. Chem.*, **1989**, *264*, 953.
6. Carter, D.; He, X.; Munson, S.; Twigg, P.; Gernert, K.; Broom, M., and Miller, T. *Science*, **1989**, *244*, 1195.
7. Lin, Y.-S. and Hlady, V. *Colloids and Surfaces B: Biointerfaces*, **1994**, *2*, 481.
8. Takahara, A.; Kojio, K.; Ge, S., and Kajiyama, T. *J. Vac. Sci. Technol. A*, **1996**, *14*, 1747.
9. Petrash, S.; Sheller, N.; Dando, W., and Foster, M. *Langmuir*, **1997**, *13*, 1881.
10. Sheller, N.; Petrash, S., and Foster, M. *Langmuir*, **1998**, *14*, 4535.
11. Wertz, C. and Santore, M. *Langmuir*, **2001**, *17*, 3006.
12. Wojciechowski, P. and Brask, J. *Colloids and Surfaces B: Biointerfaces*, **1993**, *1*, 107.
13. Ge, S.; Kojio, K.; Takahara, A., and Kajiyama, T. *J. Biomater. Sci., Polym. Ed.*, **1998**, *9*, 131.
14. Yang, Z.; Galloway, J., and Yu, H. *Langmuir*, **1999**, *15*, 8405.
15. Takahara, A.; Ge, S.; Kojio, K., and Kajiyama, T. *J. Biomater. Sci., Polym. Ed.*, **2000**, *11*, 111.
16. Su, T.; Green, R.; Wang, Y.; Murphy, E., and Lu, J. *Langmuir*, **2000**, *16*, 4999.

17. Silberzan, P.; Leger, L.; Ausserre, D., and Benattar, J. *Langmuir*, **1991**, *7*, 1647.
18. Parikh, A.; Allara, D.; Azouz, I., and Rondelez, F. *J. Phys. Chem.*, **1994**, *98*, 7577.
19. McGovern, M.; Kallury, K., and Thompson, M. *Langmuir*, **1994**, *10*, 3607.
20. Fadeev, A. and McCarthy, T. *Langmuir*, **1999**, *15*, 3759.
21. Fadeev, A. and McCarthy, T. *Langmuir*, **1999**, *15*, 7238.
22. Stafford, C.; Fadeev, A.; Russell, T., and McCarthy, T. *Langmuir*, **2001**, in press.
23. Liu, Y.; Wolf, L., and Messmer, M. *Langmuir*, **2001**, *17*, 4329.
24. Wasserman, S.; Tao, Y., and Whitesides, G. *Langmuir*, **1989**, *5*, 1074.
25. Fadeev, A. and McCarthy, T. *Langmuir*, **2000**, *16*, 7268.
26. Tremsina, Y.; Sevastianov, V.; Petrash, S.; Dando, W., and Foster, M. *J. Biomater. Sci., Polym. Ed.*, **1998**, *9*, 151.
27. Wertz, C. and Santore, M. *Langmuir*, **1999**, *15*, 8884.
28. Stenberg, M. and Nygren, H. *Journal de Physique*, **1983**, *44*, 83.
29. Arwin, H. *Appl. Spect.*, **1986**, *40*, 313.
30. Tengvall, P.; Lundstrom, I., and Liedberg, B. *Biomaterials*, **1998**, *19*, 407.
31. Lin, Y.-S.; Hlady, V., and Gölander, C.-G. *Colloids and Surfaces B: Biointerfaces*, **1994**, *3*, 49.
32. Prime, K. and Whitesides, G. *JACS*, **1993**, *115*, 10714.
33. Sigal, G.; Mrksich, M., and Whitesides, G. *JACS*, **1998**, *120*, 3464.
34. Adamson, A., *Physical Chemistry of Surfaces*, 4th Ed. 1982, New York: John Wiley & Sons. 664.
35. Baskin, A. and Boissonnade, M., in *Proteins at Interfaces II: Fundamentals and Applications*, T. Horbett and J. Brash, Editors. 1995, American Chemical Society: Washington, DC. p. 209.

APPENDIX A

LIVING ANIONIC POLYMERIZATION

A.1. Introduction

Anionic polymerization is an elegant and versatile tool that, once mastered, affords the synthetic polymer chemist the ability to prepare polymers with well-defined chemical structures, predictable molecular weights and narrow molecular weight distributions. Sequential addition of monomers permits the synthesis of linear block copolymers having controlled composition and molecular architecture. The chemistry used to terminate the polymerization also allows for precise control of end-group functionality as well as the ability to form star-branched block copolymers. However, living anionic polymerization requires rigorous purification of monomers and solvents, while all material handling has to be done either under high vacuum or inert gas atmospheres to exclude atmospheric contaminants and moisture. To do this, the synthetic polymer chemist must build an understanding of the possible sources of contamination and how to circumvent them. This requires judicious choice of chemicals, drying methods, handling procedures and some creativity in glassware design. Once mastered, this powerful technique can be used to prepare a multitude of unique materials such as homopolymers, block copolymers, and end-functionalized polymers. Several reviews of living anionic polymerization exist in literature.¹⁻³

Anionic polymerization involves the generation of a carbanion propagating species that proceeds to be active with respect to monomer addition until terminated by an externally added electrophile, and requires the absence of chain transfer and

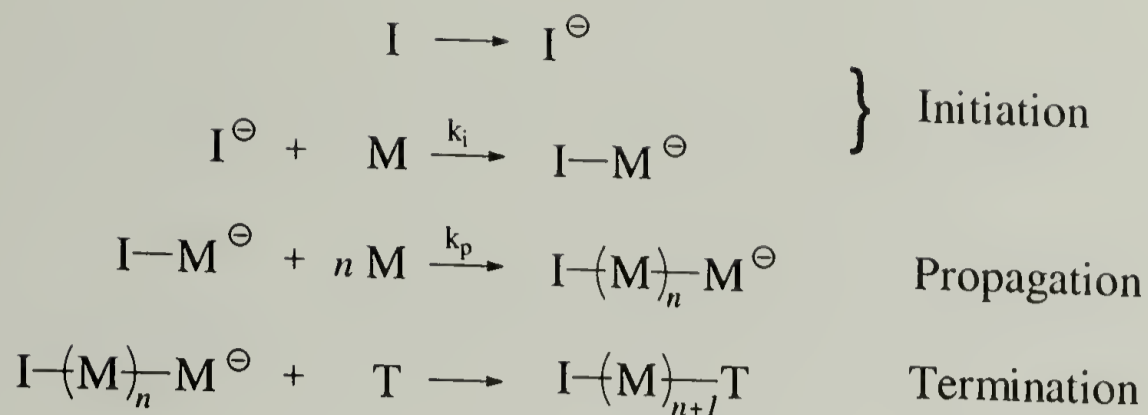


Figure A.1. Schematic mechanism for living anionic polymerization with controlled termination.

termination throughout the polymerization reaction. This process was first described by Zeigler in the 1930's⁴⁻⁶ and was later demonstrated in full by Szwarc in 1956,^{7,8} and is shown schematically in Figure A.1. These polymerizations can be termed 'living' only when the propagating anion retains its reactivity throughout the polymerization reaction, and thus can reinitiate polymerization if more monomer is added. The degree of polymerization, or molecular weight, can simply be calculated by the ratio of monomer to initiator concentrations $[M]/[I]$ given that the rate of initiation is faster than the rate of propagation ($k_i \gg k_p$). These rates are highly dependent on the chemical nature of the initiator and monomer, solvent, counterion and the possible addition of Lewis bases. If $k_i \gg k_p$, the molecular weight of the resulting polymer can be described by a Poisson distribution and typically has a polydispersity index (M_w/M_n) of less than 1.10.

Monomers that can be polymerized anionically include styrenes, dienes, methacrylates, epoxides, episulfides, and cyclic siloxanes. When preparing block copolymers, the sequence of monomer addition is critical due to large disparities in chain end reactivities. Thus, one must identify the pK_a values for the respective chain ends to determine the sequence of addition, and note that chain ends will initiate polymerization

for monomers having equal or lower pK_a values, but not higher. For example, styrene ($pK_a = 41$) will initiate methacrylates ($pK_a = 27$) but oxiranes ($pK_a = 17$) will not initiate dienes ($pK_a = 43$).

The termination reaction can be altered to yield a variety of functional polymers. Reaction of living anions with carbon dioxide yields carboxylic acid-terminated polymers. Termination with ethylene oxide yields the corresponding hydroxy-terminated polymer. Amine functionality can be introduced by reaction with a protected imine or by reaction with methoxyamine. Sulfonation can be achieved by reaction of the living polymer with 1,3-propanesultone, but only after first reacting the anion with either ethylene oxide or diphenylethylene. Fluorescent labels can be introduced by reaction with derivatized diphenylethylenes, and can be included at either the chain end of a homopolymer or at the junction point of a diblock. Other functionalities can be introduced by using protected initiator chemistries, as well as by the use of protected monomers.

Living anionic polymerization was used throughout the research presented in the previous chapters. This appendix will serve to describe in detail the experimental conditions and chemistries used to synthesize the polymers needed for the work contained in this thesis, as well as those polymers synthesized to supplement current and future work within the department. This includes polymerization of homopolymers and end-functionalized homopolymers as well as block copolymers.

A.2. Experimental

A.2.1. Materials

The following chemicals were used as received: calcium hydride, tetramethylethylenediamine, dibutylmagnesium, triethylaluminum, anthracene, 2-acetylphenanthrene, aluminum trichloride, acetic anhydride, phenylmagnesium bromide, and *sec*-butyllithium (all purchased from Aldrich); benzene, nitrobenzene, acetic acid, magnesium sulfate, tetrahydrofuran, methanol, ethanol (anhydrous), hexanes, hydrochloric acid, potassium hydroxide, and acetone (all purchased from Fisher). All wash solvents were HPLC grade. Carbon dioxide (Coleman grade) was purchased from Merriam Graves and was dried by passing it through activated alumina to remove polar impurities and a copper catalyst (Q-5 - Engelhardt) to remove traces of oxygen. House nitrogen was used for purging glassware and for creating an inert atmosphere. All indications show that house N₂ was more than adequate for anionic polymerizations.

The following chemicals were used after rigorous purification as outlined in the appropriate sections: styrene, methyl methacrylate, and diphenylethylene (all purchased from Aldrich). Deuterated styrene was purchased from Cambridge Isotopes and was purified in the same manner as its hydrogenated counterpart. Polymerization solvents (benzene, THF) and dilution solvents (hexanes) were purified as described elsewhere⁹ and were available on a solvent line for dispensing. This consisted of passing the solvent through activated alumina to remove polar impurities and a copper catalyst (Q-5 - Engelhardt) to remove oxygen. THF will react with the catalyst Q-5; therefore it was purchased degassed and was sparged with N₂ before installation on the solvent line.

The initiator of choice for all polymerization reactions was *sec*-butyllithium. A stock solution of *sec*-butyllithium was prepared by diluting an aliquot of 1.3M *sec*-BuLi by a factor of 10x with hexanes obtained from the solvent line. The concentration of the stock solution was checked initially by synthesizing a homopolymer of polystyrene, and was continually checked by observing the accuracy of molecular weights obtained in later polymerizations.

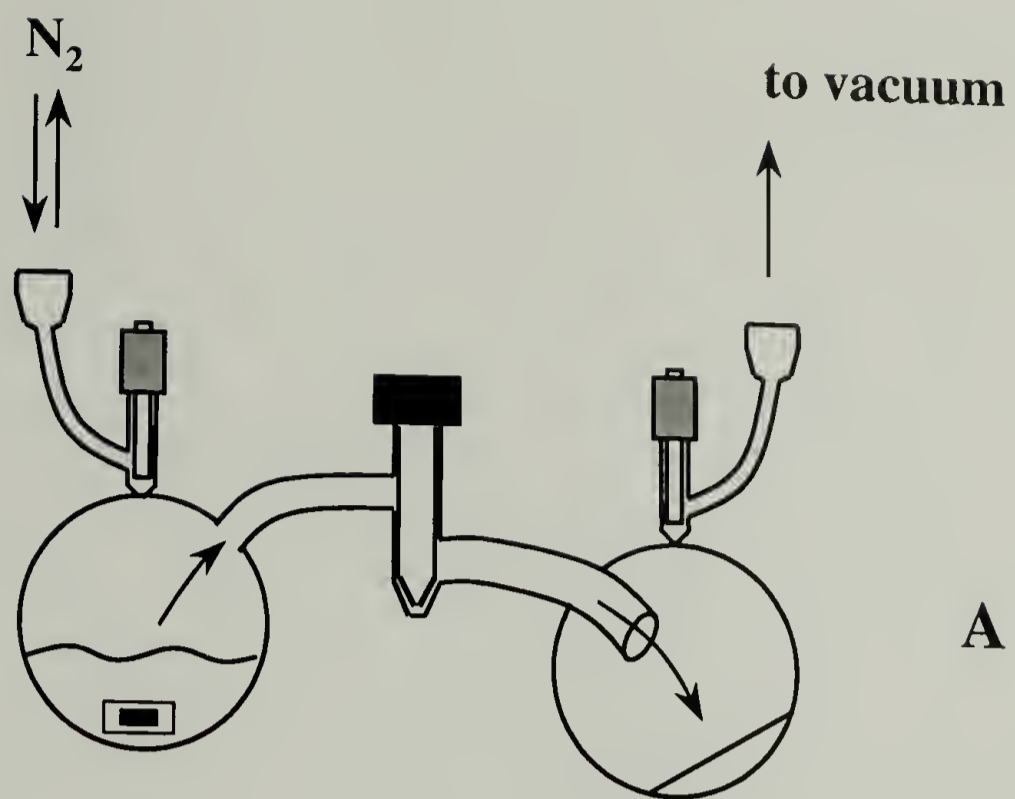
A.2.2. Methods

All syntheses were performed using Schlenk techniques under nitrogen atmosphere. This involves transfer of chemicals within a contained inert environment. This can be achieved by judicious design of purification glassware and polymerization flasks, which utilize antechambers that can be purged with N₂ prior to the opening of a sealed joint to the air-sensitive reactants. A female 14/20 ground glass joint that is capped with a rubber septum and attached to 4mm Teflon[®] stopcock joint can create this antechamber. Through experience, it was determined that 4mm Teflon[®] stopcock joints are very sensitive to scratches and other damage that renders them unreliable for air-sensitive chemistry. It was found that 3mm Rotaflo[®] joints (Ace Glass) were more durable and reliable over longer periods of time. Therefore, all glassware described here contains these Rotaflo[®] joints unless otherwise noted. Also, ground glass joints were avoided due to possible contamination by high-vacuum grease (other than the 14/20 joints connecting to vacuum).

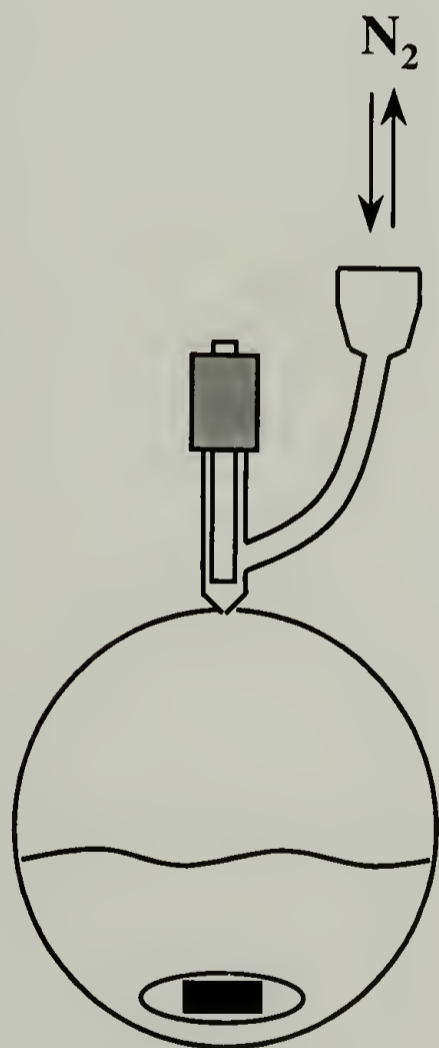
Prior to any reaction, all glassware was cleaned in a base-bath and rinsed with copious amounts of house purified (reverse osmosis) water. The glassware was then

dried at 135 °C for at least 12 h, assembled hot, flamed under vacuum with a heat gun and then back-filled with nitrogen three times before addition of any reagents. Gas-tight syringes, needles and cannulae were rinsed with THF, hexanes, 1 M HCl, 1 M KOH, water and acetone, in that order. Syringes were dried at 135 °C for at least 12 h, flushed with nitrogen while cooling, and then fully assembled under constant nitrogen flow. Cannulae were dried at 135 °C for at least 12 h and flushed with nitrogen while cooling.

Monomer purification was carried out in a custom-designed trap-to-trap distillation apparatus. A schematic of this glassware is shown in Figure A.2 (A). It consists of two 100-mL round-bottom flasks connected by a 0-3 mm Teflon[®] joint (Ace Glass). A glass-covered stirbar was permanently placed inside the left half of the apparatus. Antechambers were created using female 14/20 joints connected to Rotaflo[®] stopcocks. The angle of the Rotaflo[®] joint had to be decreased to allow for the insertion of 22-gauge cannulae. After the glassware was properly dried as described earlier, a given volume of monomer was added to the left bulb along with the appropriate drying agent. Once the monomer was dry as observed by color indication, the monomer was then distilled under vacuum and condensed to a solid in the second bulb using liquid N₂. It should be noted that some monomers are very sensitive to heat (especially in the presence of the respective drying agent) so all distillations should be carried out at room temperature, unless otherwise noted. As the monomer evaporates and distills, the bulb will become quite cold and will limit the rate of further evaporation, so gentle heating with one's hands is adequate in speeding up the process. When enough monomer was collected in the distillate bulb, the purified monomer was then allowed to warm to room temperature and could then be measured out via syringe.



A



B

Figure A.2. Custom-designed glassware for monomer purification (A) and polymerization reactions (B).

Polymerizations were carried out in a similar type of glassware. An antechamber equipped with a Rotaflo[®] stopcock was attached to a 250-mL round-bottom flask. Again, a glass-covered stirbar was permanently placed in the flask. The shape of the stirbar has a significant effect on the rate of stirring, with ellipsoidal stirrers being ideal. It has been observed that insufficient stirring leads to broadening of the polymer molecular weight distribution. A schematic of the polymerization flask used in this work is shown in Figure A.2 (B).

A.3. Synthesis of Polystyrene Homopolymers

The synthesis of polystyrene homopolymers became the standard reaction by which to determine initiator concentrations, test new glassware designs and hone handling techniques. The result of all this experimentation was a plethora of polystyrenes having a range of molecular weights, all of which found their way into experiments of every kind. The solvent of choice for this reaction was benzene because the rate of propagation is slow. Reactions can also be carried out at room temperature and benzene inherently has very low water content. Toluene and cyclohexane could have also been used. The reaction scheme for polymerization of styrene is shown in Figure A.3.

Styrene monomer was purified first by distillation from CaH_2 at reduced pressure. Styrene has a tendency to autopolymerize at elevated temperatures, so distillation was carried out at reduced pressure (10 mm of Hg), resulting in a boiling point of $\sim 60^\circ\text{C}$. Just prior to polymerization, an excess of styrene monomer was stirred over dibutylmagnesium until a persistent yellow color was observed, indicating dryness. It was then degassed by several freeze-pump-thaw cycles, followed by trap-to-trap

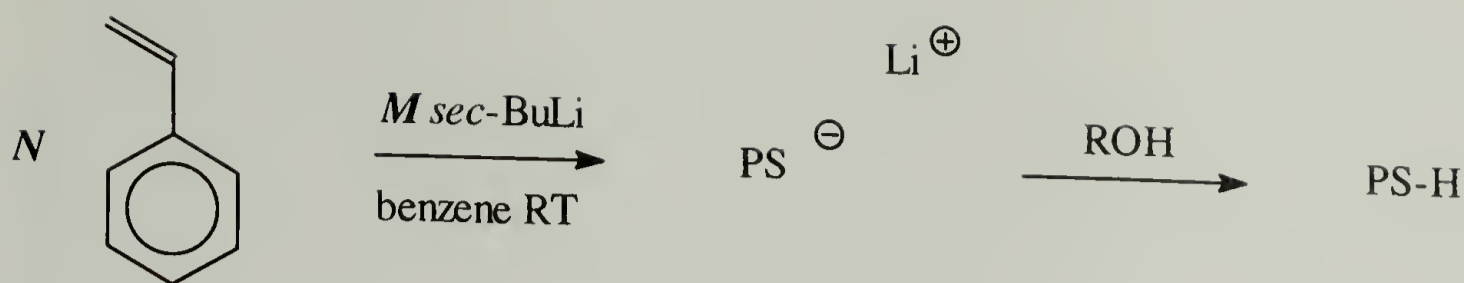


Figure A.3. Anionic polymerization of styrene initiated with sec-butyllithium and terminated with a simple alcohol.

distillation to isolate pure, dry monomer. Benzene (~100 mL) was obtained from the solvent line after flaming the reaction flask under vacuum and backfilling with N₂ three times.

A typical reaction was conducted as follows. Benzene was taken from the solvent line as described earlier. Monomer was distilled as noted above. Prior to addition of any reagents, care was taken to ensure that the rate of stirring in the polymerization flask was sufficient and stable. A calculated amount of diluted *sec*-butyllithium was added to the reaction flask via gas-tight syringe. Initiator should be added first since the addition of the first monomer unit is the fastest step, therefore the rate of monomer addition will not be as critical. The appropriate amount of styrene monomer was then added again via gas-tight syringe (~5.0 mL). The solution turns a shade of orange (depending on the concentration of chain-ends) indicating successful initiation and propagation. The reaction was allowed to continue overnight for convenience. It should be noted that the reaction retains its full color overnight, indicating that the glassware is successful in maintaining a sufficiently dry nitrogen atmosphere over an extended period of time. At the end of the reaction period, degassed ethanol was added via cannula to terminate the reaction. The polymer was precipitated by cannulating the solution out of the reaction flask into stirring methanol and filtered. If the product was too fine a powder to work

with, the polymer was redissolved in tetrahydrofuran, reprecipitated into an excess of methanol, filtered and dried under vacuum at 70 °C for several days.

Polymer molecular weights and distributions were determined by gel permeation chromatography (GPC) relative to calibration with polystyrene. The GPC system was equipped with Polymer Laboratories PL gel columns (10^4 , 10^3 , 10^2 Å), a Polymer Laboratories LC 1120 HPLC pump with THF as the mobile phase, and an IBM LC9563 Variable UV detector set at 254 nm. A representative GPC trace of a polystyrene homopolymer produced by living anionic polymerization technique as described above is shown in Figure A.4. This particular polymer has a $M_n = 147K$ and a $pdi = 1.03$. The peak at ~32 minutes corresponds to an internal standard, toluene, that is added to the solution prior to injection, enabling the software to make minor adjustments due to small variations in flow rate and injection time.

A.4. Synthesis of Carboxylic Acid End-functionalized Polystyrene

Quirk et al.¹⁰ studied the reaction of poly(styryl)lithium with carbon dioxide under a variety of conditions to produce end-carboxylated polymers. It was determined that under certain conditions one can achieve 100% carboxylation of the living chain-ends with no evidence of the dimer ketone or trimer alcohol. A schematic representation of the chemistry involved in producing carboxylated polystyrene is shown in Figure A.5. This chemistry was easily adaptable to the experimental setup in our laboratories, therefore making the synthesis of carboxylic acid end-functionalized polystyrene trivial.

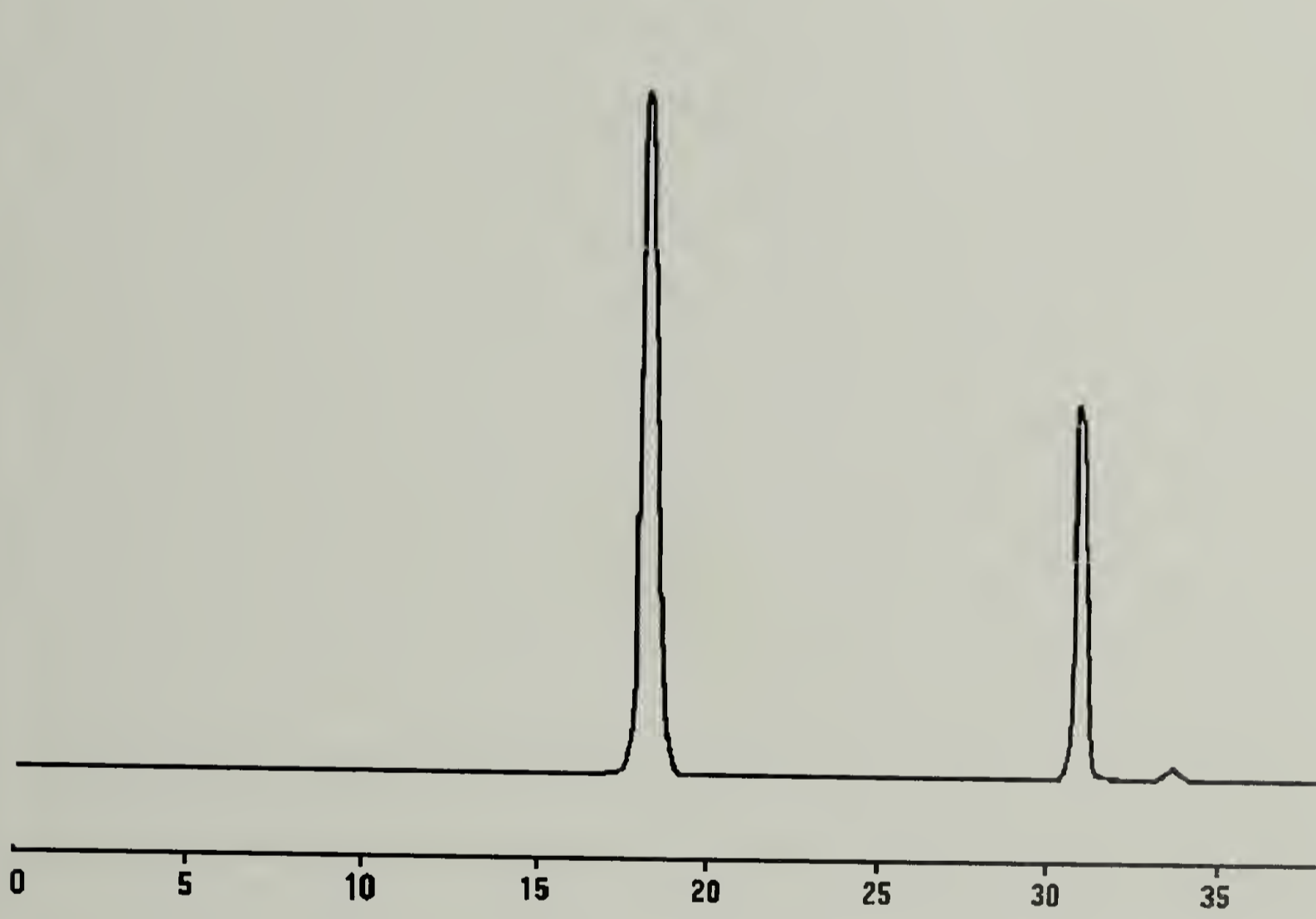


Figure A.4. Representative GPC chromatogram of a polystyrene homopolymer synthesized by living anionic polymerization.

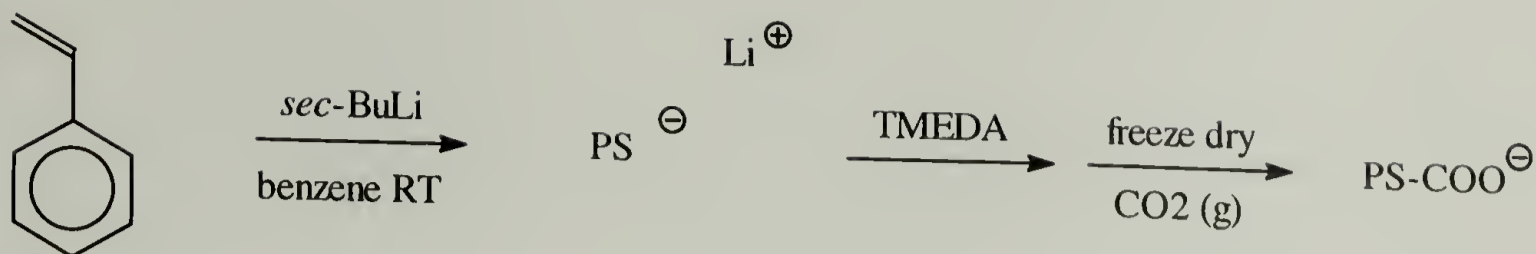


Figure A.5. Anionic polymerization of styrene followed by several steps to yield the carboxylated polymer.

In brief, poly(styryl)lithium is synthesized in benzene using *sec*-butyllithium as the initiator, as described earlier. Once all monomer is consumed, the addition of CO_2 without any precautions would result in 28% of the dimeric ketone and 12% of the trimeric alcohol,¹⁰ since polymeric organolithiums exist as a dimeric species in benzene. Addition of a Lewis base to organolithiums is known to break up these associations, so the procedure was modified to include the addition of tetramethylethylenediamine (TMEDA), resulting in the monomeric organolithium compound. Further isolation of chain-ends from one another was achieved by freeze-drying the polymer solution before introduction of CO_2 . This procedure results in no detectable amounts of the dimer or trimer species.

A typical carboxylation reaction proceeded as follows. Styrene was purified as described in the preceding section. Polymerization was initiated in benzene using a calculated amount of *sec*-BuLi and was allowed to continue overnight for convenience. During this time, tetramethylethylenediamine (TMEDA) was purified by distillation from CaH_2 followed by trap-to-trap distillation after addition of a few drops of concentrated *sec*-BuLi. A two-fold excess of TMEDA (calculated from the number of living chain-ends) was then added to the polymerization flask via syringe. The solution quickly turns from orange to red in color, proving the efficiency of TMEDA to break up the

aggregation of PS-Li. The solution was allowed to stir for 5 min, at which time it was placed into liquid N₂ to freeze the solution. The reaction flask was then attached to a vacuum line, and the solid solution was pumped under full vacuum (~10 mTorr) overnight to completely remove all traces of solvent. The resulting solid retained its reddish tint throughout the process. Carbon dioxide was then introduced into the reaction flask by first purging the antechamber with 15 psi CO₂ gas, then exposing the solid poly(styryl) anion to a blanket of CO₂ overnight. The color of the solid dissipated quickly upon exposure to CO₂, but diffusion of gaseous CO₂ through a glassy matrix occurs very slowly. Therefore the solid was left under CO₂ overnight to ensure complete reaction of the chain-ends. Afterwards, the solid polymer was dissolved in THF containing 10% v/v 1M HCl for 12 hr to hydrolyze the lithium salt and yield the carboxylic acid-terminated polymer. The end-capped polymer was then precipitated into an excess of methanol, recovered by filtration, and dried under vacuum at 70 °C for several days.

The efficiency of the carboxylation reaction was checked by TLC with toluene as the eluent, and compared to PS-H prepared as described in the polystyrene homopolymer section. Toluene was chosen as the eluent since it was to be the solvent used for adsorption studies, and should be a clear indicator of whether or not the polymer adsorbs from this solvent. Several molecular weight PS-COOH samples were prepared, and those having molecular weights below 41K showed no elution ($R_f = 0$) while those having molecular weight greater than 41K, as well as the PS-H homopolymer, eluted completely ($R_f = 1$). This is in good agreement with previous work by Iyengar et al.¹¹

A.5. Synthesis of P(S-b-MMA) Block Copolymers

The synthesis of block copolymers of styrene and methyl methacrylate was undertaken to fulfill the need for materials in the Russell research group. This section will detail the synthetic approaches used to prepare diblock copolymers, P(S-b-MMA), as well as diblock copolymers having one block deuterated, P(dS-b-MMA). The ratio of segments A/B in an AB-type block copolymer will dictate the morphology of the material. In general, a ratio of 90/10 results in spherical domains of B within a matrix of A; a ratio of 70/30 results in cylinders of B surrounded by a matrix of A; a ratio of 50/50 yields a lamellar structure of alternating sheets of A and B. These ratios are calculated based on volume fractions of each component in the block copolymer. It should be obvious that these types of materials demand the precision and control that only living anionic polymerization can afford. More recent techniques, such as TEMPO-mediated polymerizations,^{12,13} are making significant advances in the preparation of similar block copolymers, but it has yet to be determined if materials prepared in this fashion can compete with those made by anionic methods.

The synthesis of block copolymers of styrene and methyl methacrylate is more tedious and involved than the preparation of simple homopolymers. The acrylate group in MMA can undergo several side reactions that must be precluded by careful choice of reaction conditions. The acrylate anion is also too weak (the pK_a of the conjugate acid is 27) to initiate styrene ($pK_a = 41$), so the order of monomer addition is critical: styrene must be polymerized first followed by methyl methacrylate. But the styryl anion is a strong nucleophile and will attack the acrylate group on MMA, causing chain transfer and/or termination. Therefore, the styryl anion must be weakened by reaction with

diphenylethylene (DPE) prior to addition of MMA. Reaction of poly(styryl)lithium with DPE will lower the pK_a of the active anionic center, as well as present an anion that is too sterically hindered to attack the acrylate group on MMA. The use of a polar monomer (i.e. MMA) also requires the use of a polar solvent such as tetrahydrofuran (THF), and lower temperatures must be used to minimize chain transfer and termination reactions. A schematic representation of the synthesis of P(S-b-MMA) by living anionic methods is shown in Figure A.6.

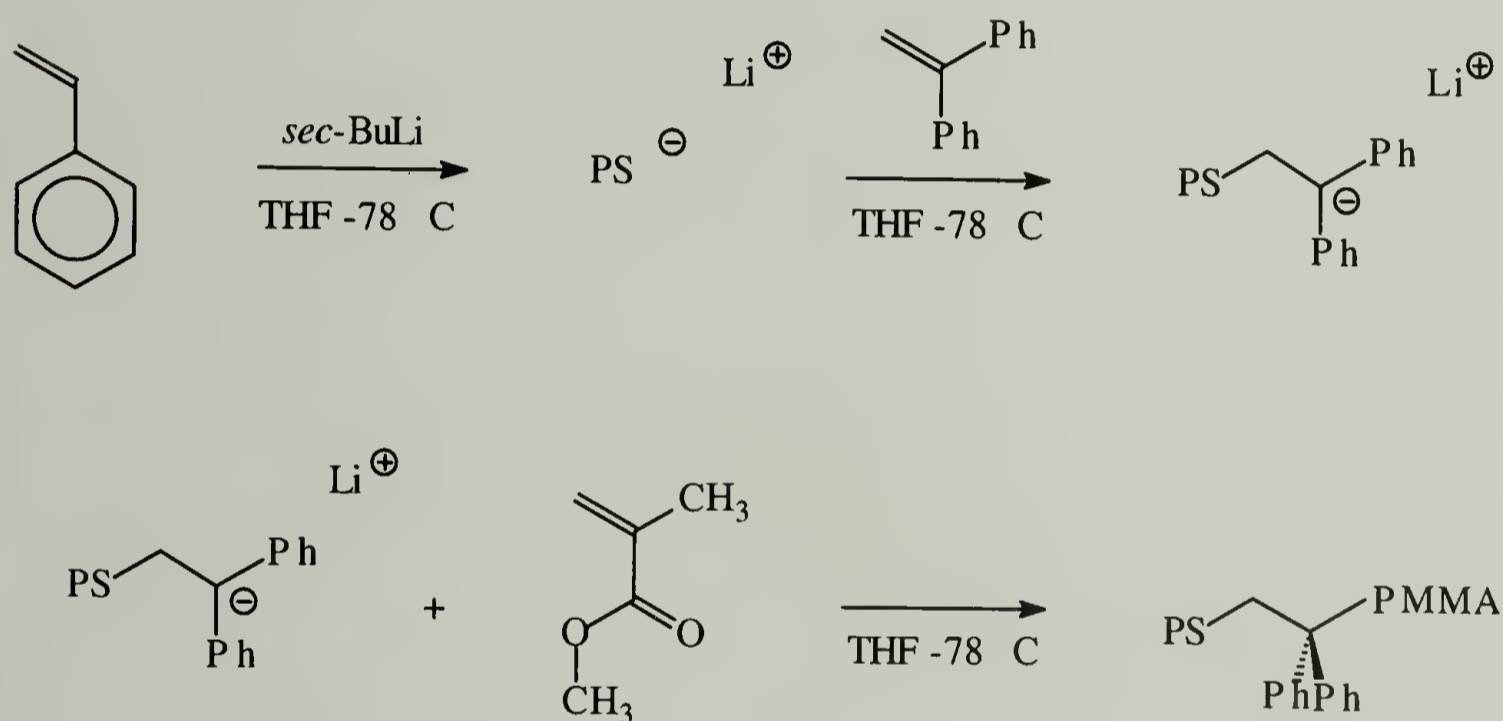


Figure A.6. Anionic polymerization of styrene followed by capping with diphenylethylene, which is then used to polymerize methyl methacrylate to produce a block copolymer, P(S-b-MMA).

A typical polymerization proceeded as follows. Styrene was purified as described in the preceding section. Methyl methacrylate was purified first by distillation from CaH₂ at reduced pressure (~100 mTorr, b.p.~ 60°C). Just prior to polymerization, an excess of MMA was thoroughly degassed by several freeze-pump-thaw cycles before the addition of triethylaluminum (TEA). TEA was added dropwise to the degassed MMA

until a persistent (faint) yellow color was observed. If any oxygen is present in the MMA, TEA will react with it to form a radical species that will then proceed to initiate polymerization of MMA in the flask. Therefore, the MMA was immediately distilled from TEA by trap-to-trap distillation as described for styrene. The purified monomer can then be measured out by syringe. Diphenylethylene (DPE) was purified by trap-to-trap distillation after addition of a few drops of concentrated *sec*-BuLi. DPE boils at 270 °C at ambient conditions, so even under full vacuum DPE must be heated to ~65 °C in order to distill.

Tetrahydrofuran (THF) was obtained from the solvent line just prior to polymerization. The reaction flask was then cooled to -78 °C using a dry ice/isopropanol bath. A calculated amount of initiator was then transferred into the reaction flask via gas-tight syringe, followed by a preset amount of styrene (~5.0 mL). Upon addition of styrene, the polymerization mixture turned yellow indicating successful initiation. After 15 minutes, a few drops of DPE were cannulated into the reaction flask, and the reaction mixture turned red proving efficient crossover. At this point, a small aliquot of PS-Li was removed in order to check the molecular weight of the PS block. Several drops of the poly(styryl)lithium solution were cannulated directly into degassed ethanol, filtered and dried before performing GPC. After 5 minutes, a calculated amount of MMA was added via syringe at which time the solution turns colorless. After 15 minutes, the polymerization was terminated by the addition of degassed ethanol. The solution was allowed to warm to room temperature, precipitated into methanol, filtered, and dried under vacuum at 70 °C for several days. The polymer was then purified by Soxhlet extraction with cyclohexane to remove any polystyrene homopolymer as a result of

termination upon addition of MMA. Cyclohexane is a theta solvent for polystyrene and a non-solvent for the block copolymer. At higher styrene contents (i.e. 90/10 P(S-b-MMA)), the diblock may form micelles and pass through the extraction thimble, making purification of these diblocks very difficult. The extraction also served to remove residual DPE since it was used in excess.

Characterization of the block copolymers involved GPC to determine molecular weight and polydispersity, followed by NMR to calculate the ratio of styrene to methyl methacrylate. To show how these results are used, examples of each characterization technique are shown in Figures A.7 – A.11. The molecular weight of the PS block was determined from GPC of the aliquot removed just prior to addition of MMA. The GPC chromatogram of the homopolymer is shown in Figure A.7. The GPC chromatogram of the block copolymer prior to purification is shown in Figure A.8. Clearly, a shoulder can be seen at longer elution times indicating the presence of PS homopolymer that was terminated when MMA was added. There also is a considerable amount of residual DPE in the diblock copolymer sample. After Soxhlet extraction, the homopolymer is successfully removed as well as the residual DPE. The GPC chromatogram of the purified block copolymer is shown in Figure A.9. [NOTE: It is imperative that all residual homopolymer be removed before conducting NMR and before conducting any experiments since the presence of homopolymer could significantly influence any results obtained subsequently. Therefore, all diblock copolymers should be extracted with cyclohexane even if homopolymer cannot be detected by GPC.] Unfortunately, the molecular weight of a diblock copolymer calculated by GPC is incorrect since the hydrodynamic volume of block copolymer can be drastically different than polystyrene,

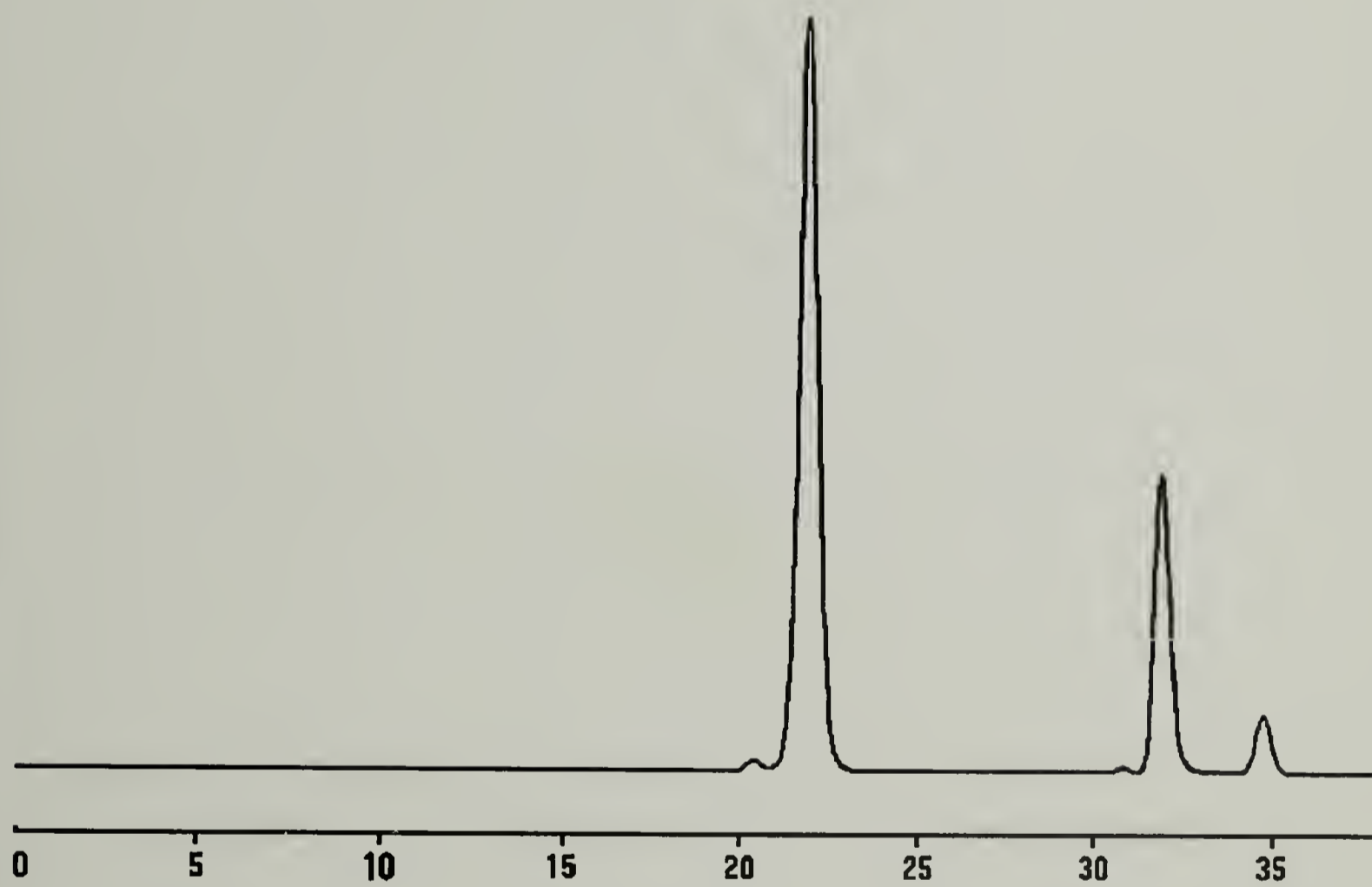


Figure A.7. Representative GPC chromatogram of P(S-b-MMA) synthesis: aliquot removed to characterize the molecular weight of the PS block.

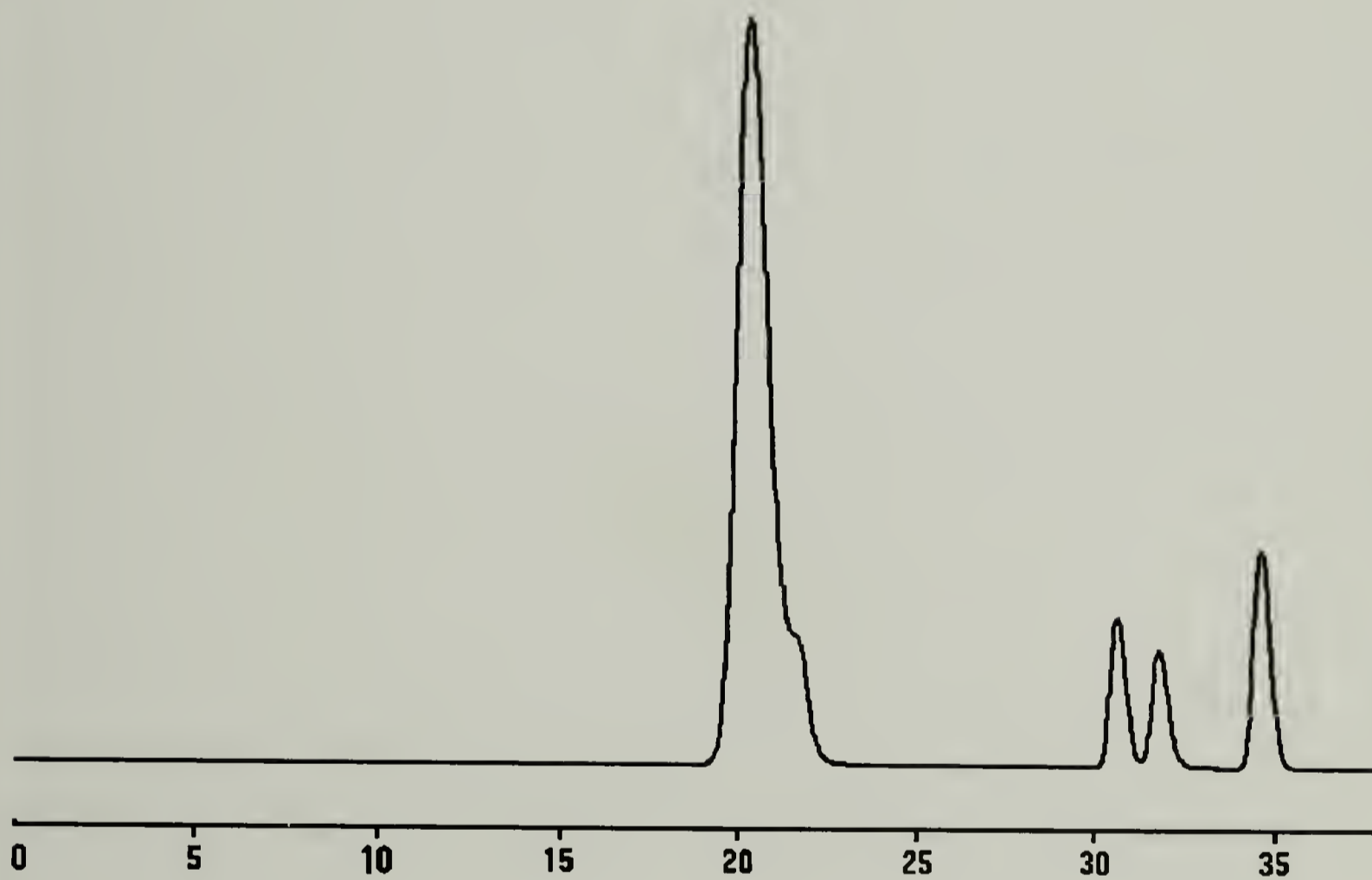


Figure A.8. Representative GPC chromatogram of P(S-b-MMA) synthesis: block copolymer before extraction to remove residual PS homopolymer and diphenylethylene.

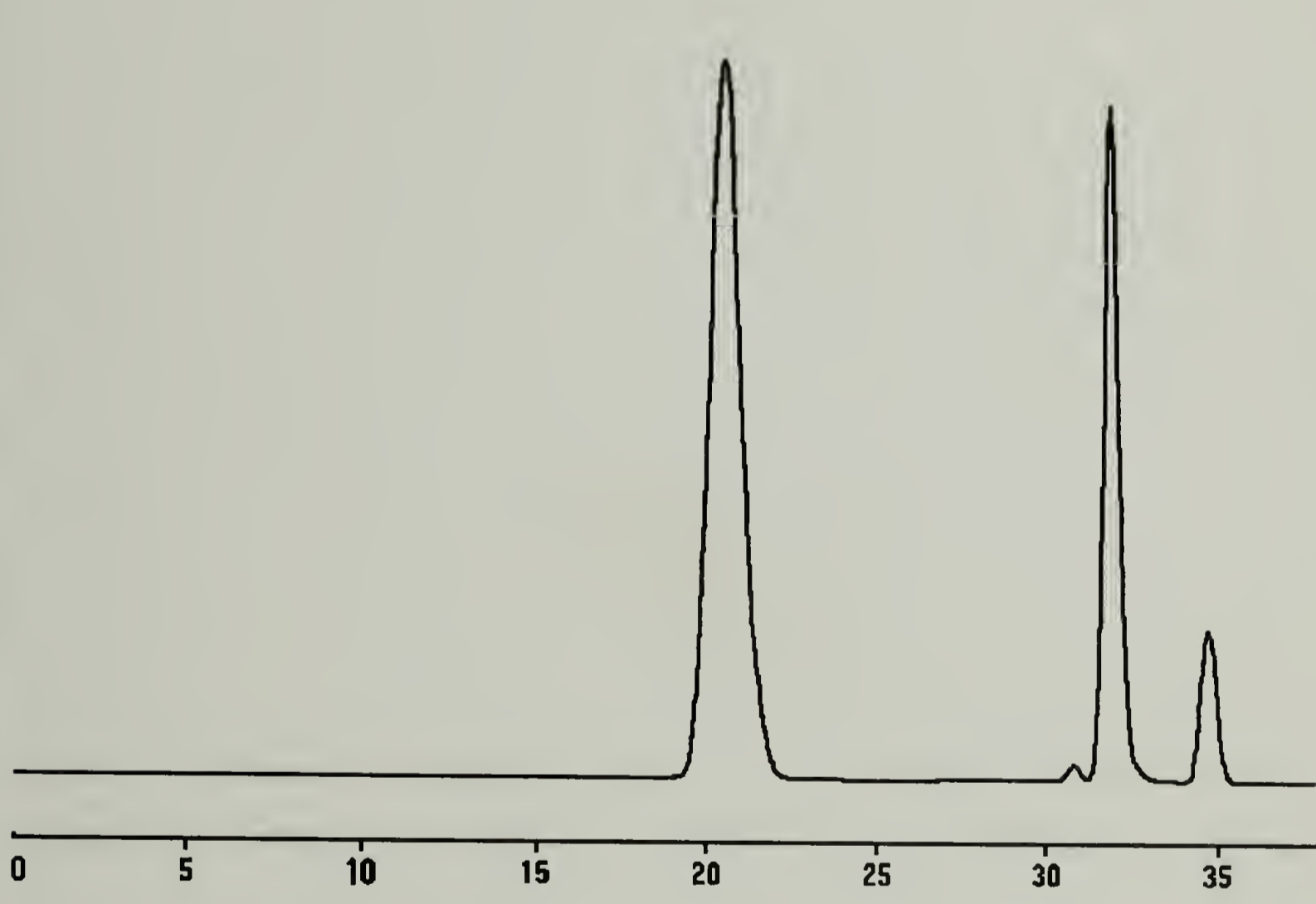


Figure A.9. Representative GPC chromatogram of P(S-b-MMA) synthesis: block copolymer after purification.

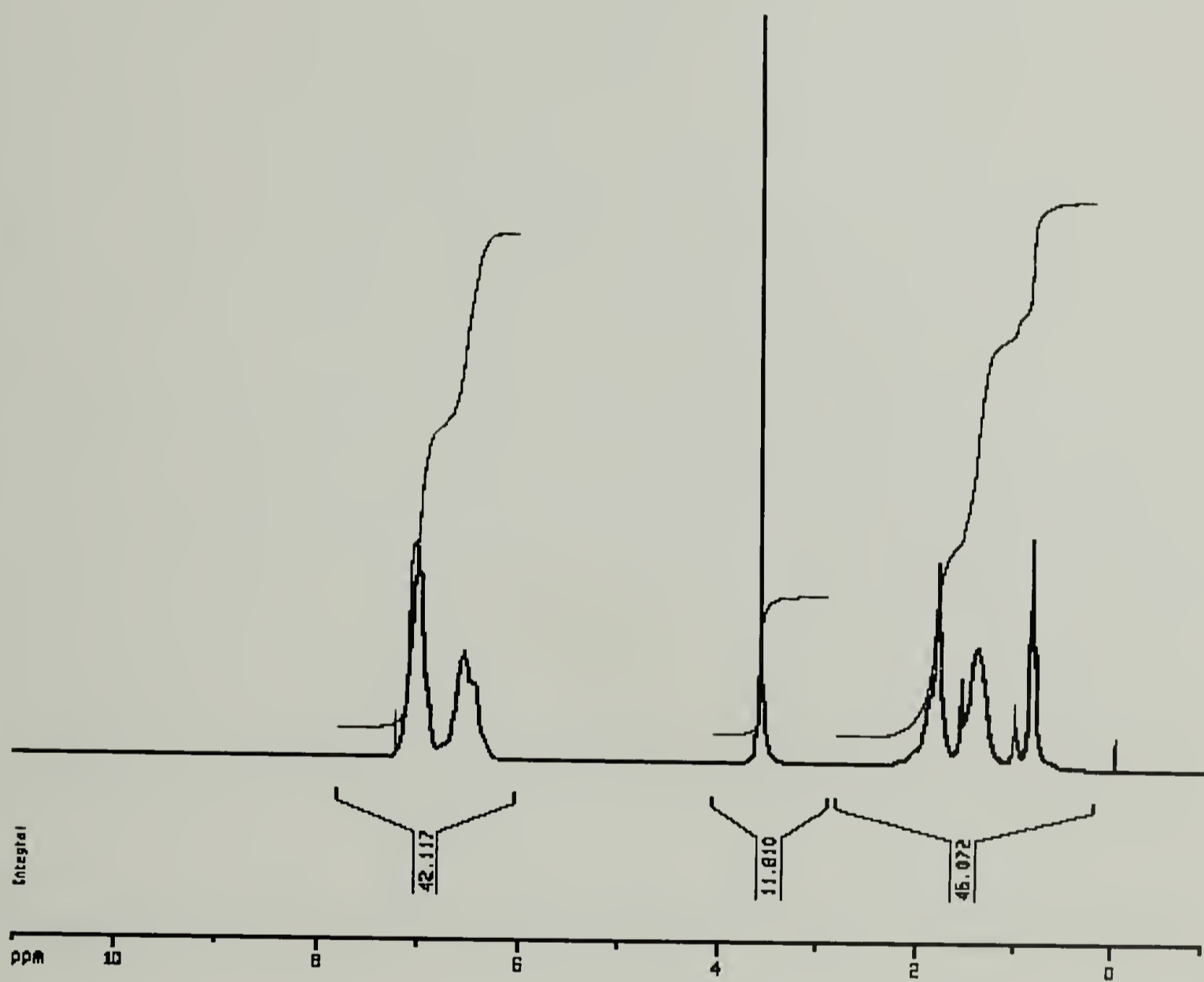


Figure A.10. Representative ^1H NMR trace of P(S-b-MMA) for determination of block copolymer composition.

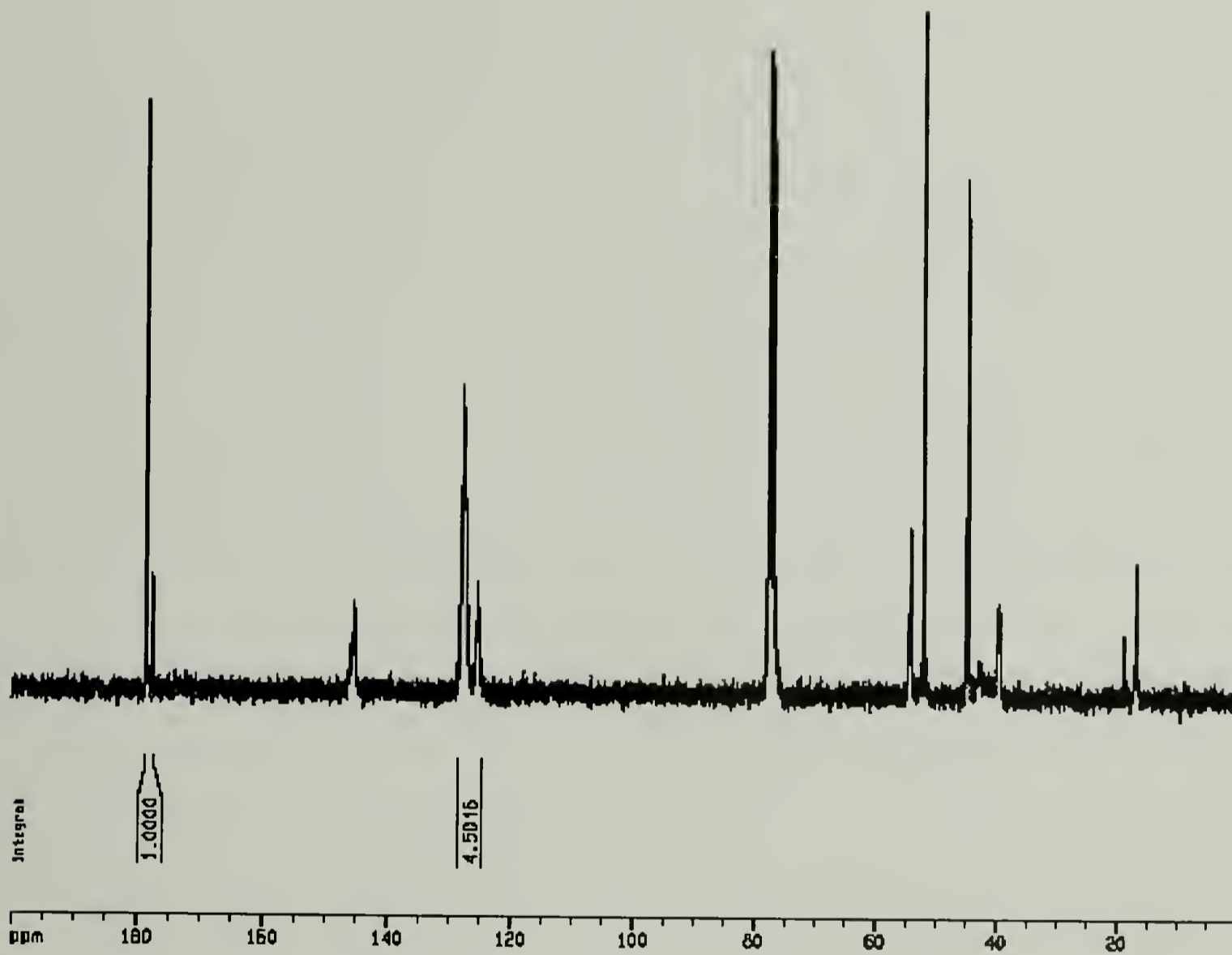


Figure A.11. Representative quantitative ^{13}C NMR trace of P(dPS-b-MMA) for determination of block copolymer composition where one block is deuterated.

which is used as calibration standards. Therefore, the GPC chromatogram of the purified diblock serves only to prove removal of homopolymer and DPE as well as provide an estimate of the polydispersity. The molecular weight of the diblock copolymer can only be calculated using the ratio of styrene to methyl methacrylate as determined by ^1H NMR (Figure A.10). The peaks of interest in the ^1H NMR are the aromatic protons (6.0-7.5 ppm) and the methacrylate protons (3.6 ppm). If deuterated styrene has been used in the synthesis of the polystyrene block, ^1H NMR is now useless in determining copolymer composition, and therefore a quantitative ^{13}C experiment must be conducted. An example of a quantitative ^{13}C experiment is shown in Figure A.11. The peaks of interest are the carbonyl carbon (~180 ppm) and the aromatic carbons (~125-130 ppm).

A.6. Synthesis of Fluorescently Labeled Polystyrene

The synthesis of anthryl- and phenanthryl-label polystyrene was performed to supplement the research efforts of the Watkins research group. The project was to explore the diffusion of polymers across interfaces while exposed to supercritical CO_2 investigated by non-radiative energy transfer (NRET) experiments. The synthesis of these polymers proved to be more involved than initially expected, requiring the synthesis of unique monomers. These monomers were derivatives of diphenylethylene with one phenyl group being replaced by either an anthryl- or phenanthryl-moieity. Diphenylethylene (DPE) is known to not undergo homopolymerization under anionic conditions, therefore DPE and its derivatives can be used as capping agents in living anionic polymerization to yield the end-functionalized polymer. This section will illustrate the small molecule chemistry involved in the synthesis of the fluorescent

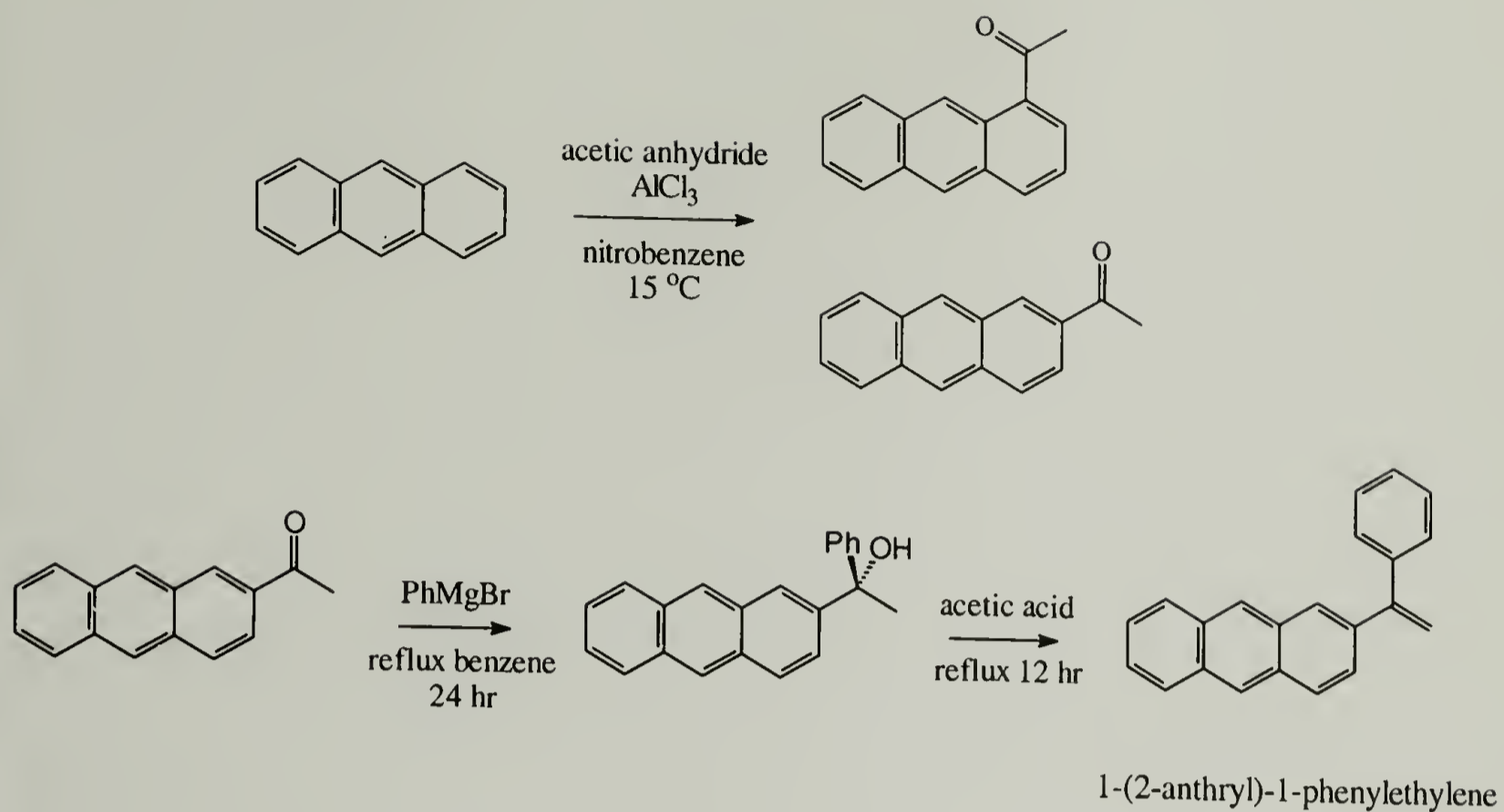
monomers, as well as the inclusion of these monomers in a capping reaction of poly(styryl)lithium followed by the purification of the polymer products.

The synthesis of 1-(2-anthryl)-1-phenylethylene had been reported.¹⁴ The synthesis of 1-(2-phenanthryl)-1-phenylethylene had not been reported, but the 9-substituted monomer had been¹⁴ and the 2-substituted monomer was expected to follow the same chemistry with only minor alterations. The synthetic scheme is shown in Figure A.12. While 2-acetylphenanthrene was commercially available, 2-acetylanthracene was not and had to be prepared by Friedel-Crafts reaction of anthracene with acetic anhydride in the presence of AlCl_3 . This reaction was carried out in nitrobenzene at 15 °C. It should be noted that Friedel-Crafts acylation results in only single additions to aromatic rings, which then deactivates the ring to further substitution. Under these conditions, the reaction favors the formation of the 2-substituted product with the 1- and 9-substituted products being impurities. These can easily be removed by recrystallization from benzene/hexanes due to the poor solubility of the 2-substituted product. The purity of 2-acetylanthracene was checked by ^1H NMR, and is shown in Figure A.13. Prior to purification, three peaks at 2.7-2.9 ppm, attributed to the 1-, 2-, and 9-substituted acetyl methyl group, could be observed and only the 2-substituted peak remains upon purification. The product, 2-acetylanthracene, was then dissolved in warm benzene and 1.5 molar excess of 3M phenylmagnesium bromide was added dropwise via gas-tight syringe. The solution was refluxed under N_2 for 24 hr. The reaction was then poured into an ice/water mixture and the water layer was extracted with benzene. The organic layer was dried over magnesium sulfate and rotovaped to yield the alcohol product. ^1H NMR showed the presence of the both the alcohol and final, dehydrated product as well.

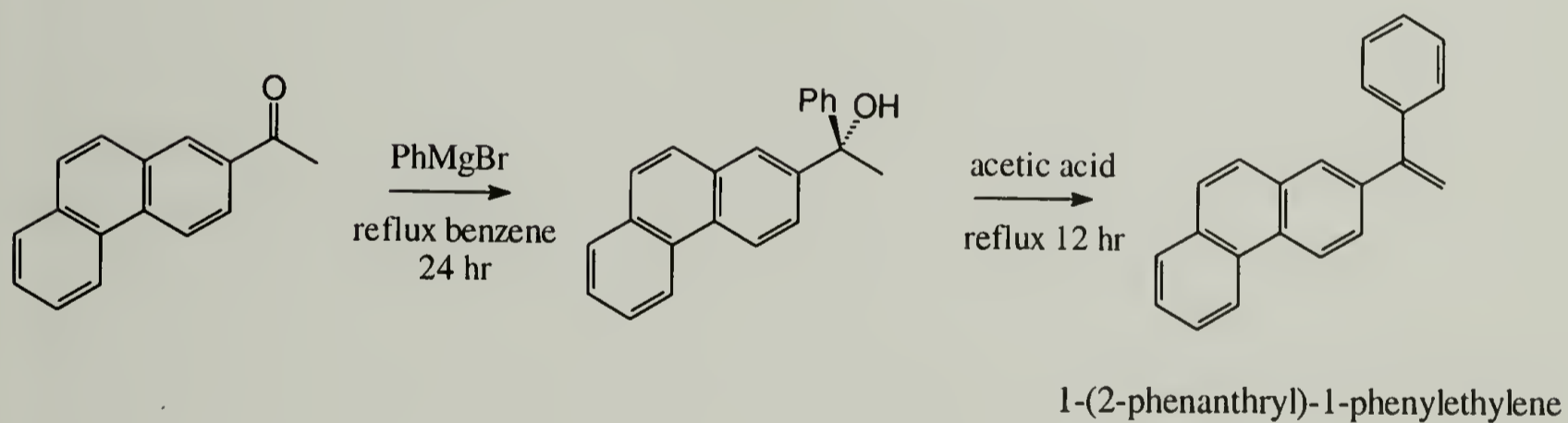
Dehydration of the alcohol was accomplished by refluxing in acetic acid for 12 hr to yield 1-(2-anthryl)-1-phenylethylene. The monomer was further purified by recrystallization from benzene/hexanes. The purity of the monomer was checked by ^1H NMR (see Figure A.14) and was determined to be ~100%.

The synthesis of 1-(2-phenanthryl)-1-phenylethylene was carried out in a similar fashion as the anthryl compound, beginning with treatment of 2-acetylphenanthrene with phenyl Grignard followed by dehydration of the alcohol to yield the vinyl monomer. The solubility of the phenanthryl monomer is much higher than the anthryl, which made purification by recrystallization difficult. Thus, the phenanthryl monomer can only be obtained at ~98% purity as determined by ^1H NMR (see Figure A.15).

Preparation of the fluorescently labeled polymers followed the synthesis of polystyrene homopolymers with the inclusion of the termination with anthryl- and phenanthryl-substituted monomers. The reaction scheme is shown in Figure A.16 using the anthryl-substituted monomer as an example. A typical polymerization proceeded as follows. Styrene was purified as described in the preceding sections. Polymerization was initiated in benzene using a calculated amount of *sec*-BuLi and was allowed to continue overnight for convenience. During this time, the fluorescent monomers (1.2 molar excess with respect to concentration of chain ends) were added to separate polymerization flasks that contained 24/40 ground glass joints to facilitate working with solids. The flasks were heated mildly using heating mantles (~50 °C) overnight under vacuum. Care was taken not to sublime the materials during this process. Dry benzene was then added to solubilize the monomers prior to addition of poly(styryl)lithium.



A



B

Figure A.12. Synthesis of chromophore monomers that contain anthryl (A) and phenanthryl (B) moieties. Monomer A required synthesis of the starting material, 2-acetyl anthracene.

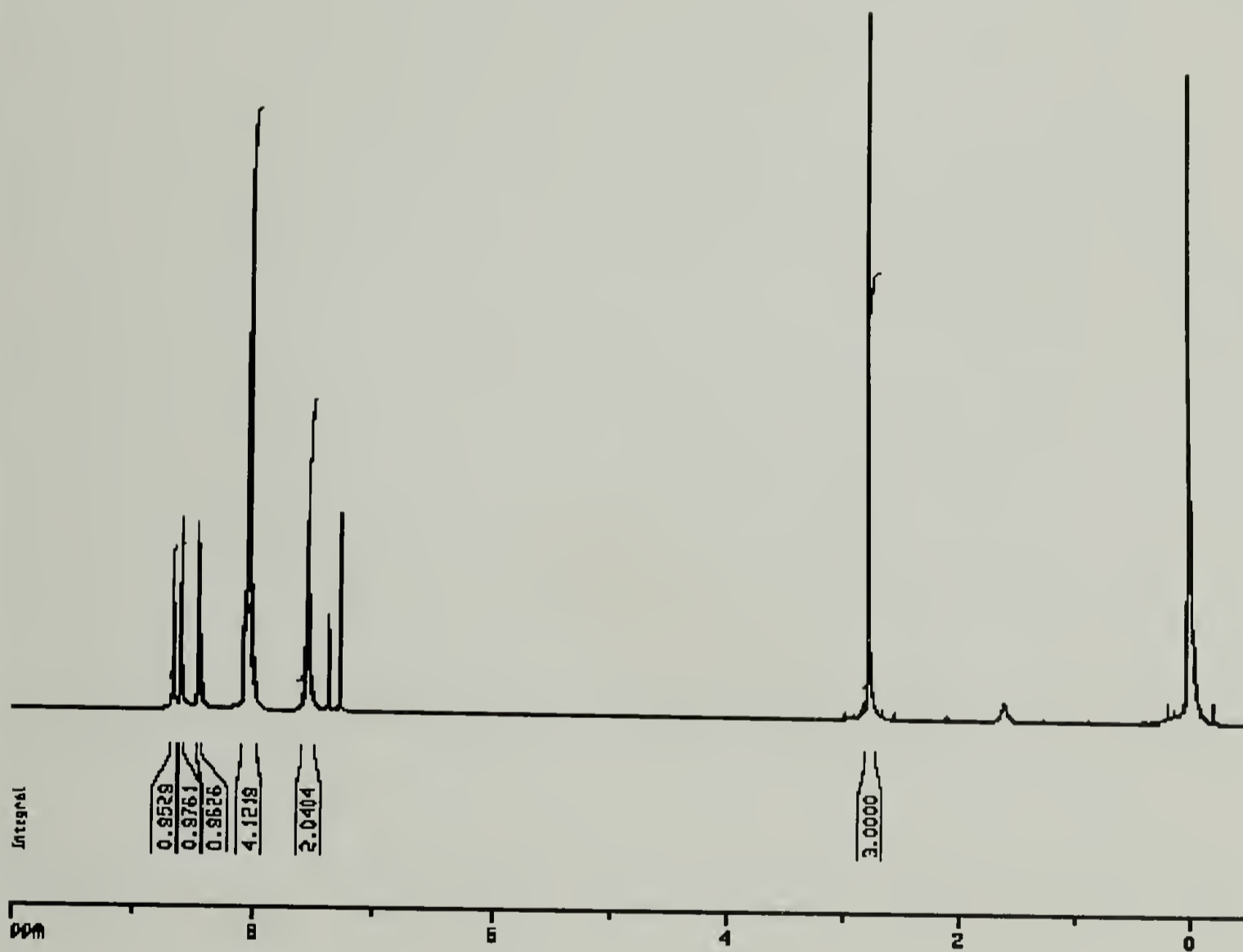


Figure A.13. ^1H NMR of starting material, 2-acetyl anthracene, after purification.

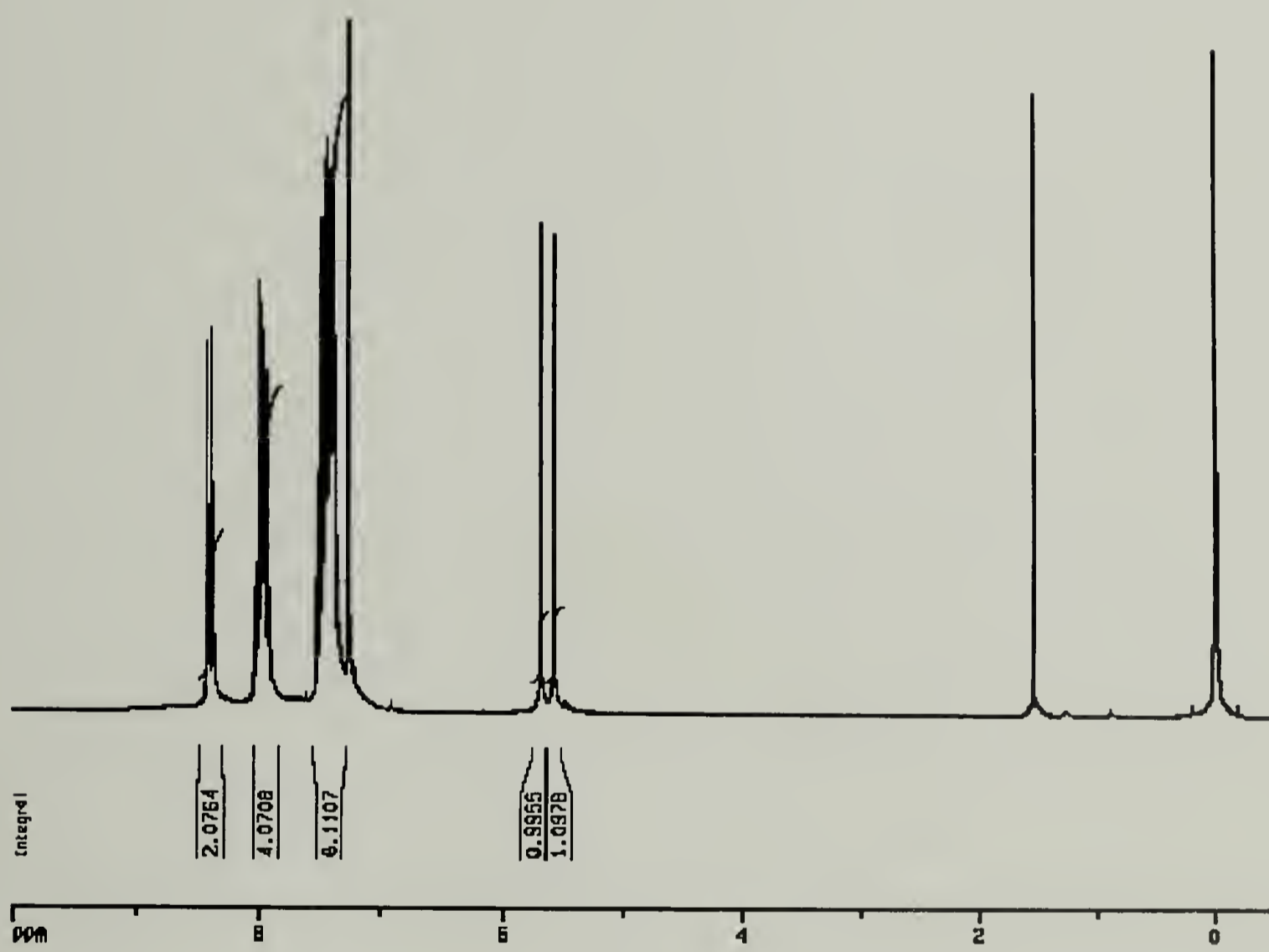


Figure A.14. ^1H NMR of 1-(2-anthryl)-1-phenylethylene after purification.

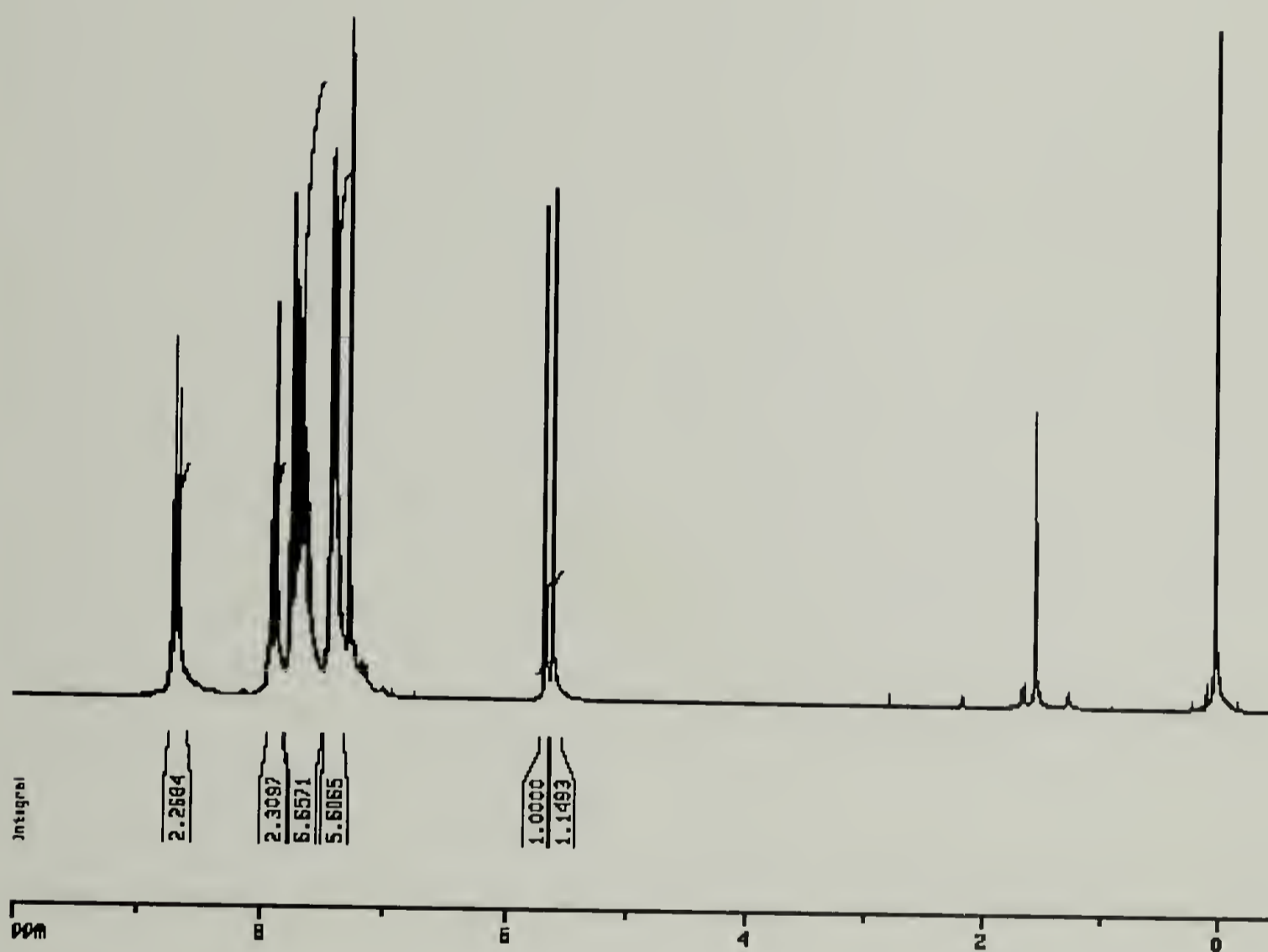


Figure A.15. ^1H NMR of 1-(2-phenanthryl)-1-phenylethylene after purification.

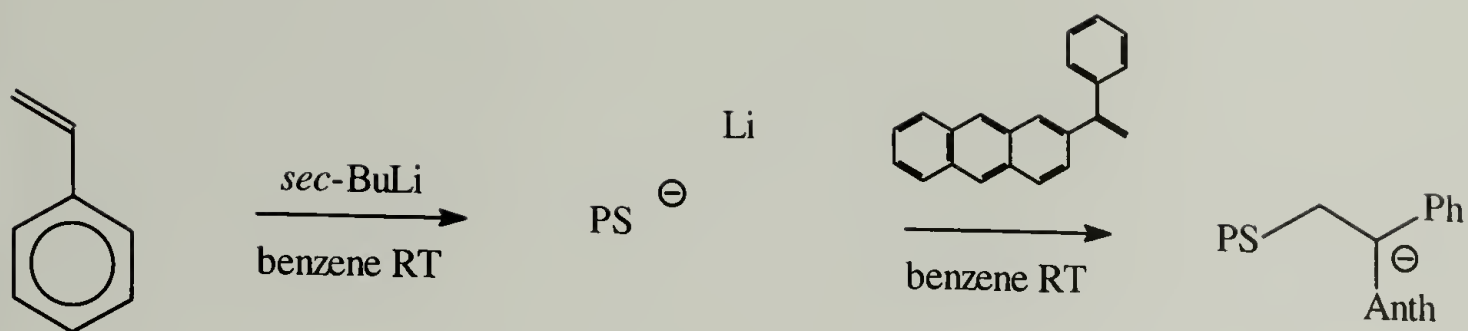


Figure A.16. Anionic polymerization of styrene initiated with *sec*-butyllithium and terminated with fluorescent monomer (A).

Half of the poly(styryl)lithium solution was then cannulated into the flask containing the solution of anthryl monomer, while the other half was cannulated into the flask containing the solution of phenanthryl monomer. This ensured both the anthryl- and the phenanthryl-labeled polymers had identical molecular weights and polydispersity. The experimental setup for the end-capping reactions is shown in Figure A.17.

The polymerizations were terminated with degassed ethanol, and the polymers were precipitated in methanol and dried. Since the experiments to be carried out involve the diffusion of polymer chain ends, any residual monomer trapped in the polymer upon precipitation could lead to erroneous data and misinterpretation. Therefore, it is vital that all residual monomer be removed from the polymer before any experiments are conducted. Purification of the polymers was achieved by reprecipitation, with the expectation that most of the monomer will remain in the THF/methanol mixture upon precipitation. The polymer was dissolved in THF and precipitated in methanol several times until no residual monomer was detected. This purification method was followed by GPC, as shown in Figure A.18 and A.19 for the anthryl- and phenanthryl-capped polymers, respectively. The monomers elute at ~31 minutes in the chromatograms (the internal standard, toluene, elutes at ~32 minutes). It can be seen that after three

reprecipitations all residual monomer is removed. It should also be noted that these samples contain a small amount ($< 1\%$) of the coupled dimeric product (PS-PS), but its presence should not affect the experiments to be conducted.

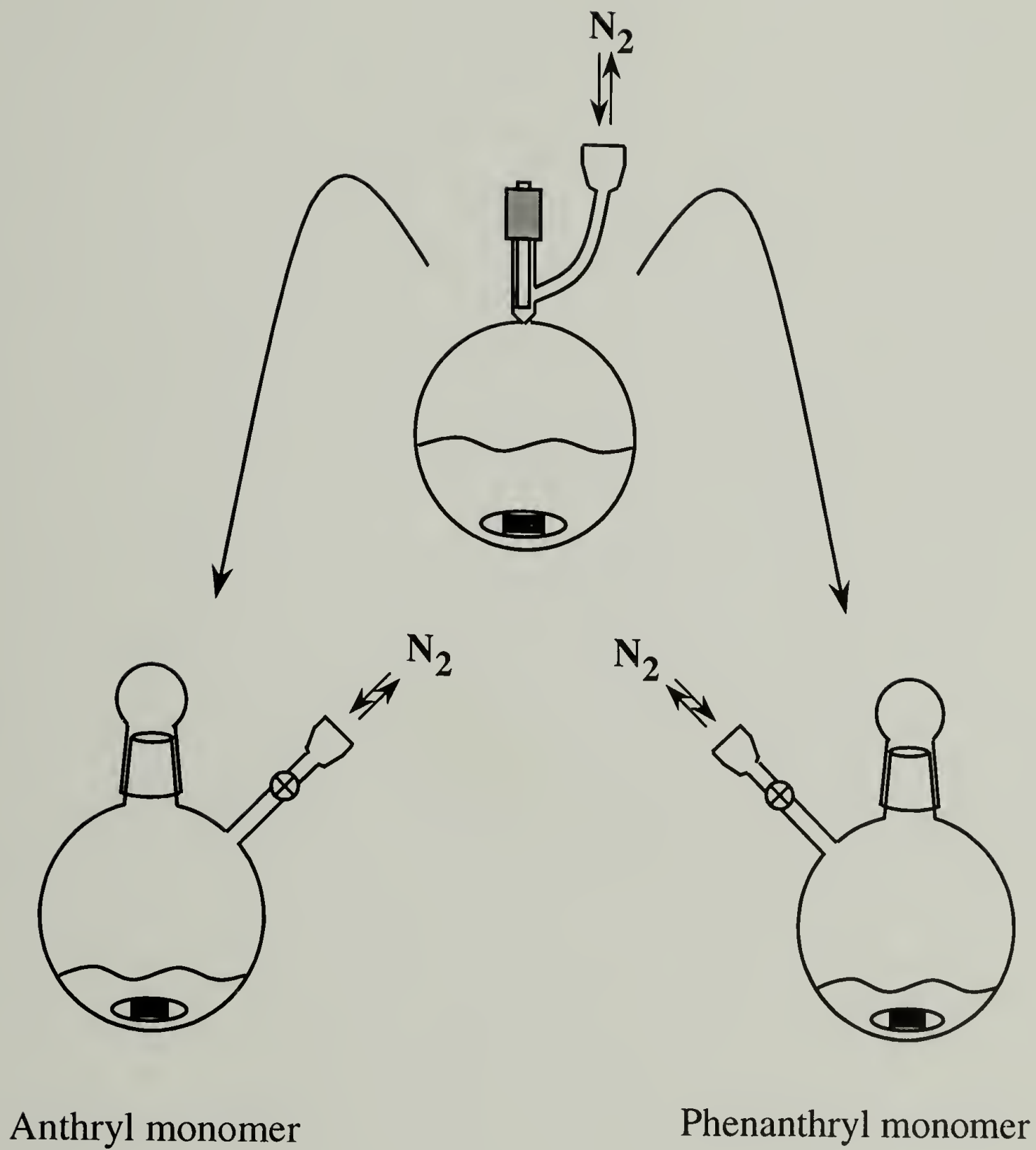


Figure A.17. One-batch reaction for synthesizing both anthryl- and phenanthryl-labeled PS having exactly the same molecular weight and polydispersity.

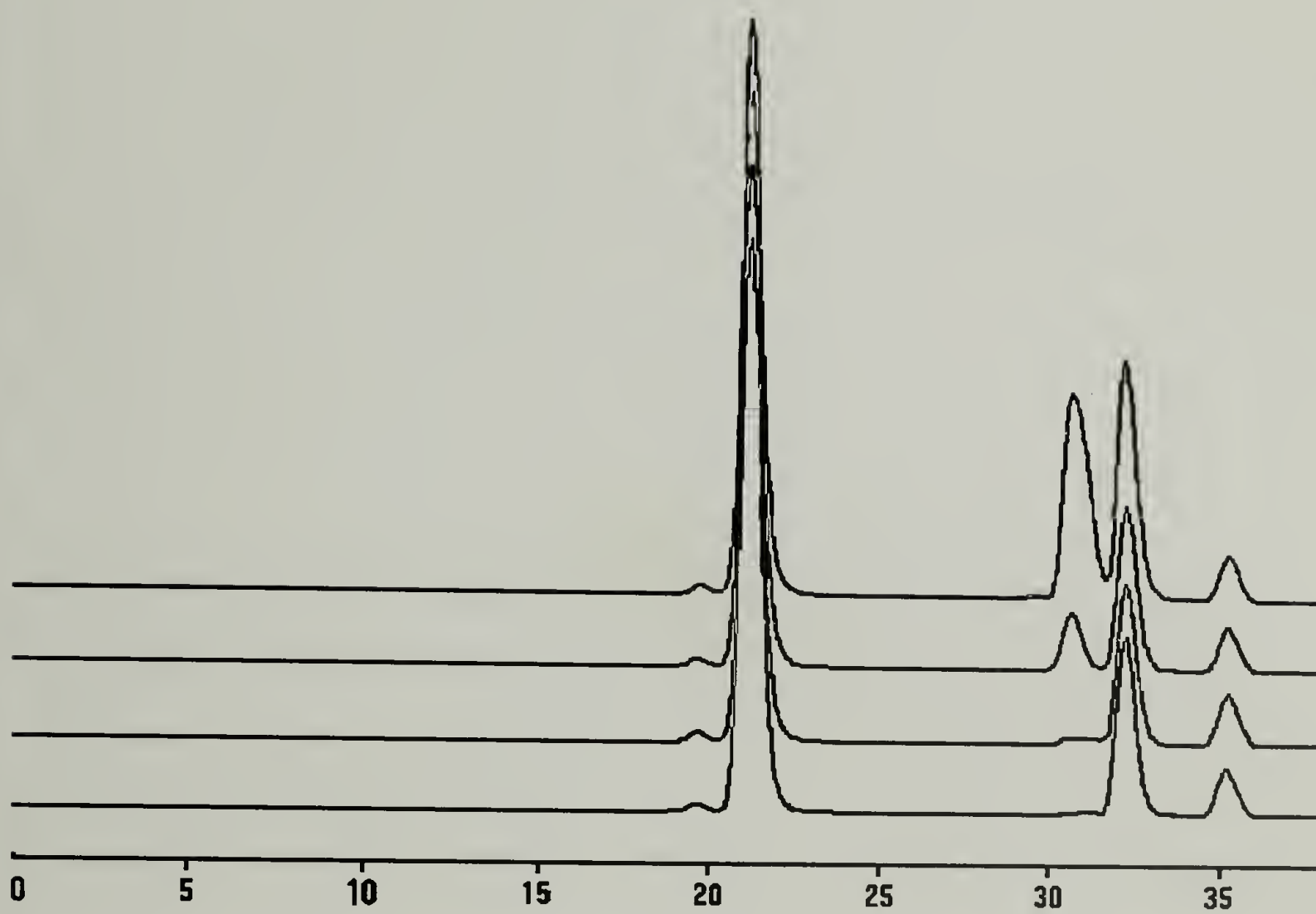


Figure A.18. GPC chromatogram of PS-Anth showing the removal of residual anthryl monomer by reprecipitation.

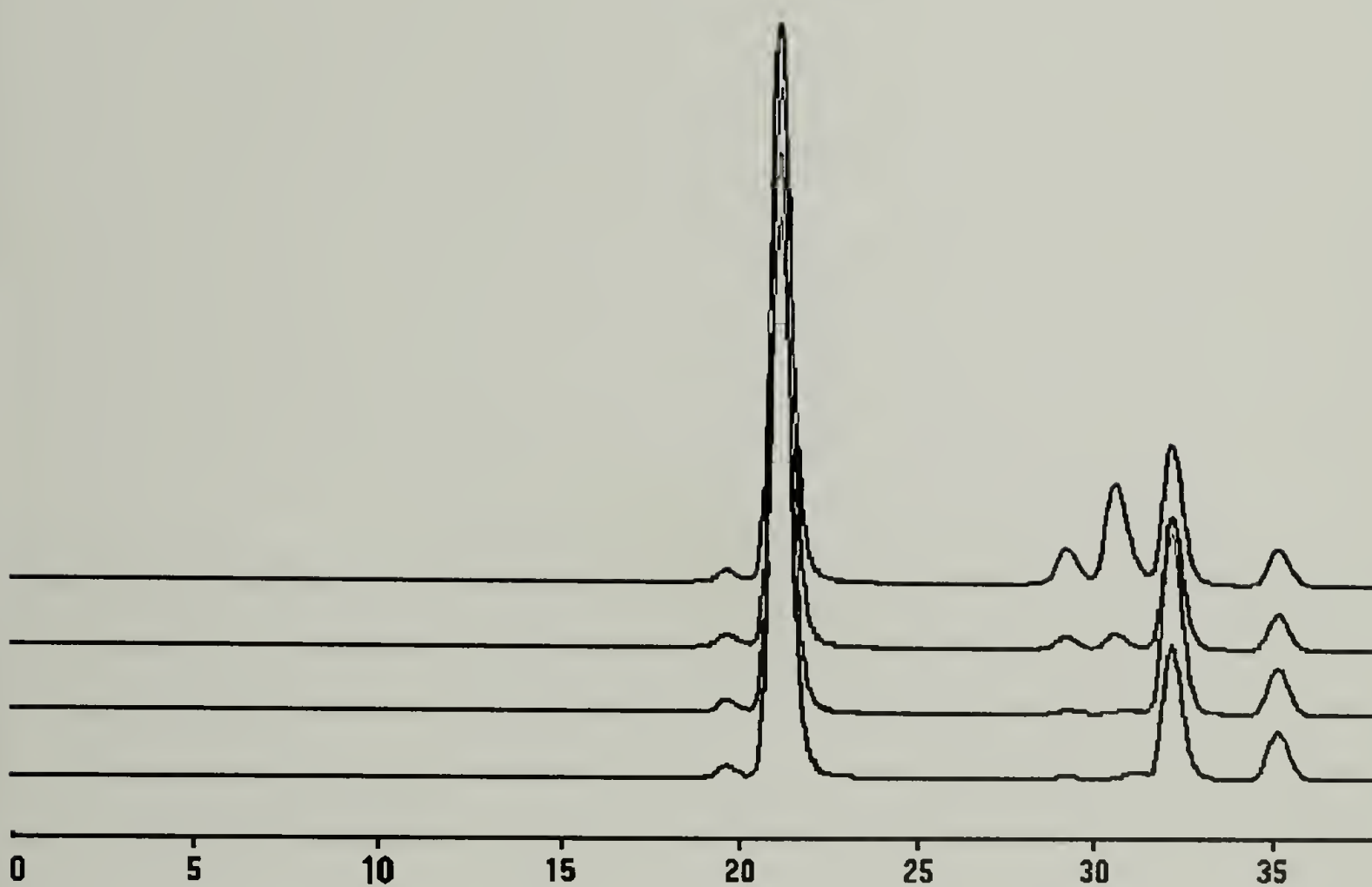


Figure A.19. GPC chromatogram of PS-Phen showing the removal of residual phenanthryl monomer by reprecipitation.

A.7. References Cited

1. Quirk, R.; Kinning, D., and Fetters, L., in *Comprehensive Polymer Science*, G. Allen, Editor. 1989, Pergamon Press: Oxford. p. 1.
2. Quirk, R., *Anionic Synthesis of Polymers with Functional Groups*. 1st Ed. ed, ed. G. Allen. Vol. 7. 1989, Oxford: Pergamon Press. 83.
3. Hsieh, H. and Quirk, R., *Anionic Polymerization: Principles and Practical Applications*. 1996, New York: Marcel Dekker. 727.
4. Zeigler, K.; Colonius, H., and Schafer, D. *Annu. Chim.*, **1929**, 473, 36.
5. Zeigler, K. and Schafer, D. *Annu. Chim.*, **1930**, 479, 150.
6. Zeigler, K.; Jakob, L.; Wolltham, H., and Wenz, A. *Annu. Chim.*, **1934**, 511, 64.
7. Szwarc, M. *Nature*, **1956**, 178, 1168.
8. Szwarc, M.; Levy, M., and Milkovich, R. *JACS*, **1956**, 78, 2656.
9. Pangborn, A.; Giardello, M.; Grubbs, R.; Rosen, R., and Timmers, F. *Organometallics*, **1996**, 15, 1518.
10. Quirk, R.; Yin, J., and Fetters, L. *Macromolecules*, **1989**, 22, 85.
11. Iyengar, D., PhD Thesis, University of Massachusetts, Polymer Science and Engineering, **1992**.
12. Burguiere, C.; Dourges, M.-A.; Charleux, B., and Varion, J.-P. *Macromolecules*, **1999**, 32, 3883.
13. Benoit, D.; Harth, E.; Fox, P.; Waymouth, R., and Hawker, C. *Macromolecules*, **2000**, 33, 363.
14. Hruska, Z.; Vuillemin, B.; Riess, G.; Katz, A., and Winnik, M. *Makromol. Chem.*, **1987**, 193, 1987.

APPENDIX B

FOAMING OF THIN FILMS / TRSAXS

B.1. Introduction

The use of supercritical carbon dioxide (SC CO₂) in producing microcellular foams has gained acceptance not only in the academic realm but also in the industrial sector. But one critical question arises when contemplating the adaptation of SC CO₂ foaming to more intricate and demanding applications such as the production of low dielectric thin film materials. That question concerns the possible limitations in size scales of the porosity attainable using SC CO₂ as a blowing agent. Two approaches will be discussed in this section that seek to better understand the foaming process in general and aim to quantify the critical length scales that are dominant when striving to foam smaller and thinner materials. The first approach will be to investigate the foaming of polymer thin films in order to ascertain the critical thickness at which pore formation becomes impossible. The second will be to observe the nucleation and growth of pores via small angle x-ray scattering (SAXS).

It has been well established that rapid decompression of a SC CO₂ / polymer mixture results in a microcellular foam encased by a nonporous skin.¹⁻³ The formation of the nonporous skin has been attributed to the rapid diffusion of CO₂ from the free surface of the sample, resulting in a depletion layer where nucleation of pores cannot occur. It has also been shown¹ (Figure B.1) that the thickness of this nonporous skin decreases as the saturation pressure increases, reaching a minimum plateau at pressures above 4000 psi (27 Mpa). It has been experimentally observed in our labs that the skin thickness

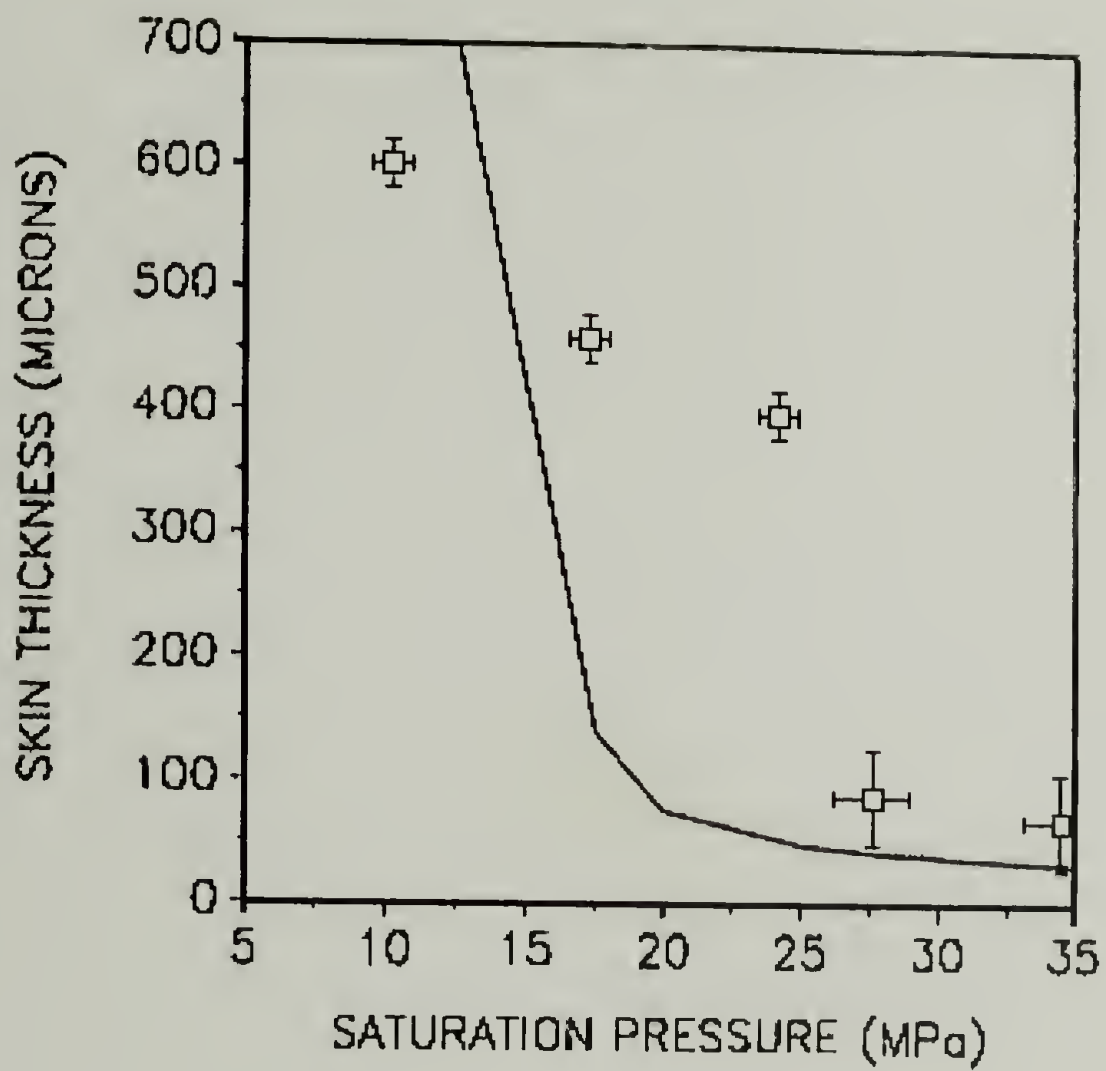


Figure B.1. Effect saturation pressure on the skin thickness of bulk PMMA foaming using SC CO₂. The solid line is a model prediction.¹

decreases with increasing foaming temperature in bulk samples. This is counterintuitive since the diffusivity of CO₂ increases with temperature and therefore should result in a thicker depletion layer. But the average cell diameter increases with increasing temperature, so the surface of the sample will be forced to increase in area to accommodate the increasing volume of the sample. Therefore, it is impossible to estimate the actual depletion region due to the large expansion of the sample subsequent to depressurization. This depleted layer (skin) has been observed to range in thickness from 100 μm down to 2 μm. The high diffusion coefficient of SC CO₂ ($D = 2.44 \times 10^{-6} \text{ cm}^2/\text{s} = 244 \text{ μm}^2/\text{s}$) will be problematic when trying to foam materials that are thinner than the thickness of this nonporous skin. The experiments to be conducted will involve mapping out the pressure and temperature effects on the foaming of polymer thin films. Confinement of the films between a gas barrier such as a metal layer should circumvent the problem of diffusion of CO₂ from the free surface and will be studied subsequently.

The second set of critical parameters to be studied is the nucleation and growth of pores in the SC foaming process. Goel and Beckman² applied classical nucleation theory to the supercritical foaming process in order to develop a model predicting the effects of temperature and pressure on the resulting cellular structure. In their derivation, it was shown that the critical nucleus size could be given by the following equation:

$$r_c = \frac{2\gamma}{\Delta P} \quad (1)$$

where r_c is the radius of the critical nucleus, γ is the surface energy of the bubble interface, and ΔP is the pressure drop in the system. Using this equation, the critical radius can be calculated as a function of CO₂ pressure for homogeneous nucleation in a

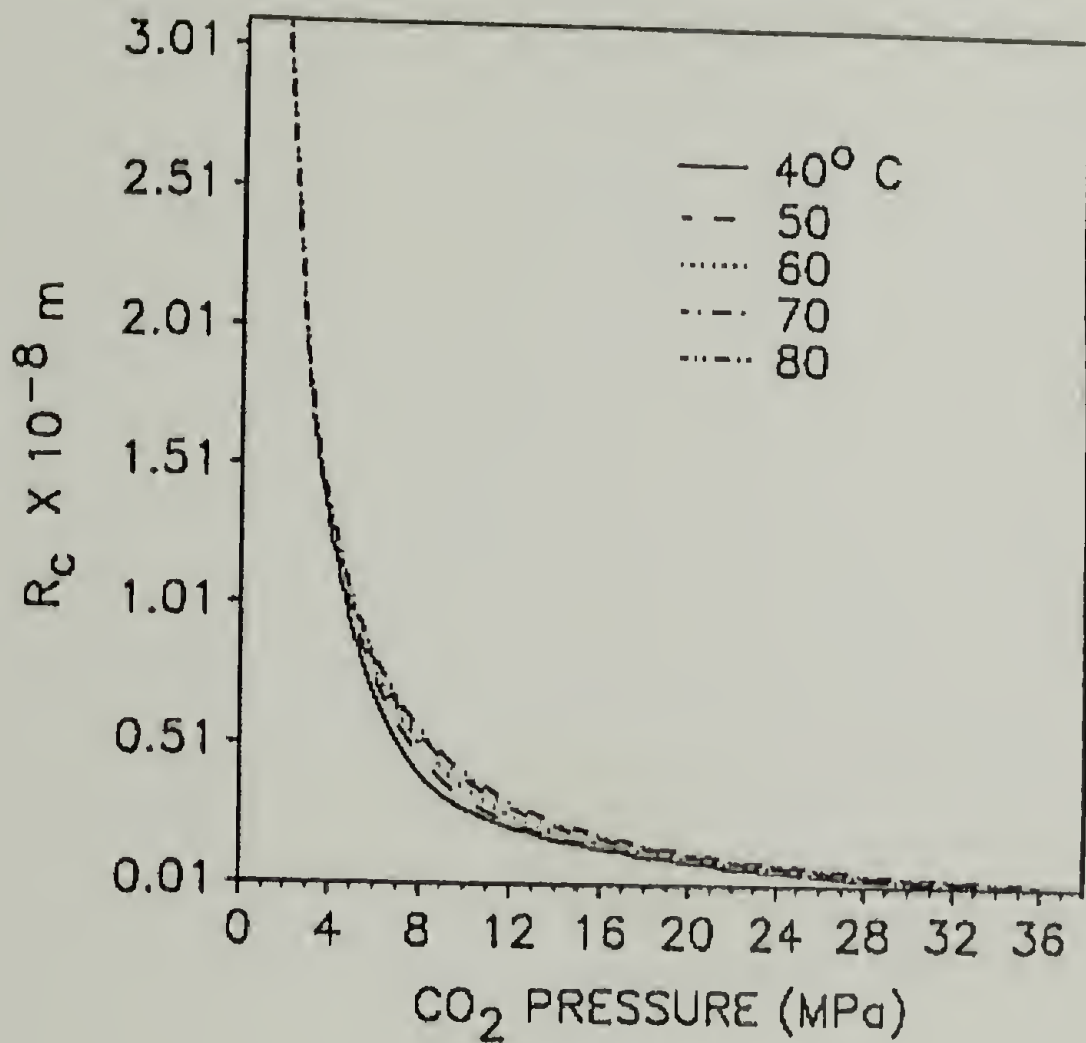


Figure B.2. Critical radius for homogeneous nucleation as a function of saturation pressure in a PMMA/CO₂ system undergoing a rapid pressure quench.²

PMMA/CO₂ system as shown in Figure B.2. For pressures above 2000 psi (13 MPa) there is little dependence of the critical radius on the CO₂ pressure, and in addition the model predicts a critical radius on the order of 15 – 30 Å. If this is indeed true, the nucleation process should be detectable by SAXS, and the growth of these pores could be followed over a reasonable q range. In order to follow the early stages of nucleation and growth, experiments will require use of a synchrotron source for x-rays, which will provide a high intensity of x-rays that enable time-resolved experiments to be conducted while maintaining reasonable signal-to-noise ratios. A series of pressure quenches (ΔP) will be conducted at different temperatures, and the scattered intensity will be recorded as a function of time after the pressure quench (time-resolved SAXS). The scattered intensity will be analyzed by methods developed by Guinier, which allows for the extrapolation of a critical radius of nucleation as well as the growth rate of the pores. Several reviews and texts are dedicated to SAXS and data analysis.^{4,5}

B.2. Experimental

B.2.1. Sample Preparation

Films of polystyrene (M_n - 147K, pdi - 1.03) were solution cast onto glass slides (25 mm x 75 mm) from THF. The glass slides were cleaned with ethanol and dried with compressed air prior to solution casting. The concentration and total volume of the solution were used to control the final dry film thickness. Films were removed from the glass slides by scoring the edges of the slides and gently sliding a razor blade underneath the film. The films were then placed on larger glass slides (50 mm x 75 mm) to facilitate annealing. Samples were annealed under vacuum by gradually increasing the temperature of the oven until the samples were above T_g . Annealing above T_g ensures complete removal of residual solvent and allows for relaxation of internal stresses in the film. Digital calipers were used to measure the actual film thickness of each sample within an accuracy of 0.1 μm . The thickness of each sample was measured at six points across the sample and then averaged to yield the thickness reported. Each film was then divided into smaller samples (dimensions - 7 mm x 25 mm) by cutting across the width of the film.

Thin films of polystyrene ($t < 10 \mu\text{m}$) were prepared by using a drawdown method on silicon wafers. Judicious choice of solution concentration and drawdown bar allowed for precise control of the dry film thickness. Films were dried at 80 °C under vacuum for several days to remove residual solvent. The thickness of each film was measured using a Dektak Profilometer (Veeco Instruments) by scratching the film with a

razor blade and measuring the step height. The films were removed by floating them off in water and placing them on glass slides for drying.

Confined films were prepared by evaporating aluminum on one or both sides of free standing films. While almost any metal could have been used as a gas barrier, aluminum was chosen due to its ease of evaporation. Approximately 300 Å of aluminum was used to coat the samples.

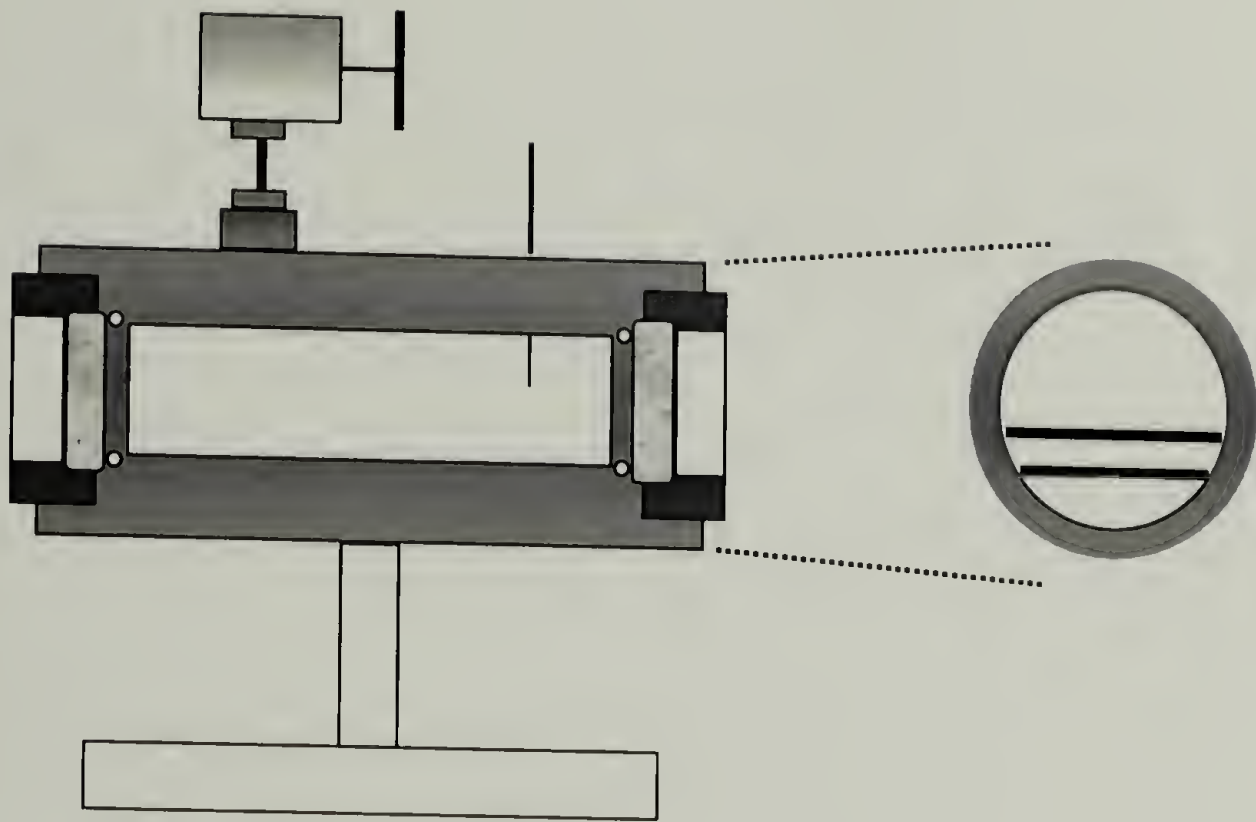
B.2.2. Foaming of Thin Films

Films prepared by either solvent casting or drawdown method were placed in a high-pressure view cell. The view cell is shown schematically in Figure B.3 (a). This cell was used in order to maintain the films in a horizontal position throughout the experiment. Multiple samples could be placed in the view cell, allowing for rapid surveying of multiple film thicknesses under exactly identical foaming conditions. The view cell was filled using an ISCO syringe pump to the desired pressure while being maintained at the experimental temperature. The time required to reach equilibrium uptake of CO₂ will be greatly diminished due to the short path length the CO₂ must travel in the thin films. Therefore, soak times of 1 h were used in all experiments unless noted. If the films were metallized on both sides, the path length becomes much greater since the CO₂ can only diffuse in from the edges of the sample, therefore the soak time was increased to 24 h for those samples. At the end of the soak period, the pressure was rapidly released at which point the samples would foam, and the samples were recovered. Qualitative analysis of the sample proved whether or not the sample foamed simply by

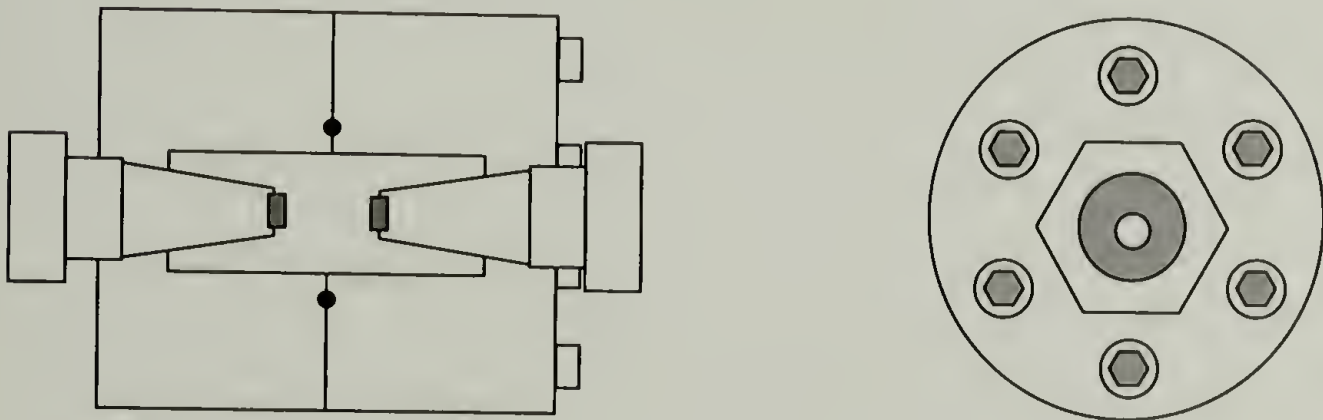
observing the opacity of the sample. The foams were further characterized by scanning electron microscopy (SEM) of the cryo-fractured surface.

B.2.3. TRSAXS

Small-angle x-ray experiments were conducted on the AP-PRT Beamline X27C at the National Synchrotron Light Source (NSLS) at Brookhaven National Labs, Upton, NY. The beam had an energy range of 6 – 20 keV, energy resolution ($\Delta E/E$) of 1.1% at 9.5 keV, and a photon flux of 10^{12} photons/s. A high-pressure x-ray scattering cell was built to conduct these experiments, and is shown schematically in Figure B.3 (b). One requirement for the cell was it had to have diamond windows for high x-ray transparency and the ability to withstand high pressures. Samples of polystyrene ($M_n = 85K$, $pdi = 1.02$) were compression molded as described in Chapter 1. The thickness of the samples was 0.5 mm and the cell volume was less than 3 mL. The cell was filled using an ISCO syringe pump to the desired pressure while being maintained at the experimental temperature. After a given soak period (45 min), the pressure was released via an external trigger connected to a solenoid valve in-line with the x-ray cell. The trigger also signaled the computer to begin data acquisition. The scattered intensity was measured using a 1-D gas-filled wire detector due to its fast response time. The number of counts on either side of the main beam could be added together since the scattering should be isotropic. This allowed for a doubling of the total intensity to be analyzed and boosted the signal-to-noise ratio. Background scans were performed just prior to release of pressure on each sample and were later subtracted from the data.



(a)



(b)

Figure B.3. Schematic drawings of (a) the high-pressure view cell used in the foaming of thin films and (b) the high-pressure x-ray scattering cell with diamond windows.

B.3. Results and Discussion

B.3.1. Foaming of Thin Films

A series of films ranging in thickness were prepared either by solvent casting or by a drawdown method. These films were then subjected to rapid decompression under a variety of experimental conditions. Initial experiments were conducted with the intention to quickly survey the conditions that were optimal for foaming of very thin films.

Experiments were conducted at two pressures (3000 psi and 8000 psi) and over a range of temperatures (40 – 100 °C). The simplest method to ascertain whether or not the sample had foamed is to examine the film for opacity. If the sample becomes opaque (i.e. scatters visible light) then it can be safely assumed that the film has foamed. It must be understood, though, that this simple visual test indicates the presence of pores large enough to scatter light; the presence of pores smaller than the wavelength of light cannot be detected using this method, and supplemental analysis must be performed (e.g. SEM, FESEM).

The results of these experiments are tabulated in Table B.1. Along with the foaming conditions and the film thickness, the samples are labeled as follows: 'y' denotes the sample was opaque by visual inspection, 'n' denotes the sample was clearly not opaque, and '~' indicates that the film was hazy but not completely opaque. Those samples labeled with '~' were taken as the cutoff point in film thickness below which the films were too thin to foam under the experimental conditions. Initially, the depressurization of the high-pressure cell was over a period of 6-8 seconds in order to alleviate the formation of dry ice, which results from the rapid cooling of the CO₂ as it

Table B.1. Foaming of free standing thin films under various conditions.

P=3000 psi	172 μm - y	P=8000 psi	14 μm - n	P=8000 psi	60 μm - y
T=40 °C	78 μm - y	T=40 °C	6 μm - n	T=80 °C	14 μm - y
	41 μm - ~		5 μm - n		10 μm - y
	10 μm - n		4 μm - n		9 μm - y
	8 μm - n		3 μm - n		8 μm - y
					6 μm - y
P=3000 psi	80 μm - y	P=8000 psi	60 μm - y		5 μm - ~
T=60 °C	40 μm - ~	T=60 °C	14 μm - y		4 μm - n
	11 μm - n		6 μm - ~		3 μm - n
	6 μm - n		5 μm - ~		
P=3000 psi	80 μm - y	P=8000 psi	80 μm - y	P=8000 psi	4 μm - y
T=80 °C	30 μm - y	T=80 °C	32 μm - y	T=80 °C ^a	3 μm - y
	10 μm - ~		10 μm - ~		2 μm - y
	7 μm - n		7 μm - n		1 μm - n

^a used rapid decompression (neglect the fact that dry ice forms in HP vessel due to temperature drop)

expands. Later experiments (as noted in Table B.1) employed an extremely rapid depressurization (2-3 sec) and ignored the fact that dry ice forms within the high-pressure view cell.

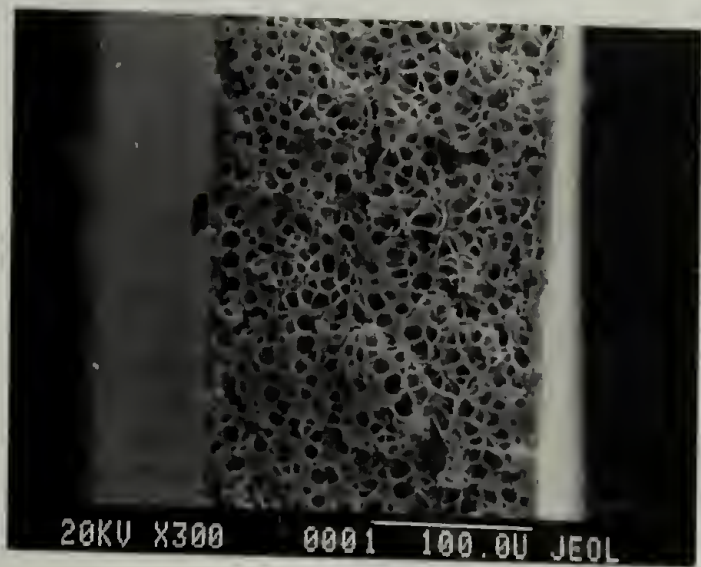
As expected, an increase in saturation pressure allowed for foaming of thinner films. The thinnest films that could be foamed at 3000 psi was $\sim 10 \mu\text{m}$, while films as thin as $5 \mu\text{m}$ could be foamed at 8000 psi. This is due to the increase in nucleation density and a corresponding decrease in skin thickness with increasing pressure as shown by Goel et al.¹ Utilizing the extremely rapid depressurization further lowered the limiting film thickness, allowing for the foaming of films with thicknesses of $2 \mu\text{m}$. This is the thinnest film that could be foamed in these experiments. It was shown that a $1 \mu\text{m}$ film could not be foamed under identical conditions, and free standing films thinner than $1 \mu\text{m}$ could not be handled easily.

Increasing the foaming temperature resulted in the ability to foam thinner films at both pressures studied. At 3000 psi, an increase in temperature from 40°C to 80°C pushed the foaming limit from $40 \mu\text{m}$ to $10 \mu\text{m}$. Similar results were seen for 8000 psi. This could be due to the decrease in viscosity of the substrate with increasing temperature, lowering the barrier for cell growth. An increase in temperature also results in a decrease in CO_2 density (see Figure 1.2), but it is unclear how a decrease in CO_2 density would affect the nucleation and growth of pores in thin films.

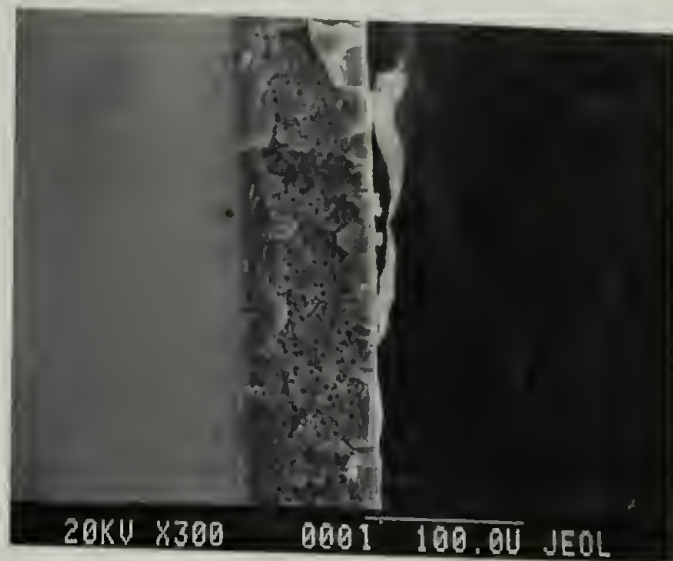
Several of the thin film foams were characterized by scanning electron microscopy (SEM). Figure B.4 shows SEM micrographs of films foamed at 40°C and 3000 psi. The $172 \mu\text{m}$ sample clearly foamed similarly to a bulk sample under these conditions.⁶ Thinner films begin to deviate from what is typically observed for bulk

samples. The 78 μm sample exhibits smaller cells and a decreased nucleation density. This can be expected since more CO_2 is able to diffuse from the free surfaces, thus leaving less CO_2 for nucleation and growth of pores. The 41 μm sample was deemed the cutoff between foamed and unfoamed samples, and it is clear from the SEM micrograph that this is indeed a justified conclusion. The pores are very sparse and are on the order of 1 μm in diameter. Similar results are seen for foaming conditions of 3000 psi and 60 $^\circ\text{C}$. SEM micrographs of samples prepared under these conditions are shown in Figure B.5. Again, the pore diameters approach $\sim 1 - 2 \mu\text{m}$ for the thinner films. Included in the figure is a SEM micrograph of the 11 μm sample. The majority of this sample indeed had not foamed, but interestingly a few pores could be found along the sample's edges, indicating that some heterogeneous nucleation occurred at the interface in contact with the glass slide support.

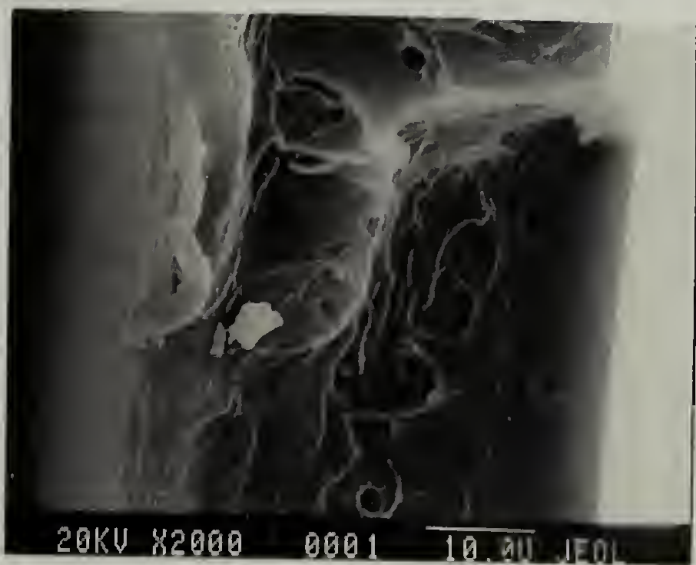
The results of the previous experiments indicate that films below 2 μm cannot be foamed by the decompression of CO_2 . Therefore, the next set of experiments explored the foaming of constrained films of polystyrene. Samples of different thicknesses were prepared having aluminum evaporated on either one or both sides of the samples. This metal layer should act to negate diffusion of CO_2 from the free surface, trapping the CO_2 in the interior of the film. The drawback to doing this is that longer soak times must be used to allow for CO_2 diffusion into the sample from the unmetallized edges of the sample. Shown in Figure B.6 are foams prepared from three metallized films: (a) 100 μm metallized on only one side, (b) 100 μm metallized on both sides, and (c) 50 μm metallized on both sides. Metallization on only one side of the sample does not appear to drastically enhance the foaming characteristics of the 100 μm sample (compare to the 80



(a)

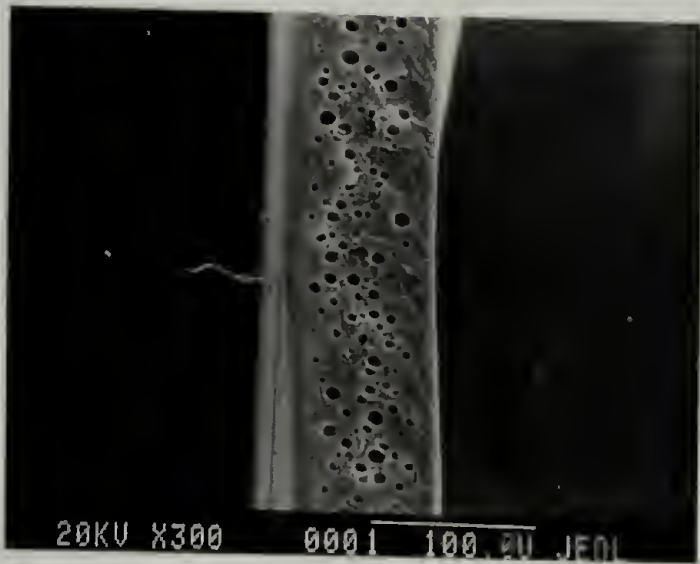


(b)

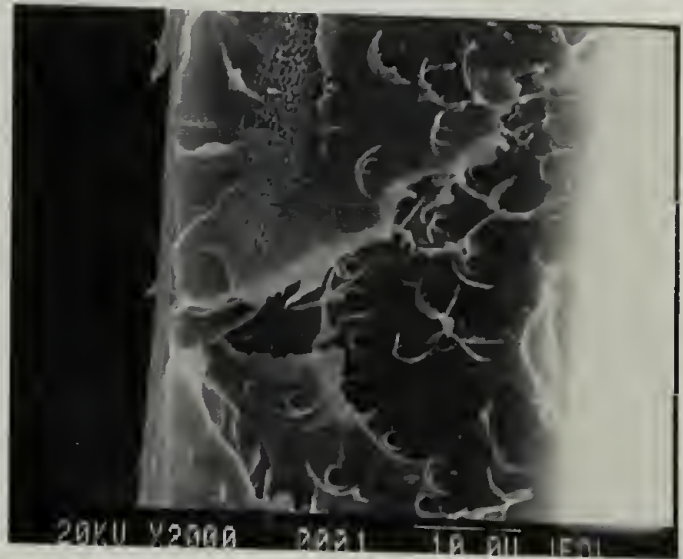


(c)

Figure B.4. SEM micrographs of fracture surfaces of unconfined thin film foams: (a) 172 μm , (b) 78 μm , and (c) 41 μm . Foaming conditions were 40 $^{\circ}\text{C}$ and 3000 psi.



(a)

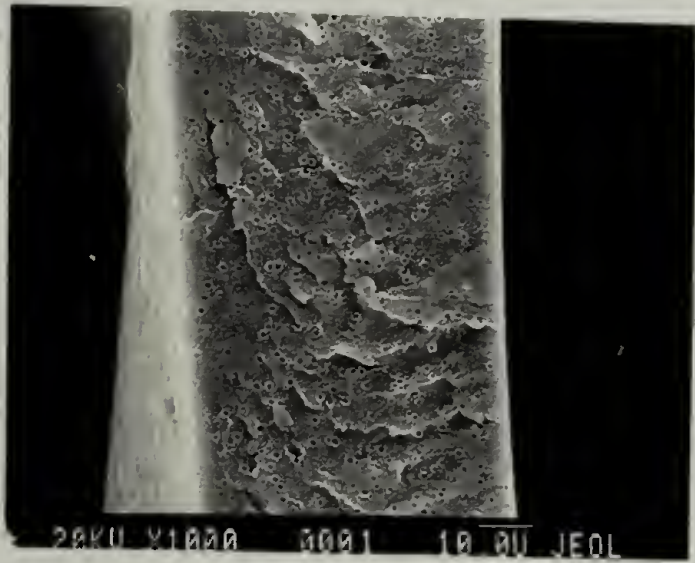


(b)

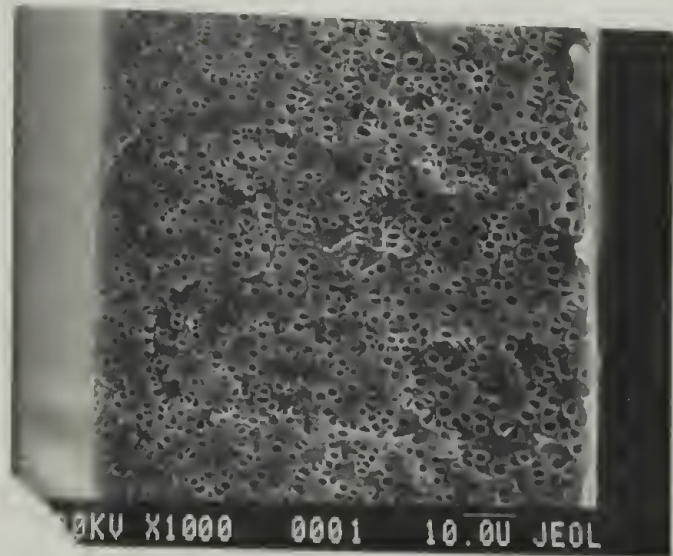


(c)

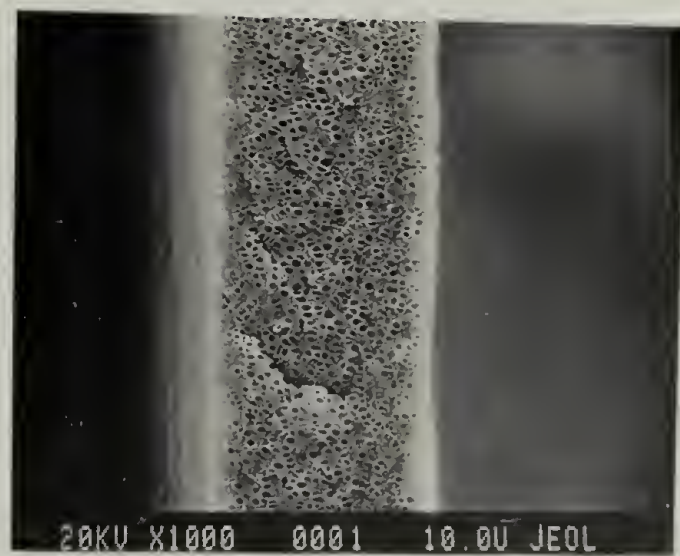
Figure B.5. SEM micrographs of fracture surfaces of unconfined thin film foams: (a) 80 μm , (b) 40 μm , and (c) 11 μm . Foaming conditions were 60 $^{\circ}\text{C}$ and 3000 psi.



(a)



(b)



(c)

Figure B.6. SEM micrographs of fracture surfaces of confined thin film foams: (a) 100 μm M/F, (b) 100 μm M/M, and (c) 50 μm M/M. Foaming conditions were 40 $^{\circ}\text{C}$ and 3000 psi. M denotes metallized surface and F denotes free surface on each side of the film, respectively.

μm sample in Figure B.4 (b)). In marked contrast, the films that were metallized on both sides exhibited an increase in both cell density and cell diameter. Another noteworthy point is that there does not appear to be any differences in the cellular structure of the 100 μm and 50 μm samples when constrained on both sides by a metal. Thus by metallizing the surface of the films, we have eliminated diffusion of CO_2 from the free surface, forcing the CO_2 to undergo nucleation and growth. Therefore, both films have equal amounts of CO_2 upon foaming and the resulting cellular structure in each sample is identical.

Next, samples were prepared that had metal on one side and only half of the other side. This would allow a single experiment to be conducted on one sample in order to study the effect of metallization on only one (M/F) or both sides (M/M) of the film concurrently. The process is outlined in Figure B.7. This greatly reduces the number of samples needed as well as reduces the characterization time for each sample. This

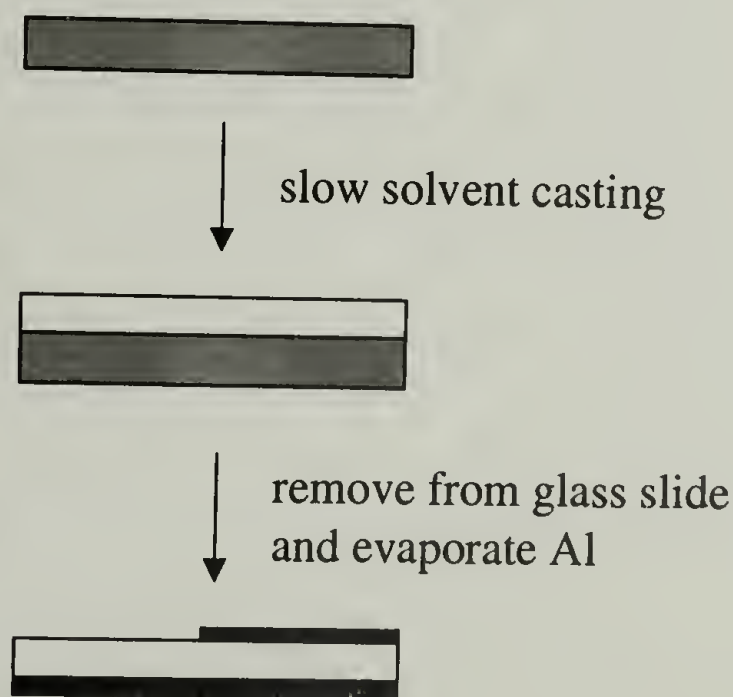


Figure B.7. Schematic illustrating film preparation having a metallized layer on one complete side of the film, but only on half of the opposite side.

method will also provide insight as to what happens at the boundary between the two regions of the sample.

SEM micrographs of three samples (100 μm , 50 μm , and 10 μm) prepared by this method are shown in Figures B.8 - B.10. Foaming conditions were 80 °C and 8000 psi. The SEM micrograph of a bulk sample foamed under identical conditions is shown in Figure B.11. The region of each sample that is confined on both sides by aluminum possesses cell densities and cell diameters that are comparable to the bulk sample. On the other hand, the region of each sample that is confined on only one side of the film appears to foam in a somewhat anomalous fashion, having a high density of very small cells. Similar results are seen for all three samples, indicating that this effect is real and reproducible to some extent. A clear transition region can be seen in SEM, traversing from the M/F region to the M/M region. It is not clear why this behavior is observed. But it is clear that metallization of the film on both sides can effectively increase the concentration of CO₂ remaining inside the film by eliminating diffusion of CO₂ from the free surface. Thus, films prepared in this fashion exhibit a cellular structure identical to bulk samples under the conditions explored here.

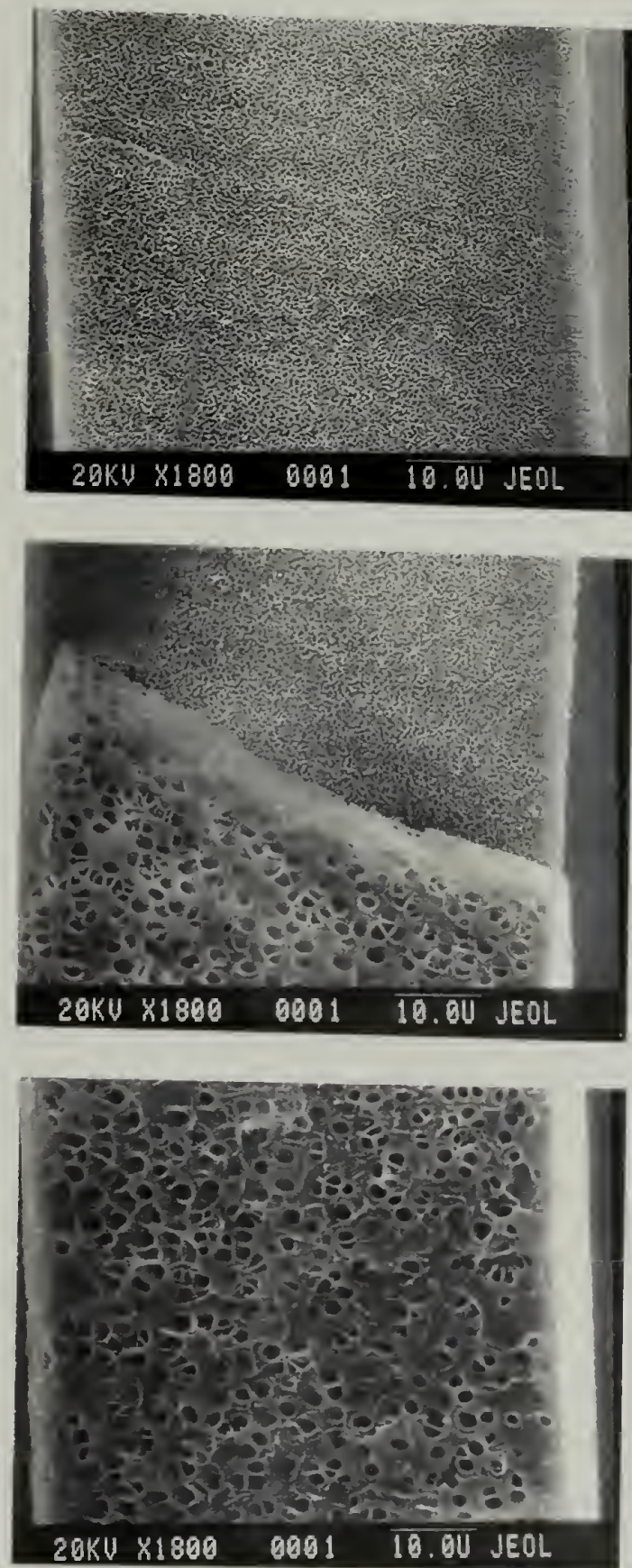


Figure B.8. SEM micrographs of fracture surfaces of a 100 μm confined thin film foam that has been metallized on one side only (top image) and metallized on both sides (bottom image), along with the transition region. Foaming conditions were 80 $^{\circ}\text{C}$ and 8000 psi.

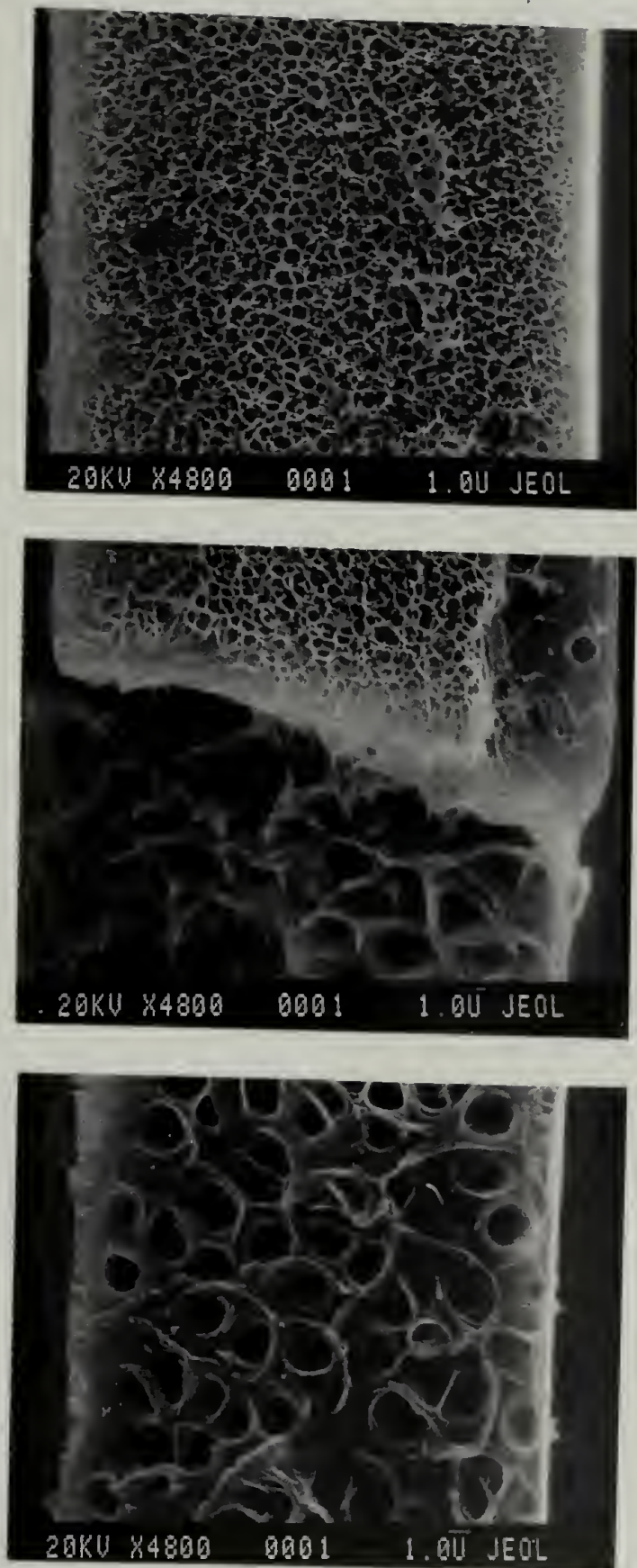


Figure B.9. SEM micrographs of fracture surfaces of a 50 μm confined thin film foam that has been metallized on one side only (top image) and metallized on both sides (bottom image), along with the transition region. Foaming conditions were 80 $^{\circ}\text{C}$ and 8000 psi.

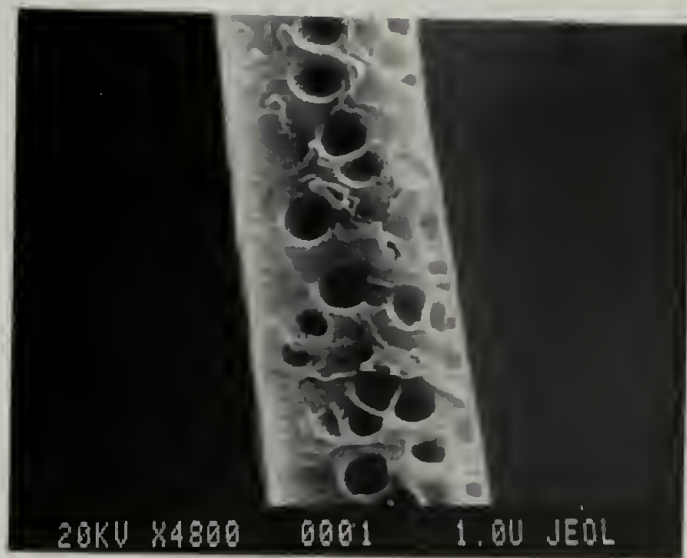
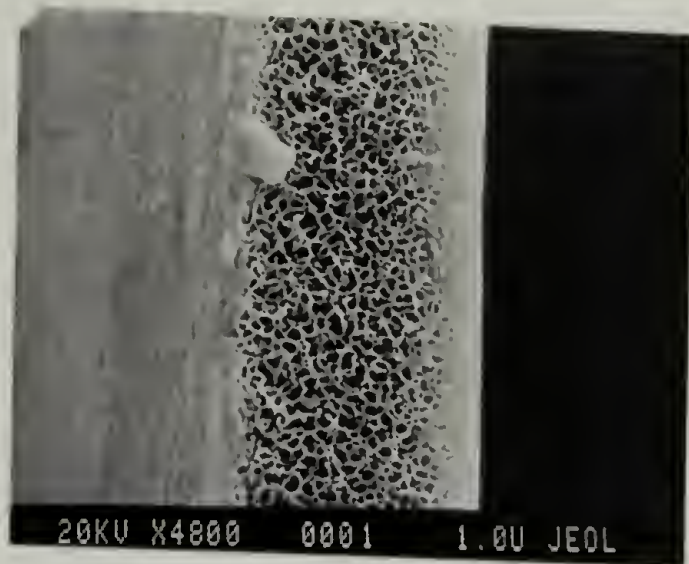


Figure B.10. SEM micrographs of fracture surfaces of a 10 μm confined thin film foam that has been metallized on one side only (top image) and metallized on both sides (bottom image). Foaming conditions were 80 $^{\circ}\text{C}$ and 8000 psi.

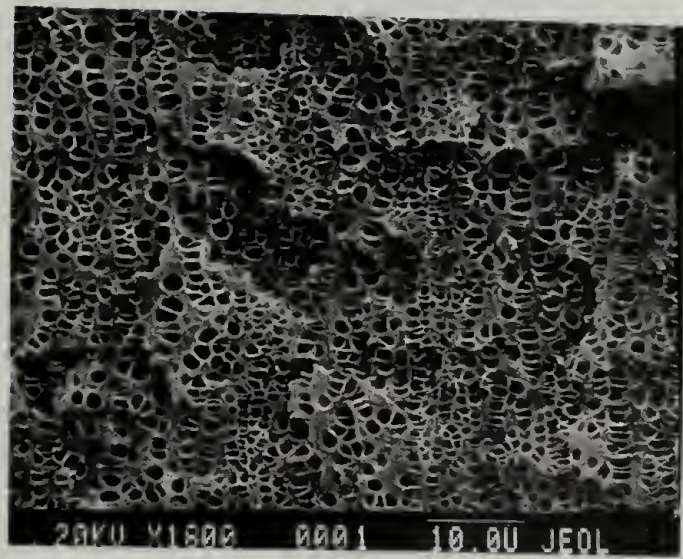


Figure B.11. SEM micrograph of the fracture surface of a bulk PS sample foamed at 80 °C and 8000 psi.

B.3.2. Kinetics of Foaming Followed by Time-resolved SAXS

Foaming experiments were conducted in the high-pressure x-ray cell illustrated in Figure B.3 (b). The volume of the cell was only a few mL, allowing for rapid depressurization to be conducted by triggering a solenoid valve. Samples were prepared having a thickness of $0.5 \mu\text{m}$, therefore reasonably short soak times could be used. Previous experiments outlined in the previous section indicated that samples of this thickness would behave similarly to a bulk material under these foaming conditions. Initial experiments explored the effects of foaming pressure as well as foaming temperature on the scattering pattern observed. Pressure quenches in all cases were taken to atmospheric pressure (0 psi_a).

Figures B.12 and B.13 display the time-resolved scattered intensity as a function of q for pressure drops of 2000psi, 3000 psi, 4000 psi, and 5000 psi, all at a temperature of 40°C . The raw scattering data has been normalized by background subtraction and 5-point smoothed. In all cases, the scattered intensity increases with increasing time for the range of $0.01 < q < 0.1$. For a ΔP of 5000 psi, the scattering data quickly reaches an upper limit within 10 seconds, after which no change in the scattered intensity can be seen. A ΔP of 2000 psi shows the greatest degree of time-dependence of the scattering data, showing good resolution almost 60 seconds after depressurization. Increasing the foaming temperature to 50°C produces similar results with regard to pressure dependence but the time-scales are considerable shorter, as shown in Figures B.14 and B.15. Since the acquisition times were reduced to 0.1 seconds in these cases, there is considerably more scatter to the data, even after 5-point smoothing, but the trends are the same as seen in the experiments at 40°C .

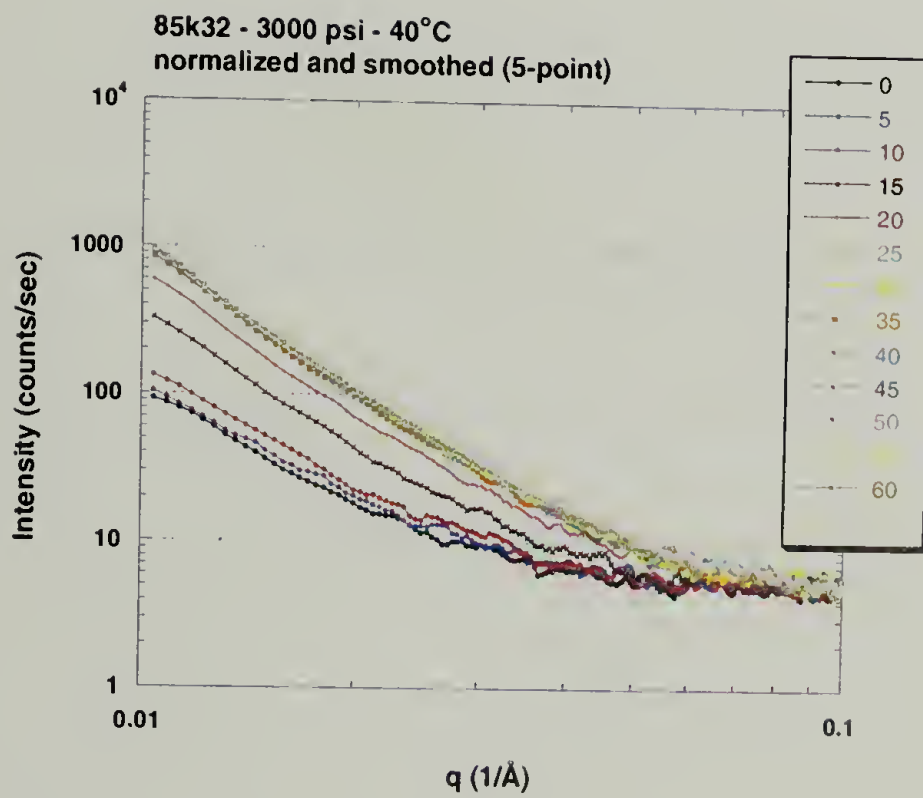
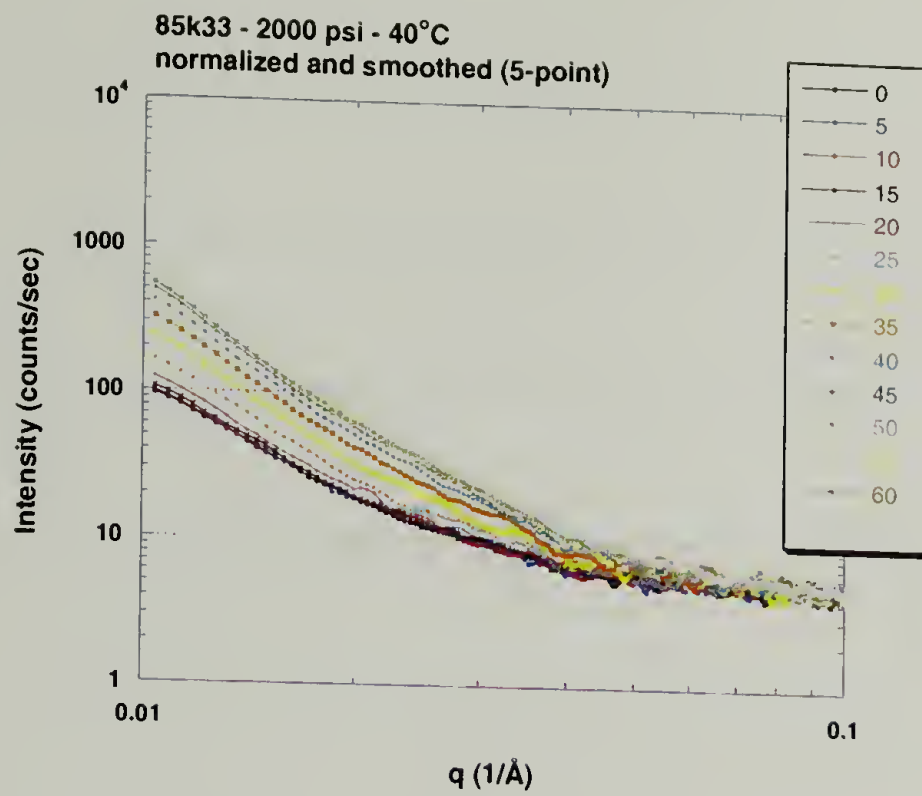


Figure B.12. Scattered intensity as a function of q for pressure quenches (ΔP) of 2000 psi and 3000 psi at 40 °C.

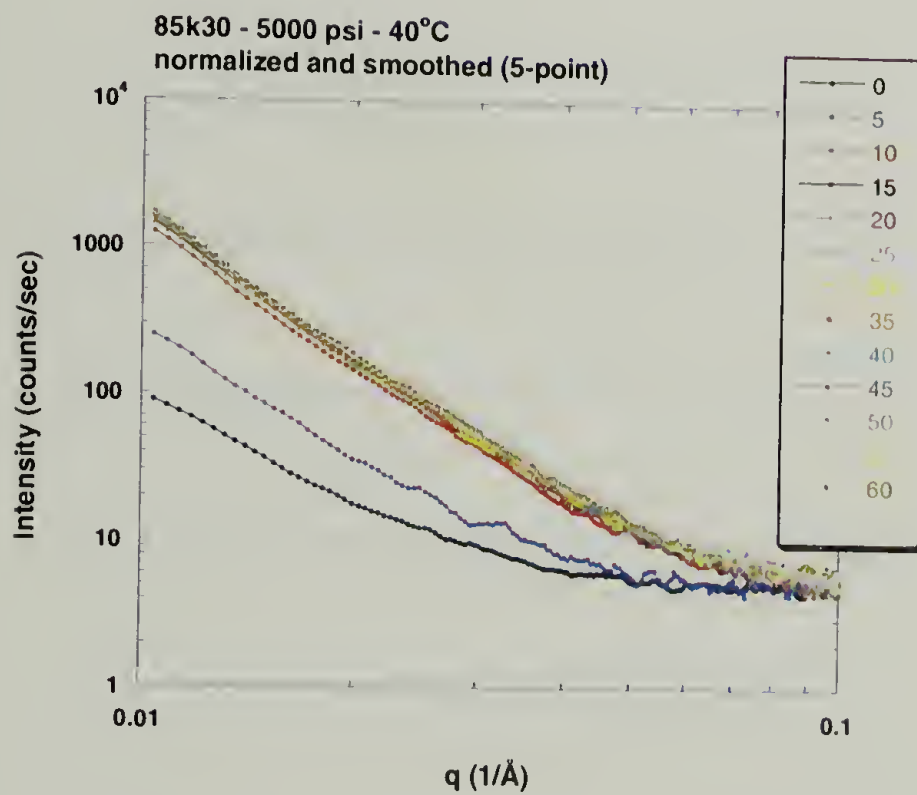
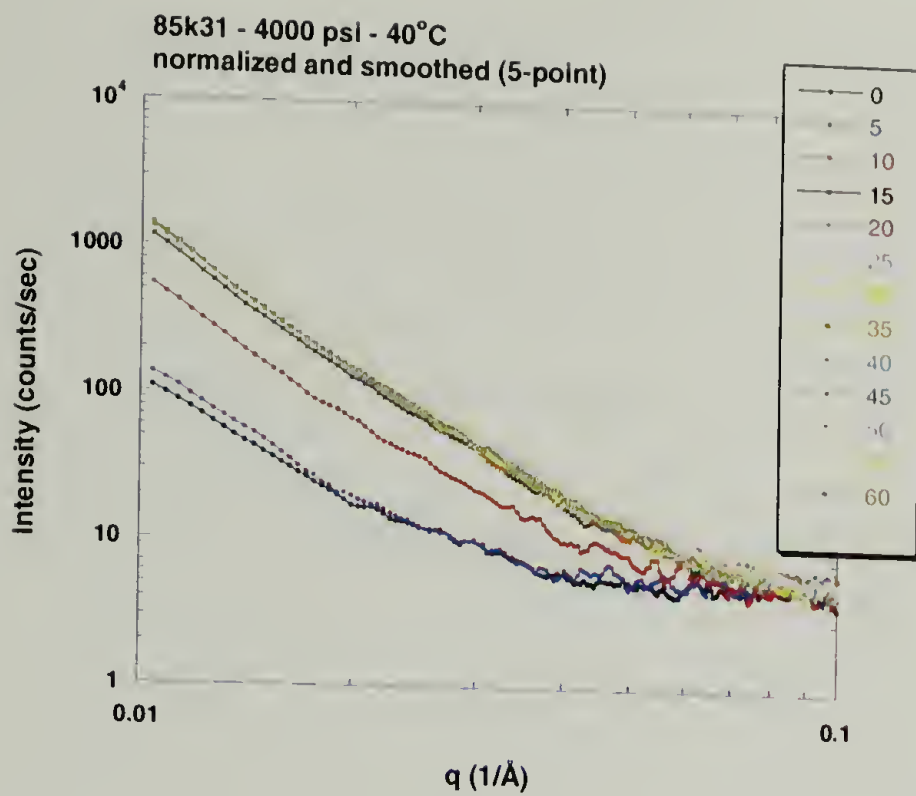


Figure B.13. Scattered intensity as a function of q for pressure quenches (ΔP) of 4000 psi and 5000 psi at 40 °C.

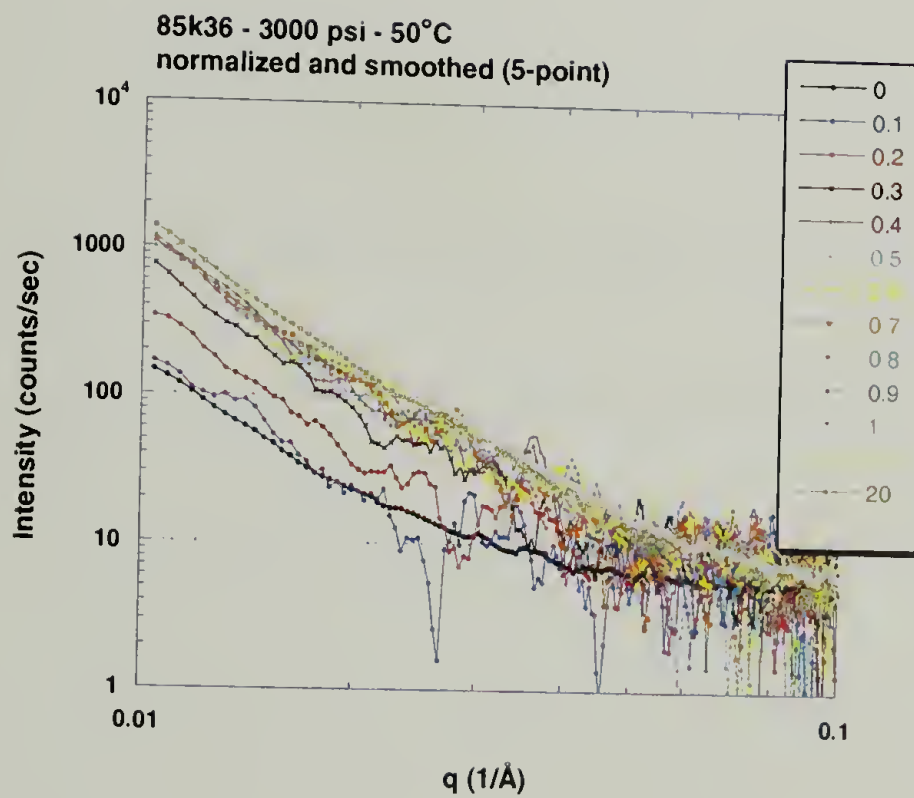
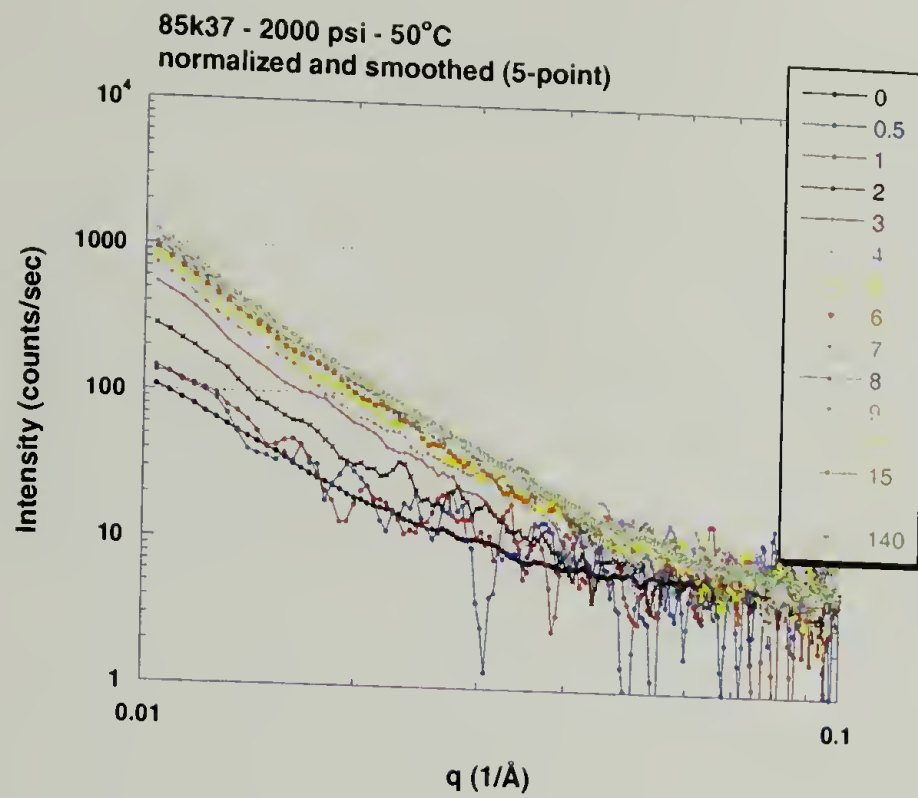


Figure B.14. Scattered intensity as a function of q for pressure quenches (ΔP) of 2000 psi and 3000 psi at 50 °C.

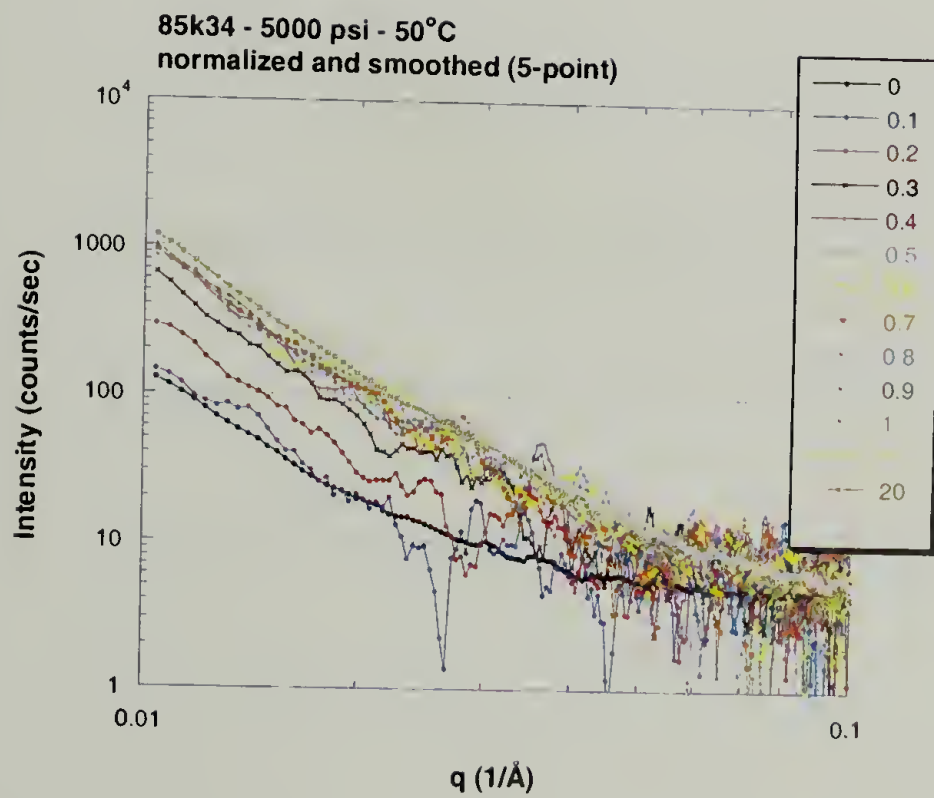
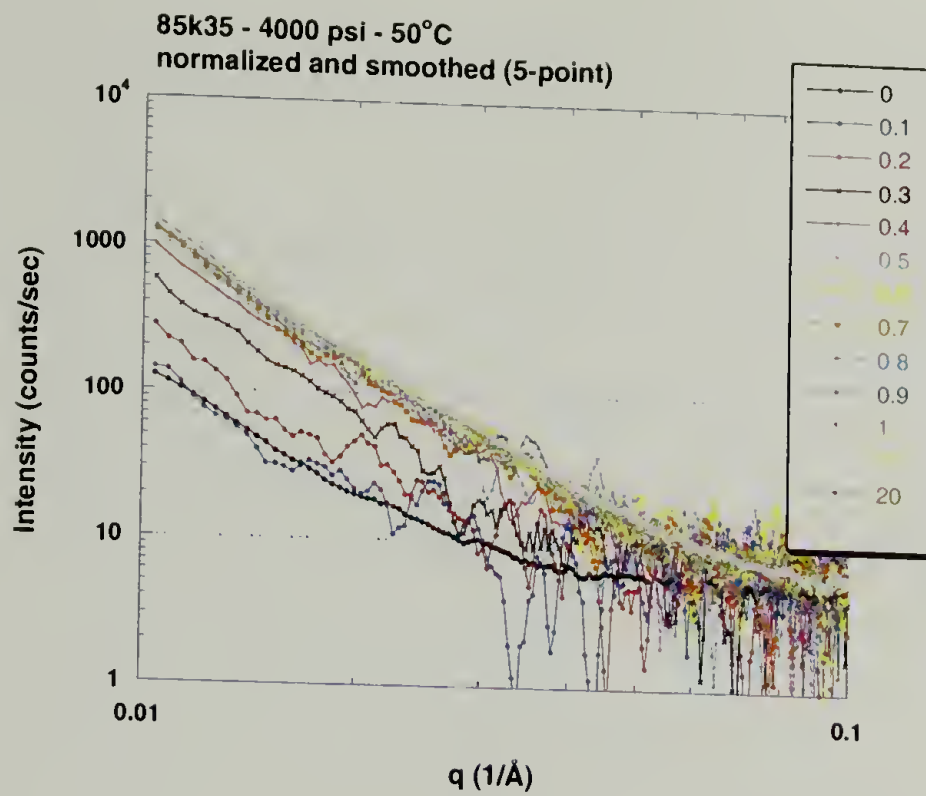


Figure B.15. Scattered intensity as a function of q for pressure quenches (ΔP) of 4000 psi and 5000 psi at 50 °C.

The scattering data was analyzed by several methods. Guinier first described the scattering from a dilute, monodisperse system of randomly oriented, isolated particles as function of scattering angle. This universal law is known as Guinier's Law and can be described as follows:

$$I(q) = I_o \exp\left(-\frac{q^2 R^2}{3}\right) \quad (2)$$

where I is the scattered intensity, I_o is the total incident intensity, q is the scattering vector ($q = 4\pi/\lambda \sin(\theta/2)$), and R is the radius of the scatterer. By this equation, plotting $\ln[I(q)]$ vs. q^2 should give linear curves having slopes of $-R^2/3$. Departure from linearity can occur at higher q due to deviation from a monodisperse system of scatterers. Guinier's Law should also be applied to systems only when $qR \leq 1$. A Guinier plot of the scattering data collected for $\Delta P = 2000$ psi at 40°C is shown in Figure B.16. The data is linear over the q range shown, but there is no apparent change in slope of the curves with increasing time after depressurization. A model Guinier plot is also shown in Figure B.16 for a critical radius (R_c) of 30 \AA and a growth rate of $15 \text{ \AA}/\text{sec}$. It is immediately obvious that the real data are not capturing any nucleation and/or growth of pores in these experiments. The data was also analyzed by fitting to Porod as well as Debye-Buche scattering laws, with little success. Fractal scattering was also explored in data analysis but there is no direct evidence that the porosity is fractal in nature.

Illustrated in Figure B.17 are two possible mechanisms for pore formation in these experiments. Mechanism (a) corresponds to the original expectations from these experiments: formation of a critical pore size, followed by growth of these pores with time. The scattering data strongly suggest that this is not the case. We propose a different mechanism for generating the observed scattering data. It is conceivable that

the rate of pore formation is too rapid to be detected even by TRSAXS, and we are following only the change in electron density as the CO₂ undergoes the transition from a dense SC fluid phase to a gas. This is illustrated in Figure B.17 (b). In this case, the porosity is formed almost immediately and the only observable changes are the difference in electron densities (Δn_e) between the pores and the matrix. This explanation sufficiently agrees with the scattering data.

Conducting foaming experiments in the view cell equipped with an external digital camera and monitor further supported these conclusions. The view cell (Figure B.3 (a)) was turned on its side so that the sapphire windows were horizontal, and the digital camera was placed below the bottom sapphire window while the cell was illuminated through the top sapphire window. Samples could then be placed on the bottom sapphire window and were directly visible through the window with the digital camera. Bulk samples of PS were placed in the view cell, and CO₂ was introduced via the ISCO pump to the desired pressure (5000 psi) at the elevated temperatures (50 °C). After a soak period of 3 h, the view cell was vented to atmospheric pressure ($\Delta P = 5000$ psi). As observed through the video monitor, the sample became instantaneously opaque, indicating that the size of the pores was already larger than the wavelength of visible light. Similar experiments were conducted with the variation of adding an isolated dead volume that the cell could be vented against, thus controlling the depth of pressure quench. Again, a sample was soaked in CO₂ at 5000 psi at 50 °C for 3 h. The view-cell was then vented against the dead volume, resulting in a pressure quench from 5000 psi to 3000 psi ($\Delta P = 2000$ psi). Again, the sample became immediately opaque. These experiments indicate that the foaming process is happening on time scales that are too

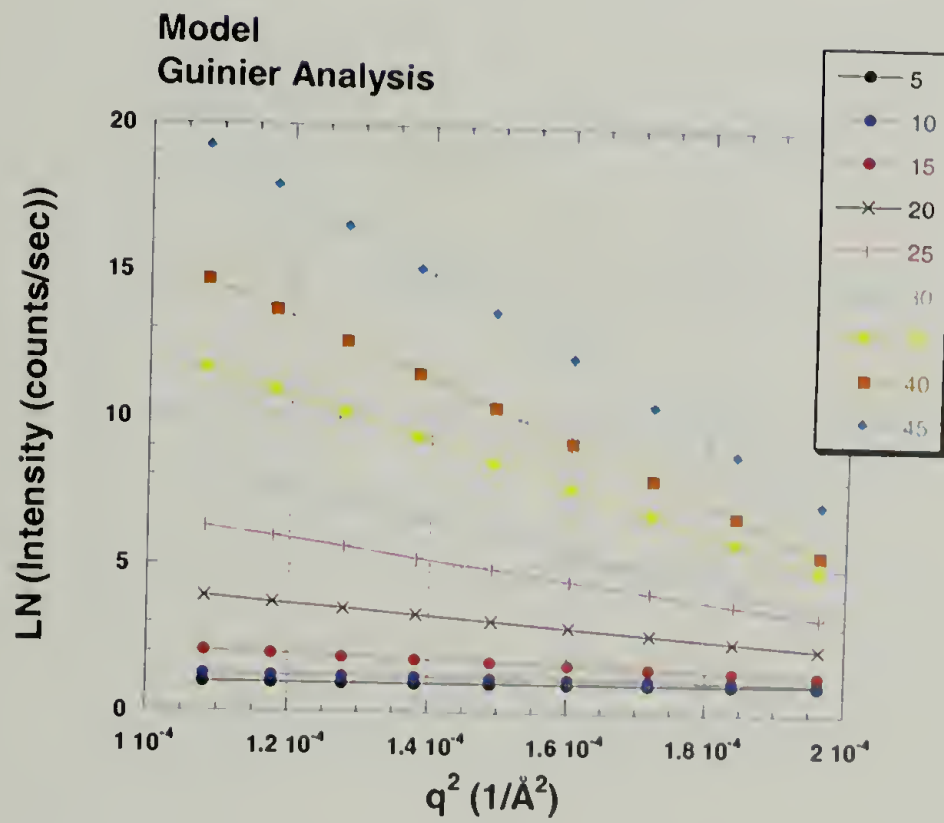
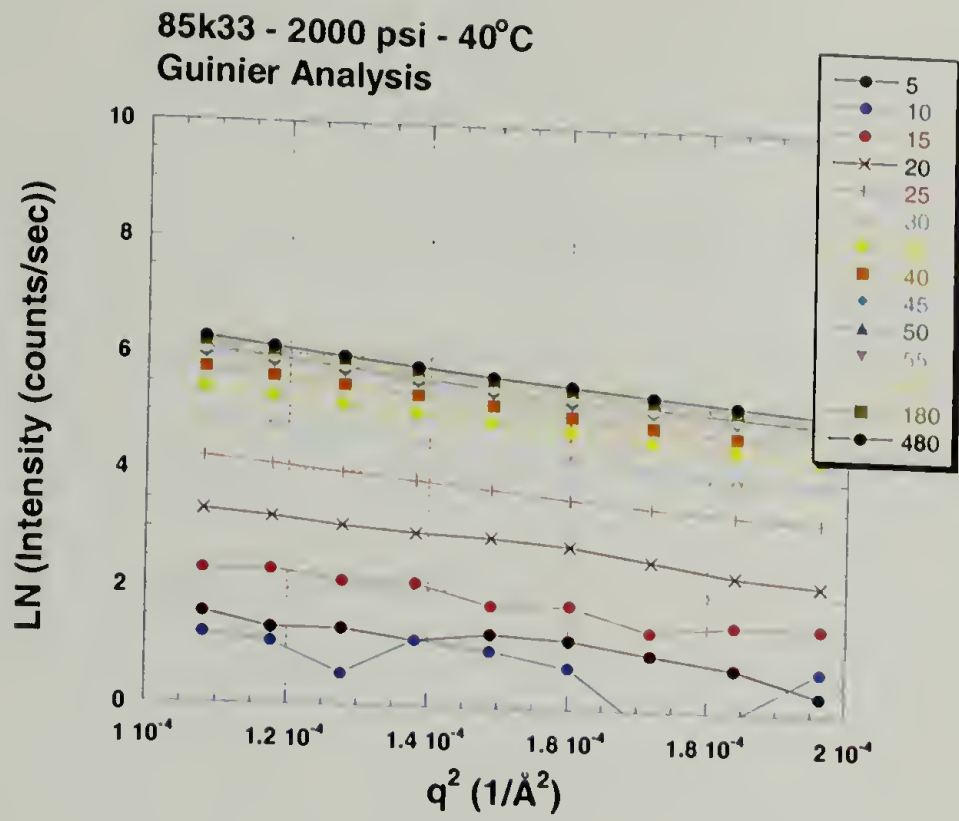
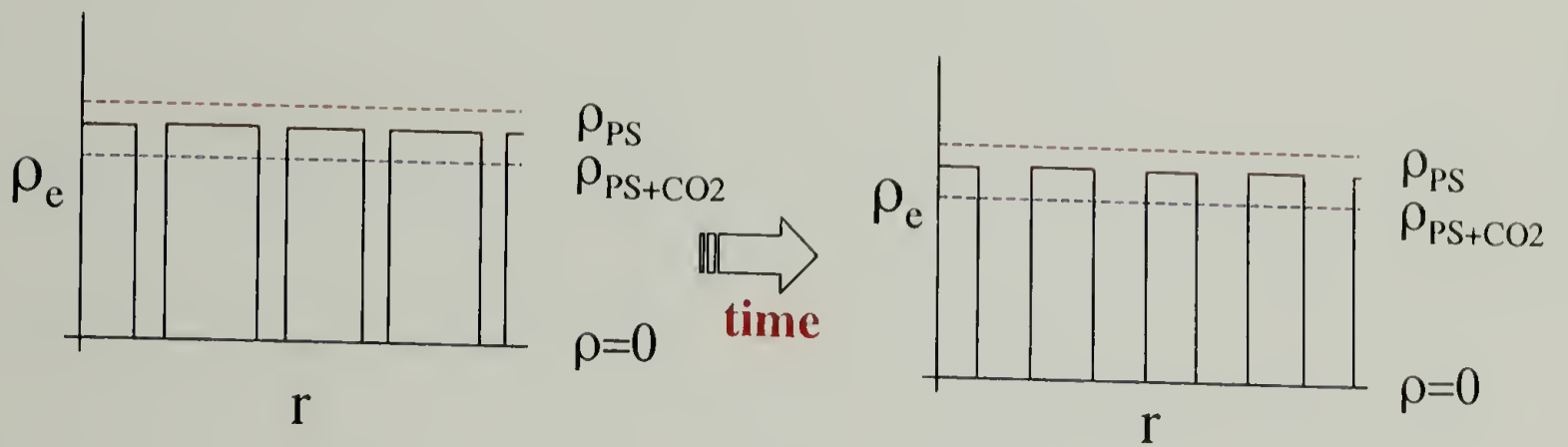
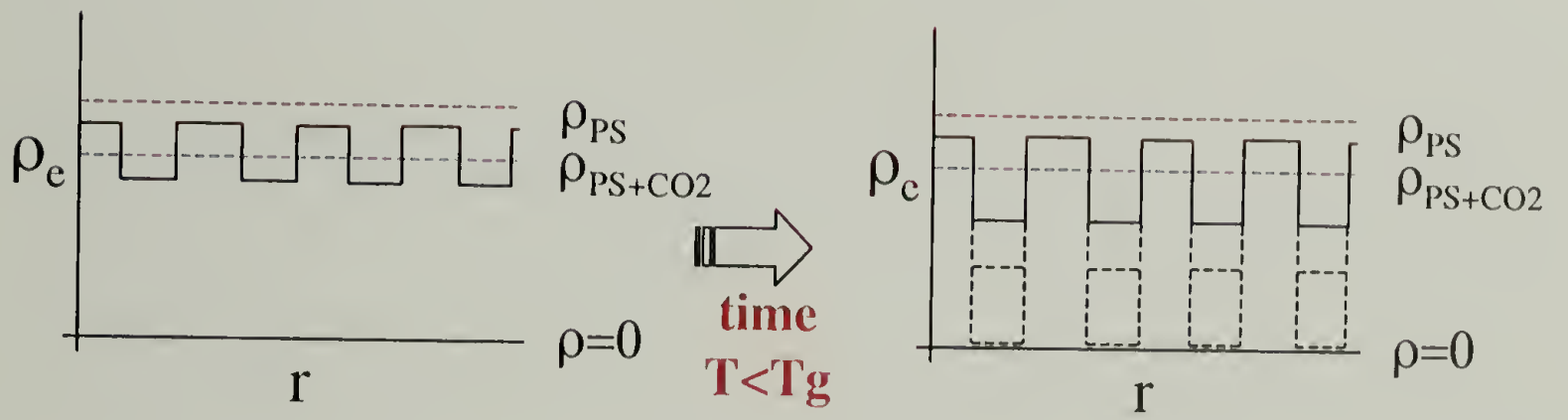


Figure B.16. Guinier plot for a pressure quench (ΔP) of 2000 psi at 40 °C. Included is a model Guinier plot for a growth rate of 15 Å / sec.



(a)



(b)

Figure B.17. Schematic illustrating two possible mechanisms for pore formation defined in terms of electron densities.

rapid to be observed even by TRSAXS. So these experiments reinforce the notion that the scattering experiments are not capturing the growth of pores, but simply following the change in electron density as CO₂ undergoes the transition from a dense SC fluid to a gas.

B.4. Conclusions

Experiments were designed to probe the critical length scales and dimensions in the foaming of polymers using SC CO₂. A survey of thin film foaming was conducted, and results indicate that films greater than ~100 μm behave very similar to bulk samples. Experiments suggest that rapid diffusion of CO₂ from the free surface severely hinders the ability to foam films less than 10 μm thick. Conditions were optimized to test the minimum film thickness that can be foamed, and at 8000 psi and 80 °C that limit was determined to be 2 μm. Confinement between a gas barrier such as an evaporated layer of aluminum was shown to enhance the foaming ability of thin films by prohibiting diffusion of CO₂ from the free surface. This comes at the expense of requiring longer soak times to allow diffusion of CO₂ into the sample from the unconfined edges of the film.

TRSAXS was explored as a technique to study the nucleation process and growth rate of pores in SC foaming. Scattering data was obtained over a range of pressure quenches and at two temperatures. The data was analyzed by methods developed by Guinier, Porod, and Debye-Buche, as well as fractal scattering. The scattering curves failed to obey any of these universal laws. It was concluded that the experiments failed to capture the nucleation and growth process, and the data simply reflected the transition of the SC CO₂ from a dense fluid to a gas, and the accompanying change in electron

density/contrast. This conclusion was further tested by experiments conducted in a view-cell while monitoring the transmission/absorbency of visible light. In these experiments, the samples became instantaneously opaque indicating the size of the pores was already on the order of the wavelength of light. Thus, going back to the TRSAXS experiments, the pore size quickly grew to the order of microns, too large to be detectable by x-rays. The data only reflect the change in electron density/contrast of the system as the CO₂ diffuses out of the sample.

B.5. References Cited

1. Goel, S. and Beckman, E. *Polym. Eng. Sci.*, **1994**, *34*, 1148.
2. Goel, S. and Beckman, E. *Polym. Eng. Sci.*, **1994**, *34*, 1137.
3. Kumar, V. and Weller, J. *Polym. Eng. Sci.*, **1994**, *34*, 169.
4. Alexander, L., *X-Ray Diffraction Methods in Polymer Science*. 1969, New York: Wiley-Interscience. 582.
5. Russell, T., in *Handbook on Synchrotron Radiation*, G. Brown and D. Moncton, Editors. 1991, Elsevier Science: New York. p. 379.
6. Arora, K.; Lesser, A., and McCarthy, T. *Macromolecules*, **1998**, *31*, 4614.

APPENDIX C

SUPPLEMENTAL DATA FOR CHAPTERS 2 AND 3

C.1. XPS Data for Polymer Adsorption to Silane-modified Surfaces

Table C.1. XPS data (75° take-off angle) for surfaces modified with Tris(TMS) via vapor phase reaction for increasing amounts of time.

Sample	atomic concentrations (%)				thickness nm
	C	O	Si	N	
clean Si	7.54	43.25	49.21	-	0
Tris(TMS) ¼ h	7.92	42.16	49.92	-	<0.1
Tris(TMS) ½ h	7.61	43.75	48.64	-	0.1
Tris(TMS) 1 h	10.14	43.25	46.61	-	0.3
Tris(TMS) 4 h	11.06	42.59	46.35	-	0.4
Tris(TMS) 24 h	11.83	42.75	45.42	-	0.6
Tris(TMS) 59 h	10.96	42.01	47.03	-	0.7
Tris(TMS) 72 h	11.10	41.57	47.33	-	0.7
Tris(TMS) 93 h	12.95	41.28	45.77	-	0.8

Table C.2. XPS data (75° take-off angle) for surfaces modified with Tris(TMS)/ABDMS via vapor phase reaction.

sample	atomic concentrations (%)				thickness nm
	C	O	Si	N	
clean Si / ABDMS	26.93	33.20	38.15	1.71	1.0
Tris(TMS) 1 h / ABDMS	29.34	31.80	36.76	2.09	1.2
Tris(TMS) 4 h / ABDMS	30.44	32.45	35.14	1.97	1.5
Tris(TMS) 24 h / ABDMS	26.33	34.22	37.93	1.52	1.1
Tris(TMS) 72 h / ABDMS	26.10	34.31	38.45	1.13	1.0

Table C.3. XPS data (75° take-off angle) for 11K PS-COOH adsorbed from toluene to surfaces modified with Tris(TMS) via vapor phase reaction for increasing amounts of time.

sample	atomic concentrations (%)				thickness nm
	C	O	Si	N	
clean Si	50.11	25.79	24.10	-	2.3
Tris(TMS) ½ h	31.65	32.54	35.81	-	1.3
Tris(TMS) 1 h	32.79	31.92	35.28	-	1.2
Tris(TMS) 4 h	33.36	30.33	36.31	-	1.0
Tris(TMS) 24 h	23.31	36.73	39.96	-	0.8
Tris(TMS) 51 h	21.58	36.39	42.03	-	0.5
Tris(TMS) 72 h	20.17	37.52	42.31	-	0.4
Tris(TMS) 93 h	14.93	39.41	45.66	-	0.2

Table C.4. XPS data (75° take-off angle) for 11K PS-COOH adsorbed from cyclohexane (35 °C) to surfaces modified with Tris(TMS) via vapor phase reaction for increasing amounts of time.

sample	atomic concentrations (%)				thickness nm
	C	O	Si	N	
clean Si	67.98	13.89	18.13	-	3.4
Tris(TMS) 1 h	58.59	18.23	23.18	-	2.4
Tris(TMS) 4 h	58.00	18.77	23.23	-	2.3
Tris(TMS) 24 h	34.66	29.81	35.52	-	0.9
Tris(TMS) 72 h	32.31	31.35	36.34	-	0.8

Table C.5. XPS data (75° take-off angle) for 41K PS-COOH adsorbed from toluene to surfaces modified with Tris(TMS) via vapor phase reaction for increasing amounts of time.

sample	atomic concentrations (%)				thickness nm
	C	O	Si	N	
clean Si	23.58	37.15	39.27	-	1.3
Tris(TMS) 1 h	24.37	35.98	39.65	-	0.8
Tris(TMS) 4 h	21.89	36.30	41.81	-	0.6
Tris(TMS) 24 h	17.17	39.17	43.66	-	0.5
Tris(TMS) 51 h	17.98	39.35	42.68	-	0.5
Tris(TMS) 72 h	18.88	38.83	42.29	-	0.4

Table C.6. XPS data (75° take-off angle) for 11K PS-COOH adsorbed from toluene to surfaces modified with Tris(TMS)/ABDMS via vapor phase reaction.

sample	atomic concentrations (%)				thickness nm
	C	O	Si	N	
clean Si / ABDMS	42.30	26.83	29.47	1.40	0.9
Tris(TMS) 1 h / ABDMS	42.90	25.53	30.10	1.47	0.8
Tris(TMS) 4 h / ABDMS	50.76	21.81	25.81	1.62	-
Tris(TMS) 24 h / ABDMS	34.02	30.01	35.13	0.83	0.3
Tris(TMS) 72 h / ABDMS	31.23	31.59	35.98	1.20	0.2

Table C.7. XPS data (75° take-off angle) for 11K PS-COOH adsorbed from THF to surfaces modified with Tris(TMS)/ABDMS via vapor phase reaction.

sample	atomic concentrations (%)				thickness nm
	C	O	Si	N	
clean Si	30.14	33.03	35.14	1.7	0.4
Tris(TMS) 1 h	28.88	33.09	36.38	1.66	0.1
Tris(TMS) 4 h	30.14	33.43	34.82	1.61	<0.1
Tris(TMS) 24 h	27.40	33.95	37.16	1.50	<0.1
Tris(TMS) 72 h	20.62	36.48	42.22	0.68	<0.1

C.2. XPS Data for Protein Adsorption to Silane-modified Surfaces

Table C.8. XPS data (75° take-off angle) for organosilane-modified surfaces before and after protein (BSA) adsorption.

sample	atomic concentrations (%)				
	C	O	Si	F or S	N
C ₁₈ SAM	42.44	29.55	28.00	-	-
C ₁₈ SAM / BSA	51.45	24.51	18.87	-	5.17
C ₁₈ CAM	21.54	36.34	42.12	-	-
C ₁₈ CAM / BSA	39.77	27.67	28.64	-	3.92
C ₈ F ₁₃	12.11	35.81	41.39	10.70	-
C ₈ F ₁₃ w/ BSA	27.02	30.83	31.79	6.77	3.58
TMS	10.17	42.12	47.72	-	-
TMS w/ BSA	34.82	29.37	30.44	-	5.37
TPS	13.27	42.16	44.57	-	-
TPS w/ BSA	32.93	30.59	30.02	-	6.47
APS	14.28	37.91	46.55	-	1.27
APS w/ BSA	39.19	28.03	26.66	-	6.12
TFP	10.42	40.72	44.96	3.91	-
TFP w/ BSA	44.51	25.58	23.13	1.84	4.95
Acetoxy	10.57	42.80	46.63	-	-
Acetoxy w/ BSA	36.18	30.13	27.64	-	6.05
Carbomethoxy	17.69	37.91	44.40	-	-
Carbomethoxy w/ BSA	36.87	26.43	29.70	-	7.00
DMDC	13.36	40.45	46.20	-	-
DMDC w/ BSA	32.68	30.51	31.64	-	5.16
PEG	14.31	36.22	48.37	-	1.10
PEG w/ BSA					

-continued next page-

Table C.8. continued.

sample	atomic concentrations (%)				
	C	O	Si	F or S	N
MPTES	28.68	33.99	30.55	6.79	-
MPTES w/ BSA	45.28	25.52	19.46	3.95	5.79
MPTES-SO ₃ H	32.02	33.75	27.78	6.45	-
MPTES-SO ₃ H w/ BSA	36.07	31.35	23.23	5.00	4.34
TVS-OH	11.66	41.24	47.09	-	-
TVS-OH w/ BSA	24.57	33.12	37.04	-	5.27
clean Si	9.77	40.48	49.75	-	-
clean Si / BSA	16.28	36.70	46.44	-	0.58

Abbreviations:

- C₁₈ SAM – octadecyltrichlorosilane C₁₈ CAM - octadecyldimethylchlorosilane
- TMS – trimethylchlorosilane DMDC – dimethyldichlorosilane
- TPS – triphenylchlorosilane TFP - trifluoropropyl dimethylchlorosilane
- C₈F₁₃ – (tridecafluoro-1,1,2,2-tetrahydrooctyl)dimethylchlorosilane
- APDMS - aminopropyl dimethylmethoxysilane
- Acetoxy – acetoxypyl dimethylchlorosilane
- Carbomethoxy - carbomethoxydecyl dimethylchlorosilane
- MPTES – mercaptopropyltriethoxysilane
- MPTES-SO₃H – MPTES oxidized to the corresponding sulfonate (SO₃H) using H₂O₂
- PEG – isocyanopropyl dimethylsilyl monolayer reacted with PEG₄₀₀ at 70 °C for 4 days.
- TVS-OH – trivinylchlorosilane oxidized to the tri-ol using BH₃

Table C.9. XPS data (75° take-off angle) for Tris(TMS) mixed surfaces before and after protein (BSA) adsorption.

sample	atomic concentrations (%)				
	C	O	Si	F or S	N
Tris(TMS) 1h	11.41	43.45	45.14	-	-
Tris(TMS) 1h w/ BSA	36.38	29.85	27.71	-	6.05
Tris(TMS) 24h	8.70	42.78	48.52	-	-
Tris(TMS) 24h w/ BSA	34.59	30.02	29.22	-	6.18
Tris(TMS) 72h	10.81	43.40	45.79	-	-
Tris(TMS) 72h w/ BSA	40.43	27.88	25.38	-	6.31
Tris(TMS) 140h	11.99	42.73	45.29	-	-
Tris(TMS) 140h w/ BSA	43.06	26.67	25.17	-	5.11

Table C.10. XPS data (75° take-off angle) for Tris(TMS) / TMS mixed surfaces before and after protein (BSA) adsorption.

sample	atomic concentrations (%)				
	C	O	Si	F or S	N
Tris(TMS) 1h / TMS	11.25	43.19	45.56	-	-
Tris(TMS) 1h / TMS w/ BSA	37.81	29.69	26.71	-	5.79
Tris(TMS) 24h / TMS	10.18	42.55	47.26	-	-
Tris(TMS) 24h / TMS w/ BSA	38.71	28.89	26.75	-	5.65
Tris(TMS) 72h / TMS	10.98	42.93	46.09	-	-
Tris(TMS) 72h / TMS w/ BSA	39.70	28.51	26.51	-	5.28
Tris(TMS) 140h / TMS	11.45	43.23	45.33	-	-
Tris(TMS) 140h / TMS w/ BSA	34.46	32.14	29.88	-	3.53

Table C.11. XPS data (75° take-off angle) for Tris(TMS) / TVS-OH mixed surfaces before and after protein (BSA) adsorption

sample	atomic concentrations (%)				
	C	O	Si	F or S	N
Tris(TMS) 1h / -OH	11.82	43.03	45.15	-	-
Tris(TMS) 1h / -OH w/ BSA	34.79	30.37	28.59	-	6.25
Tris(TMS) 24h / -OH	14.54	41.18	44.28	-	-
Tris(TMS) 24h / -OH w/ BSA	36.20	29.38	28.30	-	6.12
Tris(TMS) 72h / -OH	11.99	42.46	45.55	-	-
Tris(TMS) 72h / -OH w/ BSA	36.92	29.12	27.55	-	6.42
Tris(TMS) 140h / -OH	13.93	41.52	44.54	-	-
Tris(TMS) 140h / -OH w/ BSA	39.88	28.23	25.99	-	5.89

Table C.12. XPS data (75° take-off angle) for Tris(TMS) / APDMS mixed surfaces before and after protein (BSA) adsorption

sample	atomic concentrations (%)				
	C	O	Si	F or S	N
Tris(TMS) 1h / -NH ₂	14.73	40.93	43.58	-	0.76
Tris(TMS) 1h / -NH ₂ w/ BSA	32.79	30.88	29.74	-	6.59
Tris(TMS) 24h / -NH ₂	13.55	40.79	45.09	-	0.57
Tris(TMS) 24h / -NH ₂ w/ BSA	38.09	28.16	27.05	-	6.71
Tris(TMS) 72h / -NH ₂	15.53	41.09	42.91	-	0.47
Tris(TMS) 72h / -NH ₂ w/ BSA	36.90	29.23	27.13	-	6.73
Tris(TMS) 140h / -NH ₂	13.35	41.24	44.99	-	0.42
Tris(TMS) 140h / -NH ₂ w/ BSA	39.22	27.85	26.26	-	6.67

BIBLIOGRAPHY

- Adamson, A., *Physical Chemistry of Surfaces, 4th Ed.* 1982, New York: John Wiley & Sons. 664.
- Alexander, L., *X-Ray Diffraction Methods in Polymer Science.* 1969, New York: Wiley-Interscience. 582.
- Arora, K.; Lesser, A., and McCarthy, T. *Polymer Engineering and Science*, **1998**, *38*, 2055.
- Arora, K.; Lesser, A., and McCarthy, T. *Macromolecules*, **1998**, *31*, 4614.
- Arora, K.; Lesser, A., and McCarthy, T. *Macromolecules*, **1999**, *32*, 2562.
- Arwin, H. *Applied Spectroscopy*, **1986**, *40*, 313.
- Aubert, J. and Clough, R. *Polymer*, **1985**, *26*, 2047.
- Bain, C. and Whitesides, G. *Langmuir*, **1988**, *5*, 1370.
- Baskin, A. and Boissonnade, M., in *Proteins at Interfaces II: Fundamentals and Applications*, Horbett, T. and Brash, J., Editors. 1995, American Chemical Society: Washington, DC. p. 209.
- Benoit, D.; Harth, E.; Fox, P.; Waymouth, R., and Hawker, C. *Macromolecules*, **2000**, *33*, 363.
- Bos, O.; Labro, J.; Fischer, M.; Witling, J., and Janssen, L. *Journal of Biological Chemistry*, **1989**, *264*, 953.
- Brash, J. and Horbett, T., eds. *Proteins at Interfaces: Physiochemical and Biochemical Studies.* 1987, American Chemical Society: Washington, DC. 706.
- Bungert, B.; Sadowski, G., and Arlt, W. *Fluid Phase Equilib.*, **1997**, *139*, 349.
- Burguiere, C.; Dourges, M.-A.; Charleux, B., and Varion, J.-P. *Macromolecules*, **1999**, *32*, 3883.
- Carter, D.; He, X.; Munson, S.; Twigg, P.; Gernert, K.; Broom, M., and Miller, T. *Science*, **1989**, *244*, 1195.
- Carvalho, B.; Tong, P.; Huang, J.; Witten, T., and Fetters, L. *Macromolecules*, **1993**, *26*, 4632.

- Clark, M.; Kendall, J., and DeSimone, J. *Macromolecules*, **1997**, *30*, 6011.
- Colton, J. and Suh, N. *Polymer Engineering and Science*, **1987**, *27*, 500.
- Colton, J. and Suh, N. *Polymer Engineering and Science*, **1987**, *27*, 485.
- Colton, J. and Suh, N. *Polymer Engineering and Science*, **1987**, *27*, 493.
- Creager, S. and Clarke, J. *Langmuir*, **1994**, *10*, 3675.
- Culler, S.; Ishida, H., and Koenig, J. *Journal of Colloid and Interface Science*, **1985**, *106*, 334.
- de Gennes, P. *Macromolecules*, **1980**, *15*, 492.
- DeSimone, J.; Guan, Z., and Elsbernd, C. *Science*, **1992**, *257*, 945.
- DeSimone, J.; Maury, E.; Menciloglu, Y.; McClain, J.; Romack, T., and Combes, J. *Science*, **1994**, *265*, 356.
- Eberhart, R.; Munro, M.; Frautschi, J., and Tingey, K. *IEEE/Engineering in Medicine and Biology Society Annual Conference*, **1986**, 1680.
- Fadeev, A. and McCarthy, T. *Langmuir*, **1999**, *15*, 7238.
- Fadeev, A. and McCarthy, T. *Langmuir*, **1999**, *15*, 3759.
- Fadeev, A. and McCarthy, T. *Langmuir*, **2000**, *16*, 7268.
- Ferreira, P.; Ajdari, A., and Leibler, L. *Macromolecules*, **1998**, *32*, 3994.
- Fleer, G.; van Male, J., and Johner, A. *Macromolecules*, **1999**, *32*, 845.
- Fleer, G.; van Male, J., and Johner, A. *Macromolecules*, **1999**, *32*, 825.
- Freij-Larsson, C.; Jannasch, P., and Wesslen, B. *Biomaterials*, **2000**, *21*, 307.
- Ge, S.; Kojio, K.; Takahara, A., and Kajiyama, T. *Journal of Biomaterials Science - Polymer Edition*, **1998**, *9*, 131.
- Goel, S. and Beckman, E. *Polymer Engineering and Science*, **1994**, *34*, 1137.
- Goel, S. and Beckman, E. *Polymer Engineering and Science*, **1994**, *34*, 1148.
- Goel, S. and Beckman, E. *AIChE Journal*, **1995**, *41*, 357.

- Grasel, T.; Pierce, J., and Cooper, S. *Journal of Biomedical Materials Research*, **1987**, *21*, 815.
- Hayes, H. and McCarthy, T. *Macromolecules*, **1998**, *31*, 4813.
- Heid, S.; Effenberger, F.; Bierbaum, K., and Grunze, M. *Langmuir*, **1996**, *12*, 2118.
- Henn, G.; Bucknall, D.; Stamm, M.; Vanhoorne, P., and Jérôme, R. *Macromolecules*, **1996**, *29*, 4305.
- Holmes-Farley, S.; Bain, C., and Whitesides, G. *Langmuir*, **1988**, *4*, 921.
- Holmes-Farley, S.; Reamey, R.; McCarthy, T.; Deutch, J., and Whitesides, G. *Langmuir*, **1985**, *1*, 725.
- Horbett, T. and Brash, J., eds. *Proteins at Interfaces II: Fundamentals and Applications*. 1995, American Chemical Society: Washington, DC. 561.
- Hruska, Z.; Vuillemin, B.; Riess, G.; Katz, A., and Winnik, M. *Makromol. Chem.*, **1987**, *193*, 1987.
- Hsieh, H. and Quirk, R., *Anionic Polymerization: Principles and Practical Applications*. 1996, New York: Marcel Dekker. 727.
- Iler, R., *The Chemistry of Silica*. 1979, New York: John Wiley & Sons.
- Israelachvili, J. and Gee, M. *Langmuir*, **1989**, *5*, 288.
- Iyengar, D., PhD Thesis, University of Massachusetts, Polymer Science and Engineering, **1992**.
- Iyengar, D. and McCarthy, T. *Macromolecules*, **1990**, *23*, 4344.
- Kim, M.; Fetters, L.; Chen, W., and Shen, Y. *Macromolecules*, **1991**, *24*, 4216.
- Kumakura, M.; Yoshida, M., and Asano, M. *Journal of Applied Polymer Science*, **1990**, *41*, 177.
- Kumar, S.; Suter, U., and Reid, R. *Fluid Phase Equilib.*, **1986**, *29*, 373.
- Kumar, V. and Suh, N. *Polymer Engineering and Science*, **1990**, *30*, 1323.
- Kumar, V. and Weller, J. *Polymer Engineering and Science*, **1994**, *34*, 169.
- Kung, E.; Lesser, A., and McCarthy, T. *Macromolecules*, **1998**, *31*, 4160.

- Kung, E.; Lesser, A., and McCarthy, T. *Macromolecules*, **2000**, *33*, 8192.
- Leibler, L.; Ajdari, A.; Mourran, A.; Coulon, G., and Chatenay, D., in *Ordering in Macromolecular Systems*, Teramoto, A., Kobayashi, M., and Norisuje, T., Editors. 1994, Springer-Verlag: Berlin, Heidelberg. p. 353.
- Leyden, D.; Kendall, D., and Waddell, T. *Anal. Chim. Acta*, **1981**, *126*, 207.
- Lin, Y.-S. and Hlady, V. *Colloids and Surfaces B: Biointerfaces*, **1994**, *2*, 481.
- Lin, Y.-S.; Hlady, V., and Gölander, C.-G. *Colloids and Surfaces B: Biointerfaces*, **1994**, *3*, 49.
- Liu, Y.; Wolf, L., and Messmer, M. *Langmuir*, **2001**, *17*, 4329.
- Maaloum, M. and Courvoisier, A. *Macromolecules*, **1999**, *32*, 4989.
- Maoz, R. and Sagiv, J. *Journal of Colloid and Interface Science*, **1984**, *100*, 465.
- Mathauer, K. and Frank, C. *Langmuir*, **1993**, *9*, 3446.
- McCafferty, E. and Wightman, J. *Journal of Colloid and Interface Science*, **1997**, *194*, 344.
- McGovern, M.; Kallury, K., and Thompson, M. *Langmuir*, **1994**, *10*, 3607.
- Mingalyov, P.; Fadeev, A.; Staroverov, S.; Lisichkin, G., and Lunina, E. *J. Chromatogr.*, **1993**, *646*, 267.
- Mittal, K., ed. *Adhesion Aspects of Polymeric Coatings*. 1983, Plenum Press: New York. 657.
- Mounir, E.; Takahara, A., and Kajiyama, T. *Polymer Journal*, **1999**, *31*, 89.
- Munch, M. and Gast, A. *Polymer Communications*, **1989**, *30*, 324.
- Napper, D., *Polymeric Stabilization of Colloidal Dispersions*. 1983, London: Academic Press. 428.
- Ortiz, C. and Hadziioannou, G. *Macromolecules*, **1999**, *32*, 780.
- Pangborn, A.; Giardello, M.; Grubbs, R.; Rosen, R., and Timmers, F. *Organometallics*, **1996**, *15*, 1518.
- Parikh, A.; Allara, D.; Azouz, I., and Rondelez, F. *Journal of Physical Chemistry*, **1994**, *98*, 7577.

- Petrash, S.; Sheller, N.; Dando, W., and Foster, M. *Langmuir*, **1997**, *13*, 1881.
- Pradhan, D.; Chen, C., and Radosz, M. *Ind. Eng. Chem. Res.*, **1994**, *33*, 1984.
- Prime, K. and Whitesides, G. *Journal of the American Chemical Society*, **1993**, *115*, 10714.
- Quirk, R., *Anionic Synthesis of Polymers with Functional Groups*. 1989, Oxford: Pergamon Press. 83.
- Quirk, R.; Kinning, D., and Fetters, L., in *Comprehensive Polymer Science*, Allen, G., Editor. 1989, Pergamon Press: Oxford. p. 1.
- Quirk, R.; Yin, J., and Fetters, L. *Macromolecules*, **1989**, *22*, 85.
- Reiter, G.; Auroy, P., and Auvray, L. *Macromolecules*, **1996**, *29*, 2150.
- Russell, T., in *Handbook on Synchrotron Radiation*, Brown, G. and Moncton, D., Editors. 1991, Elsevier Science: New York. p. 379.
- Scheutjens, J. and Fleer, G. *Journal of Physical Chemistry*, **1979**, *83*, 1619.
- Scheutjens, J. and Fleer, G. *Journal of Physical Chemistry*, **1980**, *84*, 178.
- Sheller, N.; Petrash, S., and Foster, M. *Langmuir*, **1998**, *14*, 4535.
- Shi, C.; Huang, A.; Kilic, S.; Xu, J.; Enick, R.; Beckman, E.; Carr, A.; Melendez, R., and Hamilton, A. *Science*, **1999**, *286*, 1540.
- Shull, K. *Faraday Discuss.*, **1994**, *98*, 203.
- Shull, K. *Macromolecules*, **1996**, *29*, 2659.
- Sigal, G.; Mrksich, M., and Whitesides, G. *Journal of the American Chemical Society*, **1998**, *120*, 3464.
- Silberzan, P.; Leger, L.; Ausserre, D., and Benattar, J. *Langmuir*, **1991**, *7*, 1647.
- Singh, N.; Karim, A.; Bates, F., and Tirrell, M. *Macromolecules*, **1994**, *27*, 2586.
- Singh, N.; Karim, A.; Bates, F.; Tirrell, M., and Furusawa, K. *Macromolecules*, **1994**, *27*, 2586.
- Siqueira, D.; Reiter, J.; Breiner, U.; Stadler, R., and Stamm, M. *Langmuir*, **1996**, *12*, 972.

- Stafford, C.; Fadeev, A.; Russell, T., and McCarthy. *Langmuir*, **2001**, in press.
- Stassin, F.; Halleux, O., and Jérôme, R. *Macromolecules*, **2001**, *34*, 775.
- Stenberg, M. and Nygren, H. *Journal de Physique*, **1983**, *44*, 83.
- Stouffer, J. and McCarthy, T. *Macromolecules*, **1988**, *21*, 1204.
- Su, T.; Green, R.; Wang, Y.; Murphy, E., and Lu, J. *Langmuir*, **2000**, *16*, 4999.
- Su, Z.; Wu, D.; Hsu, S., and McCarthy, T. *Macromolecules*, **1997**, *30*, 840.
- Szwarc, M. *Nature*, **1956**, *178*, 1168.
- Szwarc, M.; Levy, M., and Milkovich, R. *Journal of the American Chemical Society*, **1956**, *78*, 2656.
- Takahara, A.; Ge, S.; Kojio, K., and Kajiyama, T. *Journal of Biomaterials Science - Polymer Edition*, **2000**, *11*, 111.
- Takahara, A.; Kojio, K.; Ge, S., and Kajiyama, T. *Journal of Vacuum Science & Technology A - Vacuum Surfaces and Films*, **1996**, *14*, 1747.
- Taunton, H.; Toprakcioglu, C.; Fetters, L., and Klein, J. *Macromolecules*, **1990**, *23*, 571.
- Tengvall, P.; Lundstrom, I., and Liedberg, B. *Biomaterials*, **1998**, *19*, 407.
- Tremsina, Y.; Sevastianov, V.; Petrash, S.; Dando, W., and Foster, M. *Journal of Biomaterials Science - Polymer Edition*, **1998**, *9*, 151.
- Vincent, B. *Adv. Colloid Interface Sci.*, **1974**, *4*, 193.
- Vitt, E. and Shull, K. *Macromolecules*, **1995**, *28*, 6349.
- Wang, W.; Kramer, E., and Sachse, W. *Journal of Polymer Science: Polymer Physics Edition*, **1982**, *20*, 1371.
- Wasserman, S.; Tao, Y., and Whitesides, G. *Langmuir*, **1989**, *5*, 1074.
- Watkins, J. and McCarthy, T. *Macromolecules*, **1994**, *27*, 4845.
- Wertz, C. and Santore, M. *Langmuir*, **1999**, *15*, 8884.
- Wertz, C. and Santore, M. *Langmuir*, **2001**, *17*, 3006.
- Wojciechowski, P. and Brask, J. *Colloids and Surfaces B: Biointerfaces*, **1993**, *1*, 107.

- Xia, J.; Johnson, T.; Gaynor, S.; Matyjaszewski, K., and DeSimone, J. *Macromolecules*, **1999**, *32*, 4802.
- Yamamoto, S.; Tsujii, Y., and Fukuda, T. *Macromolecules*, **2000**, *33*, 5995.
- Yang, X.; Shi, J.; Johnson, S., and Swanson, B. *Langmuir*, **1998**, *14*, 1505.
- Yang, Z.; Galloway, J., and Yu, H. *Langmuir*, **1999**, *15*, 8405.
- Yoo, D.; Shiratori, S., and Rubner, M. *Macromolecules*, **1998**, *31*, 4309.
- Young, A. *Journal of Cellular Plastics*, **1987**, *23*, 55.
- Zeigler, K.; Colonius, H., and Schafer, D. *Annu. Chim.*, **1929**, *473*, 36.
- Zeigler, K.; Jakob, L.; Wolltham, H., and Wenz, A. *Annu. Chim.*, **1934**, *511*, 64.
- Zeigler, K. and Schafer, D. *Annu. Chim.*, **1930**, *479*, 150.
- Zhang, H. L.; Zhang, H.; Zhang, J.; Liu, Z., and Li, H. *Journal of Colloid and Interface Science*, **1999**, *214*, 46.
- Zhuravlev, L. *Langmuir*, **1986**, *3*, 316.

